NATURAL AND ARTIFICIAL FLUORESCENCE ON 3-DIMENSIONAL BIOORGANIC NANOSTRUCTURES

A Dissertation
Presented to
The Academic Faculty

by

Craig Granberry Cameron

In Partial Fulfillment
of the Requirements for the Degree
Doctor of Philosophy in the
School of Materials Science and Engineering

Georgia Institute of Technology
May 2014

NATURAL AND ARTIFICIAL FLUORESCENCE ON 3-DIMENSIONAL BIOORGANIC NANOSTRUCTURES

Approved by:

Dr. Kenneth H. Sandhage, Advisor
School of Materials Science and Engineering
Georgia Institute of Technology

Dr. Mohan Srinivasarao
School of Materials Science and Engineering
Georgia Institute of Technology

Dr. Joshua Borneman
Electro-Optic Technology Division
Crane-Division, Naval Surface Warfare Center (NSWC Crane)

Dr. Christopher Summers
School of Materials Science and Engineering
Georgia Institute of Technology

Dr. Seth Marder
School of Chemistry and Biochemistry
Georgia Institute of Technology

Date Approved: April 3, 2014

To my parents, Hugh and Nancy Cameron,
your love and support made this accomplishment possible.

ACKNOWLEDGEMENTS

"You never know where a butterfly will lead you."

– Dr. Robert Robins, Smithsonian Institution National Museum of Natural History

Dr. Robins, your statement could not have described my Ph.D. program experience any better. The journey started with a simple question of how butterfly scales achieve their color. The *Parides sesostris* and *Morpho rhetenor* butterflies then led an adventure from the collections at the Smithsonian Institution, to the Naval Research Laboratory, Scripps Institution of Oceanography, and, finally, to the Naval Surface Warfare Center in Crane, IN. This journey would not be complete without the help of many mentors, colleagues, and friends along the way.

First and foremost, I would like to thank my advisor, Dr. Kenneth Sandhage for his guidance and encouragement. The freedom and patience that you had in letting me develop my research path and the guidance in adjusting my trajectory has been invaluable in becoming the independent researcher that I am today. Your ability to generate ideas, creative solutions, and multitasking ability has never ceased to amaze me. I would like to thank my other dissertation committee members at Georgia Tech: Dr. Christopher Summers, Dr. Mohan Srinivasarao, and Dr. Seth Marder. The time each of you has spent mentoring me and discussing science has made a lasting contribution to my career development. Your willingness to open your research laboratories to me has been invaluable for completing this work. Finally, I would like to thank Dr. Joshua Borneman from the Naval Surface Warfare Center (NSWC) in Crane, Indiana for serving on my committee. You have helped me realize the broader impact of my research on the

scientific community and provided an exemplary example of scientist and engineer. I look forward to working with you when I join Crane full-time.

My dissertation work would not be possible without research funding from my advisor (BioOptics MURI, Dr. Hugh DeLong, program manager), the Boeing Fellowship from the School of Materials Science and Engineering at Georgia Tech, and the SMART Scholarship for Service Program. I appreciate the guidance and “bridge” provided by David Acton, linking life at Georgia Tech to life at NSWC Crane. Guidance and support from colleagues at NSWC Crane is deeply appreciated: Keith Lannan, Jessica Dorsam, Aaron Cole, Dr. Kiron Mateti, and Bill Hurley. I look forward to starting work with each of you in the coming months. Support and assistance from Dr. Edward Aifer and Dr. Robert Walters at the Naval Research Laboratory in Washington D.C. is also appreciated. I am very glad that we had the opportunity to work together for a few months and look forward to continuing our interaction over the next few years.

Dr. Vincent Chen and Dr. Joseph Perry have been invaluable collaborators for investigating fluorescence on the native and coated butterfly scales. I especially appreciate the weekly brainstorming sessions with Dr. Chen. Dr. Peter Vukusic is another invaluable collaborator along with his students Alfred Lethbridge and Caroline Pouya. I owe a lot of my understanding of structural color to the countless conversations and email exchanges with each of them. The support of Dr. Dimitri Deheyn and Russell Shimada has equally been invaluable in the early investigations of fluorescence from *P. sesostris* scales. Your hospitality in San Diego, willingness to discuss ideas, and excitement for this work represent some of my fondest memories from my Ph.D. program.

I don't know where I would be without the help of Dr. Yunshu Zhang. Your assistance in keeping the lab well stocked and rapidly responding to my requests for more supply orders took away a lot of stress, enabling me to focus on my research. Dr. Ye Cai has been an incredibly helpful colleague for discussing approaches to FIB milling and providing research support through his TEM expertise. I would like to thank all members of the Sandhage group: Dr. Yunnan Fang, Ben Deglee, Brandon Goodwin, Philip Brooke, Yihong Lee, Taylor Shapiro, Ari Gordin, Dr. Stan Davis, Dr. Jonathan Vernon, Dr. Dan Berrigan, Dr. Samuel Shian, Patrick Shower, and Dr. David Lipke. Our conversations have been extremely fruitful and too numerous to recount here as well as your help regarding research equipment. I would also like to thank Terra Freking for her assistance in the School of Materials Science and Engineering Undergraduate Research Scholar Program. Being your mentor for the last year has been a rewarding and rich learning experience. I wish you the best of luck as you continue your engineering education.

Experimental research would not be complete without high tech characterization tools and the dedicated people that train users and maintain the equipment. I would like to acknowledge Joel Pikarsky for his enthusiasm, high standards, and out-standing knowledge of Focused Ion Beam (FIB) systems. All of which made a significant impact on my ability to troubleshoot and develop the milling process used in Chapter 1. I would also like to thank Eric Woods for keeping the FIB operational and his willingness to discuss processing issues. The imaging in Chapter 2 and 3 would not be possible without the help of Yolande Berta and Tiejun Zhang for SEM training and system maintenance. I would like to thank Dr. Archana Jaiswal and Dr. Mark Poggi for their assistance with troubleshooting the Quartz Crystal Microbalance and numerous discussions of the instrument operating principles. I greatly appreciate enlightening discussions and time spent assisting my research efforts from Dr. Robert Robins, Brian Harris, and Matt Bootman.

It has been a pleasure and enriching experience serving on the Library Graduate Student Advisory Board for the last two years. I would like to thank Lori Critz, Crystal Renfro, and Susan Bowman for this opportunity. My experience at Georgia Tech would not have been as satisfying without the instruction and help of numerous professors during my coursework (in no particular order): Dr. Thomas Gaylord, Dr. Anthony Yezzi, Dr. Muhannad Bakir, Dr. David Citrin, Dr. Ali Adibi, Dr. Kenneth Sandhage, Dr. Naresh Thadhani, Dr. Meilin Liu, Dr. Brent Carter, Dr. Zhong Lin Wang, Dr. Thomas Sanders, Dr. Arun Gokale, and Dr. Benjamin Klein. The material covered in each of your classes made a positive impact on my research and provided the scientific background necessary to start my career.

A very big thank you goes to Dr. Wallace Carr. The amount of respect, genuine request for input, trust, and confidence was unparalleled in my experience as a teaching assistant. I appreciate the opportunity you gave for instructing two course sessions for MSE 3210 - Heat and Mass Transfer. The experience helped me consider teaching as a possible career direction.

My experience in the MSE program would not be complete without the assistance of the following staff members: Susan Bowman, Mechelle Kitchings, Teresa Nelson, and Angie Beggs. Each of you give the MSE department its friendly and supportive attitude.

I would like to thank Alan Annicella, Barbara Vicar, and the Atlanta West Coast Swing dancing community. I’ve learned a lot from all of you, both on and off the dance floor. I would have probably gone crazy without dancing and your friendship as an outlet for my Ph.D. work. I look forward to seeing everyone again at dance events across the country. I deeply appreciate the support from my uncles, Philip and Kenneth Granberry, for tax preparation and dinners at Morton’s™ Steakhouse. Finally, I would like to thank my parents, Hugh and Nancy Cameron, for their love and support. Without it, this accomplishment (and many more) would not have been possible.

TABLE OF CONTENTS

LIST OF TABLES

Page

LIST OF FIGURES

LIST OF SYMBOLS AND ABBREVIATIONS

A.U.	Arbitrary Units
ALD	Atomic Layer Deposition
Aminosilane	N^1-(3-Trimethoxylsilylpropyl)diethylenetriamine
BCECF	2’,7’-Bis(2-carboxyethyl)-5(6)-carboxyfluorescein
EDS	Energy Dispersive X-ray Spectroscopy
Em	Emission
Ex	Excitation
FFT	Fast Fourier Transform
FIB	Focused Ion Beam
FITC	Fluorescein isothiocyanate
FWHM	Full Width at Half Maximum
LED	Light Emitting Diode
LP	Long Pass
m	Diffraction order
M. rhetenor	*Morpho rhetenor*
n	Refractive index
P. sesostris	*Parides sesostris*
Polyacrylate	Dipentaerythritol penta-/hexa-acrylate
Polyamine	Tris(2-aminoethyl)amine
PTFE	Polytetrafluoroethylene
QCM-D	Quartz Crystal Microbalance with Dissipation
SEM	Scanning Electron Microscopy
SERS	Surface Enhanced Raman Scattering
STEM HAADF	Scanning Transmission Electron Microscopy High Angle Annular Dark Field
TEM	Transmission Electron Microscopy
UV	Ultraviolet
θ	Diffraction angle (degrees)
λ	Wavelength (nm)
Λ	Grating period (nm)

SUMMARY

A challenge exists for understanding the origin of color for structurally colored, 3-dimensional bioorganic nanostructures, such as the scales of butterflies, beetles, and moths. Complex, hierarchical structures found within such scales create the overall scale appearance. The controlled alteration of color through material deposition and the addition of new optical functionalities to such structures are other areas of scientific interest. This dissertation addresses these challenges with a first-of-its-kind, systematic isolation (deconstruction) of scale component nanostructures, followed by evaluation of optical property/structure correlations. The additive deposition (constructive alteration) of emissive materials to structurally-colored templates complements this deconstructive approach towards understanding the origin of color in butterfly scales. Discoveries made through this work may help advance the bioinspired design of synthetic optical structures and subsequent color control through the addition of multilayered, emissive optical components.

Three specific research thrusts explore the use of deconstructive and constructive approaches for understanding coloration in butterfly scales. The first utilized Focused Ion Beam (FIB) milling to isolate scale component structures found within the green scales of the *Parides sesostris* butterfly. Optical appearance was correlated with different retained structural component combinations, which enabled discoveries regarding the origin of color at the scale component level. Primarily, a gyroid crystal structure with a gradient in pore spacing was found to produce the broad (green-to-blue) reflection within a single green scale. Such a discovery would not have been possible for optical examinations limited to whole scales. Next, the addition of emissive coloration from an organic fluorescent dye to the structurally colored blue scales of *Morpho rhetenor* was investigated. An approach for the layer-by-layer deposition of organic fluorescent dye multilayers was developed for the successful alteration of induced fluorescence coloration and intensity. Such films exhibited transient emissive behavior as a result of photobleaching of the fluorescent organic dye (*i.e.*, the emission intensity decreased with continued exposure to light). The starting scale structure was preserved throughout the deposition process. The deposited fluorescence layers also altered the scale reflectance. Finally, a layer-by-layer method of depositing quantum dot multilayers onto the scales of *Morpho rhetenor* butterflies was investigated. The increase in emission intensity with iterative quantum dot layer deposition was demonstrated with this method. Additionally, coated scales exhibited photoluminescent enhancement (*i.e.*, an increase in emission intensity with exposure time) due to the photophysical characteristics of the quantum dots integrated into the multilayer film. Color mixing was demonstrated between the emitted quantum dot coloration and the reflected, structural coloration of the butterfly scale template. Although the coated scale structure was preserved, reflectance was altered with this coating methodology up to 8 applied layers.

CHAPTER 1: Optical Characterization of Isolated Scale Component Nanostructures of the Butterfly, *Parides sesostris*

1.1 Summary

A challenge exists for researchers in understanding how the complex, nanostructured components found within bioorganic nanostructures, such as butterflies, cooperatively interact to produce their overall color and appearance. This challenge was addressed in this work by developing a widely applicable method of isolating butterfly scale component structures and optically interrogating the selectively deconstructed samples. This approach has improved the current understanding of the origin of color in the green scales of the *P. sesostris* butterfly.

P. sesostris scales have undergone a rigorous interrogation in this work with reflectance, transmittance, absorbance, and emission measurements. The application of FIB milling for precise scale component isolation enabled discoveries that were never apparent through prior, whole scale studies. The gathered evidence supports structural coloration from the graded spacing of pores, through the thickness of a gyroid structure, as the dominant source of scale coloration, with pore spacings distributed between 220 ± 6 nm and 259 ± 11 nm for a hexagonal polycrystal face. This work provides the first identification of chirped (*i.e.*, graded period) photonic crystal in a biological assembly. Light emission, excited from the ultraviolet (UV) to violet and having the same peak emission (538 ± 3 nm) as the scale reflectance (544 ± 11 nm), was discovered. However, such fluorescent emission did not significantly contribute to the overall scale coloration.

Imaging and reflection measurements from unmilled and ridges-removed samples supported the hypothesis of the ridge structure suppressing polycrystal iridescence. Structural analysis of the isolated ridge structure revealed two pore periodicities: 742 ± 15 nm and 228 ± 17 nm. Diffraction associated with the 742 ± 15 nm period was consistent with being the source of directional scattering observed through imaging scatterometry. The directional scattering observed on a single scale was also preserved at the wing level, across hundreds of scales, due to a preferred scale alignment.

1.2 Introduction

Coloration due to the complex nanoscale structures found within the scales of butterflies, beetles, and moths (known as "structural coloration") has attracted considerable scientific interest.[1-3] Exploration of the origin of such structural coloration has led to numerous discoveries and application development.[4-11] For example, the iridescent, blue scales found in *Morpho* butterflies have undergone numerous experimental [12-15] and simulation-based [13, 15-23] studies. The knowledge gained regarding how the complex scale structures interact with light to produce the overall coloration has enabled the synthetic replication of structures with such coloration.[24-30] A range of applications have been identified, enabled by the fundamental understanding of *Morpho* scale coloration: display technologies [24, 25], high sensitivity vapor sensors [4], and infrared detector configurations [9]. The complex scale features found on the *Morpho* butterflies represent a subset of the numerous scale morphologies responsible for vivid scale coloration in nature.[31, 32] Correlating the observed optical properties with scale structure for other, less studied species could provide a knowledge base for further discovery and application development.[1, 33]

Scale coloration cause can be the result of the cooperative interaction across numerous scale components.[3] Complexity in both structure and optical signature creates a challenge for researchers in understanding how natural structures control light.[2] Isolating and optically interrogating the nanoscale features present on an individual, butterfly scale is a way to address this challenge. This work focuses on developing and implementing such a process towards understanding the role of each structural feature on the overall coloration and appearance on a single, butterfly scale.

1.3 Literature Review

Structural coloration found in insects has been the subject of scientific investigations for over a century.[31, 34-37] Mason examined structural coloration by immersing a variety of structurally colored wing sections in fluids of different refractive indices.[31, 34-36] He found that the iridescent coloration from many species disappeared upon immersion in certain fluids.[31, 34-36] The brilliant coloration returned, once the fluid evaporated.[31, 34-36] From these experiments, Mason suggested a connection for some insect coloration to that of thin, reflecting films.[31, 34-36] Further study of insect nanostructures, via electron microscopy, revealed numerous, complex, and hierarchical nanostructures within the scales of many butterflies and beetles.[31, 38-45]

Structurally colored butterfly scales are often composed of multiple, complex nanostructures, each providing an optical contribution to the overall color and appearance of the scale.[2, 3] This complexity often makes understanding the role of each structure, within a single butterfly scale, difficult.[2] Comparison of scale structure between species with similar scale morphology and color can add insight to structure-appearance correlation.[46] This interrogation method suffers from complicated changes between each species.[46] For example, Poladian, *et. al.* compared four butterfly species containing similar polycrystal morphologies and ridge structures.[46] Both the polycrystal domain size and the average thickness of the ridge structure varied between each of the species, yet the qualitative appearance of each scale appeared similar.[46] The authors postulated that small polycrystal domains [46, 47] and large ridge structure thicknesses suppressed the iridescence (*i.e.*, angle dependent color) of the polycrystal [46]. A strategy of isolating structural features of interest and subsequent optical interrogation may alleviate the reliance on interspecies comparisons.

Focused Ion Beam (FIB) milling enables the rapid (less than 2 hours) removal of material volumes on the order of 10 μm x 10 μm x 10 μm , with high precision in location and size.[48] For this reason, FIB milling is a promising method for scale component isolation. Structurally colored butterfly scales, typically, have scale widths within the range of 40 - 100 μm.[12, 49, 50] Optical interrogation methods, such as imaging scatterometry [51], microspectrophotometry [52], and optical microscopy can interrogate areas on the order of 10 μm x 10 μm. Thus, the combination of FIB milling for the systematic scale component isolation, followed by optical interrogation with imaging scatterometry and optical microscopy, may enable the role of each structural component to be unambiguously determined.

Few attempts have been made in the literature at exposing and isolating individual structural components from photonic structures found in nature. Double-sided, sticky tape was used to delaminate the ridge structure from the polycrystal on a single *Parides sesostris* scale.[46] This method requires a great deal of luck in finding a precisely deconstructed scale, will damage the scale through the formation of pits on the scale surface [46], and can add adhesive material to the scale hampering its optical characterization. Scales can be mechanically cleaved, but such a method can lack the selectivity required to controllably remove specific scale features.[53] FIB milling was used by Wang, et al. [54] to structurally modify a butterfly scale structure, but their work did not attempt the precise separation and detailed optical interrogation of each scale component structure. Galusha, *et al.* performed top-down milling of a beetle scale to expose the photonic crystal region, buried underneath a solid, homogeneous layer.[55-57] This work [55-57] did not attempt the systematic isolation of scale components in order to determine their optical roles.

The present work seeks to create a greater understanding of the origin of the color in *P. sesostris* green scales by systematically isolating and optically interrogating particular scale component structures. An optical image of the *P. sesostris* butterfly is shown in **Figure 1 (a)**. Current understanding of the *P. sesostris* green scales is that three structural components contribute to the overall, diffuse green color: a gyroid polycrystal and a ridge structure (composed of a nanotube array and a periodic fin structure) (**Figure 1 (b)**).[32, 46, 50, 58, 59] The green color is believed to originate from the gyroid polycrystal structure.[32, 50, 58] Both modeling [50] and X-ray diffraction studies [60] show that the polycrystal is composed of grains with single-network, gyroid crystalline symmetry ($I4_132$). Structural models using Transmission Electron Microscope (TEM) images [58] and ideal gyroid structures [50] have concluded that the overall green coloration is due to such structure, as opposed to pigmentary coloration.

A schematic summarizing the literature understanding for the green scale coloration is shown in **Figure 1 (c)**. It is believed that the green color originates from the polycrystal, which is iridescent, reflecting ultraviolet (UV), blue, and green light.[50] This reflected light transmits through the ridge structure, where the UV and blue components are absorbed by a localized pigment.[46, 50] The unabsorbed green light transmits through the ridge structure and is scattered, producing the overall, diffuse, green color observed with the sample oriented ridge side up.

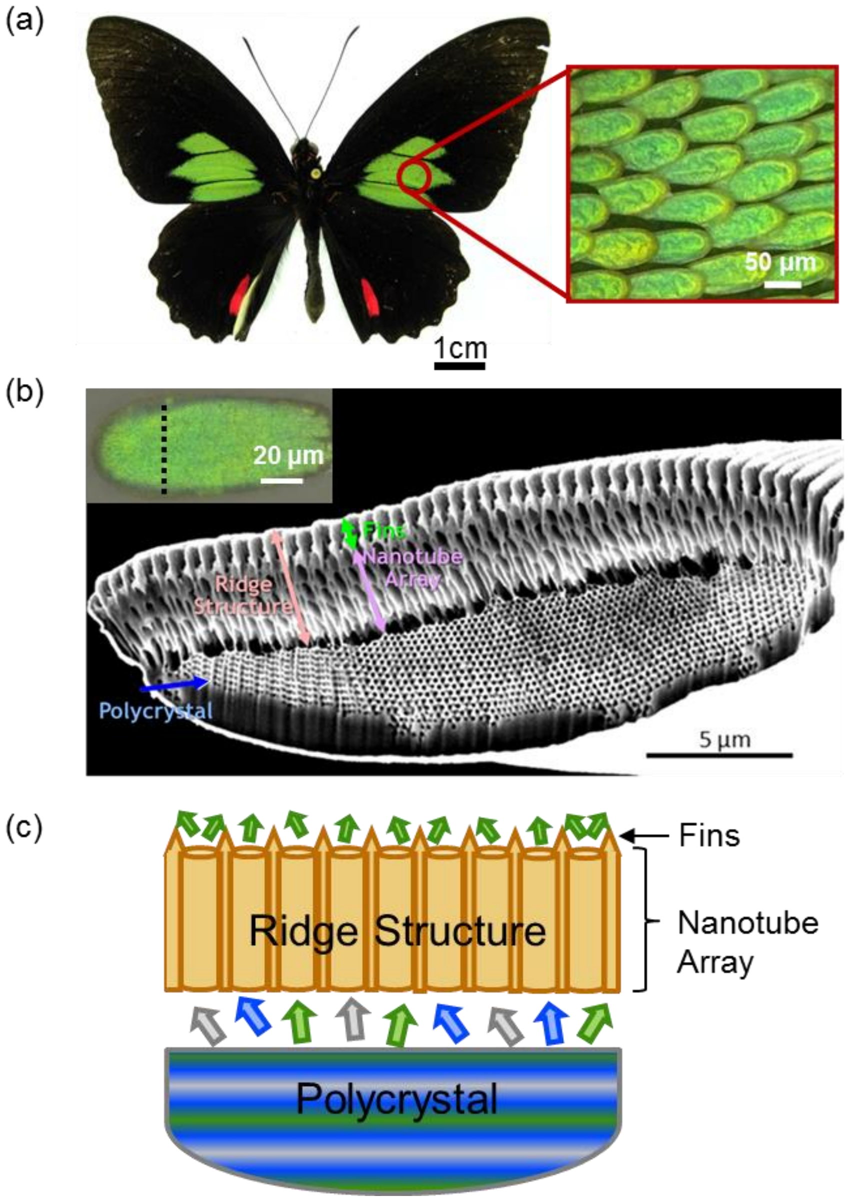

Figure 1. (a) The male butterfly, *Parides sesostris* © Smithsonian Institution National Museum of Natural History (Inset) Bright field optical image of the green scales imbricated on the forewing, forming the green patches. (b) Focused Ion Beam (FIB) cross-section of a single, green scale showing the three structural features known in the literature: polycrystal and a ridge structure composed of a nanotube array and a periodic fin structure. (Inset) single green scale in plan view showing the direction of the cross-sectional cut (dotted line). (c) Summary of literature understanding of *P. sesostris* green scale coloration.[50] The polycrystal is believed to reflect UV, blue, and green light. Blue and UV wavelengths are believed to be absorbed by a pigment localized in the ridge structure. Green wavelengths are transmitted (due to low absorption) and are scattered by the ridge structure, creating the overall, omnidirectional green coloration.

1.4 Experimental Procedures

1.4.1 Method for scale feature isolation with FIB milling

P. sesostris butterflies were purchased from The Bugmaniac (Makassar, Indonesia). Single scales were mounted to the tip of a tungsten needle (Model 7A probe, Micromanipulator Company, NV, USA) to facilitate FIB milling and optical characterization due to a greater ease of positioning the scale. Needle mounting of scales (if performed properly) also limited the materials around most of the optical structure to just native/milled scale and air.[12] Competing optical effects due to epoxy infiltration into the scale, epoxy covering part of the scale surface, or other materials on which the scale is mounted may change the scale's optical appearance (**Appendix A, Figure 64**). The interference of epoxy with the optical measurements may be mitigated by using scales that have minimal epoxy coverage and/or milling and performing characterization away from the affected region.

Scales were scraped from a given butterfly wing onto a petri dish lid with the use of a pointed tip, soft, nylon, bristle paintbrush (McMaster Carr, GA, USA). A micromanipulator probe holder and station (Micromanipulator Company, NV, USA) were used to position a needle (Model 7A probe, Micromanipulator Company, NV, USA) above the scale. 5-minute epoxy (Gorilla 5 minute Epoxy, OH, USA) was mixed and applied to the needle tip with a 1 mL plastic pipet tip (VWR International, PA, USA). Excess epoxy was removed from the needle tip by repeatedly making contact between petri dish and needle tip, away from the to-be-mounted scale. This helped minimize the infiltration of excess epoxy into the scale. The epoxy-bearing needle was then lowered onto the scale until contact was made. The needle, with the attached scale, was raised so that both were no longer in contact with the petri dish. Approximately five minutes was then allowed for the epoxy to dry. A new batch of epoxy was mixed prior to every scale-to-needle mounting. Otherwise, mounted scales fell off of the needle tip if the epoxy was considerably cured prior to scale mounting. **Figure 2** provides an example of a single butterfly scale (*Morpho rhetenor*, in this case) mounted to a needle tip, as described above.

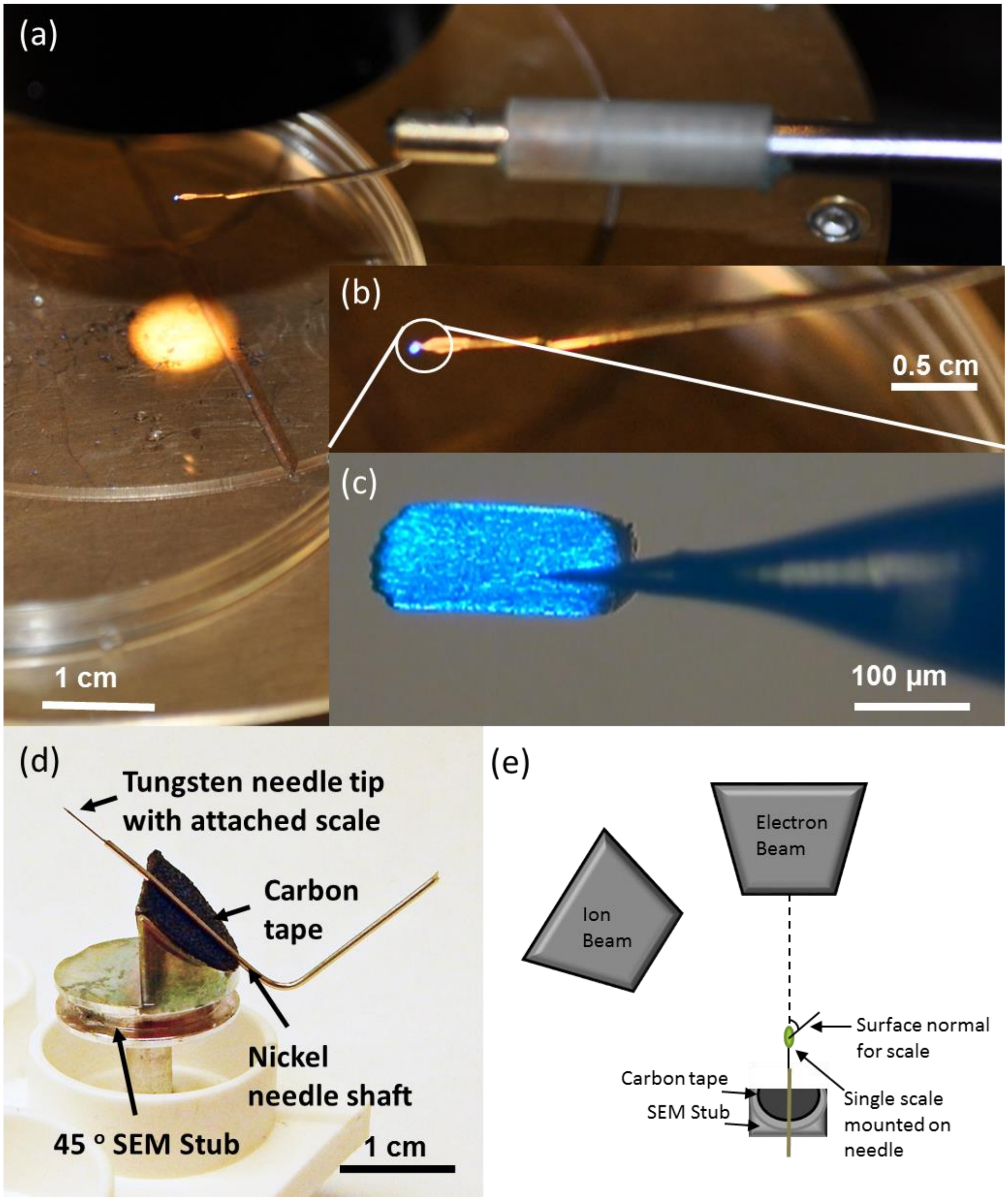

Figure 2. Optical images of progressively increasing magnification (a to c) showing a single *Morpho rhetenor* scale successfully mounted to a needle tip. (d) Optical image of needle-mounted scale fixed to a 45 ° SEM stub for subsequent FIB milling. (e) Schematic illustrating the typical, relative position of the needle-mounted scale to the ion and electron beam columns inside the FIB sample chamber. The scale was typically oriented with the surface normal (in ridge-side-up orientation) at a 45 ° angle to the viewing direction of the electron column (indicated by the dotted line).

A needle (with a fixed, single scale at the needle tip) was fixed to a 45 ° oriented, aluminum Scanning Electron Microscopy (SEM) stub (Ted Pella, CA, USA) with a square of carbon tape (Ted Pella, CA, USA) and then inserted into the FIB/SEM chamber (Nova Nanolab 200 FIB/SEM, FEI, OR, USA) (**Figure 2 (d, e)**). Typically, the scale was oriented ridge-up, tilted at approximately 45 ° relative to the viewing direction from the electron column as indicated in **Figure 2 (e).** However, the scale orientation was altered if such a scale orientation did not provide the proper alignment of the scale with respect to the milling orientation as described in **Figure 3**.

Milling was performed using a 30 keV accelerating voltage and ion beam currents ranging from 0.5 to 3.0 nA, after the sample was positioned appropriately. All milling of native scales was performed with respect to a gold ion milling reference (*i.e.,* a sputter rate of 1.5 $\mu m^3/(nA \cdot s)$). This sputter rate approximated the milling of the native scale material well, reducing the overall milling time. Timely milling of harder materials, such as crystalline titania, may be accomplished by switching the milling reference to Si_3N_4, or a similar material. The sample was then removed from the chamber and subsequent optical interrogation was performed.

Appropriate positioning and FIB milling of the sample was accomplished by first milling a cross-sectional cut through the thickness of the butterfly scale (using the predefined "cleaning cross-section" pattern on FEI FIB systems). The sample was moved such that the newly exposed cross-sectional face was observed in the ion beam view-screen as shown in **Figure 3 (a)**, for a native *P. sesostris* scale. Another cleaning cross-section pattern was defined over the scale component that was to be removed (**Figure 3 (b)**). For example, it was desired that the base of the scale be removed, so as to expose the polycrystal in **Figure 3**. An ion beam current of typically 1.0 - 3.0 nA, was used for the bulk removal of the scale material. Significant surface roughness, often referred to as “curtaining” [48], remained after the first milling step (**Figure 3 (c)**). **Figure 5** provides an example of curtaining for a cross-sectional face. The curtaining (**Figure 3 (c))** in the milled section (a region approximately 100 nm thick) was removed by a subsequent ion milling at a lower ion beam current [48], typically at 0.5 nA, so as to leave a relatively smooth surface for optical interrogation, with minimal FIB milling artifacts (**Figure 3 (d)**). A clean bottom surface may be observed in **Figure 3 (e)** in cross-sectional view with the exposed surface shown in **Figure 3 (f)**.

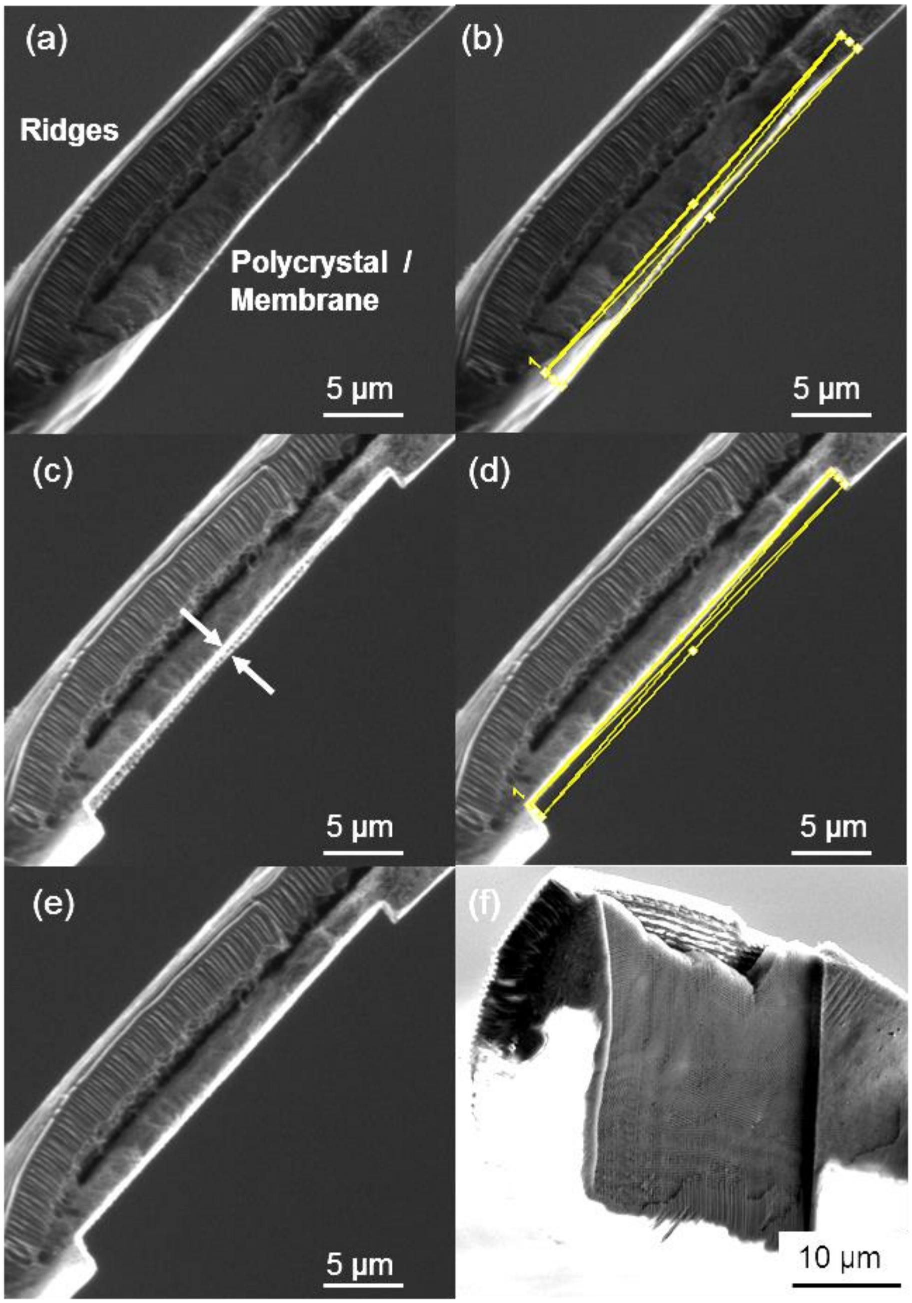

Figure 3. Illustration of scale feature isolation through FIB milling. (a) A cross-sectional face of the scale was found/created and then viewed via the ion beam. (b) A milling pattern, “cleaning cross-section” (for FEI systems) was selected and applied at a moderate ion beam current (1.0 – 3.0 nA). (c) A slight roughness (a region approximately 100 nm thick) can be observed at the interface, referred to as “curtaining” [48] (highlighted by white arrows). (d) A new cleaning cross-section pattern was defined at a lower ion beam current (0.3 – 1 nA) in order to remove the curtaining leftover from the higher ion beam current mill. (e) The final, cleaned interface was produced. (f) The view was rotated approximately 90 ° (with the assistance of switching to the electron beam, for imaging) to observe the newly exposed scale surface. This entire process may be completed with a native scale (*i.e.*, no metallic sputter coating required).

Scale components could be rapidly (less than 2 hours) isolated from the original, native, *P. sesostris* green scale using the FIB milling method described above, without the application of a conductive metal film. The size of the milled region could be varied to fit the desired application for optical/spectroscopic interrogation. For instance, samples intended for study with a microspectrophotometry system (smallest beam size of approximately 12 μm x 12 μm) had milled regions at least 20 μm wide and 20 μm long in order to accommodate the measurement.

Prior FIB milling procedures for studying butterfly/beetle scales utilized a top-down milling approach (**Figure 4 (b)**) to remove a homogenous cover layer encapsulating a polycrystal.[55-57] Such a method has worked well for the removal of homogenous material because platinum deposition [55] assists in milling uniformity with ion milling at low ion beam currents [48, 61]. However, this method would cause considerable non-uniformity in modification of a porous template with significant, spatial contrasts in material density (*i.e.,* chitin/air/chitin/air…). The lower density regions would be milled more rapidly than the higher density regions, resulting in uneven milling throughout the scale thickness.

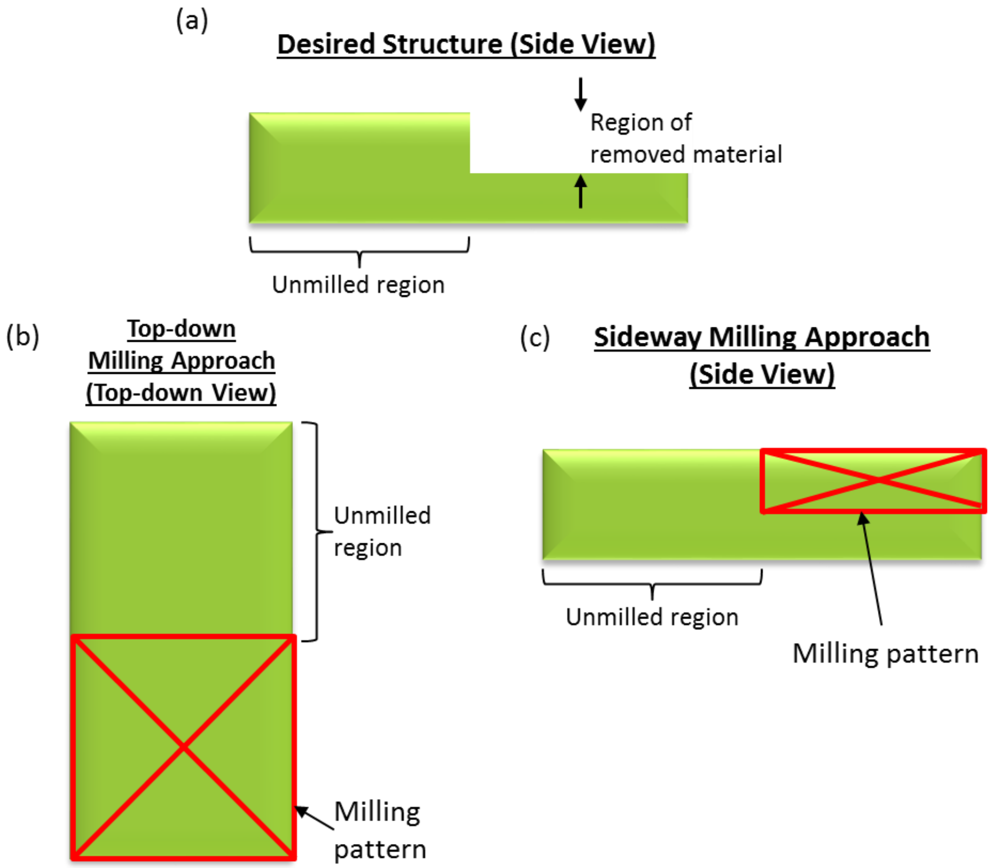

Figure 4. Top-down versus side-milling approaches for FIB milling. (a) The desired structure after FIB milling, indicating the unmilled region and the region of removed material. Two approaches could be applied to achieve the desired partially milled structure: (b) top-down milling (viewed from top-down) and (c) sideway milling (shown in side view). In both cases, the red outline indicates the approximate position of the milling pattern as seen through the ion beam in the FIB system.

The FIB milling method utilized in this work improved upon the processes in the existing literature [55-57] by enabling the rapid (less than 2 hours) removal of complex nanoscale features possessing significant variations in material density. This was achieved by FIB milling the nanostructured component through a sideway milling approach (**Figure 4 (c)**). Such a method enabled the uniform removal of nanostructured scale regions possessing a significant variation in spatial material density (*i.e.*, without uneven milling of the isolated scale structure). This was a result of the complete (sideway) removal of the scale material underneath the milling pattern as shown in

Figure 4 (c). In contrast, the top-down milling approach (**Figure 4 (b)**) relied on the termination of FIB milling after the desired thickness of material had been removed in order to achieve a similar result.

Use of a FIB tool enabled scale component isolation, and subsequent optical characterization, but such a process did have limitations. FIB milling of the *P. sesostris* butterfly has been limited to milling only on a single side of the scale. The scale top (ridges) or bottom (polycrystal area) could be efficiently removed, but not both on the same sample. Milling performed on both the top and bottom of the same scale resulted in warping of the scale, during the ion milling. This resulted in the nonselective milling of scale components due to scale movement with respect to the predefined milling pattern. (The scale could only be observed before and after the milling was completed. This prevented the milling from being stopped before a portion of the scale was unselectively milled.) One-sided milling of areal regions, larger than approximately 60 % of the planar scale area, failed for the same reason. Smaller regions may be milled and/or milling can be performed in the central region of the scale. Milling in the central region left portions of the whole scale intact at either end of the scale, providing greater mechanical support. Harder materials, such as inorganic scale replicas, are less prone to the above mechanical deformations during milling, enabling the milling of thinner regions with greater exposed areas.

Sample charging could also cause the scale to move while ion milling was performed. Shorter milling times (*i.e.,* reduced milling region size and increased ion beam current) occasionally fixed this issue. Viewing the sample by switching between the electron beam and the ion beam, prior to completion of the milling, also caused the sample to move uncontrollably, during the milling process.[48] It was found to be best to work solely by using the ion beam until the desired milling had been accomplished. Viewing the sample for a few seconds in “live view” with the ion beam at a very low magnification (the entire scale occupied approximately 30 % of the imaging window, or less) helped identify sample movement. No effect on the sample structure or coloration was observed by performing this latter operation.

Raster burn with either the electron or the ion beam occurred at high magnifications (50,000 x and higher). This affected the optical appearance of the sample, leaving it appearing black/darker than the un-imaged, surrounding regions. It was found to be best to save high magnification imaging until after the completion of all optical characterization. Viewing the sample, with the electron beam, where approximately 25 – 50 % of the scale was visible in the imaging window did not alter the sample color. No color change has been observed in the milled region versus the whole scale (unmilled region) for milled samples where these optimized procedures have been followed.

Finally, the ion beam can interact with some samples to “melt” the nanostructure (**Figure 5**).[61] This is a sample-dependent phenomenon (*i.e.*, scale-to-scale variation for *P. sesostris* samples) and was best mitigated by switching to a new sample once the apparent melting effect was observed. Observing the exposed cross-sectional face after the initial ion mill using either the electron or ion beam enabled determination of whether or not such apparent melting had occurred. Using ion beam currents greater than 3 nA could also cause apparent melting during the removal of bulk scale material (prior to the removal of curtaining). Epoxy infiltration into the scale, during needle mounting, may also have been responsible for this effect. Additional milling effects included the disintegration of very delicate nanoscale features, such as the thin, solid membrane at the base of the *P. sesostris* scale. The sample had to be positioned such that the membrane-area was not observed in the ion beam in order to avoid this effect. That is, the more structurally robust portions of the scale acted as barriers for the more delicate features.

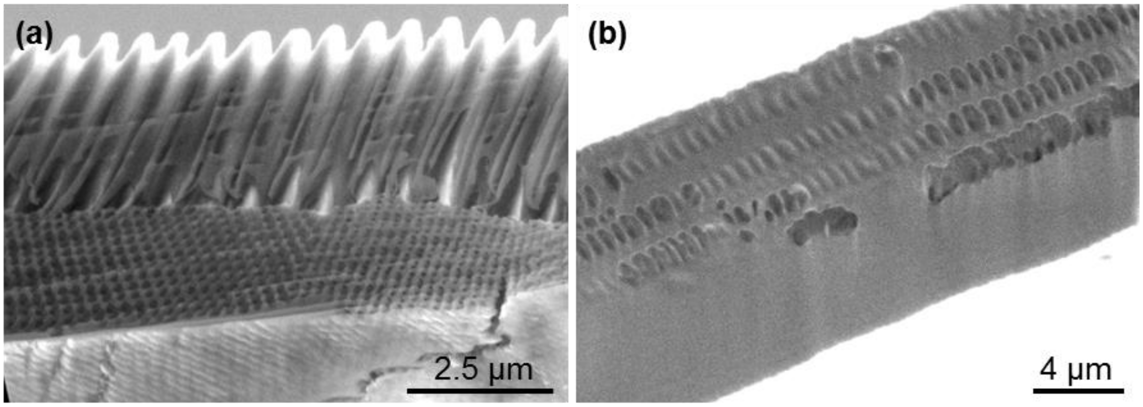

Figure 5. Example of milling artifacts observed on cross-sectional images of the *P. sesostris* green scale. (a) The curtaining (*i.e.*, lines running horizontal across the image) effect observed after high energy FIB milling. This effect may be removed by performing a subsequent, low-energy milling step. (b) Example of scale "melting", which is a sample-dependent phenomenon. It was considered best to discard the sample upon observation of such apparent melting.

1.4.2 Method of optical interrogation of isolated scale features

Structure-optical appearance correlations were obtained using a Keyence Digital Optical Microscope (VHX 600 with VH-Z250 objective, Osaka, Japan). A benefit of this microscope is the ability to generate composite images across a broad focal range. For example, the scales utilized in this study could not be captured in a single image with all portions of an individual scale in focus (**Figure 6 (a, c)**). The Keyence Digital Optical Microscope had the capability to automatically generate focus stacks, where in-focus regions from multiple images (typically 10 separate images) were merged into a single, image composite (**Figure 6 (b, d)**). This enabled the imaging of an entire FIB-milled scale with the majority of the scale components in focus. This was especially critical for qualitative analyses of polycrystal iridescence. Bright field imaging, in this system, was conducted with an approximately 90 ° angle of illumination, whereas dark field imaging was conducted with an approximately 64 ° angle of illumination.[62] Both angles were measured from a plane perpendicular to the viewing direction (**Figure 6 (e)**).[62] The white balance for each image was set by imaging a block of Teflon® in bright field imaging mode with the highest intensity available for the halogen lamp. Subsequent imaging was performed with the same lamp intensity. Detector gain was adjusted so that the brightest region of the sample was not over exposed. All imaging was performed at 1500 x (total magnification).

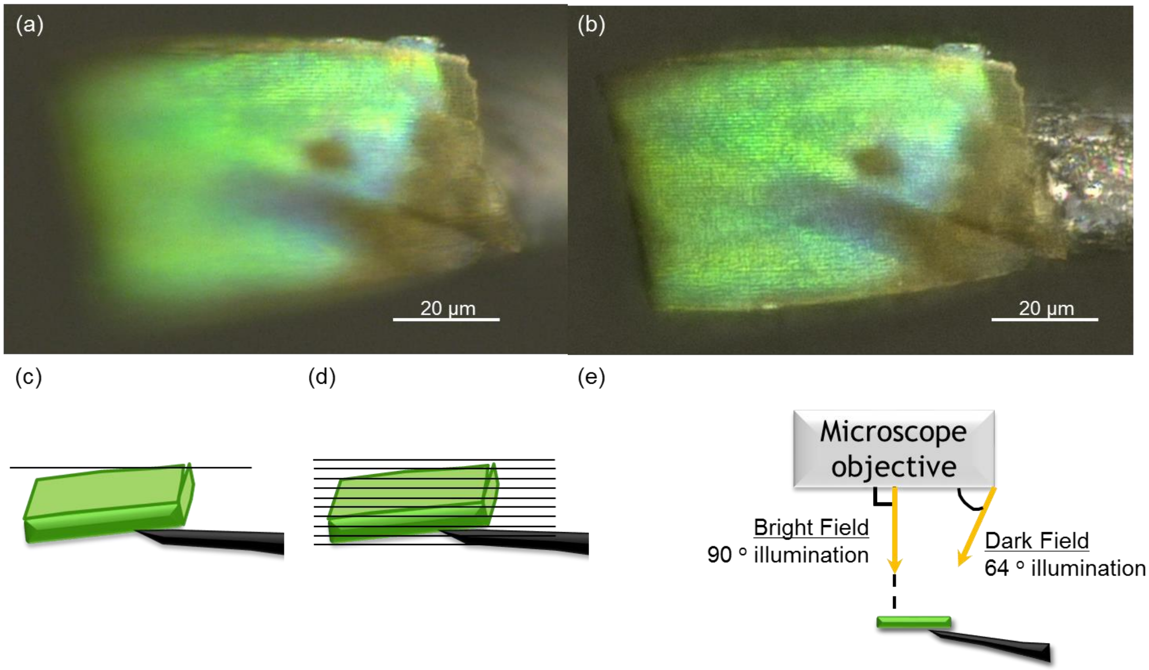

Figure 6. Image acquisition using the Keyence Digital Optical Microscope. (a) A single bright field optical image of a FIB milled scale showing a single region of the scale in focus. (b) A composite bright field optical image acquired from 10 individual images where all regions of the scale were in focus. (c) A schematic representation of the single focal plane used in the single scale image for (a). (d) A schematic representation of the 10 focal planes used in the composite image of the scale (b) where all scale features were in focus. (e) A schematic showing the angle of illumination between the bright field and dark field imaging modes, 90 ° and 64 °, respectively. The viewing direction is represented as the dotted line between the sample and the microscope objective.

Each ion-milled scale was observed under an optical microscope with the scale oriented approximately normal to the viewing angle in order to correlate scale component structure with optical appearance (except when noted). Scale orientation was achieved by changing the focus on the butterfly scale to first determine the highest and lowest point (*i.e.*, z-position) for a given scale orientation. For example, the highest feature of the scale (*i.e.*, closest point of the scale to the microscope objective) was the in-focus region for the scale in **Figure 6 (a)**. Changing the focal position for the same scale revealed that the scale was approximately positioned as shown in **Figure 6 (c)**. Such information of the scale orientation was then applied to rotating, and/or tilting, the scale such that an even loss of focus occurred across all regions of the scale with a change in the focal position of the microscope.

Single scale spectral measurements were performed using an Olympus BX60 (Olympus America, Inc., PA, USA) upright microscope. Spectral measurements were acquired with a SEE 1000 microscope spectrometer (SEE Science, MA, USA) attached to the microscope camera port with software from Craic Technologies (Version 4.3.1, Craic Technologies, CA, USA).

Single scale reflectance measurements were acquired using an Olympus MPlan N 20 x objective (0.40 numerical aperture) relative to a diffuse reflectance standard (WS-1-SL, Ocean Optics, FL, USA), illuminated by a halogen lamp (Olympus America, Inc., PA, USA). The usual measurement spot size was approximately 14 µm x 14 µm. Reflectance measurements presented in **Figure 27** utilized an Olympus 50 x SLMPLN objective (0.35 numerical aperture) due the long working distance (18 mm) and 6 µm x 6 µm spot size. Y-axis intensity values were usually reported in arbitrary units (A.U.), rather than percent reflectance relative to the standard, to account for differences in light scattering between the reference standard and the butterfly scale.[52] Single scale fluorescence spectra were acquired with an Olympus MPlan FL N 50 x objective (0.80

numerical aperture) with a 6 µm x 6 µm spot size. The resulting reported emission spectrum was the measured signal minus the dark current (*i.e.*, references were not used for emission measurements). All fluorescence imaging and spectra were acquired using a mercury lamp illumination (HBO 100 W lamp, Universal Arc Lamp Power Supply # 99030, SEE Science, MA, USA) in combination with a fluorescent filter cube (**Table 1**). All fluorescence and reflectance imaging were performed with the 20 x objective using a Nikon D300 (Nikon USA, NY, USA) camera (Manual, ISO 200, automatic white balance). The camera was attached to the camera port of the microscope with a microscope adapter (MM-SLR, Martin Microscope, SC, USA).

Table 1. Filter cubes used in single scale emission studies

Manufacturer Label (Manufacturer)	***Excitation Filter (FWHM)***	***Dichroic Mirror (Half Maximum)***	***Emission Filter (Half Maximum)***
11000v3 (Chroma Technologies)	325 – 375 nm	415 nm	425 nm
U-MNU2 (Olympus)	360 – 370 nm	400 nm	420 nm
U-MNV (Olympus)	400 – 410 nm	455 nm	455 nm
U-MNBV2 (Olympus)	420 – 440 nm	455 nm	475 nm

P. sesostris green scale appearance and spectra dramatically changed between bright field and dark field imaging modes (**Figure 11** and **Figure 12**). Analyses of the spectral variations between each imaging mode revealed that intensity, and not spectral content, changed between imaging modes. All measurements were performed on the same location on a diffuse reflectance standard. Both aperture and field stops on the microscope were fully opened, which was required for dark field imaging. Integration time was optimized in the bright field mode, which exhibited the highest reflected intensity between the two imaging modes, and was fixed at 9 ms for the duration of the analyses.

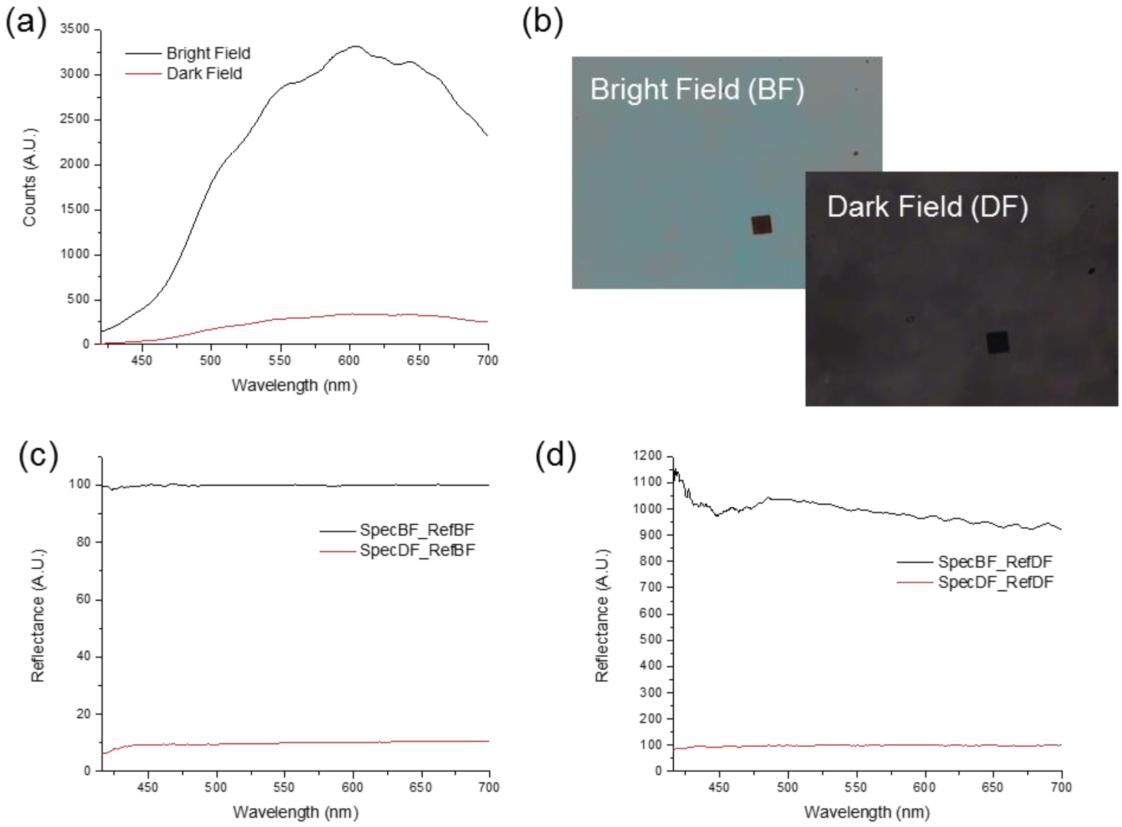

Figure 7. Characterization of bright field and dark field imaging modes on a diffuse reflectance standard. (a) Lamp spectra (*i.e.*, reference spectra with dark current subtracted) collected on a diffuse reflectance standard, demonstrating the preservation of spectral shape between either imaging mode. (b) Bright field and dark field optical images showing the measurement area (14 µm x 14 µm black box) and the qualitative difference in intensity between either imaging mode. (c) Spectral measurements of bright field (black line) and dark field (red line) with a bright field reference spectrum. (d) Spectral measurements of bright field (black line) and dark field (red line) with a dark field reference spectrum. These results confirmed that the imaging modes vary in intensity, but not in spectral content.

Figure 7 (a) shows the reference spectra (with dark current subtracted) for both imaging modes. This represented the spectrum of light detected after reflection from the diffuse reflectance standard. The same spectral shape was detected, without zero-valued intensities across the tested wavelength range for both imaging modes. Bright field and dark field images of the diffuse reflectance spectrum qualitatively demonstrated the difference in intensity of light reflected from the standard (**Figure 7 (b)**). The black square indicates the 14 µm x 14 µm measurement region for the 20 x objective used in this study. Spectral measurements with a bright field reference (**Figure 7 (c)**) and a dark field reference (**Figure 7 (d)**) confirmed intensity, rather than wavelength variations between either imaging mode. The dark field illumination reflection intensity was approximately 10 % of the bright field reflected intensity.

Long pass filter reflectance measurements, to determine if fluorescence was a significant factor in scale coloration, were conducted using a modified fluorescence filter cube (41012 FITC/GFP, Chroma Technologies, VT, USA). All filters and the mirror were first removed from the fluorescence filter cube. A 50/50 beam splitter (Catalog number: 21000, Chroma Technologies, VT, USA) was inserted in the place of the dichroic mirror. The beam splitter enabled white light reflectance and long wavelength reflectance (when the long pass filter was inserted into the excitation port of the filter cube). The long pass filter had a half-maximum wavelength of 510 nm (Catalog number: HQ510LP, Chroma Technologies, VT, USA). Comparison of the reference spectra, with and without the long pass filter, show that the filter removed light below approximately 500 nm (**Figure 8**). 7 measurements were acquired from a single scale (6 µm x 6 µm spot size) for each imaging mode for a single reference measurement using the diffuse reflectance standard. Measurements were repeated twice (21 measurements per illumination, with reference measurements acquired on 3 separate areas on the diffuse reflectance standard). Such a process enabled error analysis accounting for the natural variability in reflectance intensity and peak wavelength from the same scale, in addition to the intensity variation in reference spectra acquired on the diffuse reflectance standard.

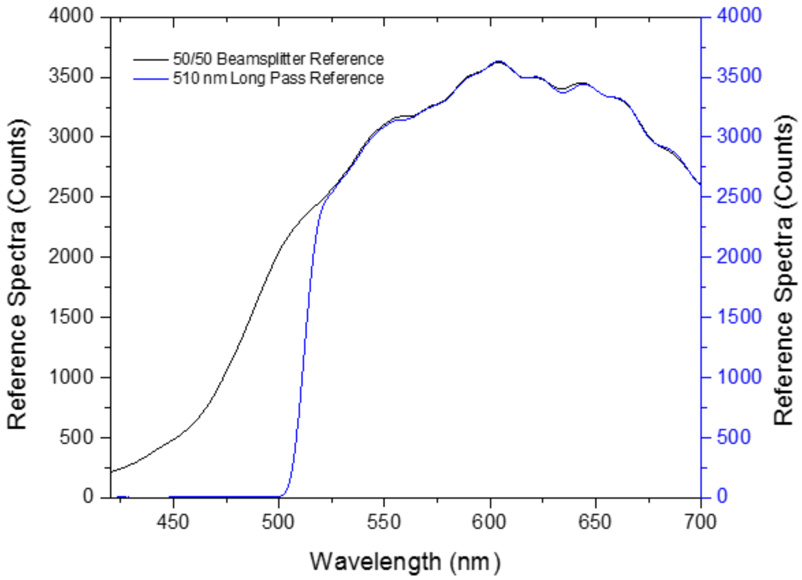

Figure 8. Comparison of reference spectra for long-pass illumination experiments. The 510 nm long pass filter effectively removed all light below 500 nm, preventing the excitation of UV-to-blue excited fluorophore or fluorophores.

Transmission and absorption measurements were conducted using the same microscope with a halogen illumination source and 20 x objective. Reference measurements varied, depending on sample mounting. For instance, single scales dispersed on a glass slide utilized a reference measurement of only the glass slide, adjacent to the scale of interest. Single scales immersed in index-matching fluid (Refractive index 1.5600 ± 0.0005 at 583.3 nm, Fluid Code: 50BN, Cargille Laboratories, NJ, USA) involved a reference spectrum including the glass slide, index fluid, and coverslip. The scale orientation in transmission was impossible to discern using transmitted light only. Switching to a low magnification, high working distance objective (5 x MPlan N, 0.10 numerical aperture, Olympus America, Inc., PA, USA), and illuminating the scales with an external white light source, enabled the determination of scale orientation. Scales oriented ridge-up exhibited a relatively constant coloration across a broad range of angles of incidence, whereas scales oriented membrane-up were iridescent. For a given sample, desired scale orientation was found and moved to the center of the field of view. The objective was switched back to 20 x, and the measurement continued. This method enabled the transmission light to remain on while finding the appropriate scale orientation, which reduced the likelihood of exposure variations in the measurement.

Absorption measurements were only conducted for scales immersed in index-matching fluid to minimize scattering contributions. The necessity of a fixed path length for the reference and sample measurements required that the absorption measurements be conducted on scales dispersed on a glass slide (*i.e.*, FIB-milled samples could not have a fixed path length if dipped into index fluid). Index fluid was always applied immediately prior to the measurement to prevent evaporative losses. **Figure 9** displays the absorption spectrum for the index-matching fluid used in this study. A Shimadzu UV-vis-NIR spectrometer (Model UV-3101PC, Shimadzu, Kyoto, Japan) was used for absorbance measurements after dispersing samples in a 1 mm quartz cuvette (courtesy of Dr. Vincent Chen, Perry Group, Georgia Institute of Technology). The plotted spectra is an average of 3 separate measurements.

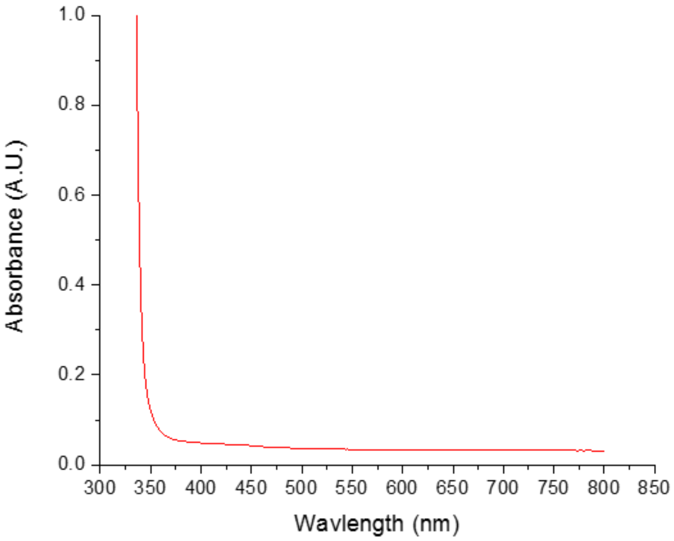

Figure 9. Absorption spectrum for the 1.5600 ± 0.0005 index-matching fluid (Fluid Code: 50BN, Cargille Laboratories, NJ, USA) used in this study. This spectrum is the average of three separate measurements. Data courtesy of Dr. Vincent Chen, Perry Group, Georgia Institute of Technology.

Confocal fluorescence microscopy was performed on a Zeiss LSM700 (Carl Zeiss, Oberkochen, Germany) instrument, courtesy of Dr. Vincent Chen, Perry group, Georgia Institute of Technology. A 405 nm, 8.9 mW laser was used for fluorescence excitation in combination with a 500 nm long pass filter for imaging. Scales were immersed in 1.5600 refractive index fluid (Code 50BN, Cargille Laboratories, NJ, USA) in-between a glass slide and cover slip. Imaging was performed with a 63 x oil immersion objective (Pln Apochromatic 63 x / 1.4 Oil Immersion DIC, Carl Zeiss, Oberkochen, Germany) using Ziess Immersol$^{\text{TM}}$ 518 F (Carl Zeiss, Oberkochen, Germany) oil between the coverslip and objective.

All spectral data analysis was performed with OriginPro 9 software (Student Version, Origin Labs, MA, USA). Relevant peak position and intensity from optical data were determined using an automated, local maxima detection algorithm within the software. All optical data were reported as an average of at least 10 spectra unless otherwise noted. All peak wavelength positions have error bars reported as ± one standard deviation.

Imaging scatterometry [51] was used to collect the hemispherical reflectance of light scattered from native *P. sesostris* individual scales and whole wing sections. All images were collected through primary beam illumination and in reflectance mode. With primary beam illumination, a beam of light is narrowly focused onto the sample through a small hole in a custom-made ellipsoidal reflector. The images from this mode may be interpreted as the hemispherical scattering pattern observed under normally incident illumination. The sample was positioned at the first focal point of the reflector with a micropipette tip or micromanipulator needle. The ellipsoidal reflector compressed the hemisphere of scattered light from the sample, focusing it to the reflector's second focal point. This second focal point coincided with the focal point of a large aperture photographic lens, which collimated the beam. The collimated light was focused by an imaging lens and captured by a digital camera. An in-house, MATLAB® routine, applied to the captured images, corrected the radial distortion caused by the collimating and imaging lenses and added a polar angle scale to the final image. All imaging scatterometry was performed by Alfred Lethbridge from Dr. Peter Vukusic's group at the University of Exeter, England.

1.4.3 Method of structure analysis from secondary electron images

Measurements of the fin and nanotube array periodicities, the membrane thickness, and gyroid polycrystal pore spacing were performed with the aid of SEM and TEM images. Images were acquired such that the feature being measured was oriented parallel with the imaging plane (*i.e.*, cross-sectional or plan-view depending on the feature). A line was drawn across multiple features and the length of the line was divided by the number of periods (*i.e.*, air voids) within the measurement line (**Figure 10 (a)**). This method [63] mitigates user error in individual feature measurements. Measurements were repeated at least 50 times for each type of analysis. One standard deviation is reported as the error.

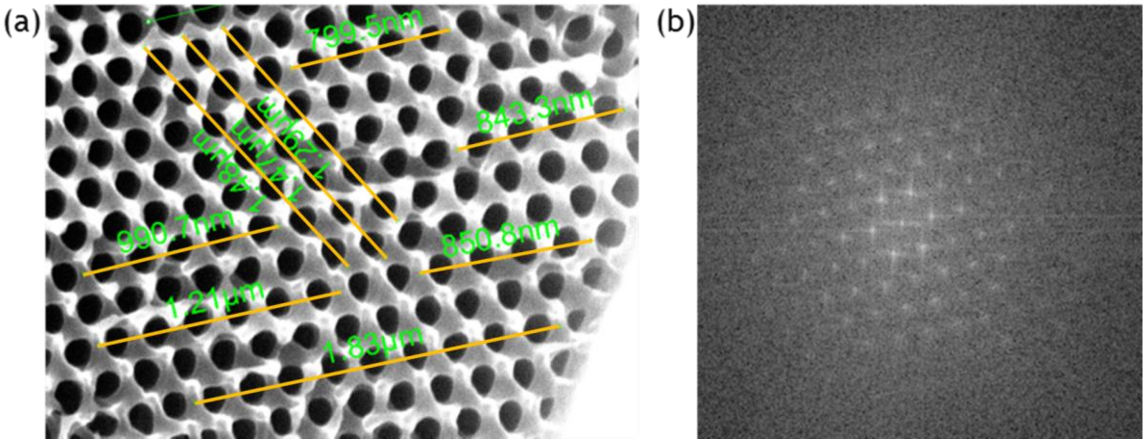

Figure 10. Measurement of the pore spacing on the hexagonal face of the gyroid polycrystal. (a) Images were acquired such that the hexagonal face was oriented parallel with the imaging plane. Measurements were taken across at least four pores, with the starting and ending points of the line terminating on approximately the center of the cuticle material. The overall line length was divided by the number of air pores to yield the average pore spacing. No less than fifty measurements were made in order to quantify scale feature dimensions. (b) Fast Fourier Transform (FFT) of the same image (without measurement lines) confirming the exposure of a hexagonal face.

Fast Fourier Transforms (FFT) were acquired using selected secondary electron images using the FFT image processing option in the ImageJ software [64]. This analysis enabled determination of the number of periodicities present in a given structure and the validation of the imaging plane being perpendicular to the normal vector from the structure surface (**Figure 10 (b)**).

Modeling of the thin film interference spectra was performed by Alfred Lethbridge, Vukusic Group, University of Exeter, England. All modeling was performed using the commercially available software, TFCalc^{TM} (Software Spectra, Inc., OR, USA), for a 68 nm thick slab of chitin (refractive index of 1.56 +0.06i) [12]. Illumination and detection angles were both assumed to be normal to the surface of the chitin slab.

1.5 Results and Discussion

The goal of this work was to investigate the origin of coloration in the *P. sesostris* green scales through an isolation and interrogation strategy enabled by FIB milling. The first step for this investigation was to understand how both sides of the unmilled scales reflect, transmit, and absorb light. Systematic removal of scale components was then conducted, so that optical appearance could be correlated with the scale component structures. Finally, optical interrogation techniques were used to provide a greater understanding for the overall scale coloration and appearance.

1.5.1 Investigation of unmilled scale reflectance, transmittance, and absorbance

Unmilled scales were dispersed on a glass slide for bright field and dark field reflectance characterization for both sides of the scale (gyroid polycrystal-up and ridge-up). Bright field imaging was conducted with a normal angle of incidence to the scale, whereas dark field was conducted with a more oblique angle of illumination. Comparing the reflection spectra from both imaging modes enabled a better understanding of iridescent coloration.

Figure 11 (a) shows the bright field and **(b)** dark field reflection spectra obtained from single scales with the ridge side oriented up. (Note: this was the same scale orientation as for the scales imbricated on the butterfly wing). The same spectral shape as well as a similar wavelength for maximum peak reflectivity were preserved through either imaging mode: 544 ± 11 nm for bright field illumination and 538 ± 9 nm for dark field illumination. Images for the same scale in either imaging mode exhibited similar appearances. These results validated the literature understanding that the ridge structure suppresses iridescence from the polycrystal, by homogenizing the angle of incidence of light reaching the gyroid polycrystal and light reflected from the gyroid polycrystal.[32, 46, 50, 58, 59]

Scales oriented with the gyroid polycrystal side up displayed a very large change in overall scale coloration when the imaging mode was switched between bright field and dark field illumination (**Figure 11 (c, d) Insets**). Additionally, there was a significant change in the overall reflectance spectral shape (**Figure 11 (c, d)**). The spectral results in **Figure 11 (d)** suggested that the dark field coloration of the gyroid polycrystal was due to the color mixing between the blue/green peak at 499 ± 12 nm and the reflection at longer wavelengths (*i.e.*, greater than 600 nm).

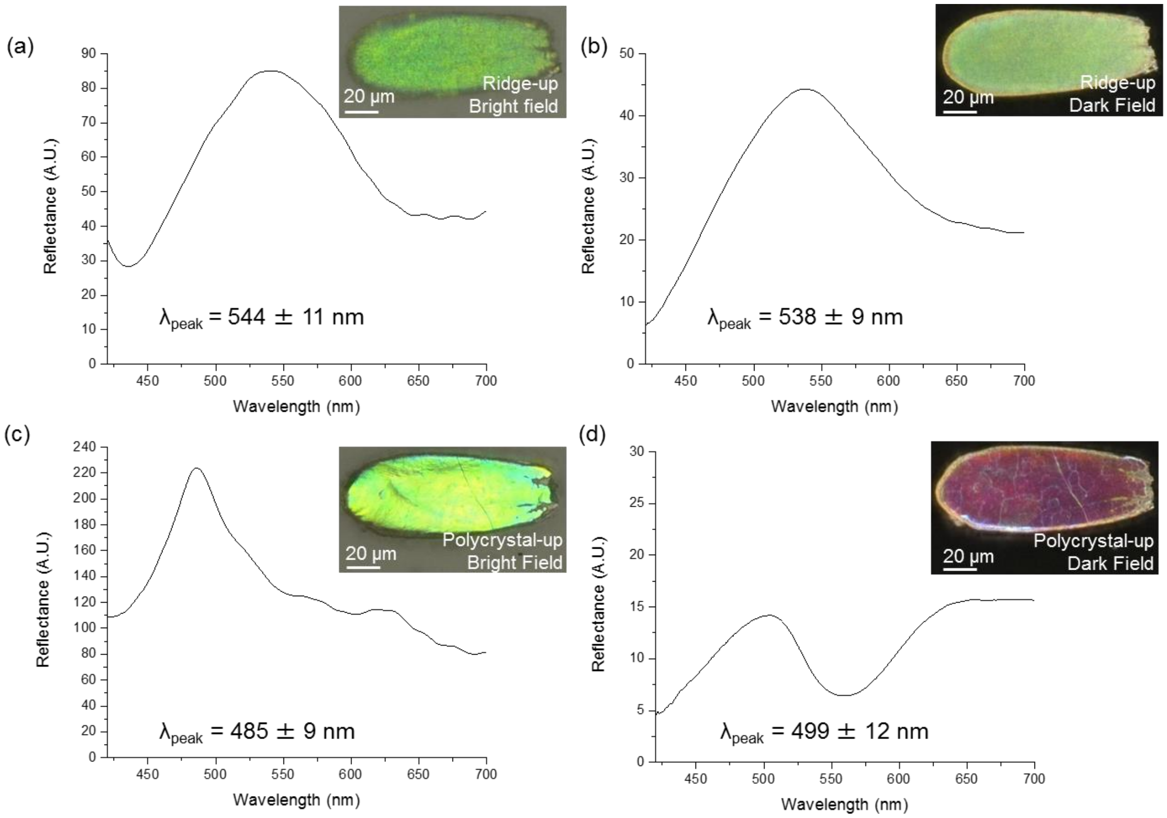

Figure 11. Bright field and dark field reflection spectra and images of *P. sesostris* green scales dispersed on a glass slide. Ridge-up coloration and spectra were very similar between (a) bright field and (b) dark field imaging modes. The polycrystal-up scale orientation displayed iridescence (for images and spectra) when switching between (c) bright field and (d) dark field imaging modes. All spectra and peak wavelength values were averages of at least 10 separate measurements with ± 1 standard deviation reported as the error (5 scales, 2 measurements per scale).

Reflection spectra from a tilted scale, oriented gyroid polycrystal side up (also on a glass microscope slide) was acquired in both bright and dark field imaging modes for further confirmation of the polycrystal iridescence. The purple coloration previously observed for the polycrystal side up in dark field imaging mode for a normal scale orientation, relative to the viewing direction, was observed for the tilted scale in bright field imaging mode (**Figure 12 (c)**). This confirmed that the dramatic change in color was a property of the scale, rather than an artifact of the dark field-imaging mode. (Note: Comparison between the bright field and dark field imaging modes presented in the experimental section demonstrated that the imaging modes differ in intensity, but not in spectral content.) Similar spectral shapes were also observed in **Figure 12 (a)** as for the dark field spectral shape reported in **Figure 11 (d)**.

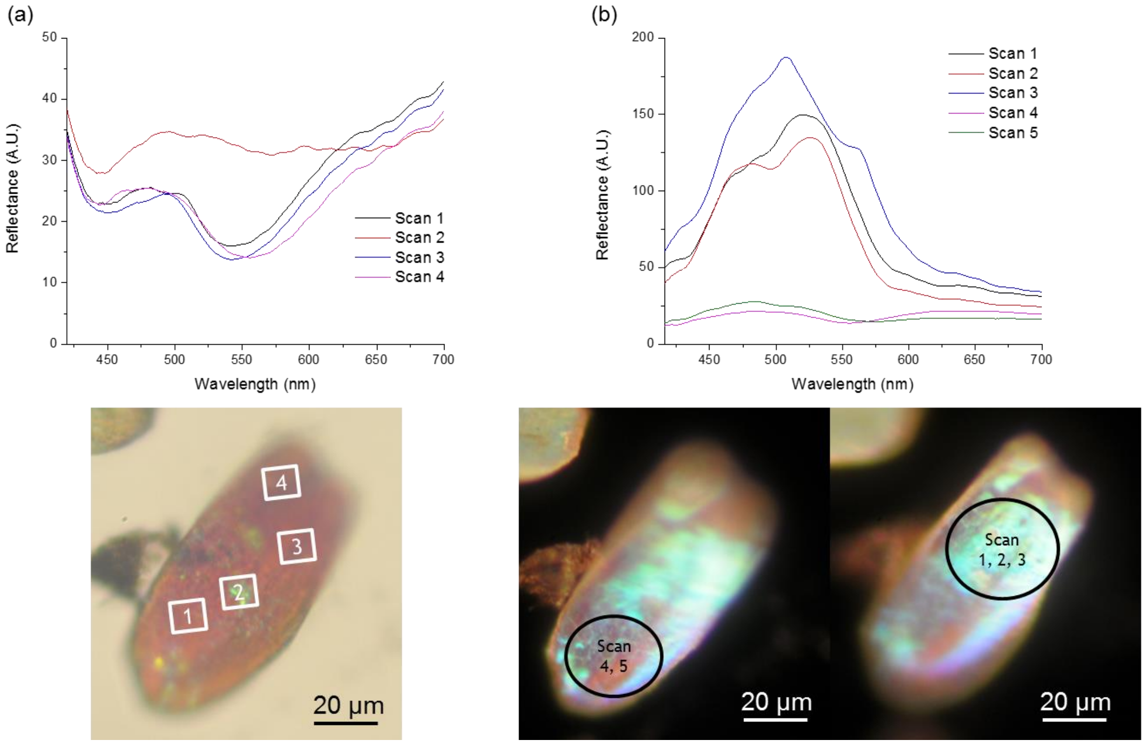

Figure 12. Iridescent reflection from the polycrystal measured for a tilted scale, oriented polycrystal-up. (a) Individual bright field spectra and images show the same spectral shape and appearance observed as when the scale was normal to the optical axis and viewed in dark field mode. Iridescent coloration from a polycrystal domain was measured in Scan 2. (b) Individual dark field spectra and images show the relatively purple coloration commonly observed in dark field for a scale oriented normal to the optical axis. Blue/green coloration was observed towards the scale base in the region of Scans 1 - 3.

Further support of polycrystal iridescence is shown in **Figure 12 (b)** with dark field imaging and spectra for the same, tilted scale as in **Figure 12 (a)**. Reflection measurement scans 1 through 3 were acquired at the base of the scale in the large patch of blue/green reflected light. Reflectance scans 4 and 5 were acquired in the relatively purple region at the other end of the scale, displaying the same spectral features observed in **Figure 12 (a)** and **Figure 11 (d)**. Such spectral data shows that considerable changes in reflected spectral shape can occur with small changes in measurement position. (Note: The measurement spot size was 14 μm x 14 μm). These results also validate prior conclusions in the literature supporting iridescence from the polycrystal.[32, 46, 50, 58, 59]

The next step in the investigation of the unmilled scales was to use index-matching fluid to optically remove the effects of structural coloration, enabling the transmission and absorption of individual scales to be characterized with minimized scattering. The use of index-matching fluid of refractive index 1.56 [12] was examined in previous investigations [50] to match that of the chitin in the *P. sesostris* butterfly. Reflection spectra and images were acquired for the *P. sesostris* green scales immersed in the index-matching fluid to validate the optical removal of the structural color inherent to the template. The index-matching fluid used in this study readily wetted and infiltrated the *P. sesostris* green scales.

Figure 13 (a) is an optical image obtained in bright field mode of a green scale immersed in the index-matching fluid, only slightly distinguishable from the background appearance. The similar coloration of the scale compared to the background persists in dark field (**Figure 13 (b)**), except near the scale edge. This red coloration around the edge of the scale suggested that the index-matching fluid may not exactly match the index of the cuticle, either in value or in dispersion. The changing scale curvature may result in the observed iridescence due to the change in the angle of incidence relative to the surface normal vector for the scale (*i.e.*, the iridescence of the polycrystal still remains to a small extent).

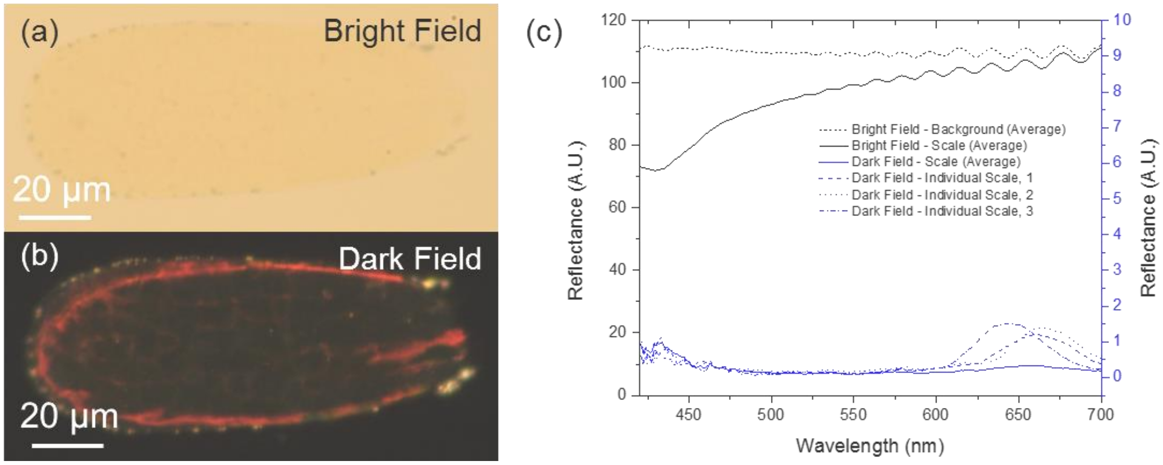

Figure 13. Reflection images and spectra of *P. sesostris* green scales in index-matching fluid (1.5600). (a) Bright field and (b) dark field optical images of the same scale. The appearance of the red coloration in dark field mode suggested that the index of the scale was not exactly matched by the index-matching fluid. (c) Bright and dark field reflection spectra showing a significant difference relative to the reflection spectra for scales in air, suggesting that the index-matching fluid has removed most of the structural coloration. All average spectra had at least 10 separate measurements (5 scales, 2 measurements per scale).

The bright field reflection spectrum of the scale infiltrated with the index-matching fluid (**Figure 13 (c)**) demonstrated that the reflection spectra of either the ridge-up or polycrystal-up orientation was no longer present. (The scale orientation could not be determined for scales immersed in the index-matching fluid). The oscillation at longer wavelengths for the sample measurements matched reflection measurements made on the background material (*i.e.*, glass slide, index fluid, and coverslip; no scale). Wavelength-values at the local maxima and minima between the background and sample measurements were identical, demonstrating that this was an artifact of the measurement configuration.

The red light reflected from the scale edge provided a very weak signal for reflection measurements. Three measurements from separate regions of the same scale are shown in **Figure 13 (c)** with a low reflected intensity. The reason for this reduced intensity in the measurement was that the relatively red, reflected light from the scale in index-matching fluid was very low relative the reference measurement on a diffuse reflectance standard. The integration time could be increased to collect more of the reflected light, but doing so risked saturating the detector during reference spectrum acquisition. (Note: The reference spectrum was required in order to account for spectral variations in the light source, objective, and detector. This enabled the sample spectrum to be measured, relative to a diffuse reflectance source.) Overall, these results indicated that the index-matching fluid largely removed the structural coloration from the scale. Subsequent transmission (**Figure 14**) and absorption measurements (**Figure 15**) on single scales dispersed in this index-matching fluid were in agreement with published reports [50] for *P. sesostris* green scales.

Transmission measurements were collected for single scales in index-matching fluid or in air to better understand the contributions of scattering on the light transmitted through the scale. Scale absorption occurred in both samples as only the scattering contribution was changed with immersion in the index-matching fluid. The oscillations observed for the reflection measurements in **Figure 13** were not present in these measurements due to differences in the reference measurement (*i.e.*, transmission versus reflection). The reference for scales in air was acquired on the glass slide only, while the reference spectrum optical path for scales in index-matching fluid included the glass slide, index fluid, and coverslip.

Scale transmittance increased at longer wavelengths for scales immersed in the index-matching fluid (**Figure 14 (a)**). This result validated prior literature data [50] in spectral shape and magnitude. However, the single scale transmission spectra for scales in air has not been discussed in the literature. A dramatic difference was observed in the transmission spectrum for scales in air versus index-matching fluid. The transmission spectrum for a scale in air (**Figure 14 (a)**) displayed a large drop in transmitted light intensity from 420 – 650 nm relative to the spectrum for a scale immersed in the index-matching fluid, suggesting that scattering provided a considerable contribution for reducing the scale transmittance. Additionally, the transmission spectra and optical images displayed very little change with scale orientation (**Figure 14**).

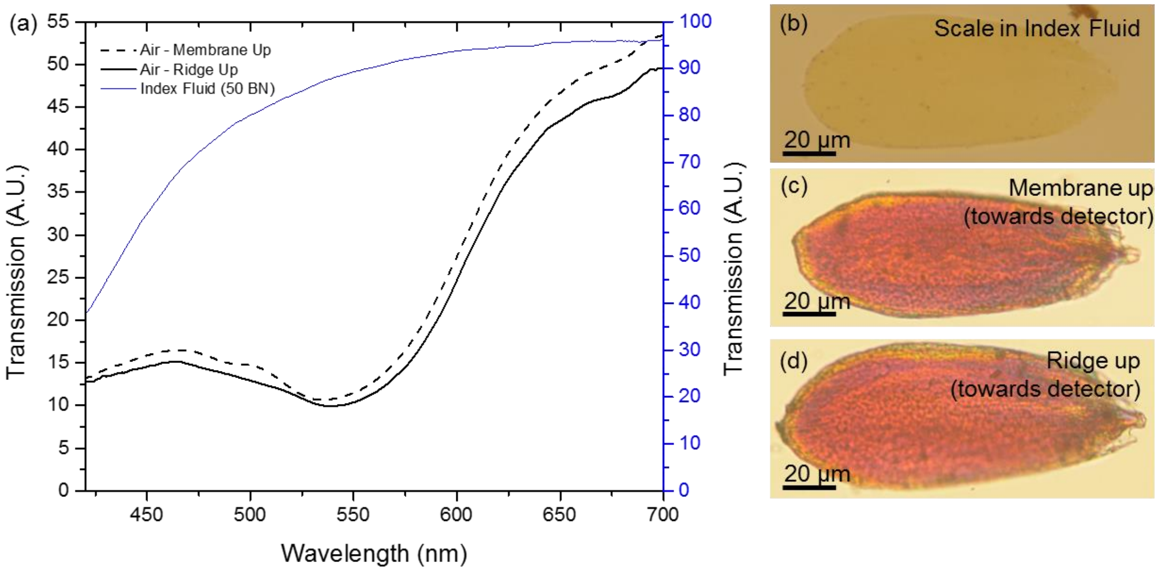

Figure 14. Transmission spectra and images of scales in index-matching fluid or in air. (a) Transmission spectra confirmed that scattering significantly contributed to the reduction of light transmitted through the scale. (Note: absorption also occurred in both measurements). Images for scales in (b) index-matching fluid or in air, oriented (c) membrane-up and (d) ridge-up. Scale orientation could not be determine for scales immersed in the index-matching fluid. All spectra were averages of at least 10 separate measurements (5 scales, 2 measurements per scale).

Absorption measurements acquired on single scales show increased scale absorbance with decreasing wavelength below 550 nm (**Figure 15 (a)**). These results validated prior literature data [50] in spectral shape and magnitude. A new contribution relative to the literature was the examination of scale absorbance below 400 nm (**Figure 15 (b)**). Green scales were dispersed in the index-matching fluid and placed in a quartz cuvette. Absorption measurements were then performed in a UV-visible spectrometer in order to circumvent instrument limitations for single scale measurements in the range from 330 – 400 nm. This measurement enabled a better understanding of the spectral shape, not the intensity, of scale absorbance for the UV to violet range. Overall, the absorption remained relatively high at low wavelengths (which was important to note for analysis of scale fluorescence, described later in this chapter). Multiple scales contributed to the absorption path length at any given time during the measurement, precluding the determination of the absorption intensity of a single scale.

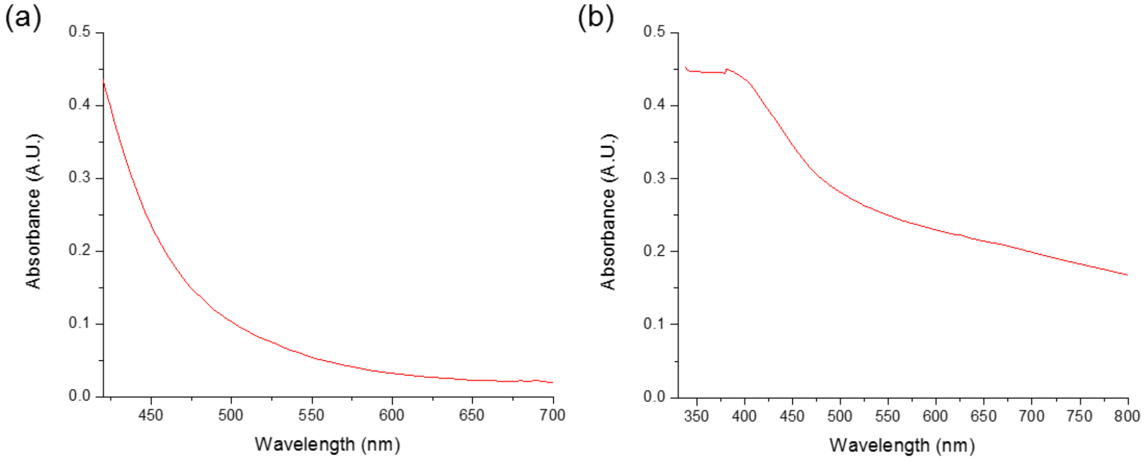

Figure 15. Absorption spectra of scales in 1.5600 refractive index fluid. (a) Single scale absorption spectrum in agreement with prior literature reports [50] (average of 10 separate measurements, across 5 separate scales). (b) Absorption spectrum from multiple scales dispersed in a quartz cuvette. The overall spectral shape displayed a broad absorbance towards lower wavelengths. This spectrum was an average over 3 separate measurements. However, absorption intensity could not be compared with single scale analyses due to the varying number of scales within the path length of the measurement. The step in the spectra near 400 nm was due to a lamp change in the instrument. Multiscale absorption spectrum courtesy of Dr. Vincent Chen, Perry Group, Georgia Institute of Technology.

1.5.2 Summary of structure – color relations enabled through FIB milling

The combination of FIB milling and secondary electron imaging has revealed four distinct structures in the *P. sesostris* green scale: a thin, solid membrane, at the scale base; gyroid polycrystal; and then a ridge structure, composed of nanotubes and fins. This confirmed prior literature regarding the latter three scale components.[32, 46, 50, 58, 59] While the thin, solid membrane has been shown in published SEM and TEM images

[2, 32, 50, 58, 60], it has never been included in the discussion of overall scale coloration. The relative position of the thin, solid membrane is shown in **Figure 16** and in secondary electron images in **Figure 18 (c)**. The thin, solid membrane, along with a portion of the adjacent gyroid polycrystal, was removed to better evaluate the color contribution associated with the solid membrane.

FIB milling was performed to isolate combinations of scale components, which were subsequently observed in bright field optical microscopy. Structural feature combinations and their observed contributions to color are summarized in **Figure 16**. Observations for both sides of the scale show that the isolated ridge structure was relatively colorless/brown (**Figure 16 (b)**). The combination of an intact scale base (*i.e.*, thin, solid membrane and gyroid polycrystal, with the ridge structure removed) exhibited a green color, as viewed from both sides of the scale (**Figure 16 (c)**). The combined polycrystal and ridge structure (with the thin, solid membrane and some adjacent gyroid polycrystal removed) appeared blue when viewed from both sides (**Figure 16 (d)**).

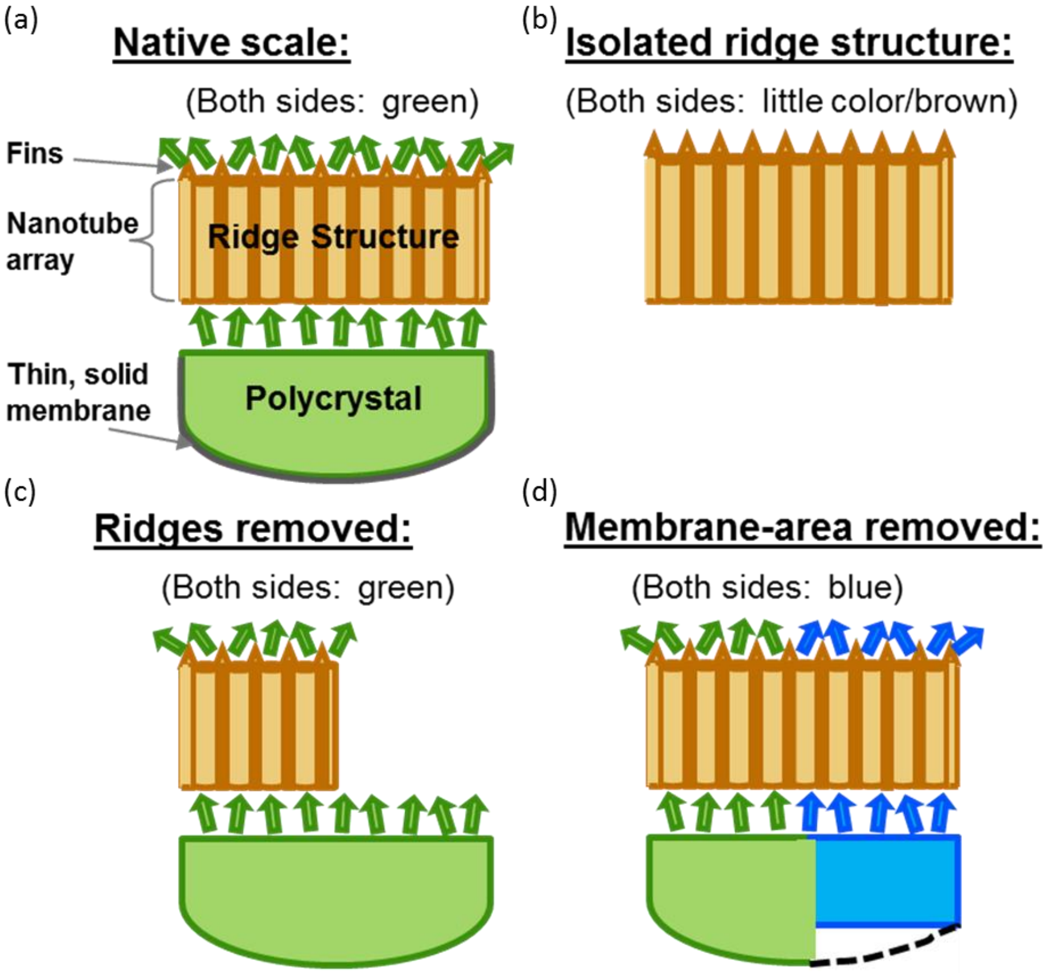

Figure 16. Summary of structure-optical appearance correlations. All color assignments were made through bright field optical microscopy. (a) The native scale appeared green when viewed from both sides. (b) The isolated ridge structure appeared colorless/brown when viewed from both sides. (c) The combined polycrystal and membrane appeared green when viewed from both sides. (d) The combination of polycrystal and ridges appeared blue when viewed from both sides. Evidence for each color assignment may be found in **Appendix A, Figure 65** through **Figure 67**.

The observation of blue light transmitted through the ridge structure after reflection from the polycrystal (with only the membrane-area removed), in addition to the green appearance of the scale when only the ridges were removed, contradicted the existing literature understanding [46, 50] for *P. sesostris* green scale coloration.

A first conclusion of spectral filtering of short wavelength light by the ridge structure was made by Poladian, *et al.* after partial scale deconstruction through repeated fracturing via tape pealing.[46] The portion of the scale revealed by the tape pealing method displayed an overall blue coloration, as mounted on carbon tape.[46] The authors noted the presence of circular defects and considered such defects to be natural features of the scale structure.[46] SEM or spectral data was not included in this publication.[46] No such circular defects have been found in the *P. sesostris* green scales throughout the course of this investigation, suggesting that the observed defects [46] were induced by fracture upon repeated tape pealing. Without SEM or spectral analysis of the partially deconstructed scale, it was difficult to determine what portion of the scale was removed by Poladian, *et al.* [46] and thus, to correlate scale structure with optical properties.

Further support for the ridge structure as a pigment filter was reported by Wilts, *et al.*[50] Their conclusions were based on imaging scatterometry obtained from both sides of a single scale, in addition to absorption measurements.[50] Blue coloration was only observed, through imaging scatterometry, on the membrane side of the scale (*i.e.*, where the ridge structure would not contribute to scale coloration).[50] The absorption measurements displayed increasing absorbance for short wavelength light.[50] The authors postulated that the absorption originated from a pigment in the ridge structure, which absorbed all blue and UV light reflected from the underlying polycrystal.[50]

The approach of Wilts, *et. al.* [50] was limited to whole scale studies. The ridges from a single scale were removed in the present work to analyze the possible role of ridge structure absorption on the overall scale coloration. **Figure 17** shows the relatively green coloration in both the milled (ridge removed) and unmilled (fully intact) regions of the scale. Reflectance measurements acquired in the milled region demonstrated a large variation in spectral shape and peak wavelength (**Figure 17 (c, d)**). This validated the conclusions of polycrystal iridescence [32, 46, 50, 58, 59]. Whole scale reflectance spectra maintained the same spectral shape with little variation in peak wavelength with lateral position. This result validated the conclusion of iridescence suppression by the ridge structure [32, 46, 50, 58, 59]. The difference in intensity between the milled and unmilled regions was attributed to the directional scattering (higher intensity, for the current specimen orientation) from the polycrystal and the diffuse scattering (lower intensity) from the whole scale region. Overall, there were a greater number of relatively blue-shifted reflection peaks from the region where the ridges were removed compared to the whole scale region. This was in agreement with the conclusions of Wilts, *et. al.*[50] (that some spectral filtering, due to absorption by a pigment, was occurring in the ridge structure). However, the hypothesis of spectral filtering by the ridge structure does not address all of the experimental findings enabled by FIB milling for scale component isolation.

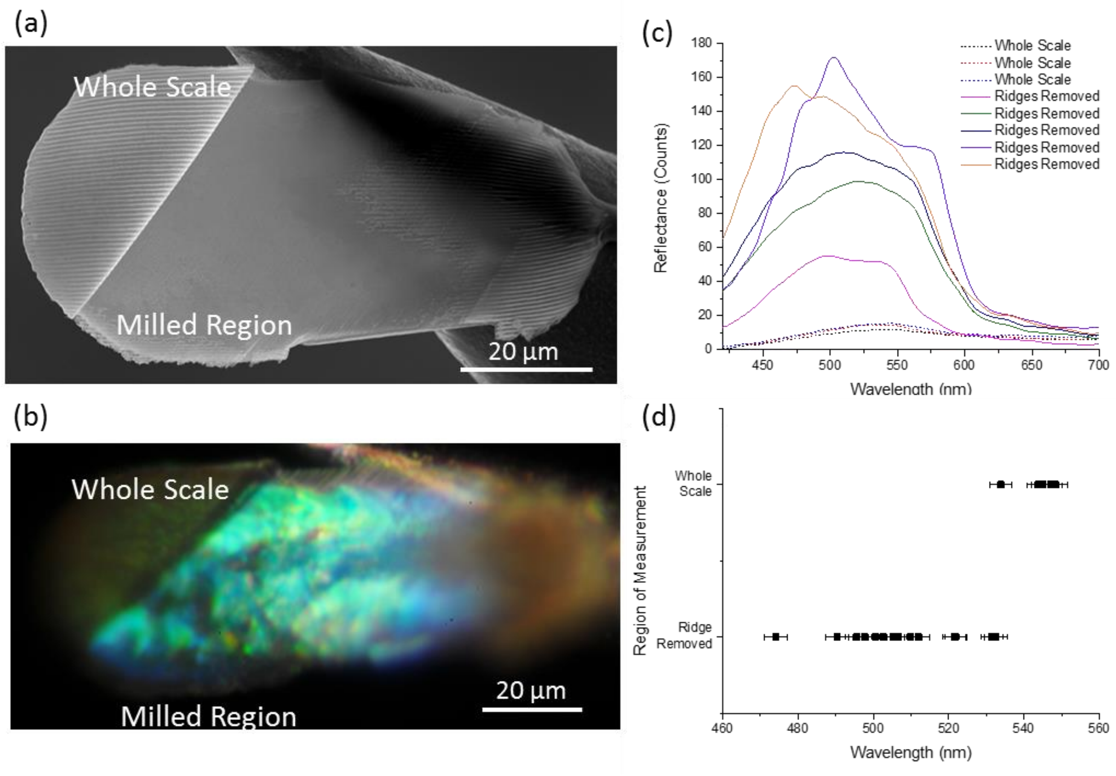

Figure 17. Spectral analysis of a single scale with the ridge structure removed. (a) Secondary electron image of scale, oriented ridge-up, with whole scale and ridge removed regions. (b) Bright field optical image of the same scale displaying relatively green coloration in the whole scale and milled regions. (c) Individual reflection spectra acquired in both regions. Peak wavelength values from the spectra in (c) with the instrument error of ± 3 nm used as the error bars.

The results presented in this study (**Figure 18 (a, b)**) demonstrate that the ridge structure was not a highly efficient, pigment filter [46, 50] for absorbing blue light. Otherwise, the scale would not appear blue through the ridges if the amount of localized absorption from this structure was as significant as previously hypothesized. Approximately 1.3 – 2.7 µm of the scale base was removed during FIB milling for the sample presented in **Figure 18 (a, b)**. This range in material thickness represents the smallest and largest measured regions, as measured in the center of the scale (at the milled / unmilled interface), viewed edge-on. The thickness variation was a result of the natural variation in scale curvature being sectioned by a planar FIB cut. These results show that the green coloration was affected by the bottom 1.3 μm of the scale.

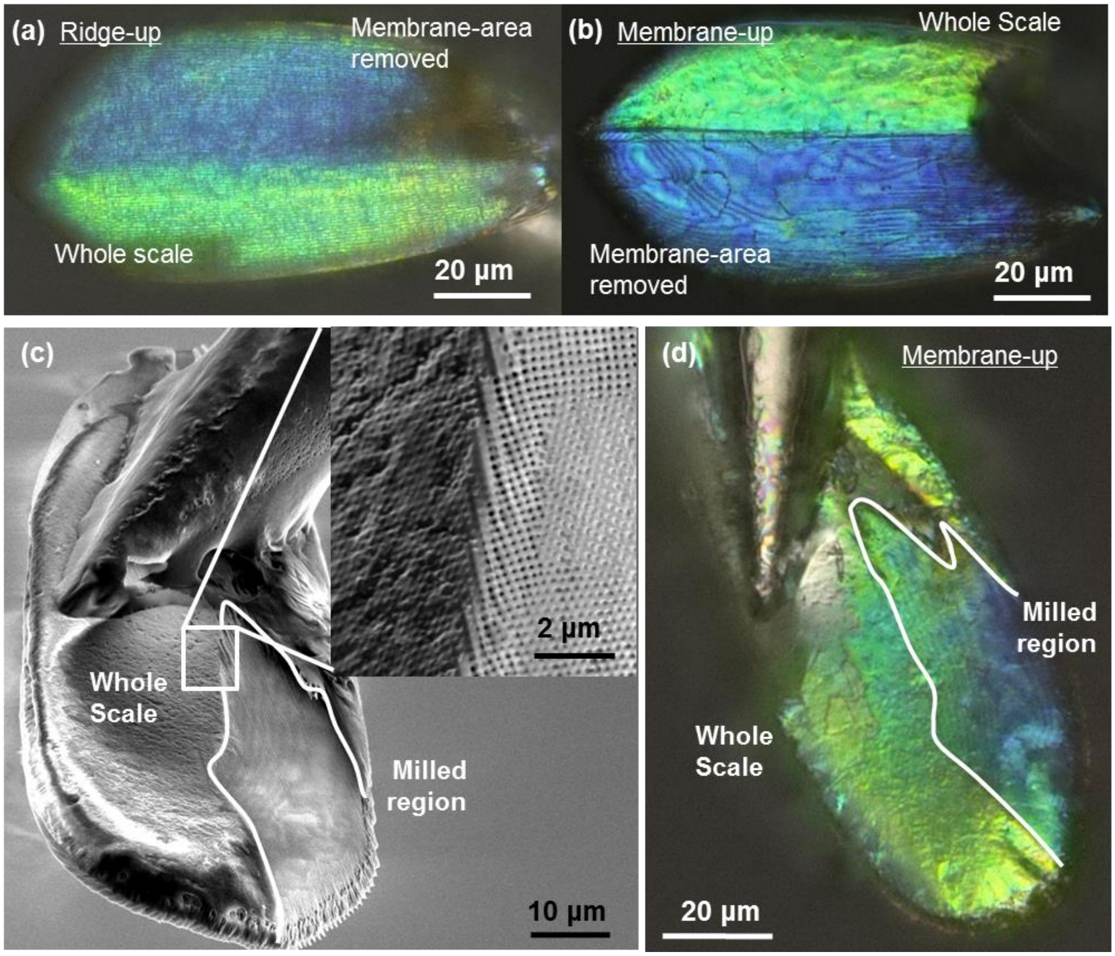

Figure 18. Optical (bright field) and secondary electron microscopy images of *P. sesostris* scales, partially FIB milled to remove the membrane-area. Sample oriented (a) ridge-up and (b) membrane-up demonstrating that the green color is affected by approximately 1.3 μm of the scale base. (c) Membrane-area removed sample milled in a wedge (a greater thickness of material was removed close to the scale tip, transitioning to no material removal towards the needle). The exposed polycrystal can be observed in (c). (d) Optical image showing that green color still exists where the thin, solid membrane has been removed. This provides evidence against coloration from thin film interference from the thin, solid membrane as the sole source of green scale coloration.

A separate sample was milled such that a gradient amount of material was removed from the scale base to better understand the nature of the newly-discovered affect of the scale base on coloration. SEM images demonstrated that the amount of material removed was greater towards the tip of the scale (maximum thickness of material removed was approximately 1.53 µm), reaching zero material removed near the scale center (**Figure 18 (c)**). Optical images of the same scale showed that the green coloration persisted in regions where the thin, solid membrane was removed (**Figure 18 (d)**). The overall blue coloration was observed towards the scale tip, where a greater amount of the gyroid polycrystal was removed, which was consistent with results on other milled scales. A suite of optical characterization methodologies were applied to milled and unmilled scales to better understand the scale coloration, starting with reflection measurements on the membrane-area removed scales.

1.5.3 Reflection spectra for the membrane-area removed sample and thin film interference coloration

Scale reflectance was measured with the scales oriented approximately normal to the optical axis and ridge side up. Measuring of FIB-milled samples oriented ridge side-up utilized the suppression of the polycrystal iridescence, inherent to the structure, towards understanding the overall scale coloration. Doing so reduced the impact of iridescence observed when the gyroid polycrystal was oriented up, which was especially important given the dramatic changes in reflection spectra as a function of small changes in measurement position (**Figure 12 (b)** and **Figure 17 (c, d)**).

Figure 19 contains the summary of reflection analyses for the membrane-area removed scale. The unmilled (fully intact scale) region displayed a broad reflection peak, which was centered at 524 ± 3 nm (average of 3 measurements on a single scale with 14 µm x 14 µm spot size), which was in the measured range of peak reflectance for a number (*i.e.*, 11) of native scales dispersed on the glass slide (*i.e.*, 524 ± 3 nm to 564 ± 3 nm). Measurements in the blue-appearing milled (membrane-area removed) region revealed a reflection peak centered at 477 ± 3 nm. Two conclusions were obtained from this result. (1) The remaining portion of the polycrystal (*i.e.,* remaining scale components in the milled region) do contribute to the overall scale coloration, as evidenced by the spectral overlap between the milled and unmilled regions. (2) The color contribution of the removed scale portion (*i.e.,* the membrane-area) was additive with respect to the remaining scale features. Attempts at isolating only the bottom 1.3 µm of the scale, to directly measure the spectral contribution of the membrane-area, were unsuccessful. This was due to mechanical deformation of the scale structure that occurred if too much scale material was removed during milling.

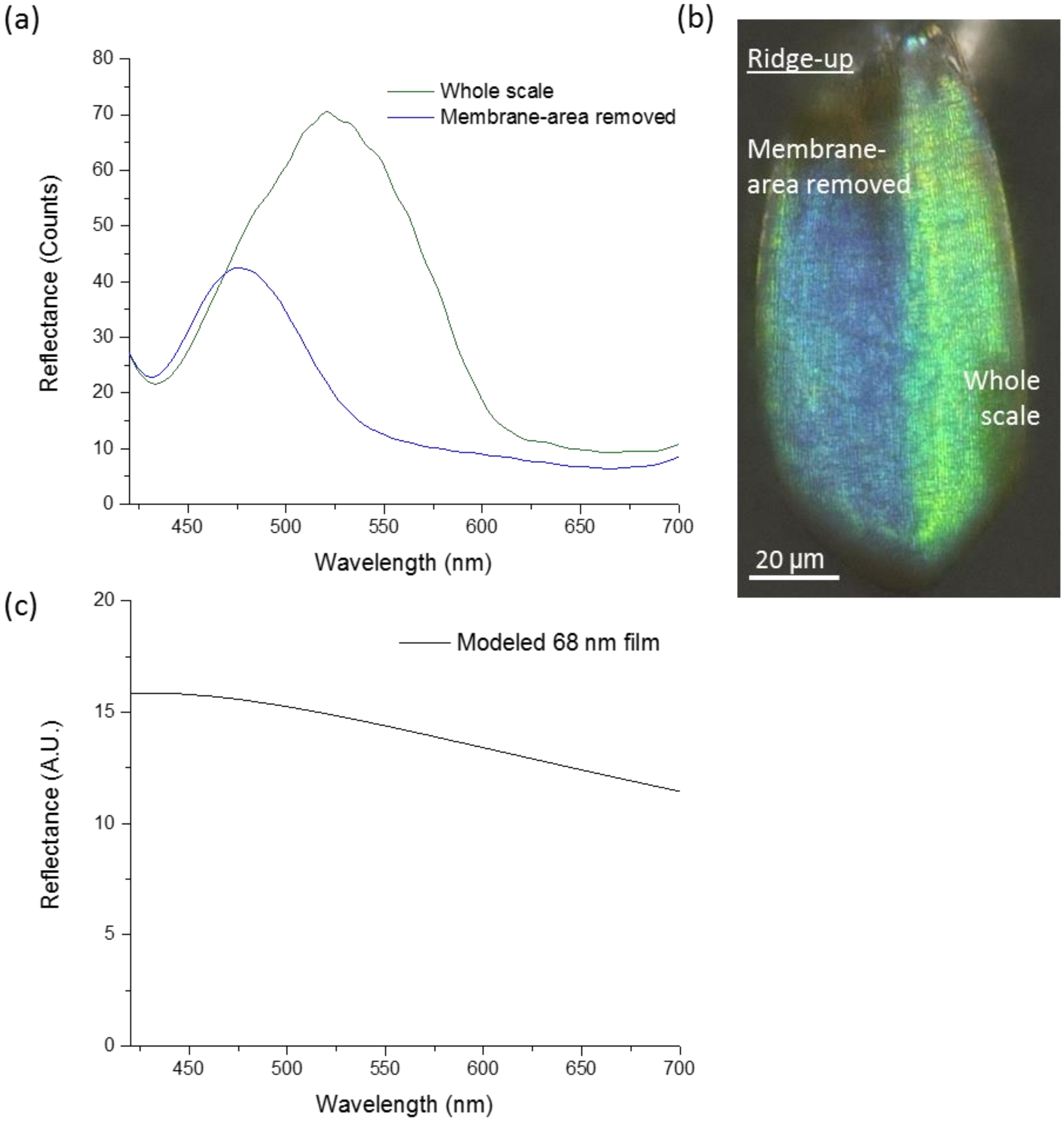

Figure 19. Spectral reflectance measurements on a membrane-area removed sample confirmed the blue appearance from the remaining polycrystal. (a) Spectral overlap between the milled and unmilled regions confirmed that the remaining portion of the polycrystal does contribute to the overall coloration. Each reflection spectrum was an average of 3 separate measurements in each region. (b) Bright field optical image of the scale, oriented ridge-up, analyzed in (a). (c) Modeling of thin film reflectance demonstrated that thin film interference was not the sole source of green coloration for the scale.

Three possible sources of additive coloration, which could produce the green color as part of the membrane-area contribution were: (1) thin film interference resulting from the thin, solid membrane, (2) light emission localized to the membrane-area, and (3) structural coloration due to an increased lattice spacing towards the scale base. The thickness of the thin, solid membrane was 68 ± 20 nm, as measured from cross-sectional TEM images (courtesy of P. Vukusic, University of Exeter). Modeling of the reflectance for a 68 nm thick film of chitin (refractive index of 1.56 + 0.06i, courtesy of A. Lethbridge, Vukusic group, University of Exeter) revealed a reflectance spectrum (**Figure 19 (c)**), which was very disparate from experimental measurements. This result demonstrated that the overall green coloration of the scale was not solely due to a thin film interference from the thin, solid membrane. Additional support for this conclusion is provided in **Figure 18 (c, d)**, where green color persists in regions where the thin, solid membrane had been removed. The remaining possibilities of color origin from the membrane-area include localized fluorescence emission and a gyroid polycrystal pore spacing distribution through the thickness of the gyroid.

1.5.4 Investigation of localized fluorescence as a scale coloration mechanism

Single scale, fluorescent emission was investigated with a suite of fluorescent filter cubes (exact excitation and emission ranges reported in the experimental section). A prior report [50] identified the possibility of fluorescence coloration through imaging, but this previous study lacked detailed spectral analyses. A summary of the emission study, in air, is presented in **Figure 20 (a)**. Essentially, the same emission spectra (spectral shape and peak emission) was produced with excitation wavelengths ranging from the UV to violet. Remarkably, the scale emission had essentially the same peak wavelength as for the scale reflectance (**Figure 20 (b)**), which suggested that the scale coloration could originate from light emission (peak emission wavelength: 538 ± 3 nm, peak reflectance wavelength: 544 ± 11 nm).

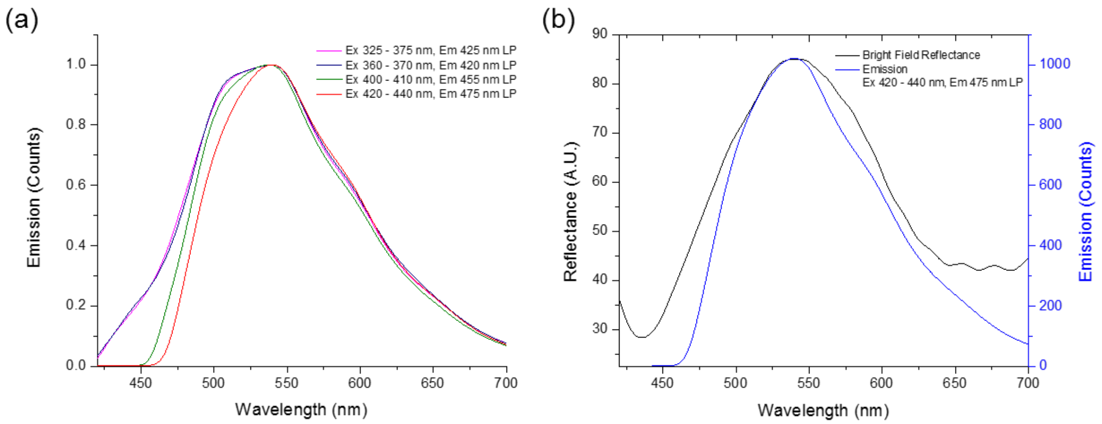

Figure 20. (a) Single scale emission spectra for scales oriented ridge-up. The same emission spectra (peak wavelength and spectral shape) was preserved with excitation ranging from the UV to the violet. (b) The emission peak wavelength (538 ± 3 nm) was the same as the peak reflectance wavelength (544 ± 11 nm), in addition to a similar spectral shape. This result suggested that the scale coloration may originate from fluorescent emission. All measurements were averaged from at least 10 separate measurements across, at least, 3 separate scales with ± 1 standard deviation as the error.

The preceding single scale, emission spectral analyses were obtained only for scales oriented ridge-up. The membrane-up emission spectrum was also investigated, as the green coloration (**Figure 18**) originates from the scale base (*i.e.*, the membrane-area). **Figure 21** shows the emission spectra for scales oriented ridge-up and ridge-down, under 420 – 440 nm excitation. Very disparate emission spectra were observed for the membrane-up relative the ridge-up samples. The membrane-up emission was characterized by a peak at 498 ± 5 nm, a local minimum occurring at 523 ± 9 nm, followed by a very broad shoulder for which a Gaussian curve could not be fitted for subsequent peak analyses. The features of the emission spectrum were roughly analogous to the dark field reflection spectrum (peak at 499 ± 12 nm and local minima at 556 ± 13 nm) (**Figure 11 (d)**). The origin of the disparate emission spectra was investigated as a potential consequence of the iridescence measured with the polycrystal oriented up (**Figure 12**), due to this similarity.

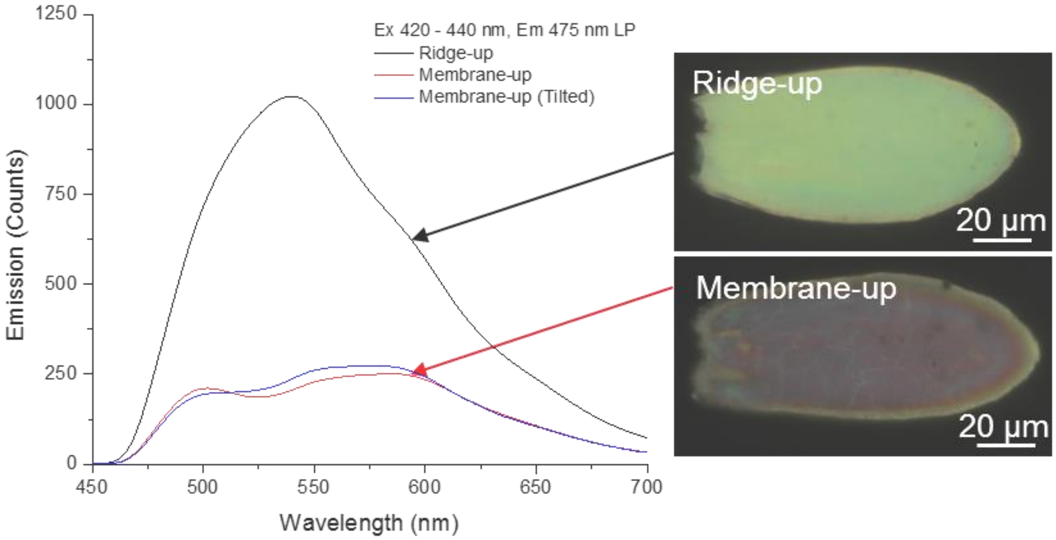

Figure 21. Comparison of membrane-up emission spectra versus ridge-up emission spectra under 420 – 440 nm excitation. Very disparate emission spectra and appearance occurred under 420 – 440 nm excitation for the ridge-up and ridge-down scale orientations. Significant differences were not observed for a tilted scale. Ridge-up and ridge-down emission spectra were averages of 18 separate measurements (6 scales with 3 measurements, each). The tilted scale spectrum was averaged across 5 separate measurements.

Emission spectra were acquired on the same tilted scale used in exploring polycrystal iridescence (**Figure 12**). The results are displayed in **Figure 21** (blue curve). A similar spectral shape was preserved for the tilted scale and the overall intensity was within the range of the measurements of scales oriented membrane-up and normal to the viewing direction. The minimal change in the emission spectrum for the tilted scale inspired the use of index-matching fluid to optically remove the possible structural modification to the emission spectrum.

Figure 22 (a, b) contains optical images of the emitted light from the scales in air or in index-matching fluid. There was an overall loss in emission intensity for scales in index-matching fluid, which could have been a result of the loss of scattering upon immersion in the index-matching fluid, absorption due to the index-matching fluid, and/or the index-matching fluid changing the environment for the fluorophore [65]. Scale orientation could not be determined upon infiltration with the index-matching fluid. However, the uniform appearance shown in **Figure 22 (b)** of the scale emission was consistent after observing over 30 different scales. In other words, the disparate scale appearance, observed for ridge-up versus ridge down in air, was not replicated for scales immersed in the index-matching fluid, which suggested that scattering from the scale features modified the emission spectrum of the scale. Supporting evidence for this conclusion was found after the emission spectrum for scales in the index-matching fluid was measured (**Figure 22 (c)**). The same spectral shape and peak intensity (539 ± 3 nm) was observed in index-matching fluid as the emission from the ridge structure oriented up for scales in air.

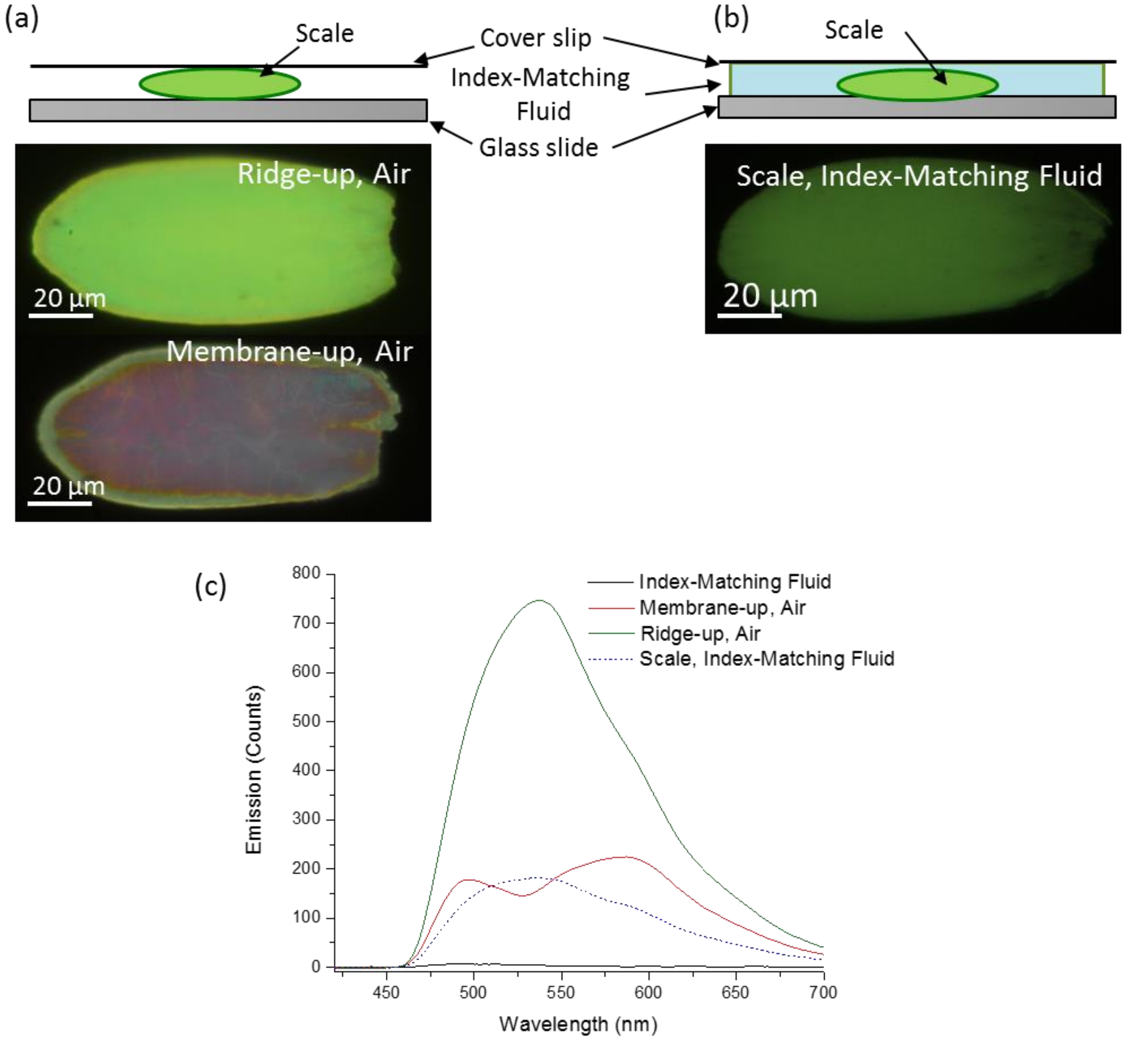

Figure 22. Comparison of single scale emission spectra for scales in air or immersed in index-matching fluid. Schematic and fluorescence images of scales in (a) air and (b) immersed in index-matching fluid. (c) Disparate emission spectra were observed between the two scale orientations in air. However, a uniform appearance of scale emission occurred upon immersion in index-matching fluid. The same peak emission was preserved as well (539 ± 3 nm for scales in index-matching fluid and 538 ± 3nm for scales, oriented ridge-up, in air). The index-matching fluid used in this study provided minimal background for the emission measurement. All measurements were averaged from at least 10 separate measurements across, at least, 3 separate scales with ± 1 standard deviation as the error.

There was a striking similarity between the quantitative emission spectra and qualitative emission imaging for scales in air (**Figure 22**) and the dark field reflection images and spectra (**Figure 11 (b, d)**), also for scales in air. The spectra from the ridge-up orientation were greater in intensity than that of the membrane-up intensity for both emission (**Figure 22**) and dark field reflection (**Figure 11 (b, d)**) measurements.

However, it was unclear why the emission spectra changed so dramatically between ridge-up and ridge down orientations in air (**Figure 21** and **Figure 22**). Future efforts may be able to explore fluorescent emission within the *P. sesostris* green scale through the use of computational modeling [16, 66].

The next investigation of scale emission focused on the distribution of the fluorophore to determine if it is localized only in the scale base or distributed throughout the rest of the scale. Localization of the fluorophore only within the membrane-area would add further evidence supporting a green color origin as a result from localized light emission. A single butterfly scale was milled to expose the blue-appearing portion of the polycrystal to test whether the fluorescent emission was localized to the removed region of the scale. Emission images and spectra confirmed that a considerable amount of the emission originated from the blue-appearing polycrystal and ridge structure. That is, the emission was not solely localized in the membrane-area of the scale (the area strongly affecting the overall green coloration).

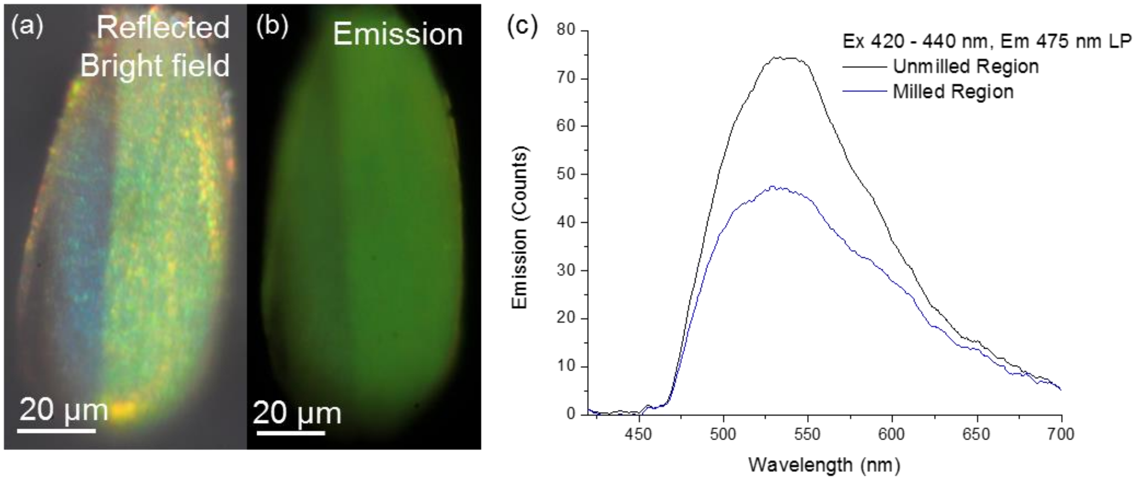

Figure 23. (a) Bright field optical image of a *P. sesostris* green scale FIB-milled to partially remove the membrane-area, exposing the blue-appearing portion of the polycrystal. (b) Emission image collected with 420 – 440 nm excitation and 510 nm long pass emission filters demonstrated the preservation of green emissive color in the milled region. (c) Emission spectra demonstrated that a considerable portion of the scale emission was due to a fluorophore present in the remaining portion of the milled scale. 3 separate scans were average in each region for the emission spectra.

Further evidence supporting the distribution of a green-emitting fluorophore throughout the scale was obtained using confocal fluorescence microscopy (courtesy of Dr. Vincent Chen, Perry Group, Georgia Institute of Technology). Emitted image collection (artificially colored green) utilized 405 nm laser as an excitation source, in combination with a 500 nm long pass filter for emitted photon collection. This method non-destructively sectioned fluorescent scale components. Structural features of the scale observed with SEM were observed in the confocal data (**Figure 24**), including the ridge structure and gyroid polycrystal region. Additionally, the confocal cross-section of the scale, which is the cross-sectional view of the 3-dimensional image composite, shows the emission distributed throughout the scale (**Figure 24**).

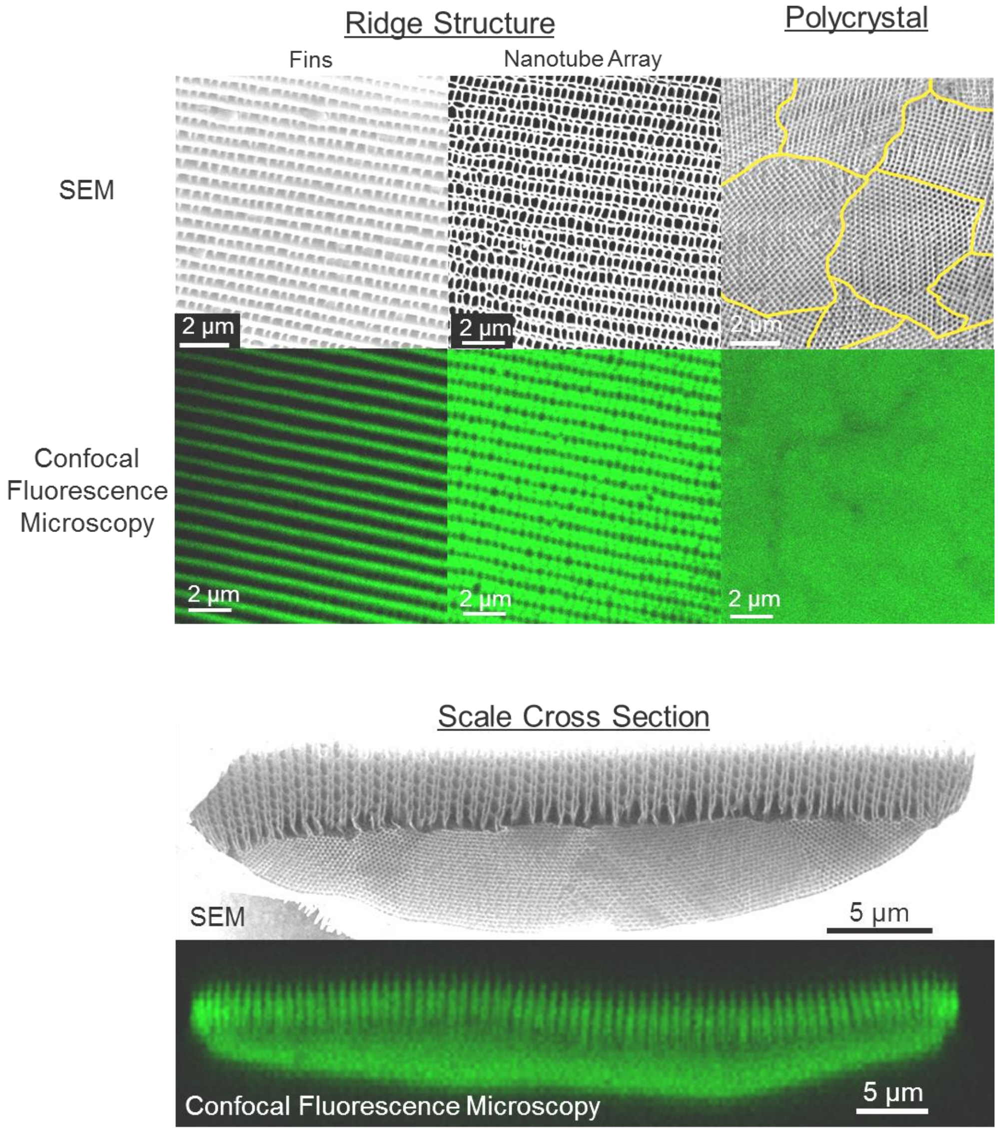

Figure 24. Confocal fluorescence microscopy confirmed fluorophore distribution throughout the scale structure. All confocal images were artificially colored green. Scale structural features observed through Scanning Electron Microscopy (SEM) were observed in the confocal fluorescence microscopy images, including the ridge structure (composed of the fins and nanotube array) and the polycrystal domain boundaries. Cross sectional confocal images indicate that the emission source was distributed throughout the scale. Confocal imaging courtesy of Dr. Vincent Chen, Perry Group, Georgia Institute of Technology.

Examination of the *P. sesostris* green scales have confirmed that the scales do emit light, that partial removal of the polycrystal portion of the scale can modify the emission, and that the fluorophore was distributed throughout the scale. The remaining question is whether or not the scale emission was the sole cause of scale coloration. Initial attempts at addressing the contribution of emission to the overall butterfly scale coloration involved photobleaching the scales under prolonged exposure to UV light (sample preparation courtesy of Russell Shimada and Dr. Dimitri Deheyn, Scripps Institute of Oceanography). Two months of continuous UV exposure were required before any color change was observed. However, structural analysis of the photobleached scales confirmed that a significant shrinkage of the gyroid polycrystal lattice had also occurred. (**Appendix A, Figure 68**). This change in polycrystal dimension convoluted the interpretation of the blue scale coloration as the polycrystal shrinkage could blue shift the structural color from the scale as well as bleach the fluorophore(s) within the scale.

Changing the scale illumination from white light to long wavelength light was used to determine the fluorescent color contribution for the scale. This method has been used, successfully, for other butterfly species [67] and did not involve any treatments that could change the physical dimensions of the scale. A fluorescence filter cube was modified to enable reflection measurements with white light illumination (using a 50/50 beam splitter) and long wavelength illumination only (using a 510 nm long pass filter). The long pass filter removed any excitation less than or equal to 510 nm from the white light source.

Figure 25 shows that the reflectance spectral shape from the same scale does not change upon removal of short wavelength illumination. This demonstrates that the scale coloration was not solely due to light emission excited by wavelengths less than or equal to 510 nm. If scale coloration was due to such fluorescence, then significant changes in the spectral shape under long wavelength illumination would occur. The contribution of fluorescence to the overall scale optical signature is within the error of the measurement (**Figure 25 (a)**).

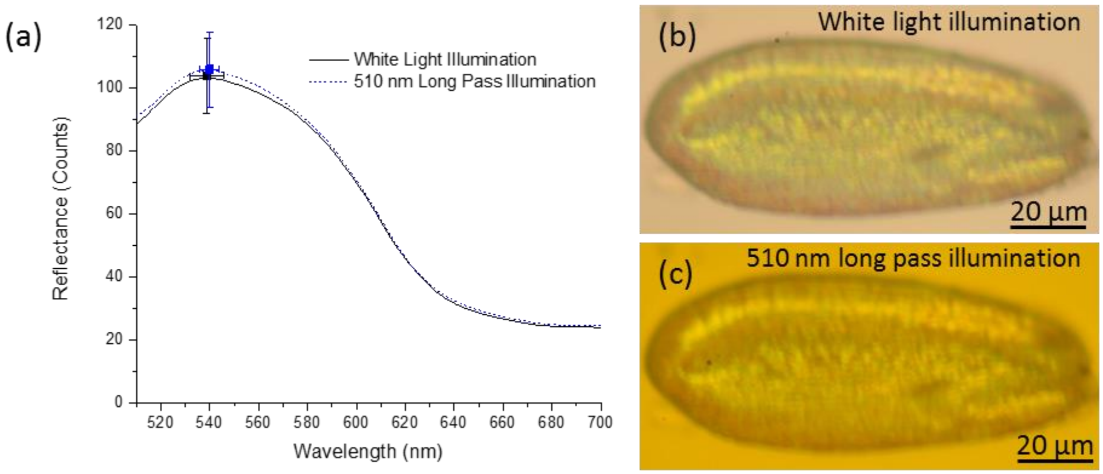

Figure 25. White light or long wavelength illumination reflection spectra for the milled and unmilled regions of a membrane-area removed scale. (a) The spectral shape of the scale reflectance was unchanged under white light versus only long wavelength illumination for both the milled and unmilled regions. Average peak reflectivity and intensity were statistically equivalent for either illumination. Optical images under (b) white light and (c) long wavelength illumination confirm the preservation of scale color.

1.5.5 Investigation of lattice spacing distribution as cause for structural origin to scale coloration

A structural origin to the *P. sesostris* scale coloration was explored by measuring the pore spacing distribution throughout the gyroid thickness. Cross-sections for the *P. sesostris* green scale were created through FIB milling and the hexagonal lattice pore spacing was measured as a function of gyroid polycrystal row. The hexagonal lattice was selected because it was easily recognized during the SEM session and has been used for previous efforts in tracking changes to the gyroid upon inorganic coating and scale replication [63]. Polycrystal domains occur laterally within the plane of the gyroid region, but not throughout the scale thickness. Thus, the lattice spacing could be quantified throughout the gyroid polycrystal thickness on a single gyroid crystal.

Quantitative analysis of the pore spacing is shown in **Figure 26**, displaying a gradient distribution of the pore spacing. The hexagonal pore spacing increased in the thickness direction of the gyroid: 220 ± 6 nm near the ridges and 259 ± 11 nm near the thin, solid membrane. This result was consistent with the hypothesis of structural coloration through a gradual increase in the lattice parameter towards the scale base. Blue coloration for scales with the bottom 1.3 µm of the scale removed could be explained by the removal of the larger lattice spacing of the gyroid in the membrane area. This would remove the longer wavelength reflection from the gyroid, leaving the overall blue coloration due to the shorter lattice spacing.

The Bragg equation,

$$\lambda = \frac{2n\Lambda\sin(\theta)}{m}, \qquad \textbf{(1)}$$

was used for a back-of-the-envelope calculation for diffracted coloration from selected pore spacings, measured from the hexagonal gyroid polycrystal face. For **Equation 1**, λ was the diffracted wavelength (nm), m was the diffracted order (set to 1), n approximated the refractive index of the diffracting medium (set to 1.56), Λ was the period of the diffraction grating (nm), and was the θ diffraction angle (degrees). The diffraction angle was fixed to 43^o. Computation of the diffracted wavelength revealed a relatively green (551 nm) and a relatively blue (468 nm) coloration, upon changing the diffraction grating period from 259 nm to 220 nm, respectively. This shift in coloration upon the reduction in grating period suggested that the reduced dimensions, near the ridges, of the measured gyroid polycrystal pore spacings could blue shift the observed structural coloration from the *P. sesostris* green scale upon the removal of the longer pore spacings near the scale base.

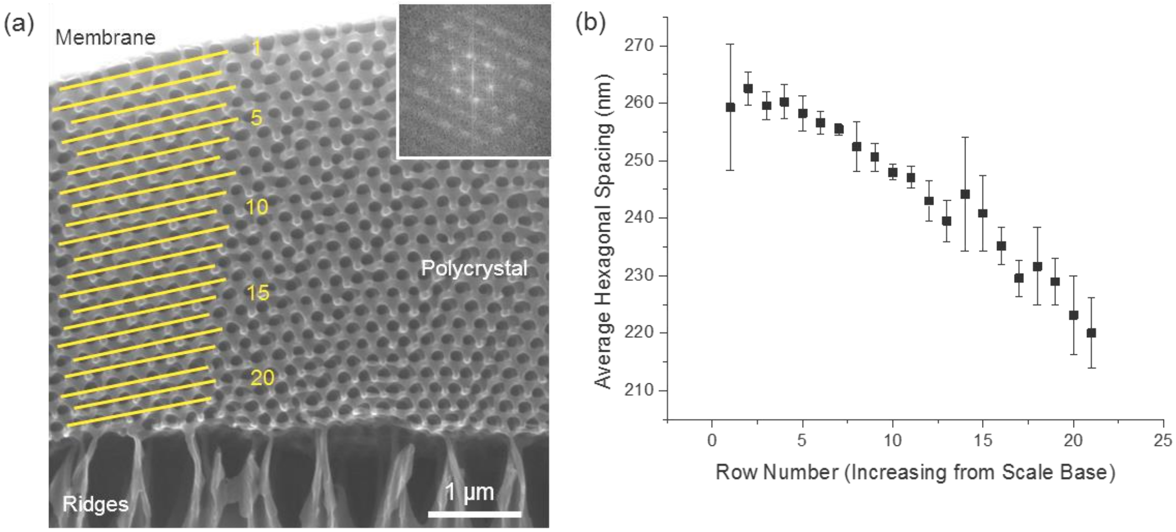

Figure 26. Lateral pore spacing distribution as measured on the hexagonal gyroid crystal face. (a) Secondary electron image of a *P. sesostris* scale cross-section, oriented with the thin, solid membrane on top and ridges at bottom. Example measurement areas are shown, indicating polycrystal row with row number increasing from scale base. (Inset) Fast Fourier Transform (FFT) of the image confirmed exposure of hexagonal polycrystal face. (b) Results of pore spacing measurements from hexagonal faces, averaged from four measurements on three separate polycrystal domains on the same scale. A larger pore spacing was found at the top of the scale, which decreased towards the ridges. This change in pore spacing was consistent with structural coloration where a more blue coloration was observed from the smaller pore spacing near the ridges.

The discovery of a gradient in the pore spacing suggested that a gradual change in peak reflected wavelength would occur if the polycrystal gyroid was appropriately sectioned using FIB milling. Such a gradient amount of gyroid material was removed in a trench from a single *P. sesostris* green scale (**Figure 27**). The smallest reflection measurement spot size of 6 µm x 6 µm was utilized for these reflection measurements to enable the highest spatial resolution across the gradient-milled scale section. Spectral measurements revealed that a gradual change in peak reflectance occurred as the reflectance was measured along the milling gradient. The first measurement, in the relatively greener region, exhibited a peak reflectance of 530 ± 3 nm, which gradually decreased to 488 ± 3 nm (**Figure 27 (c, d)**). Eventually, the reflection peak was lost within the region where only the ridge structure was retained (**Figure 27 (c)**). Many reports exist of biological coloration strategies employing 1-dimension multilayers with a graded period.[68-73] However, this work is the first report of a 3-dimensional, biological nanostructure with a graded periodicity in a periodic pore (photonic crystal-like) structure.

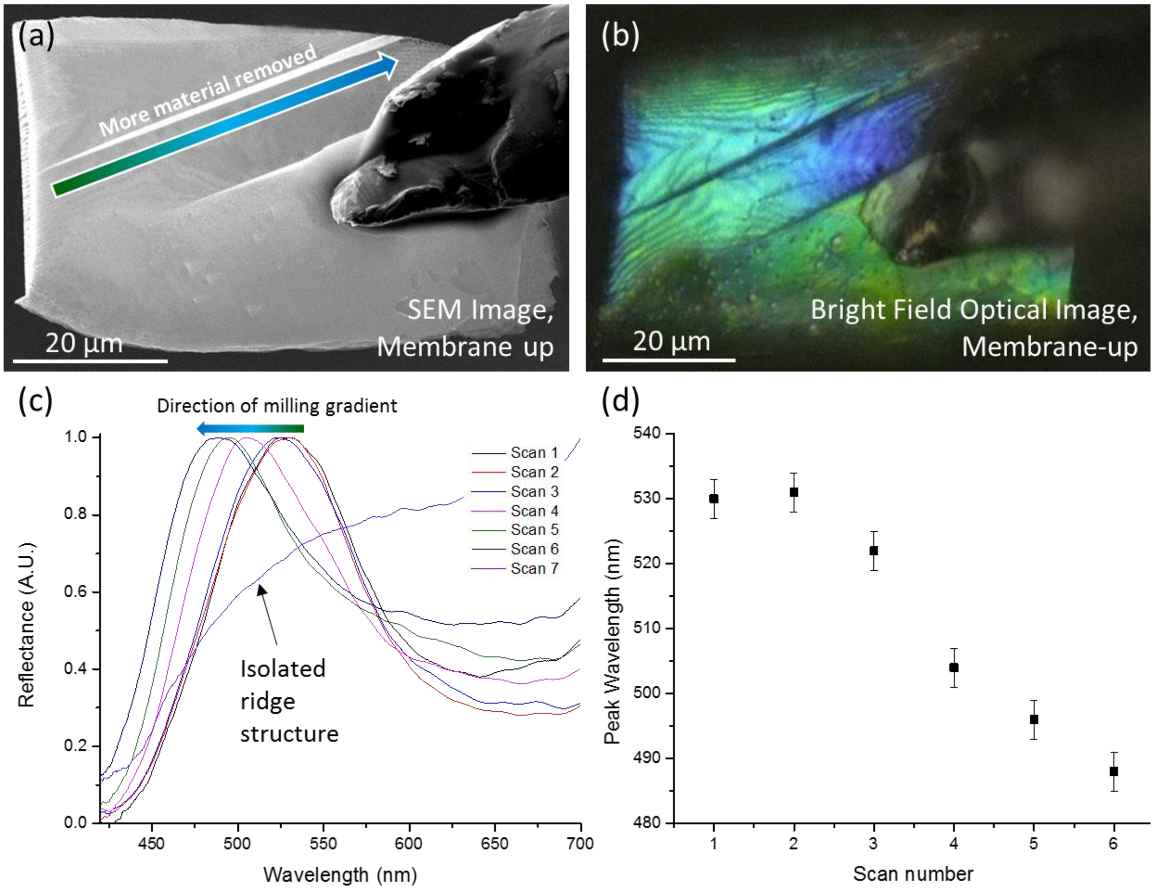

Figure 27. Reflectance analysis of a gradient milled photonic crystal scale. (a) Secondary electron image showing the gradient milled (trench) region. (b) Bright field optical image for same scale, oriented membrane-up, showed the gradient color in the direction of the FIB milled trench. (c) Normalized reflection spectra and (d) peak wavelength values show the gradual decrease in reflection peak wavelength measured across the milling gradient. Eventually the reflectance peak was lost once the isolated ridge structure was measured (Scan 7). Peak reflectance is reported as individual scans with the instrument error as the error bars (*i.e.*, 3 nm). Similar results were obtained after changing the sample position and repeating the measurement a total of 4 times.

1.5.6 Diffuse and directional scattering originates from the ridge structure

The previous analyses have shown that the ridge structure plays a relatively minor role in the overall scale coloration. That is, single scales with the ridges removed (polycrystal and membrane-area intact) retained the overall green coloration (**Figure 16**). Additionally, the overall scale coloration remained blue on both sides of the scale once a sufficient thickness of the scale base (gyroid polycrystal and thin, solid membrane) had been removed (**Figure 16**). Yet, iridescence was observed for scales oriented membrane-up, but not ridge-up (**Figure 11**). This result, as well as other studies [32, 46, 50, 58, 59], indicate that the ridge structure suppresses iridescence from the polycrystal. This effect was further studied with the isolation and interrogation approach to better understand the contribution of the ridge structure to the scattering properties of the whole scale.

Another example of polycrystal iridescence is shown in **Figure 28** for a sample selectively milled to remove the ridge structure, exposing the gyroid polycrystal and membrane-area. Two separate regions of the scale were intentionally left as whole scale regions, allowing the ridge structure scattering contribution to be characterized, relative the milled region. The differences in sample appearance, oriented ridge side up, in bright field/dark field for the milled region showed the same coloration as a native scale, oriented with the membrane facing up (**Figure 11 (c, d)**). The whole scale section retained the uniform, green coloration, independent of the angular change in the incident light in switching between imaging modes, in agreement with ridge-up bright field/dark field reflection analysis (**Figure 11**).

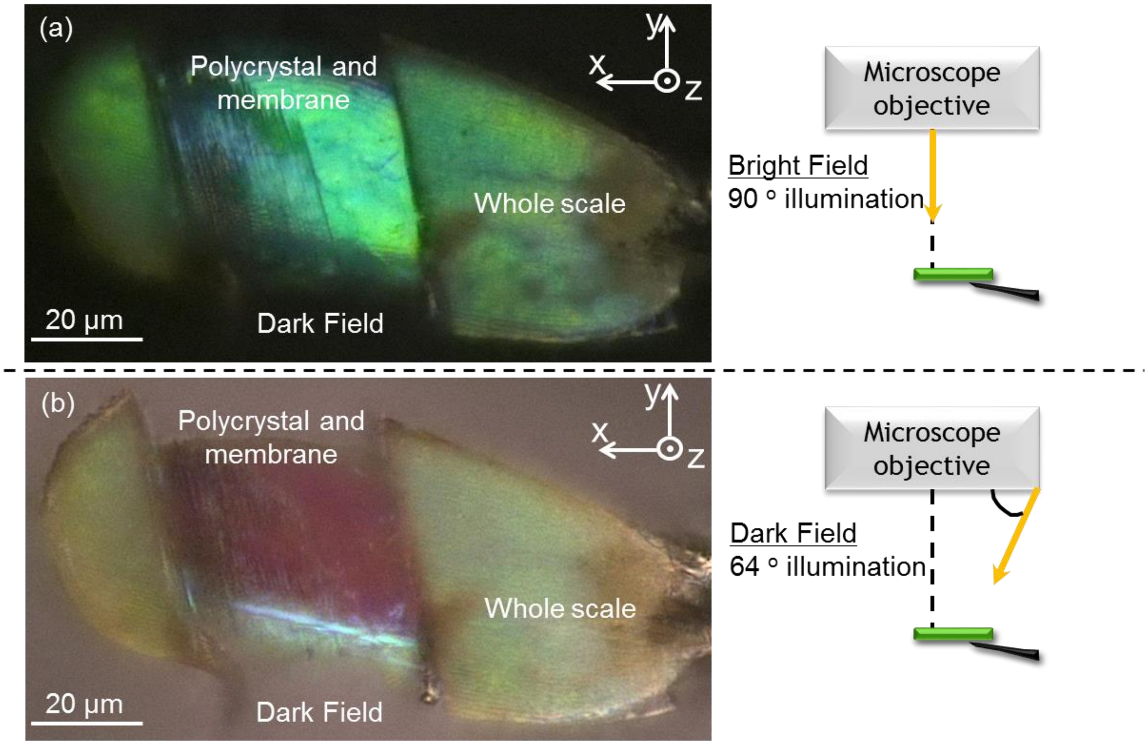

Figure 28. Polycrystal iridescence observed by changing the angle of illumination for a fixed scale position. (a) Bright field and (b) dark field optical images of a scale oriented ridge-up and normal to the viewing direction (dotted line). The dramatic change in coloration observed in the milled region, but not the whole scale region, demonstrated the importance of the ridge structure in homogenizing the angle of light transmitted to, and reflected from, the polycrystal.

Separate FIB-milled samples were imaged at two different tilt angles in bright field mode as another means of characterizing polycrystal iridescence. (Note: The previous experiment kept a fixed sample position, but changed the angle of incident light). Iridescence from the exposed polycrystal and membrane-area (*i.e.*, ridges removed) was observed when the scale orientation was altered after removal of the ridges through FIB milling (**Figure 29 (a, b)**). The brown coloration of the scale close to the point of attachment for the needle was most likely due to damage from the ion beam during focusing and/or epoxy infiltration from the needle mounting procedure. Further evidence of polycrystal iridescence is found by imaging the reflected light from a scale, oriented ridges-down, where the intact ridge structure had a minimal influence on the reflected light. An overall blue iridescence was observed for the region where the membrane-area was removed (**Figure 29 (c, d)**). Additional, green iridescence was observed in the unmilled region of the same scale. These results confirm the hypothesis that the ridge structure acted to suppress the iridescence from the polycrystal [32, 46, 50, 58, 59].

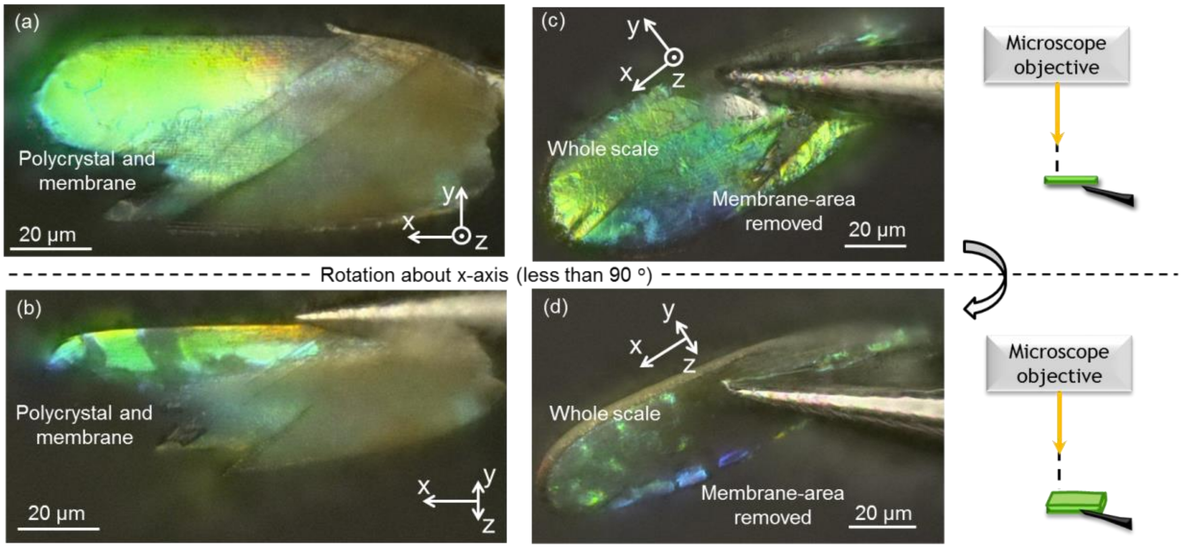

Figure 29. Polycrystal iridescence investigated by changing the scale orientation with respect to a fixed angle of incidence (bright field). (a) Optical image of a scale with ridges removed (polycrystal and thin, solid membrane intact), oriented ridge-up and normal to the optical axis. Tilting the scale revealed the iridescent polycrystal domains. (c) Scale oriented membrane-up with a portion of the membrane-area removed (ridge structure and partial polycrystal remaining) displayed an overall blue and green coloration in the milled/unmilled regions, respectively. (d) Iridescence from the polycrystal was observed in the milled and unmilled regions of the scale when the scale was tilted with respect to the optical axis.

Next, structural periodicities found within the ridge structure were correlated with the scattering observed from scales oriented ridge-up in imaging scatterometry. Analysis of SEM and TEM images of the isolated ridge structure and the native scale has revealed that the fin structure and the nanotube array share the same periodicities (**Appendix A, Figure A.6**). Two, dominant periodicities were found in the ridge structure (analysis courtesy of Alfred Lethbridge, Vukusic Group, University of Exeter). A Fast Fourier Transform (FFT) (**Figure 30 (c)**) of the isolated nanotube array (**Figure 30 (b)**) confirmed the existence of the two periodicities. The first periodicity was oriented along the scale width, with a period of 742 ± 15 nm (**Figure 30 (b)**). Diffraction from this period would produce a diffracted mode parallel with the scale width and perpendicular to the scale length. The second periodicity was oriented along the scale length with a period of 228 ± 17 nm (**Figure 30 (b)**). Diffraction from this period would occur parallel with the scale length and perpendicular to the scale width.

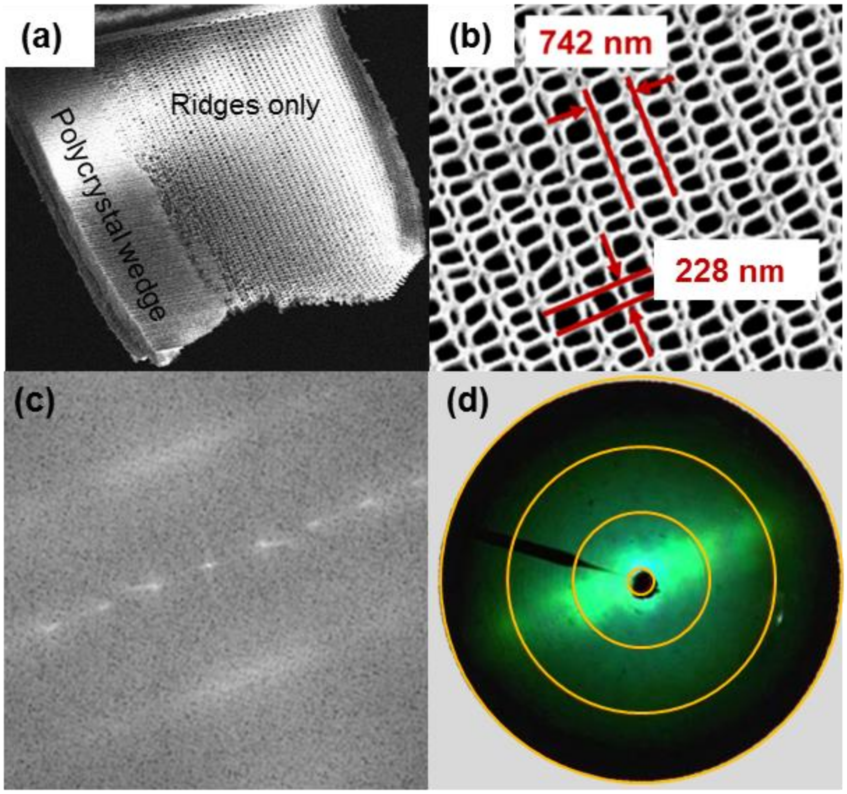

Figure 30. (a) Secondary electron image of an isolated ridge structure sample (oriented membrane side up) and (b) higher magnification of the same sample displaying the 742 ± 15 nm periodicity involved in the directional scattering and a 228 ± 17 nm periodicity, believed to be used for structural support and/or assisting the uniform scattering of light. Periodicity analysis courtesey of A. Lethbridge. (c) FFT of ridge structure secondary electron image, confirming that two periodicities exist in the ridge structure. (d) An imaging scatterogram of a native *P. sesostris* scale, oriented ridge side up, displayed diffuse and directional scattering (courtesy A. Lethbridge). Increasing scattering angle towards the outer edge of the scatterogram indicated by the concentric yellow circles starting at 5° in the center, followed by 30°, 60°, and 90°.

Wilts, et al. proposed that a highly directional scattering, observed as a green line in imaging scatterometry (**Figure 30 (d)**), on a ridge-up, *P. sesostris*, green scale was due to diffraction from the fin structure.[50] Their conclusions [50] were based on a comparison of imaging scatterometry data from other butterflies with prominent, periodic ridges [51, 74].

The observed diffraction mode (**Figure 30 (d)**) was oriented parallel with the scale width, which was consistent with directional scattering from the native scale along the 742 ± 15 nm period. No evidence of directional scattering parallel to the scale width, which would occur from the 228 ± 15 nm period, was observed in the image scatterogram in **Figure 30 (d)**. The imaging scatterometry results were consistent with prior reports [50]. However, it was still unclear if both the nanotube array and the fin structure contributed to the directional green scattering, since the two structures share this same period (**Appendix A, Figure 69**). Attempts to obtain imaging scatterometry data on fins-removed (*i.e.*, nanotube array, polycrystal, and membrane-area intact) and ridge-only (*i.e.*, nanotube array and fins) samples were unsuccessful due to the difficulty in aligning the sample and scattering from the metal needle tip. It is hypothesized that the 228 ± 17 nm periodicity in the nanotube array may be responsible for structural support and/or the creation of diffuse scattering of light transmitted to and reflected from the scale.

Prior studies on scales, in other butterfly species with prominent ridge structures, have shown the preservation of the directional scattering at a whole wing-level.[74] Imaging scatterometry used on *P. sesostris* wing sections demonstrated preservation of this directional scattering at the wing level, as a result of the periodicity within the ridge structure (**Figure 30 (b)**). Examination of the wing sections reveal an average orientation to the scales imbricated on the wing, which caused this cooperative interaction across hundreds of scales (**Figure 31 (b)**).

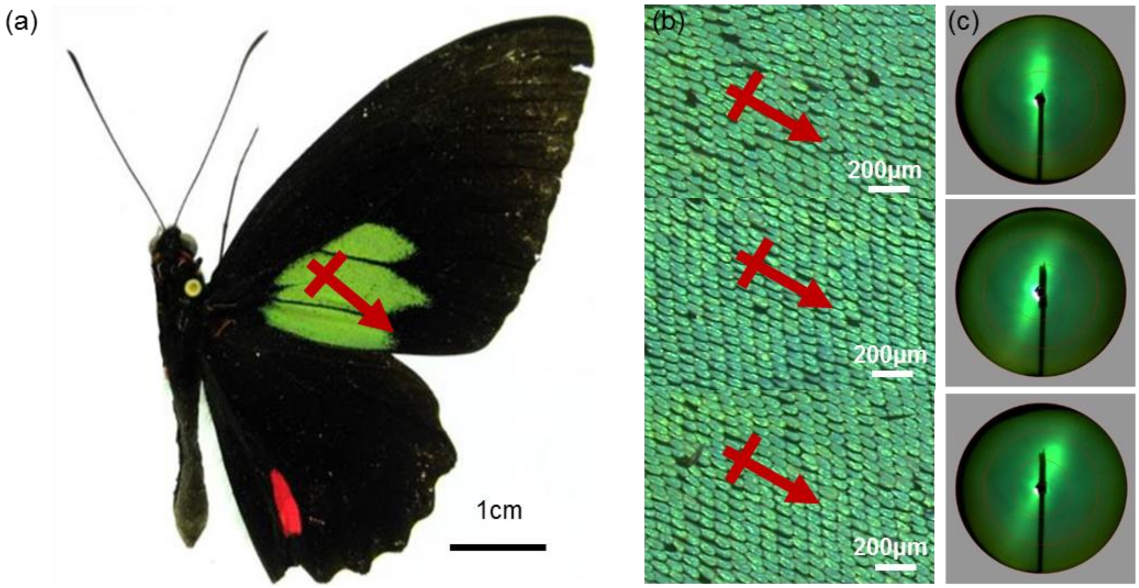

Figure 31. Photograph of native, *P. sesostris* section (©Smithsonian Institution National Museum of Natural History) with arrow indicating the longitudinal direction of the green scales, and crossbar indicating the direction of the green directional scattering. (b) Optical microscope images of each of the three green patches on the wing, with arrows indicating the average direction of the scales and the expected orientation of the directional scattering. (c) Imaging scatterometry from each wing section showing the observed directional scattering, confirming expectations from the scale orientation on the wing (data courtesy Alfred Lethbridge, Vukusic group, University of Exeter).

1.6 Conclusions

Scale component nanostructures within the green, *Parides sesostris* scales have been isolated through FIB milling and correlated with optical appearance for the first time. This interrogation has revealed four component structures: the ridge structure (composed of fins and a nanotube array), gyroid polycrystal, and a thin, solid membrane. Removal of the ridge structure (leaving the gyroid polycrystal and thin, solid membrane) resulted in a green scale coloration. The isolated ridge structure exhibited little reflected color, appearing slightly brown. When the bottom 1.3 μm of the scale was removed, which left a portion of the gyroid polycrystal and the intact ridge structure, the scale turned blue. Spectral analysis of a ridge-removed specimen (*i.e.,* gyroid polycrystal and thin, solid membrane intact) did reveal some blue wavelength components. However, the results presented in this study do not support localized absorption in the ridge structure (hypothesis presented by Wilts, *et. al.*[50]) as a dominant coloration mechanism for the

P. sesostris green scale. These observations launched a systematic approach for understanding the origin of green color from the *P. sesostris* green scales.

Reflection measurements on specimens with the scale base removed revealed a spectral overlap between the milled and unmilled spectra. This confirmed that the remaining portion of the gyroid polycrystal contributed to the overall scale coloration. Thin, film interference from the thin, solid membrane, localized fluorescent emission, and a distribution of polycrystal pore spacings were interrogated as sources for the optical contribution of the membrane-area (the bottom 1.3 µm of the scale). Measurements from TEM images provide a thin, solid membrane thickness of 68 ± 20 nm. Modeling results indicated that the light reflected from the thin, solid membrane was very broad and dissimilar from experimental measurements on the whole scale, ruling out thin film interference from the thin, solid membrane as the sole source of green coloration.

Single scale emission measurements revealed emission spectra with the same peak wavelength and spectral shape for excitation ranging from the UV to violet. The peak emission wavelength (538 ± 3 nm) was the same as the bright field, peak reflectance wavelength (544 ± 11 nm). Confocal fluorescence microscopy demonstrated that the fluorophore was distributed throughout the scale (*i.e.*, not solely localized in the bottom 1.3 µm of the scale. No change in spectral shape occurred between white light and long wavelength (using a 510 nm long pass filter) illumination for a single green scale. This demonstrated that fluorescence was not the sole, or dominant, cause of the green coloration.

Structural coloration was left as the remaining, dominant coloration mechanism after ruling out thin film interference and localized fluorescent emission. Evidence gathered through this work strongly supports coloration due to structure. The precise separation of scale component structures enabled discoveries that were never apparent from previous whole scale studies, supporting structural coloration.[32, 50, 58] A key discovery is a gradient, gyroid pore spacing. While graded structures have been found in some biological nanostructures [68-73], this discovery is the first reported, 3-dimensional bioorganic nanostructure with a graded pore spacing for control of color. The gyroid contained larger pore spacings at the scale base, near the thin solid membrane, which became progressively smaller towards the ridge structure. The appearance of an overall blue coloration when, at least, 1.3 μm of the scale base was removed could be explained by the removal of the larger pore spacings from the gyroid, which would reflect greener light. Reflectance measurements across a scale milled with a gradient amount of gyroid material removed, supported this conclusion.

Further evidence supporting structural coloration included investigations of scale transmittance and polycrystal iridescence. Comparison of scale transmittance for scales in index-matching fluid or air resulted in a loss in transmission for scales in air. Scale absorption occurs in both cases, which left changes in scattering as the likely cause of decreased transmission. This loss in scattering upon immersion in index-matching fluid occurred over a similar wavelength range as the peak reflection. Dramatic changes in peak reflectance, spectral shape, and qualitative appearance occurred with changes in scale orientation, angular change of the incident light, and selective removal of the ridge structure through FIB milling. Preservation of spectral shape and peak reflectivity, for scales oriented ridge-up, provided further evidence for the suppression of polycrystal iridescence through the ridge structure [32, 46, 50, 58, 59].

Scattering properties of the ridge structure were analyzed and two periodicities were found within the ridge structure: 228 ± 17 nm and 742 ± 15 nm. Directional scattering observed from the ridge structure through imaging scatterometry was correlated to the 742 ± 15 nm period, which was shared by the fins and nanotube array. It is hypothesized that the 228 ± 17 nm period could provide structural support for the ridge structure and or a scattering surface to assist in diffuse scattering. Directional scattering, observed on single scales, was preserved at the wing-level due to the overall scale alignment on the wing surface.

Other scale components and fluorescent emission may assist the structurally colored polycrystal in creating the overall appearance of other butterflies. Prior studies of *P. oribazus* and *P. nireus* coloration have shown similar peak emission and peak reflection wavelengths, but with very minor contributions of fluorescence to the overall scale coloration.[67] The role of fluorescence in the overall scale coloration for *P. sesostris* could be to supplement [67, 75, 76] the structural green coloration from the gyroid polycrystal. Supplementary fluorescent coloration could be assisted by the thin, solid membrane through the reflection of shorter wavelength light through the scale thickness. This could increase the effective path length of light through the scale, increasing the likelihood of absorption, and subsequent fluorescent emission. Such cooperative structure-fluorescence effects have been suggested for the *Papilio oribazus* [77], *Papilio nireus* [77], and *Troides magellanus* [75, 78].

P. sesostris green scales present a rich, multicomponent structure for future modeling and simulation studies. Modeling inspired by the gyroid polycrystal have expanded knowledge of polycrystal iridescence.[50, 79] However, utilization of 3-dimensional models acquired from the exact scale microstructure would allow further exploration of the pore spacing discovered in this work. It may be possible to generate 3-dimensional models of the entire scale thickness (thin, solid membrane; polycrystal, and ridge structure) through the use of synchrotron x-ray tomography [80] and/or FIB tomography [55]. Such realistic models may enable further exploration of light scattering from the ridge structure [15] and polycrystal [55]. Precise determination of the refractive index [65] for the *P. sesostris* scales would assist such modeling efforts. Absorption [16] and fluorescence [66] simulations could also be integrated, enabling a study of how the polycrystal could modify the spectral shape of the fluorophore(s) within the scale.

1.7 References

[1] L. P. Biro and J. P. Vigneron, "Photonic nanoarchitectures in butterflies and beetles: valuable sources for bioinspiration," *Laser & Photonics Reviews,* vol. 5, pp. 27-51, Jan 2011.
[2] P. Vukusic and R. Sambles, "Photonic structures in biology," *Nature,* vol. 424, pp. 852-855, 2003.
[3] S. Kinoshita, S. Yoshioka, and J. Miyazaki, "Physics of structural colors," *Reports on Progress in Physics,* vol. 71, Jul 2008.
[4] R. A. Potyrailo, H. Ghiradella, A. Vertiatchikh, K. Dovidenko, J. R. Cournoyer, and E. Olson, "Morpho butterfly wing scales demonstrate highly selective vapour response," *Nature Photonics,* vol. 1, pp. 123-128, Feb 2007.
[5] C. M. Eliason and M. D. Shawkey, "Rapid, reversible response of iridescent feather color to ambient humidity," *Optics Express,* vol. 18, pp. 21284-21292, Sep 2010.
[6] L. P. Biro, K. Kertesz, Z. Vertesy, and Z. Balint, "Photonic nanoarchitectures occurring in butterfly scales as selective gas/vapor sensors," in *Nature of Light: Light in Nature Ii*. vol. 7057, K. Creath, Ed., ed Bellingham: Spie-Int Soc Optical Engineering, 2008.
[7] P. R. Stoddart, P. J. Cadusch, T. M. Boyce, R. M. Erasmus, and J. D. Comins, "Optical properties of chitin: surface-enhanced Raman scattering substrates based on antireflection structures on cicada wings," *Nanotechnology,* vol. 17, pp. 680-686, Feb 2006.
[8] W. Zhang, D. Zhang, T. X. Fan, J. J. Gu, R. Ding, H. Wang, *et al.*, "Novel Photoanode Structure Templated from Butterfly Wing Scales," *Chemistry of Materials,* vol. 21, pp. 33-40, Jan 2009.
[9] A. D. Pris, Y. Utturkar, C. Surman, W. G. Morris, A. Vert, S. Zalyubovskiy, *et al.*, "Towards high-speed imaging of infrared photons with bio-inspired nanoarchitectures," *Nat Photon,* vol. 6, pp. 195-200, 2012.
[10] N. L. Garrett, P. Vukusic, F. Ogrin, E. Sirotkin, C. P. Winlove, and J. Moger, "Spectroscopy on the wing: Naturally inspired SERS substrates for biochemical analysis," *Journal of Biophotonics,* vol. 2, pp. 157-166, Mar 2009.
[11] B. T. Hallam, A. G. Hiorns, and P. Vukusic, "Developing optical efficiency through optimized coating structure: biomimetic inspiration from white beetles," *Applied Optics,* vol. 48, pp. 3243-3249, Jun 2009.
[12] P. Vukusic, J. R. Sambles, C. R. Lawrence, and R. J. Wootton, "Quantified interference and diffraction in single Morpho butterfly scales," *Proceedings of the Royal Society of London Series B-Biological Sciences,* vol. 266, pp. 1403-1411, Jul 1999.
[13] L. Plattner, "Optical properties of the scales of Morpho rhetenor butterflies: theoretical and experimental investigation of the back-scattering of light in the visible spectrum," *Journal of the Royal Society Interface,* vol. 1, pp. 49-59, Nov 2004.
[14] S. Kinoshita, S. Yoshioka, and K. Kawagoe, "Mechanisms of structural colour in the Morpho butterfly: cooperation of regularity and irregularity in an iridescent

scale," *Proceedings of the Royal Society of London Series B-Biological Sciences,* vol. 269, pp. 1417-1421, Jul 2002.

[15] J. Boulenguez, S. Berthier, and F. Leroy, "Multiple scaled disorder in the photonic structure of Morpho rhetenor butterfly," *Applied Physics a-Materials Science & Processing,* vol. 106, pp. 1005-1011, Mar 2012.

[16] A. Mejdoubi, C. Andraud, S. Berthier, J. Lafait, J. Boulenguez, and E. Richalot, "Finite element modeling of the radiative properties of Morpho butterfly wing scales," *Physical Review E,* vol. 87, Feb 2013.

[17] B. Gralak, G. Tayeb, and S. Enoch, "Morpho butterflies wings color modeled with lamellar grating theory," *Optics Express,* vol. 9, pp. 567-578, Nov 2001.

[18] M. A. Steindorfer, V. Schmidt, M. Belegratis, B. Stadlober, and J. R. Krenn, "Detailed simulation of structural color generation inspired by the Morpho butterfly," *Optics Express,* vol. 20, pp. 21485-21494, Sep 2012.

[19] R. H. Siddique, S. Diewald, J. Leuthold, and H. Holscher, "Theoretical and experimental analysis of the structural pattern responsible for the iridescence of Morpho butterflies," *Optics Express,* vol. 21, pp. 14351-14361, Jun 2013.

[20] R. T. Lee and G. S. Smith, "Detailed electromagnetic simulation for the structural color of butterfly wings," *Applied Optics,* vol. 48, pp. 4177-4190, Jul 2009.

[21] M. Kambe, D. Zhu, and S. Kinoshita, "Origin of Retroreflection from a Wing of the Morpho Butterfly," *Journal of the Physical Society of Japan,* vol. 80, May 2011.

[22] S. Berthier, E. Charron, and J. Boulenguez, "Morphological structure and optical properties of the wings of Morphidae," *Insect Science,* vol. 13, pp. 145-158, 2006.

[23] S. Banerjee and Z. Dong, "Optical characterization of iridescent wings of Morpho butterflies using a high accuracy nonstandard finite-difference time-domain algorithm," *Optical Review,* vol. 14, pp. 359-361, Nov-Dec 2007.

[24] E. Iwase, K. Matsumoto, I. Shimoyama, and Ieee, "The structural-color based on the mechanism of butterfly wing coloring for wide viewing angle reflective display," in *Mems 2004: 17th Ieee International Conference on Micro Electro Mechanical Systems, Technical Digest,* ed, 2004, pp. 105-108.

[25] L. Collins, "You ain't seen nothin' yet," *Engineering & Technology,* vol. 5, pp. 64-65, 2010.

[26] K. Chung, S. Yu, C. J. Heo, J. W. Shim, S. M. Yang, M. G. Han, *et al.*, "Flexible, Angle-Independent, Structural Color Reflectors Inspired by Morpho Butterfly Wings," *Advanced Materials,* vol. 24, pp. 2375-2379, May 2012.

[27] T. H. Wong, M. C. Gupta, B. Robins, and T. L. Levendusky, "Color generation in butterfly wings and fabrication of such structures," *Optics Letters,* vol. 28, pp. 2342-2344, Dec 2003.

[28] M. Aryal, D. H. Ko, J. R. Tumbleston, A. Gadisa, E. T. Samulski, and R. Lopez, "Large area nanofabrication of butterfly wing's three dimensional ultrastructures," *Journal of Vacuum Science & Technology B,* vol. 30, Nov 2012.

[29] A. Saito, J. Murase, M. Yonezawa, H. Watanabe, T. Shibuya, M. Sasaki, *et al.*, "High-throughput reproduction of the Morpho butterfly's specific high contrast blue," in *Bioinspiration, Biomimetics, and Bioreplication 2012*. vol. 8339, A. Lakhtakia and R. J. MartinPalma, Eds., ed, 2012.

[30] K. Watanabe, T. Hoshino, K. Kanda, Y. Haruyama, and S. Matsui, "Brilliant Blue Observation from a Morpho Butterfly-Scale Quasi-Structure," *Japanese Journal of Applied Physics,* vol. 44, pp. L48-L50, 2005.

[31] M. Srinivasarao, "Nano-optics in the biological world: Beetles, butterflies, birds, and moths," *Chemical Reviews,* vol. 99, pp. 1935-1961, Jul 1999.

[32] P. Vukusic and R. Sambles, "Shedding light on butterfly wings," in *Physics, Theory, and Applications of Periodic Structures in Optics*. vol. 4438, P. Lalanne, Ed., ed, 2001, pp. 85-95.

[33] P. Vukusic, "Natural photonics," *Physics World*, vol. 17, pp. 35-39, Feb 2004.

[34] C. W. Mason, "Structural colors in insects. I," *Journal of Physical Chemistry,* vol. 30, pp. 383-395, Mar 1926.

[35] C. W. Mason, "Structural colors in insects III," *Journal of Physical Chemistry,* vol. 31, pp. 1856-1872, Jul-Dec 1927.

[36] C. W. Mason, "Structural colors in insects II," *Journal of Physical Chemistry,* vol. 31, pp. 321-354, Mar 1927.

[37] A. A. Michelson, "On metallic colouring in birds and insects," *Philosophical Magazine,* vol. 21, pp. 554-567, Apr 1911.

[38] Ghiradel.H, T. Eisner, R. E. Silberglied, Aneshans.D, and H. E. Hinton, "Ultraviolet Reflection of a Male Butterfly - Interference Color caused by Thin-Layer Elaboration of Wing Scales," *Science,* vol. 178, pp. 1214-+, 1972.

[39] H. Ghiradella, "Development of ultraviolet-reflecting butterfly scales - how to make an interference filter," *Journal of Morphology,* vol. 142, pp. 395-409, 1974.

[40] H. Ghiradella and W. Radigan, "Development of butterfly scales. 2. Struts, lattices, and surface-tension," *Journal of Morphology,* vol. 150, pp. 279-297, 1976.

[41] H. Ghiradella, "Structure of Iridescent Lepidopteran Scales - Variations on Several Themes," *Annals of the Entomological Society of America,* vol. 77, pp. 637-645, 1984.

[42] H. Ghiradella, "Structure and Development of Iridescent Lepidopteran Scales - The Papilionidae as a Showcase Family," *Annals of the Entomological Society of America,* vol. 78, pp. 252-264, 1985.

[43] H. Ghiradella, "Structure and development of iridescent butterfly scales - lattices and laminae," *Journal of Morphology,* vol. 202, pp. 69-88, Oct 1989.

[44] H. Ghiradella, "Light and Color on the Wing - Structural Colors in Butterflies and Moths," *Applied Optics,* vol. 30, pp. 3492-3500, Aug 1991.

[45] H. Ghiradella, "Structure of Butterfly Scales - Patterning in an Insect Cuticle," *Microscopy Research and Technique,* vol. 27, pp. 429-438, Apr 1994.

[46] L. Poladian, S. Wickham, K. Lee, and M. C. J. Large, "Iridescence from photonic crystals and its suppression in butterfly scales," *Journal of the Royal Society Interface,* vol. 6, pp. S233-S242, Apr 2009.

[47] A. L. Ingram and A. R. Parker, "A review of the diversity and evolution of photonic structures in butterflies, incorporating the work of John Huxley (The Natural History Museum, London from 1961 to 1990)," *Philosophical Transactions of the Royal Society B-Biological Sciences,* vol. 363, pp. 2465-2480, Jul 2008.

[48] P. R. Munroe, "The application of focused ion beam microscopy in the material sciences," *Materials Characterization,* vol. 60, pp. 2-13, Jan 2009.

[49] K. Michielsen, H. De Raedt, and D. G. Stavenga, "Reflectivity of the gyroid biophotonic crystals in the ventral wing scales of the Green Hairstreak butterfly, Callophrys rubi," *Journal of the Royal Society Interface,* vol. 7, pp. 765-771, May 2010.

[50] B. D. Wilts, K. Michielsen, H. De Raedt, and D. G. Stavenga, "Iridescence and spectral filtering of the gyroid-type photonic crystals in Parides sesostris wing scales," *Interface Focus,* December 21, 2011 2011.

[51] D. G. Stavenga, H. L. Leertouwer, P. Pirih, and M. F. Wehling, "Imaging scatterometry of butterfly wing scales," *Optics Express,* vol. 17, pp. 193-202, Jan 2009.

[52] P. Vukusic and D. G. Stavenga, "Physical methods for investigating structural colours in biological systems," *Journal of the Royal Society Interface,* vol. 6, pp. S133-S148, Apr 2009.

[53] S. Yoshioka, H. Fujita, S. Kinoshita, and B. Matsuhana, "Alignment of crystal orientations of the multi-domain photonic crystals in Parides sesostris wing scales," *Journal of The Royal Society Interface,* vol. 11, March 6, 2014 2014.

[54] H. X. Wang, W. Zhou, and E. P. Li, "Focused Ion Beam Nano-Precision Machining for Analyzing Photonic Structures in Butterfly," in *Advanced Precision Engineering*. vol. 447-448, J. Zhao, M. Kunieda, G. Yang, and X. M. Yuan, Eds., ed, 2010, pp. 174-177.

[55] J. W. Galusha, L. R. Richey, M. H. Bartl, and Ieee, "High Resolution Three-Dimensional Reconstruction of Photonic Crystal Structure found in Beetle Scales," in *2008 Digest of the Leos Summer Topical Meetings*, ed, 2008, pp. 83-84.

[56] J. W. Galusha, M. R. Jorgensen, and M. H. Bartl, "Diamond-Structured Titania Photonic-Bandgap Crystals from Biological Templates," *Advanced Materials,* vol. 22, pp. 107-+, Jan 2010.

[57] J. W. Galusha, L. R. Richey, J. S. Gardner, J. N. Cha, and M. H. Bartl, "Discovery of a diamond-based photonic crystal structure in beetle scales," *Physical Review E,* vol. 77, May 2008.

[58] R. O. Prum, T. Quinn, and R. H. Torres, "Anatomically diverse butterfly scales all produce structural colours by coherent scattering," *Journal of Experimental Biology,* vol. 209, pp. 748-765, Feb 2006.

[59] K. Michielsen and D. G. Stavenga, "Gyroid cuticular structures in butterfly wing scales: biological photonic crystals," *Journal of the Royal Society Interface,* vol. 5, pp. 85-94, Jan 2008.

[60] V. Saranathan, C. O. Osuji, S. G. J. Mochrie, H. Noh, S. Narayanan, A. Sandy, *et al.*, "Structure, function, and self-assembly of single network gyroid (I4(1)32) photonic crystals in butterfly wing scales," *Proceedings of the National Academy of Sciences of the United States of America*, vol. 107, pp. 11676-11681, Jun 2010.

[61] D. Drobne, M. Milani, V. Leser, and F. Tatti, "Surface damage induced by FIB milling and imaging of biological samples is controllable," *Microscopy Research and Technique,* vol. 70, pp. 895-903, Oct 2007.

[62] J. Des Chenes, "Angle of Illumination for Keyence Lens, VH-Z250," C. G. Cameron, Ed., ed, 2012.

[63] J. P. Vernon, "Morphology-Preserving Chemical Conversion of Bioorganic and Inorganic Templates," Doctor of Philosophy, Materials Science and Engineering, Georgia Institute of Technology, Atlanta, GA, 2012.

[64] C. A. Schneider, W. S. Rasband, and K. W. Eliceiri, "NIH Image to ImageJ: 25 years of image analysis," *Nat Meth,* vol. 9, pp. 671-675, 2012.

[65] A. Sharma and S. G. Schulman, *Introduction to Fluorescence Spectroscopy*, First ed., 1999.

[66] E. Van Hooijdonk, S. Berthier, and J. P. Vigneron, "Bio-inspired approach of the fluorescence emission properties in the scarabaeid beetle Hoplia coerulea (Coleoptera): Modeling by transfer-matrix optical simulations," *Journal of Applied Physics,* vol. 112, Dec 2012.

[67] B. D. Wilts, T. M. Trzeciak, P. Vukusic, and D. G. Stavenga, "Papiliochrome II pigment reduces the angle dependency of structural wing colouration in nireus group papilionids," *Journal of Experimental Biology,* vol. 215, pp. 796-805, Mar 2012.

[68] C. Campos-Fernández, D. E. Azofeifa, M. Hernández-Jiménez, A. Ruiz-Ruiz, and W. E. Vargas, "Visible light reflection spectra from cuticle layered materials," *Optical Materials Express,* vol. 1, pp. 85-100, 2011/05/01 2011.

[69] A. C. Neville, "Metallic gold and silver colors in some insect cuticles," *Journal of Insect Physiology*, vol. 23, pp. 1267-1274, 1977.

[70] A. R. Parker, D. R. McKenzie, and M. C. J. Large, "Multilayer reflectors in animals using green and gold beetles as contrasting examples," *Journal of Experimental Biology,* vol. 201, pp. 1307-1313, May 1998.

[71] R. A. Steinbrecht, "Fine structure and development of the silver and golden cuticle in butterfly pupae," *Tissue and Cell,* vol. 17, pp. 745-762, // 1985.

[72] J. P. Vigneron, J. M. Pasteels, D. M. Windsor, Z. Vertesy, M. Rassart, T. Seldrum, *et al.*, "Switchable reflector in the Panamanian tortoise beetle Charidotella egregia (Chrysomelidae : Cassidinae)," *Physical Review E,* vol. 76, Sep 2007.

[73] P. Vukusic, R. Kelly, and I. Hooper, "A biological sub-micron thickness optical broadband reflector characterized using both light and microwaves," *Journal of the Royal Society Interface,* vol. 6, pp. S193-S201, Apr 2009.

[74] M. A. Giraldo, S. Yoshioka, and D. G. Stavenga, "Far field scattering pattern of differently structured butterfly scales," *Journal of Comparative Physiology a-Neuroethology Sensory Neural and Behavioral Physiology,* vol. 194, pp. 201-207, Mar 2008.

[75] J. P. Vigneron, K. Kertesz, Z. Vertesy, M. Rassart, V. Lousse, Z. Balint, *et al.*, "Correlated diffraction and fluorescence in the backscattering iridescence of the male butterfly Troides magellanus (Papilionidae)," *Physical Review E,* vol. 78, Aug 2008.

[76] E. Van Hooijdonk, C. Barthou, J. P. Vigneron, and S. Berthier, "Detailed experimental analysis of the structural fluorescence in the butterfly Morpho sulkowskyi (Nymphalidae)," *Journal of Nanophotonics,* vol. 5, Nov 2011.

[77] K. L. Yu, S. Lou, J. Ding, D. Zhang, Q. X. Guob, and T. X. Fan, "Structural integration design for enhanced photoluminescence in butterfly scales," *Soft Matter*, vol. 9, pp. 2614-2620, 2013.

[78] E. Van Hooijdonk, C. Barthou, J. P. Vigneron, and S. Berthier, "Angular dependence of structural fluorescent emission from the scales of the male butterfly Troides magellanus (Papilionidae)," *Journal of the Optical Society of America B-Optical Physics*, vol. 29, pp. 1104-1111, May 2012.

[79] C. Pouya and P. Vukusic, "Electromagnetic characterization of millimetre-scale replicas of the gyroid photonic crystal found in the butterfly Parides sesostris," *Interface Focus*, vol. 2, pp. 645-650, Oct 2012.

[80] J. H. Chen, Y. C. Lee, M. T. Tang, and Y. F. Song, "X-ray tomography and chemical imaging within butterfly wing scales," in *Synchrotron Radiation Instrumentation, Pts 1 and 2*. vol. 879, J. Y. Choi and S. Rah, Eds., ed, 2007, pp. 1940-1943.

CHAPTER 2: Fluorescent Organic Dye Multilayers on the Scales of *Morpho rhetenor*

2.1 Summary

The layer-by-layer deposition of an organic fluorescent dye to a structurally colored biological template has been explored for the first time. Specifically, the high intensity reflection from blue, *Morpho rheten*or scales were combined with the transient (*i.e.*, photobleached) emission from a synthetic, organic, fluorescent dye resulting in bimodal (reflected and emitted) coloration. The emission intensity, from iterative deposition of dye-containing layers, increased up to 10 cycles. The induced fluorescence on the scale did photobleach, dropping approximately 75 % after 130 s exposure to excitation light (460 – 500 nm) filtered from a mercury lamp. Confocal fluorescent microscopy cross-sections revealed that the emission from the applied, synthetic dye was distributed throughout the thickness of the scale nanostructure. The starting template morphology (including individual ridges and lamellae) was preserved throughout the coating process. The reflectance of as-coated samples underwent a net red shift with increased number of deposited layers. Control experiments with the fluorophore host matrix (a layer-by-layer, dendritic amplification process) also yielded red shifted reflectance as the number of deposited layers increased. Fluorescent emission from the dye did not have a measurable impact on the scale reflectance under white light illumination. Spectral overlap between the induced emission spectrum and the scale reflectance spectrum and the relatively fast photobleaching of the fluorophore excluded application of this coating process for color mixing between the emitted and reflected light.

2.2 Introduction

For over a century, naturally occurring photonic structures (such as the colored scales from butterflies, beetles, moths, etc.) have attracted considerable scientific interest for their ability to control light through complex, nanoscale features.[1-8] Mason observed the loss of color for certain insect scales upon immersion in various fluids and the return of color after the fluid had evaporated.[4, 6-8] Later, electron microscopy studies revealed intricate, 3-dimensional, hierarchical nanostructures on the scales of some insects.[4, 9-17] Scientific understanding of biological photonic structures serve as inspiration for improving existing technology and developing new solutions to technical problems.[1, 18] Such scales and biomimetic scale structures have been considered for high sensitivity vapor sensors [19-21], Surface Enhanced Raman Spectroscopy (SERS) templates [22, 23], paint [24], and infrared sensor designs [25].

Natural photonic structures (*i.e.*, no synthetic material enhancements) and biomimetic analogs have found direct some applications.[19-21] However, the addition of new chemical compositions, to tailor the optical properties, can expand scientific understanding of the original structures and create opportunities for new applications.[22, 23, 25-29] Detailed, scientific understanding of the controllable scale color alteration is required, prior to application development.

The layer-by-layer deposition of ultra-thin films is an effective means of controllably altering the reflectance of structurally colored, butterfly scales.[26-29] These coating methodologies [26-29] alter the nanostructure, provided by nature, through the simultaneous change of the refractive index contrast and filling fraction of the photonic solid [30]. Nature provides numerous examples of both structural color and fluorescence combined at the single scale level.[31-33] Yet, efforts have not been made towards imparting artificial fluorescence and structural color alteration on biological templates with layer-by-layer processes. This work seeks to understand how two modes of color control may be used to alter the color of a bioorganic nanostructure. These two color control modes are the addition of artificial fluorescence with controllable emission intensity and structural color alteration, based on the number of deposited layers.

2.3 Literature Review

Butterflies utilize a limited range of materials in building their photonic structures.[2, 34] However, the complex nanostructures within their scales inspire applications encompassing technologies from the UV to the microwave spectrum.[2, 18] The manipulation of these nanostructures with synthetic materials allows for a greater understanding of the original template and create opportunities for new applications.[2, 34]

Many different routes have been examined for chemical modification and enhancement of natural photonic structures (*i.e.,* scales of butterflies, beetles, and diatom microshells). These approaches include the following: polymer templating [35-37], chalcogenide depositions [38, 39], inorganic layer-by-layer coatings and ceramic conversions [26, 29, 40-53], and metal/metal alloy depositions [54, 55]. The layer-by-layer deposition of inorganic materials through Atomic Layer Deposition (ALD) and surface sol-gel is a very effective method for achieving subnanometer control over the deposited layer thickness.[26-29, 56] Only these two methods have demonstrated controllable reflectance alteration from a bioorganic template through iterative film deposition.[26-29] Emissive components have been incorporated into the structures of butterfly scales [50, 57] and diatom frustules [58-64]. These methods utilized thermal treatments [50, 57, 60, 61, 64], covalent attachment (*i.e.*, single surface functionalization, no multilayer) [58, 62], or incorporated the emissive components into the structure during cell growth [58, 59, 63]. The goal of this research is to explore the use of room temperature, fluorescent, layer-by-layer coatings to (1) preserve the starting template material, (2) study the reflectance alteration, and (3) understand how emission intensity can be tailored.

The value in a multilayered approach for fluorophore-containing layers is that the absorption/emission intensity can be increased beyond the extent possible with a given single functionalization of a 2-dimensional surface. Various multilayer approaches have achieved such a result: chalcogenide nanoparticle films [65-68], organic fluorescent dyes [69-71], rare earth elements [72], and gold nanoparticles [73, 74]. Organic fluorescent dyes as the emissive multilayer component are of particular interest for this work. Prior methods have used electrostatic [71] and covalent bonding [69, 70] to integrate organic fluorescent dyes into multilayered films. Integration of the organic dye into a polymer matrix has been successful in increasing the fluorescence emission with each applied layer.[71] Fluorescence quenching has been reported in some cases where the host matrix is inorganic (*i.e.*, titania).[75, 76] For this reason, a layer-by-layer, polymeric film is desired to serve as the host matrix for the integration of an organic, fluorescent dye.

The dendritic amplification process illustrated in **Figure 32** [77, 78] is an attractive coating method for emissive component integration. It offers a conformal approach for controlling functional group chemistry and density with nanometer thickness resolution.[77] This process begins by reacting an aminosilane molecule with hydroxyl groups on a hydroxyl-containing surface. The resulting amine groups, protruding from the surface, are iteratively exposed to solutions of a hyperbranched acrylate and then a polyamine, respectively. The deposition of hyperbranched precursors can increase the functional group density with each new cycle.

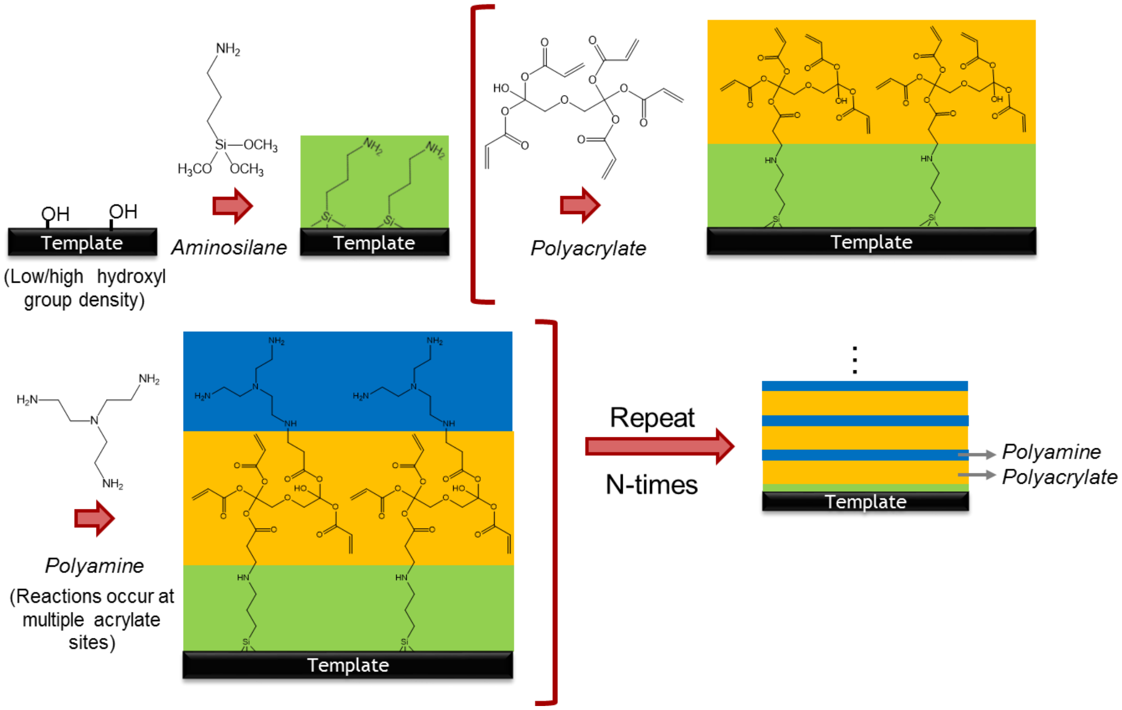

Figure 32. Schematic of a layer-by-layer dendritic amplification process. First, a hydroxyl-bearing surface is functionalized with an aminosilane. Subsequent layers are iteratively deposited, first polyacrylate and then polyamine layers. Additional control over surface group chemistry can be achieved by terminating a final polyacrylate layer to glucosamine [78] or tris(hydroxymethyl)aminomethane [77] to generate a hydroxyl-rich surface.

The iridescent blue scales of the *Morpho rhetenor* butterfly (**Figure 33 (a - c)**) were selected as the template for this investigation. The origin of scale coloration from the intricate scale component structures (**Figure 33 (d)**) has undergone considerable modeling [79-88] and experimental characterization [80, 86, 89, 90]. Additionally, there are no reports of fluorescence from the *M. rhetenor* scales, making this template ideal for characterization of structural color and fluorescent intensity alteration as a function of applied, fluorophore-containing layers.

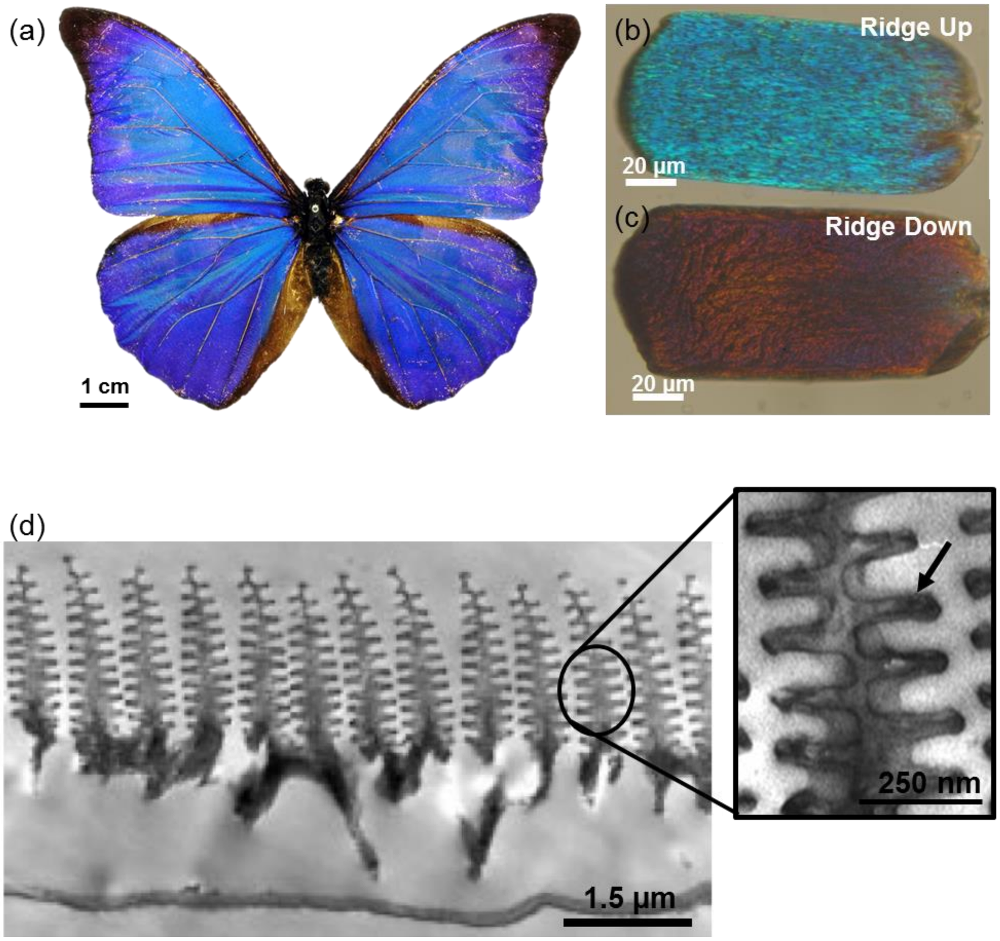

Figure 33. Optical and TEM images of the butterfly, *Morpho rhetenor*. (a) Optical image of the *Morpho rhetenor* butterfly © Smithsonian Institution National Museum of Natural History. Optical images of the iridescent blue scale responsible for the overall scale coloration, oriented (b) ridge-up and (c) ridge down. Coloration is dominantly structural in origin for scales oriented ridge-up. Ridge down orientation color is primarily due to an absorbing pigment at the scale base. (d) TEM image [89] of the scale cross-section showing the intricate, multilayer ridge structure, responsible for the overall blue coloration. (Inset) Higher magnification of the ridge structure with black arrow indicating the position of an individual lamella. (TEM images courtesy P. Vukusic)

Modeling efforts [79-88], corroborated by experimental work on whole, native scales [80, 86, 89, 90], have demonstrated that numerous scale features contribute to the overall scale reflection. The blue color originates from the multilayered ridge structure through interference and diffraction.[79, 87, 89, 90] A pigment, primarily located in the scale base, absorbs the long wavelength light transmitted through the ridges.[79, 81, 89, 90] This localized absorption, presumably due to melanin, reduces the long wavelength reflectivity, enhancing the overall blue appearance for the scale.[79, 81, 89, 90] Spectral contributions are also provided by the offset lamella on either side of a single ridge, as well as an increased angular distribution of the reflected light from the scale normal vector.[80, 82, 84, 85] The ridge tip taper, tilt, and irregular height help create the broad angular distribution of this color.[80, 83, 84, 86, 87, 89, 90]

The analysis of fluorescent layer-by-layer coatings applied to the *M. rhetenor* blue scales focused on the characterization of scales oriented ridge-up. This scale orientation provides a structural color [79, 87, 89, 90], for controllable alteration by the filling fraction and refractive index contributions of the coating material. Additionally, it will serve as a platform for understanding how the layer-by-layer deposition of an organic fluorescent dye can enable fluorescent intensity alteration, based on the number of applied layers.

2.4 Experimental Procedures

2.4.1 Template preparation and precursor multilayer coating procedure

Morpho rhetenor eusebes specimens, collected from Brazil, were purchased from InsectSale.com. Butterfly wing sections were cut into approximately 1 x 1 cm sections using a straight edge razor on a polyethylene cutting board (McMaster Carr, GA, USA). Wing sections were immersed and gently shaken for 1 minute in 200 proof, anhydrous isopropyl alcohol (ACROS Organics, Geel, Belgium) as an initial cleaning treatment. The isopropyl alcohol-soaked wing sections were deposited into a clean petri dish, the alcohol was removed, and the wing sections were dried, at room temperature, under flowing nitrogen (Ultra High Purity, AirGas, PA, USA) at approximately 27 mL/s for 3 minutes. The dried wing sections were carefully removed with a clean pair of tweezers and placed into a fresh petri dish for layer-by-layer deposition. Care must be taken in the drying step as the wing sections can be blown off of the petri dish once sufficiently dried. An approach to mitigate this form of sample loss involves partially sealing the petri dish lid and base with Parafilm M (SPI Supplies, PA, USA) so that the nitrogen nozzle can dry the inside of the chamber, with a gap between the dish lid and base that is small enough that the butterfly wing sections could not be blown out of the container.

All dendritic amplification precursors were purchased from Sigma Aldrich, MO, USA and used without further purification. N^1-(3-Trimethoxylsilylpropyl)diethylenetriamine (Technical grade) was used as the aminosilane precursor for the dendritic amplification process and was dissolved in ethanol (Anhydrous, 200 proof, Koptec, PA, USA) to a final concentration of 20 vol% aminosilane in ethanol. The polyacrylate (Dipentaerythritol penta-/hexa-acrylate) and polyamine (Tris(2-aminoethyl)amine, 96%) precursors were both diluted to 10 wt% solutions in ethanol (*i.e.,* separate solutions). All solutions were thoroughly mixed before use with a desktop vortexer (Vortex Genie 2, Scientific Industries, NY, USA) until the solutions were homogenous and clear. All solutions were protected from light through storage in amber glass bottles (Catalog number: 89042-910, VWR International, PA, USA). A 20 vol % of (3-aminopropyl)triethoxysilane (99%, Sigma Aldrich, MO, USA) in ethanol was used for testing the dye functionalization, but was not used for further multilayer deposition. Solutions were stored per manufacturer's recommendations: aminosilane and polyamine inside a dry, nitrogen atmosphere glovebox and polyacrylate in dark storage cabinet under ambient laboratory conditions.

The organic fluorescent dye, 2',7'-Bis(2-carboxyethyl)-5(6)-carboxyfluorescein (BCECF, Sigma Aldrich, MO, USA), was received as a dry powder in 1 mg quantities and were stored, as-received in a -20 ^{o}C freezer. BCECF was dissolved in ethanol to a final concentration of 1 mg/mL (4 mL total) and stored in a 15 mL centrifuge tube (VWR International, PA, USA) wrapped in Aluminum foil, inside a 4 ^{o}C refrigerator when not in use for coatings. The dye solution was reused for each multilayer deposition.

All precursor reactions were conducted at room temperature. Deposition times for the dendritic amplification steps (*i.e.*, aminosilane, polyacrylate, and polyamine) were determined after *in situ* analysis using a quartz crystal microbalance. Briefly, the layer-by-layer dendritic amplification process was applied to a SiO_2-bearing surface. *In situ* analysis of the deposition revealed that the frequency shift plateaued in under 10 minutes for the aminosilane and polyamine steps. Comparison of the overall film growth (monitored by revealing the frequency shift with the number of applied layers) between 1 hour long incubations and 10 minute incubations for the aminosilane and polyamine exposures showed no statistical differences. The deposition of the polyacrylate layers did not plateau after a 1 hour incubation. As a result, the deposition time for this step (60 minutes) was fixed at the same period for as previously published work [77, 78]. A detailed description of the experimental results is presented in **Appendix B**.

Figure 34 shows the order of precursor deposition. First, the aminosilane was deposited onto the hydroxylated butterfly scale surface. Then polyacrylate and polyamine layers were iteratively applied. BCECF was functionalized to the surface by depositing aminosilane layers before and after the dye deposition. Further multilayer deposition continued with polyacrylate and polyamine depositions. All samples were copiously washed with ethanol between each precursor step. Exposure times for each precursor were as follows: 10 minutes for aminosilane, 1 hour for polyacrylate, 10 minutes for polyamine, and 1 hour for BCECF.

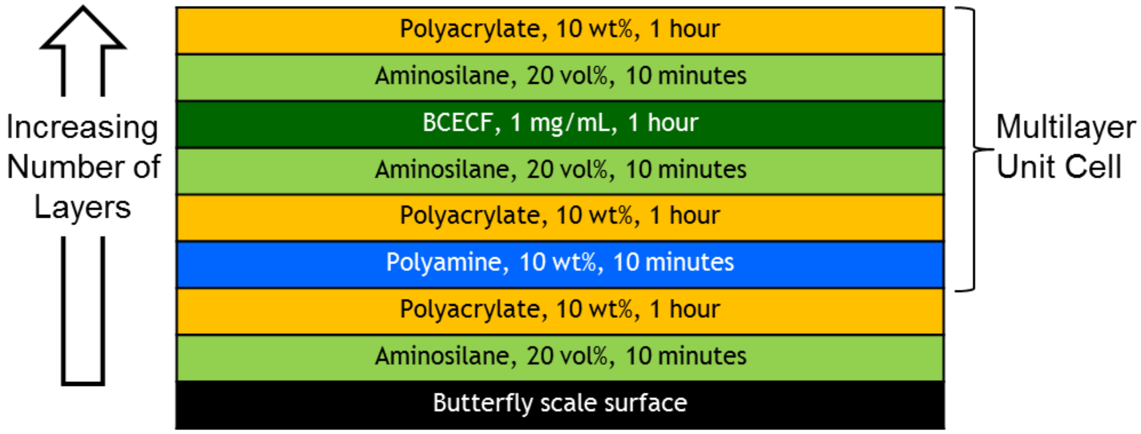

Figure 34. Schematic detailing the layer-by-layer deposition of organic fluorescent dye multilayers. The unit cell for the organic dye containing layers was repeated a desired number of times to increase the fluorescence emission intensity with each successive layer.

2.4.2 Precursor incubation methodology for multilayer coatings on *M. rhetenor*

A methodology was developed which relied on depositing the butterfly wing sections (with some liquid) between petri dish incubation chambers in between washing steps in a custom funnel/stopcock. Wing section and precursor incubation was conducted in a 60 x 15 mm petri dish (VWR International, PA, USA), placed inside of a 100 x 15 mm petri dish (VWR International, PA, USA), and held together with adhesive tape (**Figure 35 (a)**). A Kimwipe (Kimberly-Clark, TX, USA) was folded and placed underneath the smaller petri dish to absorb errant liquids (**Figure 35 (a, b)**). It was important to use a separate secondary containment (*i.e.*, the 100 x 15 mm petri dish) for each unique precursor. Precursor polymerization could occur (as a result of the mixing between spilled precursors within the same secondary containment), resulting in a thick white precipitate spread throughout the container and across samples if this step was not followed. All precursor incubations were carried out on a rocker table (Model 260350, Boekel Scientific, PA, USA). Gentle mixing of the wing sections in the precursor solutions was important as vigorous mixing (and sonication) could result in removal of scales from the wing membrane.

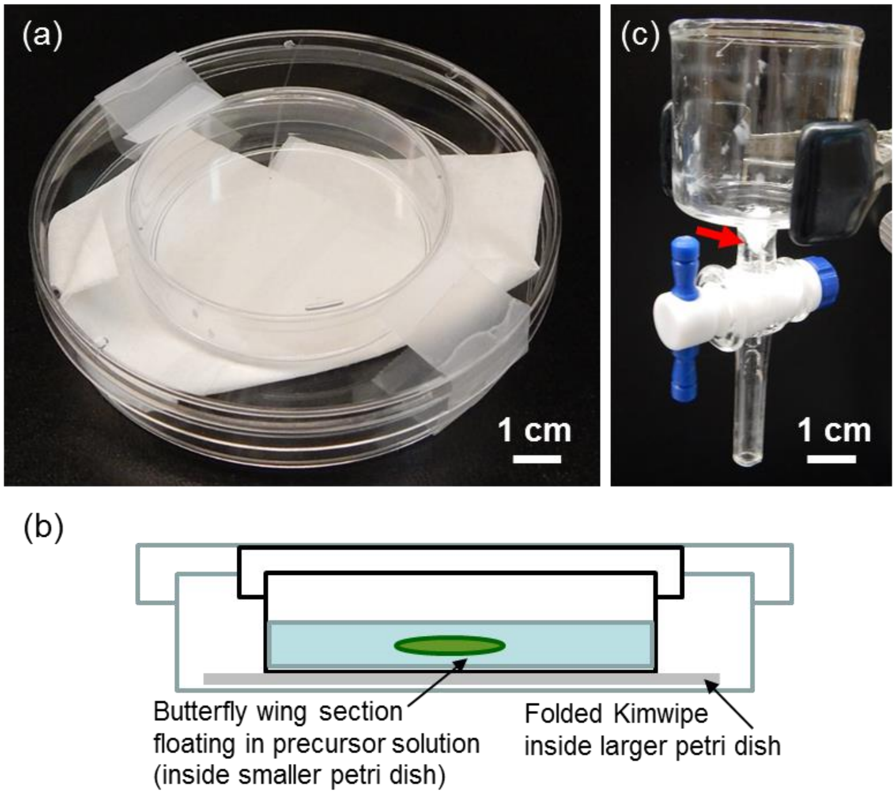

Figure 35. Equipment used for the application of layer-by-layer fluorescent coatings. (a) Petri dish system for butterfly wing section incubation. Butterflies and 10 mL of precursor solution were incubated for a fixed time in the inner, smaller petri dish. The larger petri dish provided secondary containment and assisted in keeping the smaller petri dish sealed (with help of adhesive tape). (b) Cross-sectional view of the petri dish incubation system illustrating the butterfly wing section incubation. The light blue line indicates the larger petri dish, while the black outline represents the smaller petri dish inside the larger petri dish. (c) Washing steps were performed using a custom glass funnel with stopcock. A PTFE mesh plug (indicated by red arrow) was used to prevent loss of the wing sections with the waste liquid.

Sample washing was performed using a custom funnel/stopcock with a total volume of 35 mL (**Figure 35 (b)**). A plug of fine, polytetrafluoroethylene (PTFE) mesh (McMaster Carr, GA, USA) was used to occupy a majority of the neck leading to the stopcock to prevent sample loss. The PTFE plug was replaced at the end of each day. Samples were copiously washed with approximately 40 mL of 200 proof ethanol. A small amount of ethanol was added at the end of the wash step (just enough to suspend the wing sections) and the contents of the funnel were poured into the next incubation container. The coating process continued until a desired number of cycles was applied. Coated wing sections were removed after completing the ethanol wash. A 1 mL autopipette was used to syphon the remaining ethanol from the wash step.

Dye deposition was performed by placing the wing sections in the 15 mL centrifuge tube containing the dye solution after washing the wing sections with ethanol. The dye solution was reused for each deposition step. Incubation of the wing sections in a 15 mL tube enabled better retention of the dye solution, and thus, reduced the cost of coating process. Wing sections were handled only at the edges with fine-tip tweezers (no serration) to minimize scale damage due to handling. Upon completion of the dye incubation step, the solution was poured into another 15 mL container for further use and the wing sections were thoroughly washed in ethanol using the custom funnel/stopcock. Further incubation steps were performed as previously described.

Efforts were made to minimize sample exposure to light throughout the coating process. BCECF-coated samples did photobleach upon prolonged light exposure. Minimizing sample exposure to light during the coating process mitigated loss in emission intensity due to photobleaching, prior to sample characterization. All coating work and precursor incubations were performed in a fume hood with internal lights turned off (*i.e.*, the main laboratory lights remained on). All incubations were performed with aluminum foil wrapped around the incubation chamber.

Samples were stored after terminating the surface with polyacrylate layers and a thorough ethanol wash. Wing sections were dried under nitrogen and then a small section of the wing was removed for optical and electron microscopy characterization. The remaining wing sections were placed in a small petri dish, wrapped in aluminum foil, placed in a small Ziploc® bag, and stored in a -20 ^{o}C freezer until further use. All samples for optical characterization were stored under ambient conditions and wrapped in aluminum foil to protect from light.

2.4.3 Optical characterization of organic dye multilayer-bearing *M. rhetenor* scales

Coated scales were removed from the wing membrane by gently brushing the coated wing section with a soft, nylon bristle paintbrush (McMaster Carr, GA, USA) onto an as-received glass microscope slide (Catalog number: 16004-418, VWR International, PA, USA). The brush was thoroughly cleaned before and after every contact with a wing section by blowing the bristles with nitrogen. Tapping the brush on the surface of a clean glass slide, followed by visual observation, validated that scales were no longer entrained within the brush. The glass slide was stored in a 100 mm x 15 mm petri dish (VWR International, PA, USA) with a square of carbon tape (Ted Pella, CA, USA) to keep the slide position fixed. All petri dishes that contained samples were wrapped in aluminum foil and stored until optical characterization.

Optical measurements were performed using an Olympus BX60 (Olympus America, Inc., PA, USA) upright microscope. Spectral measurements were acquired with a SEE 1000 microscope spectrometer (SEE Science, MA, USA) attached to the microscope camera port with software from Craic Technologies (Version 4.3.1, Craic Technologies, CA, USA).

Single scale reflectance measurements were acquired using an Olympus MPlan N 20 x objective (0.40 numerical aperture) relative to a diffuse reflectance standard (WS-1-SL, Ocean Optics, FL, USA), illuminated by a halogen lamp (Olympus America, Inc., PA, USA). The illumination spectrum for this lamp is shown in **Figure 37**. The measurement spot size was approximately 14 x 14 µm. Y-axis intensity values are reported in arbitrary units (A.U.), rather than percent reflectance relative to the standard, to account for differences in light scattering between the reference standard and the butterfly scale.[91] Single scale fluorescence spectra were acquired with an Olympus MPlan FL N 50 x objective (0.80 numerical aperture) with a 6 µm x 6 µm spot size. The resulting emission spectrum was the measured signal minus the dark current (*i.e.*, references were not used for emission measurements). All fluorescence imaging and spectra were acquired using a mercury lamp illumination (peak emission of 365 nm, HBO 100 W lamp, Universal Arc Lamp Power Supply # 99030, SEE Science, MA, USA) in combination with a fluorescent filter cube (Chroma Technologies, VT, USA). Excitation light was filtered to transmit 460 – 500 nm (full width at half maximum). The emission filter enabled light transmission above 510 nm (half-maximum wavelength). The dichroic mirror half-maximum wavelength was 505 nm. All imaging was performed with the 20 x objective using a Nikon D300 (Nikon USA, NY, USA) camera (Manual, ISO 200, automatic white balance). The camera was attached to the camera port of the microscope with a microscope adapter (MM-SLR, Martin Microscope, SC, USA).

Variation in peak reflectivity across all four wings of a single butterfly were analyzed to determine the noise limit in comparing peak reflectivity from single scales coated with varying numbers of applied layers. Two separate *M. rhetenor* butterflies were analyzed. A representative butterfly is shown in **Figure 36** where white circles highlight the 8 different areas from which scales were removed for optical analysis. Scales were removed from the wing section with a clean paintbrush, as described above, and dispersed on a glass slide (*i.e.*, single scale characterization, rather than wing section). 6 separate scales were measured with 3 measurements within each scale. This provided 18 measurements for each region for a total of 144 measurements across an entire butterfly. The average peak wavelength and ± one standard deviation range for the blue scales from the two butterflies were 466 ± 6 nm and 467 ± 6 nm. An error of 6 nm was used whenever scales from separate wing sections were compared to reflect the overall certainty in the butterfly peak reflection.

Figure 36. Error analysis of the peak reflection wavelength across an entire butterfly. Optical image of the four butterfly wings from a single butterfly. White circles denote the 8 separate areas from which scales were acquired. All 144 reflection spectra were acquired from single scales dispersed on a glass slide from one of the two butterflies. A ± one standard deviation range from two separate butterflies was ± 6 nm. This error was applied as the minimum error associated with measuring the peak wavelength from scales acquired from separate wing section areas.

All statistical information is presented as an average with error bar ranges as ± one standard deviation. 18 separate reflection measurements (6 separate scales, with 3 measurements within each scale) were performed to determine the peak wavelength of coated scales. Single scale emission measurements were obtained from 18 separate analyses on 18 separate scales. Multiple measurements on a single scale were avoided to mitigate against intensity variations due to photobleaching. Long pass reflection measurements were used to determine the extent of the fluorescent contribution to the white light illumination reflection spectra (**Figure 37**). 24 measurements were acquired from a single scale (8 measurements, across 3 different reference files). 3 different reference files were obtained to account for the variation in intensity due to different measurement positions on the diffuse reflectance standard (refer to **Chapter 1** for additional details of this method). A single replicate coating experiment was conducted, which validated the trends observed with the emission intensity increase and red-shifted reflectance with the number of applied layers (**Appendix D, Figure 75 (a, b)**).

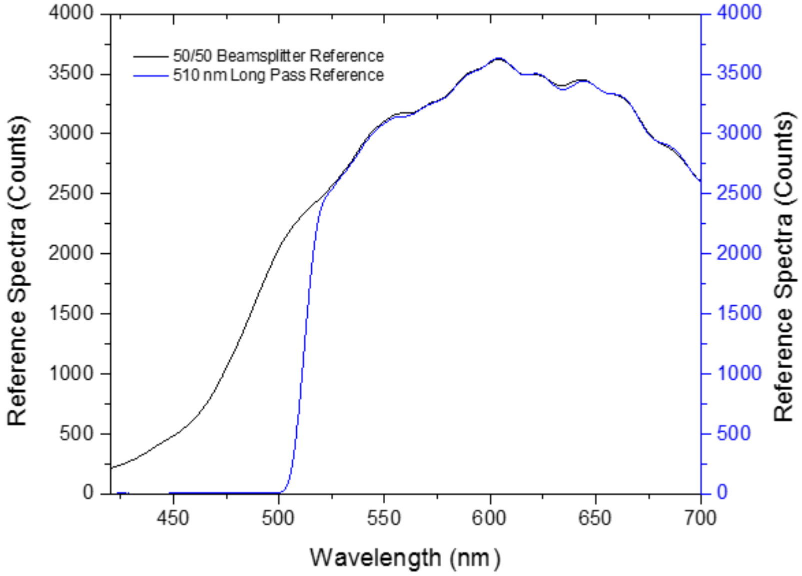

Figure 37. Comparison of reference spectra for long-pass illumination experiments. The 510 nm long pass filter effectively removed all light below 500 nm, preventing the excitation of the applied fluorophore.

Confocal fluorescence microscopy was performed on a Zeiss LSM700 (Carl Zeiss, Oberkochen, Germany) instrument, courtesy of Dr. Vincent Chen, Perry group, Georgia Institute of Technology. A 488 nm, 0.2 mW laser was used for fluorescence excitation in combination with a 510 nm long pass filter for imaging. Scales were immersed in 1.5600 refractive index fluid (Code 50BN, Cargille Laboratories, NJ, USA) in-between a glass slide and cover slip. A 25 µm Kapton® spacer (KPT-1/8, KaptonTape.com, CA, USA) was used around the edge of the cover slip (in-between the glass slide and cover slip) to provide a fixed thickness. Imaging was performed with a 63 x magnification oil immersion objective (Pln Apochromatic 63 x / 1.4 Oil Immersion DIC, Carl Zeiss, Oberkochen, Germany) using Ziess Immersol^{TM} 518 F (Carl Zeiss, Oberkochen, Germany) oil between the coverslip and objective lens.

A Shimadzu UV-vis-NIR spectrometer (Model UV-3101PC, Shimadzu, Kyoto, Japan) was used for in-solution absorbance measurements for BCECF in ethanol (0.196 mg/mL) after dispersing samples in a 1 mm quartz cuvette. A Horiba Fluorolog 3 (Model Number: FL-1000, Jobin Yvon, NJ, USA) spectrofluorometer was used to acquire in-solution fluorescence spectra.   A xenon lamp is used for excitation with single monochromators placed before and after the sample chamber. A photomultiplier tube was used for detection and the measured signal was corrected for variations in the excitation lamp. Excitation was set to 454 nm with a 3 nm bandpass for both excitation and emission slits. The reported spectra and peak absorption and emission values represent the averages across 3 separate solution measurements. Analyses of in-solution quantum dot absorption and emission were courtesy of Dr. Vincent Chen, Perry Group, Georgia Institute of Technology.

2.4.4 Structural characterization of organic dye multilayers on *M. rhetenor* scales

Scanning electron microscopy (SEM) was performed using a Hitachi SU8010 microscope (Hitachi, Tokyo, Japan). Double-sided carbon tape was affixed to an aluminum SEM stub (Ted Pella, CA, USA) to serve as the sample holder. Single scales, dispersed on a glass slide were placed on the carbon tape by inverting the SEM aluminum stub and gently pressing down on the glass slide containing the dispersed single scales. Visual inspection after the removal of the aluminum stub confirmed that some scales were transferred to the carbon tape in both ridge-up and ridge-down orientations. This method provided a sufficient number of scales for SEM imaging and preserved the relatively limited amount of samples.

2.5 Results and Discussion

2.5.1 Design of the multilayer deposition process

The organic dye, 2’,7’-Bis(2-carboxyethyl)-5(6)-carboxyfluorescein (BCECF, **Figure 38 (inset)**), was selected based on the presence of multiple carboxyl functional groups, which were utilized in the layer-by-layer deposition process. Surface passivation could occur if the majority of surface sites were occupied by molecules with only one reactive group, inhibiting further layer deposition.[92] Absorption and emission spectra for the dye molecule (in ethanol, 0.196 mg/mL) exhibit a broad absorption with peak intensity at 461 ± 1 nm and an emission peak with a maximum intensity at 526 ± 1 nm (**Figure 38**, courtesy V. Chen, Perry group, Georgia Institute of Technology), respectively.

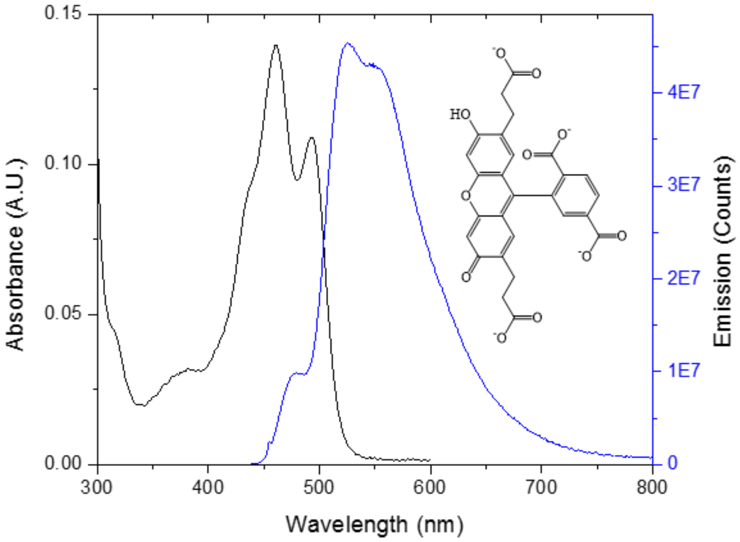

Figure 38. Absorption and emission spectra for the organic fluorescent dye, 2’,7’-Bis(2-carboxyethyl)-5(6)-carboxyfluorescein (BCECF) in ethanol (0.196 mg/mL). The peak absorbance is at 461 ± 1 nm and peak emission is 526 ± 1 nm (excited at 454 nm). Data courtesy of Dr. Vincent Chen, Perry Group, Georgia Institute of Technology.

Three functionalization approaches were applied for integrating BCECF into a multilayer film. A schematic of the multilayer unit cell is shown in **Figure 39 (a)** with the separate agents individually used for BCECF integration identified as (1), (2), and (3) in **Figure 39 (a)**. Emission spectra collected from 3 functionalized samples are shown in **Figure 39 (b)** as well as two control samples: uncoated *M. rhetenor* scales and *M. rhetenor* scales coated with only 2 dendritic amplification layers. The two control samples displayed similarly low emission intensities. A relatively small amount of emission was observed for (1) (*i.e.*, (3-aminopropyl)triethoxysilane). Relatively large emitted intensities were observed for BCECF multilayer integration via (2) and (3) (*i.e.*, N^1-(3-Trimethoxylsilylpropyl)diethylenetriamine, and (3) Tris(2-aminoethyl)amine, respectively). The average peak intensity is shown in **Figure 39 (c)** for comparison of the three separate integration methods.

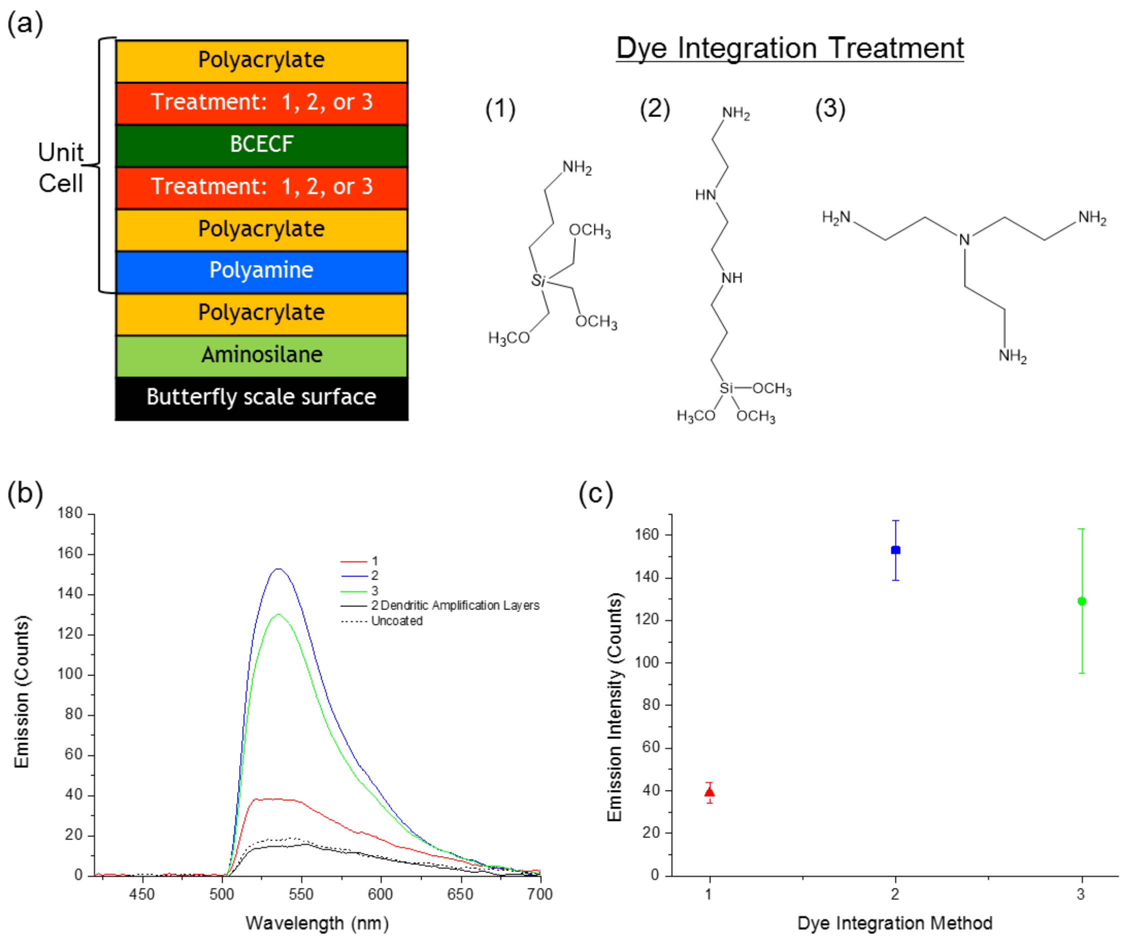

Figure 39. Schematic illustrating the incorporation of the organic fluorescent dye, BCECF, into the layer-by-layer dendritic amplification process. The unit cell for further studies of organic dye multilayers is highlighted. Three means of integrating BCECF were attempted using: (1) (3-aminopropyl)triethoxysilane, (2) N^1-(3-Trimethoxylsilylpropyl)diethylenetriamine, or (3) Tris(2-aminoethyl)amine. (b) Average emission spectra for coated scales, oriented ridge-up. (c) Summary of emission intensity for each of the dye integration methods. Treatment (2) was selected for BCECF multilayer integration. All spectra and peak intensity values were averaged from at least 10 separate measurements on 10 separate scales with ± one standard deviation as the error.

Emission collected from coated scales suggested that amine-rich surfaces were necessary for fluorescent emission. Acrylate-terminated scales functionalized with (1) may have some free amines present due to precursor polymerization before, or during, film deposition (due to water contamination). Sterically accessible amines [77] deposited prior to the first polyacrylate step (*i.e.*, the first polyamine deposition) may also have contributed. These free amines may have been responsible for the higher fluorescent emission from the background signal of uncoated and two dendritic amplification layer samples. Considerable fluorescence emission was collected for scales treated with (2) and (3). BCECF integration functionalization with (2) (*i.e.,* N^1-(3-Trimethoxylsilylpropyl)diethylenetriamine) was used for subsequent dye multilayer integration. This surface treatment is referred to herein as an "aminosilane" treatment for simplicity. These results suggested that the organic fluorescent dye was incorporated into the multilayer film at least partially through electrostatic attraction between the carboxyl groups on the dye and the amine-terminated surface.

2.5.2 Coated scale fluorescence analysis as a function of multilayer number

M. rhetenor scales were coated with increasing number of dye-containing layers (*i.e.,* the dye multilayer unit cell in **Figure 39**) and the emission spectrum was collected from each dye sample. Qualitative images and quantitative spectral analyses indicated that the fluorescence emission increased as the number of dye containing layers increased from 1 to 10 layers (**Figure 40**). The average peak emission wavelength across all coated samples was 541 ± 3 nm.

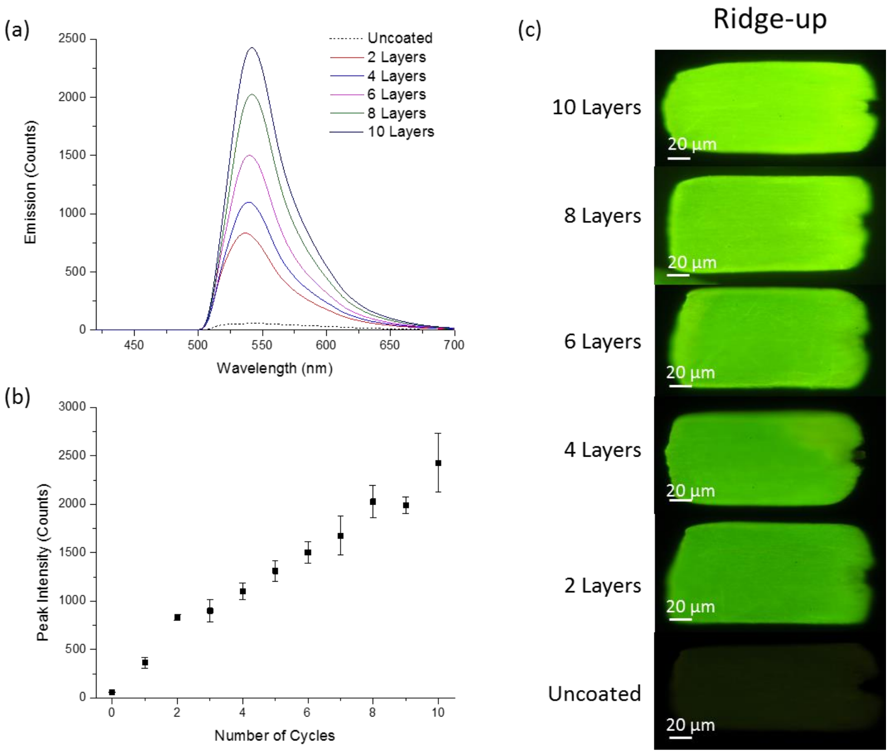

Figure 40. Summary of induced emission analysis of organic dye multilayer coated *M. rhetenor* scales. (a) Averaged emission spectra (peak wavelength of 541 ± 3 nm) for dye-coated samples, up to 10 layers, demonstrating an increase in emission intensity with subsequent dye layer deposition. (b) Peak intensity increased up to 10 layers. (c) Optical images showing an increase in intensity of the green-emitting fluorophore with increasing number of layers. All spectra and peak intensity values were averaged from at least 10 separate measurements on separate scales with ± one standard deviation as the error range.

The photostability of the organic fluorescent dye multilayers was characterized by collecting emission spectra as a function of exposure time. **Figure 41** shows the (a) spectral and (b) peak intensity variation over a 130 s exposure period for a 10-dye layer coated sample. The emission intensity dropped approximately 75 % over the tested time interval. Note: Emission measurements, summarized in **Figure 40**, were all collected within 5 s of scale exposure to the excitation light to mitigate the effects of photobleaching. The percentage decrease after subsequent measurements for the photobleaching time series are shown in **Figure 41 (c)**. All samples displayed similar intensity decreases over the tested time interval.

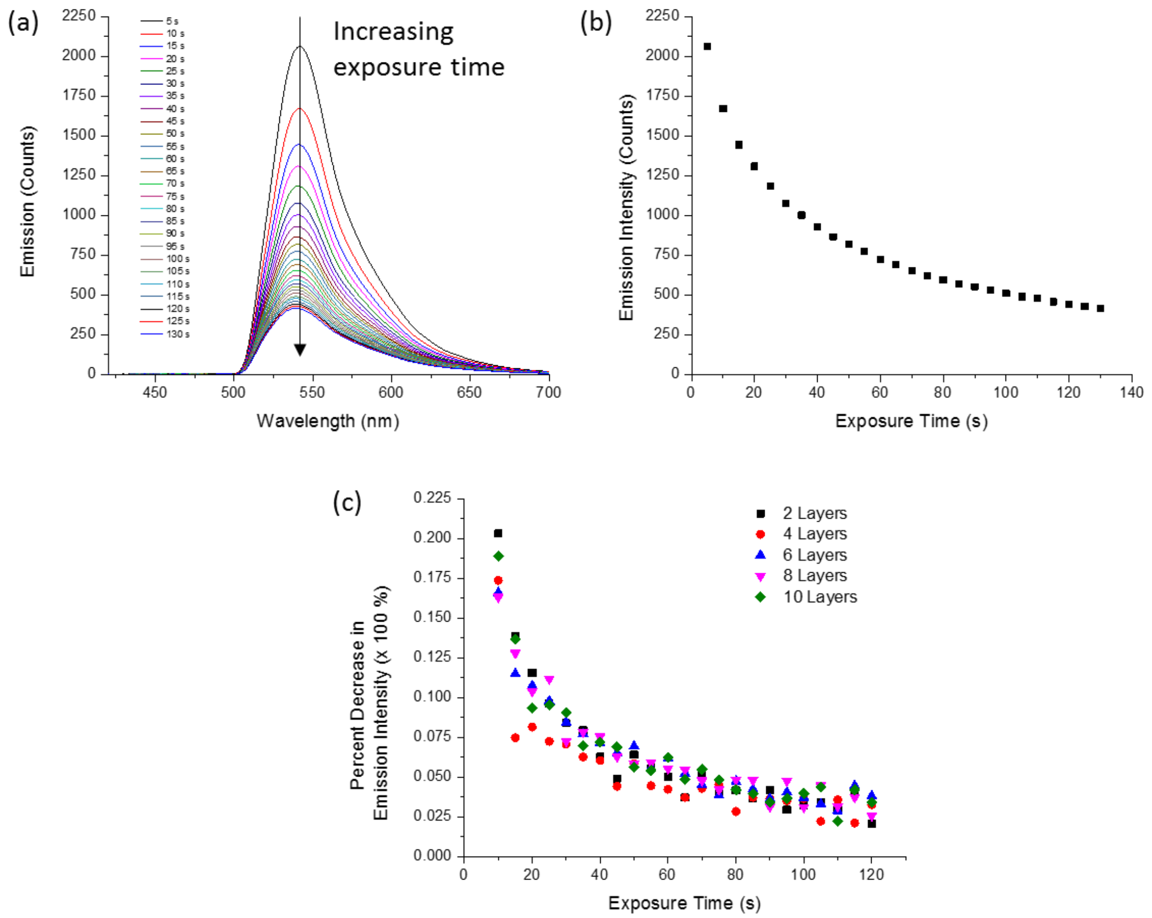

Figure 41. Emission intensity decrease with increased exposure time to excitation light (460 – 500 nm). (a) Emission spectra collected in 5 s intervals from the same spot on a *M. rhetenor* scale coated with 10 dye-containing layers, resulting in approximately 75 % drop in emission intensity over a 130 s exposure period. (b) Peak intensity values from the same sample. (c) Percent decrease in emission intensity, normalized to the preceding emission measurement within a time series of a given sample. All coated samples displayed the same photobleaching trend.

The surface polarity gradient discovered [93] throughout the thickness of the ridges in *Morpho* butterflies may affect the film continuity due to a spatially varying surface chemistry. However, a confocal fluorescence microscopy optical cross-section of a sample coated with 9 dye-containing layers demonstrated a distribution of fluorescent emission throughout the scale thickness (**Figure 42 (a)**). Control experiments, conducted under the same illumination and detection conditions revealed that the measured intensity was due to the fluorophore applied to the scale, rather than to the uncoated scale material

(**Figure 42 (b, c)**). An intensity comparison between the coated and uncoated scale was acquired by integrating the intensity for a fixed area (1600 µm^2) over all optical sections. An example measurement area is shown in **Figure 42 (c)** relative to the width and length of a single, coated scale. Three separate scales were measured for both uncoated and 9 dye-containing multilayer samples (*i.e.,* total of 6 measurements). On average, the coated specimens were 56 x brighter in overall emission intensity. The effects of photobleaching were minimized through raster of the laser beam for a short dwell time (1.3 µs/pixel with an approximate pixel size of 0.04 µm^2/pixel). Only one image (*i.e.,* exposure to the excitation source) was acquired for each measured scale. All confocal analyses were courtesy of Dr. Vincent Chen, Perry Group, Georgia Institute of Technology.

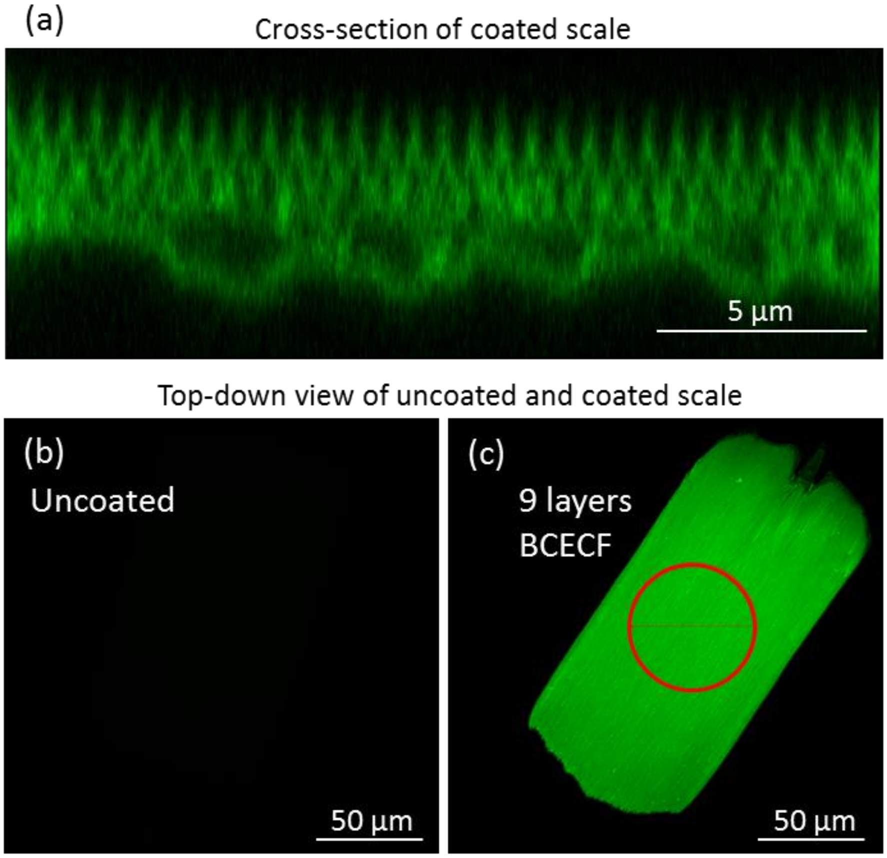

Figure 42. Confocal fluorescence microscopy analyses of dye-functionalized and uncoated scales. (a) Optical cross section of the emitted light from a single scale demonstrating the distribution of the applied, synthetic fluorophore throughout the scale thickness after 9 applied dye-containing layers. Representative confocal images of (b) uncoated and (c) 9 dye-containing multilayer scales. The red circle indicates the area over which the intensity was integrated for each sample. Comparison between the detected intensity between three separate samples, each, for uncoated and coated specimens reveal that the coated samples were approximately 56 x brighter than the uncoated butterfly scales. This confirmed that the detected emission intensity was due to the applied synthetic fluorophore in the optical cross-section of a single scale (a). Note: the images were artificially colored green. All confocal analyses were courtesy of Dr. Vincent Chen, Perry Group, Georgia Institute of Technology.

2.5.3 Coated scale reflectance analysis as a function of multilayer number

Figure 43 shows that the peak reflectance for the coated scales red shifted as the number of coating layers increased. The initially blue, uncoated scales obtained a relatively green coloration with a greater number of applied layers. This progressive color change could be either a result of structural color or fluorescence emission (or both). Contributions of the multilayer coating to the scale photonic structure, through either enhanced refractive index and increased coating thickness could red-shift the peak reflectance.[29] Alternatively, an increased amount of the green-emitting fluorophore for the higher number of layers could induce the relatively green coloration.

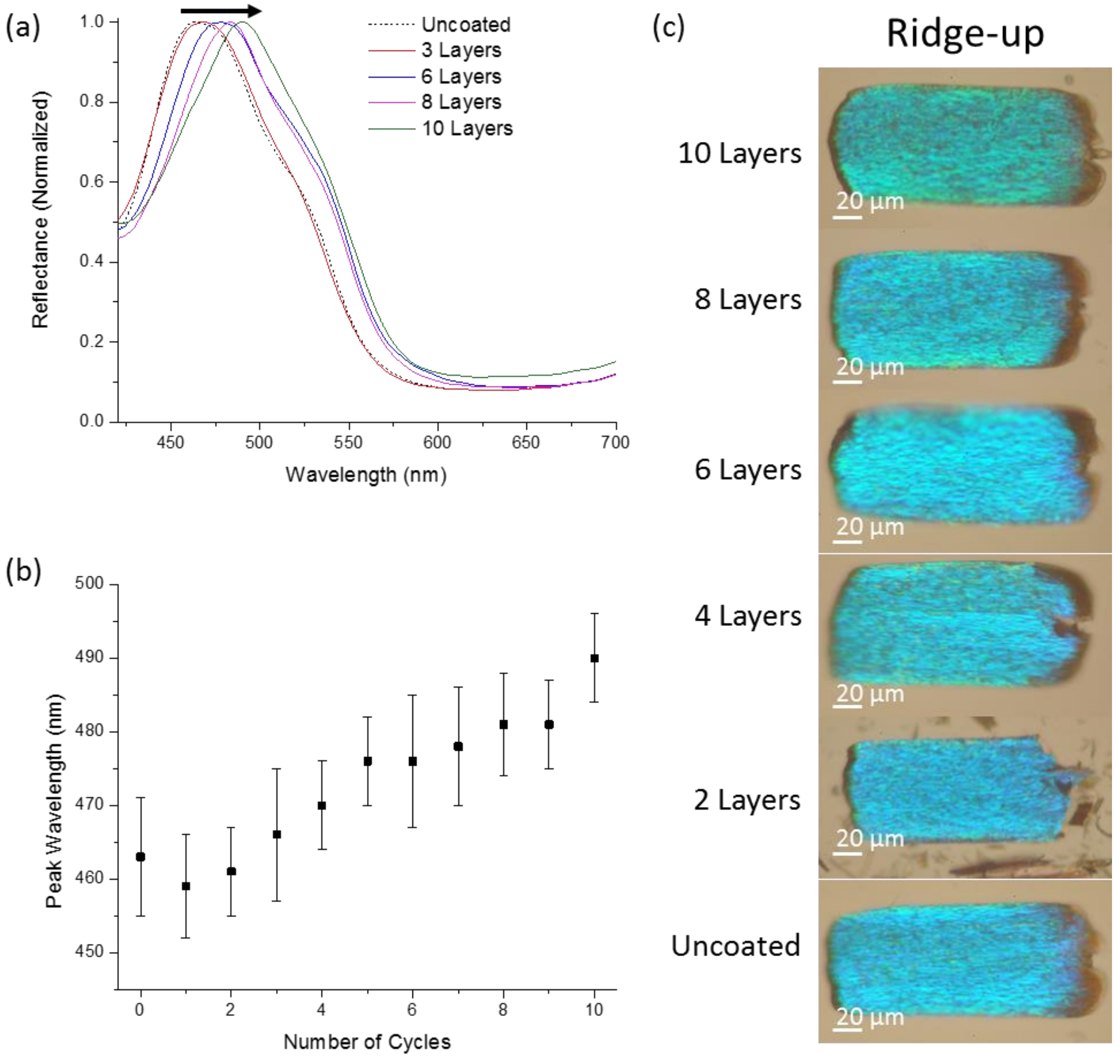

Figure 43. Reflectance analysis of *M. rhetenor* scales iteratively coated with fluorescent organic dye multilayers. (a) Average reflectance spectra, normalized to the peak wavelength, demonstrating the overall red shift in peak reflection as a function of applied layers. (b) Peak wavelength variation as a function of dye-containing layers. (c) Bright field optical images for an uncoated scale and coated scales, demonstrating the overall shift in color from blue to green. All spectra and peak wavelength values were averaged from at least 10 separate measurements on separate scales with ± one standard deviation as the error.

Two experiments were performed to identify which coloration mechanism was responsible for the overall scale coloration: time series with exposure to white light and long pass illumination to remove any fluorophore excitation light. A scale coated with 10 dye layers was selected for this analysis as this sample displayed the greatest fluorescent intensity and had the greatest red-shifted reflectance (peak wavelength of 491 ± 6 nm). The reflectance time series in **Figure 44 (a)** indicates that the reflection spectra, under the tested illumination conditions, did not have a transient component. This suggested that fluorescence, even briefly, did not have a significant impact on the overall scale coloration.

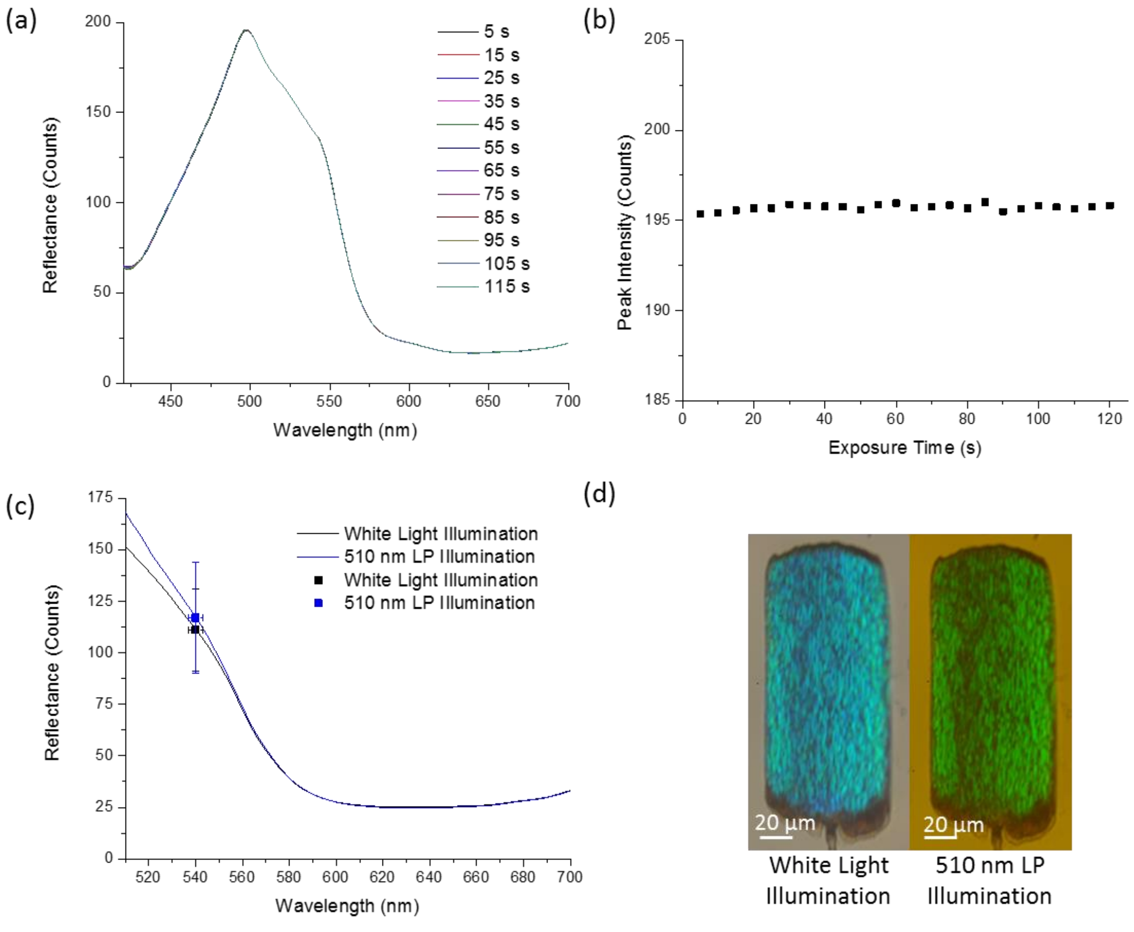

Figure 44. Determination of fluorescence contribution to coloration origin for *M. rhetenor* scales coated with 10 dye layers. (a) White light illumination time series detailing a consistent reflectance spectrum with respect to time. (b) Peak intensity at 491 ± 6 nm for the same sample, displaying very little variation in intensity with exposure time. (c) White light (black) and long wavelength (blue, 510 nm long pass filter (LP)) illumination of a separate scale. Removal of short wavelength illumination, which excites the fluorophore functionalized to the scale surface, does not result in any change in spectral shape. (d) Optical images of the same scale under both illumination conditions. These results show that the overall scale coloration, under white light illumination, is structural, rather than emissive, in origin.

A fluorescence filter cube was modified for white light and long wavelength illumination for quantitative reflection spectra and qualitative imaging. The dichroic mirror was replaced with a 50/50 beam splitter and a 510 nm long pass filter was used (or not) in the filter cube excitation port to control the illumination spectrum. Both white light reflection spectra (*i.e.*, without the long pass filter) and long wavelength reflection spectra shared the same spectral shape (**Figure 44 (c)**). Additionally, the average intensity values at 541 ± 3 nm (*i.e.*, the peak emission of fluorophore-coated scales) were equivalent between either imaging mode. This result confirmed the hypothesis that the reflected color change was due to the thickness and refractive index contributions to the photonic structure in the *M. rhetenor* scales.

Further validation of reflectance alteration by the layer-by-layer coating was obtained by analyzing the reflectance alteration for *M. rhetenor* scales coated with only the dendritic amplification process (*i.e.*, no fluorophore). The results of the reflection analysis (**Figure 45**) show that the scale coloration was red-shifted by an increased number of applied coatings.

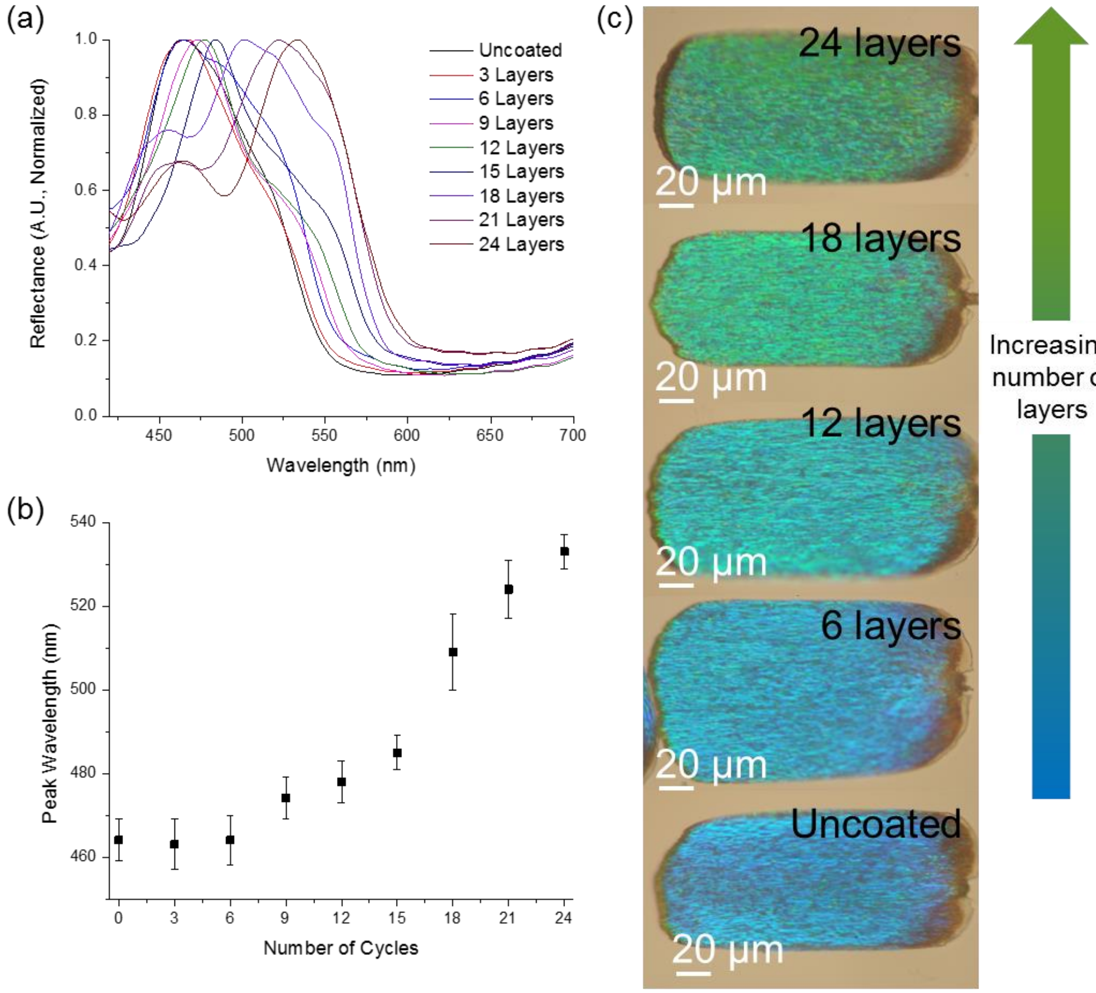

Figure 45. Control experiment of *M. rhetenor* scales iteratively coated with only the dendritic amplification process (*i.e.*, no organic fluorescent dye). (a) Average reflectance spectra, normalized to the peak wavelength, demonstrating an overall red shift with increasing number of layers. (b) Peak wavelength analysis and (c) bright field optical images demonstrating the same trend of an overall red shift with increasing number of layers. All spectra and peak wavelength values were averaged from at least 10 separate measurements on separate scales with ± one standard deviation as the error.

2.5.4 Structural characterization of organic dye multilayers on *M. rhetenor* scales

Scanning electron microscope (SEM) (**Figure 46 (b, d, e)**) and transmission electron microscope (TEM) (**Figure 46 (c)**) images detail the structural features found within the *M. rhetenor* blue scales (**Figure 46 (a)**). The scale cross section in **Figure 46 (c)** reveals multiple, periodically spaced ridges with periodic lamella structures (**Figure 46 (c), white arrows**). The overall blue scale coloration is created through interference and diffraction from both of these structures.[79, 87, 89, 90] Plan view SEM images show the parallel series of ridges (**Figure 46 (d)**). High-magnification imaging reveals the parallel lamella structure on a single ridge, indicated by the white arrows in (**Figure 46 (e)**).

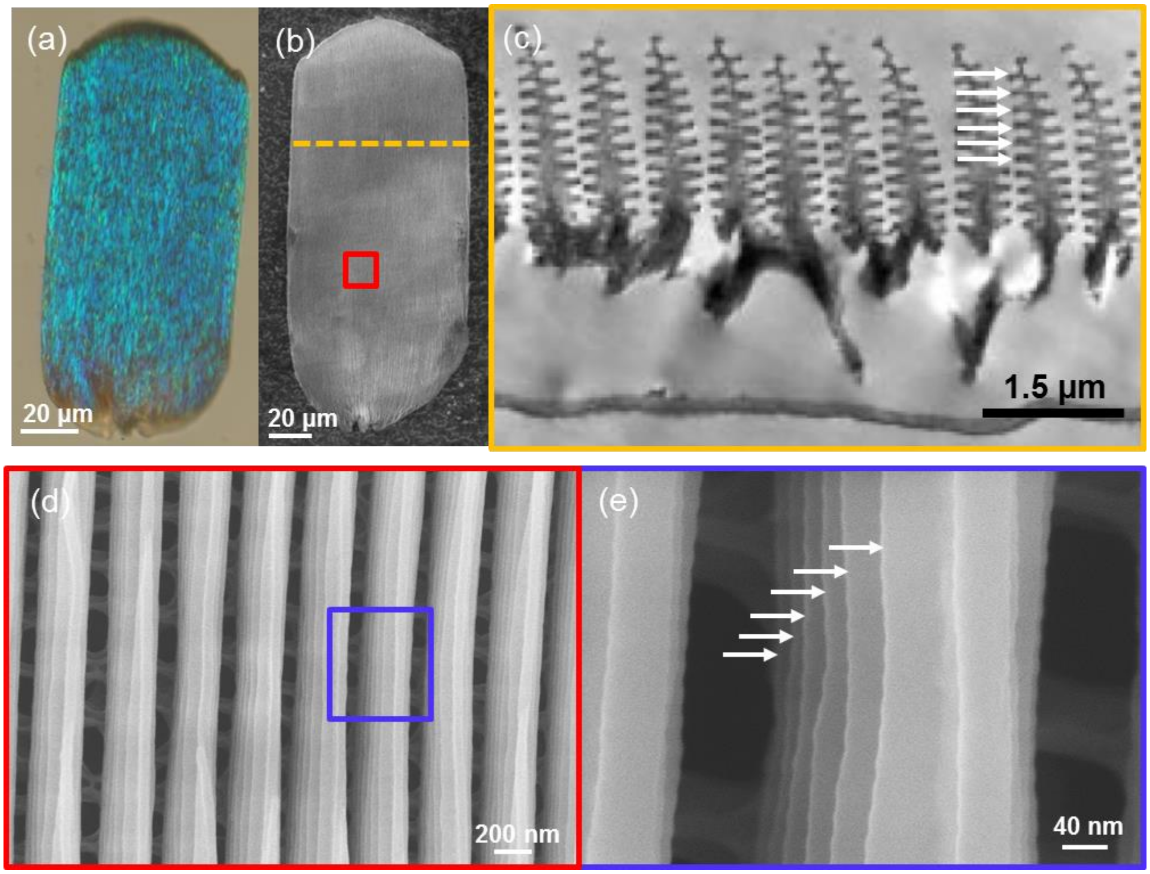

Figure 46. Introduction to the uncoated, *M. rhetenor* scale structure. (a) Bright field optical image of single, blue scale oriented ridge-up. (b) Secondary electron image of another blue scale, oriented ridge-up. (c) TEM cross section of scale structure provided courtesy P. Vukusic, University of Exeter [89]. White arrows highlight the individual lamella responsible for the structural coloration of the overall scale.
(d) Plan view (intermediate magnification) of the parallel ridge structure and (e) high magnification of a single ridge. White arrows highlight the individual lamella, from a top-down view.

Secondary electron imaging of selected, dye-coated samples revealed that the butterfly scale structure (*i.e.*, ridges and individual lamella) was preserved throughout all coating cycles (**Figure 47 (a – h))**. Samples coated with only dendritic amplification layers also retained the scale structure throughout all tested coating layers (**Figure 47 (i – q)**).

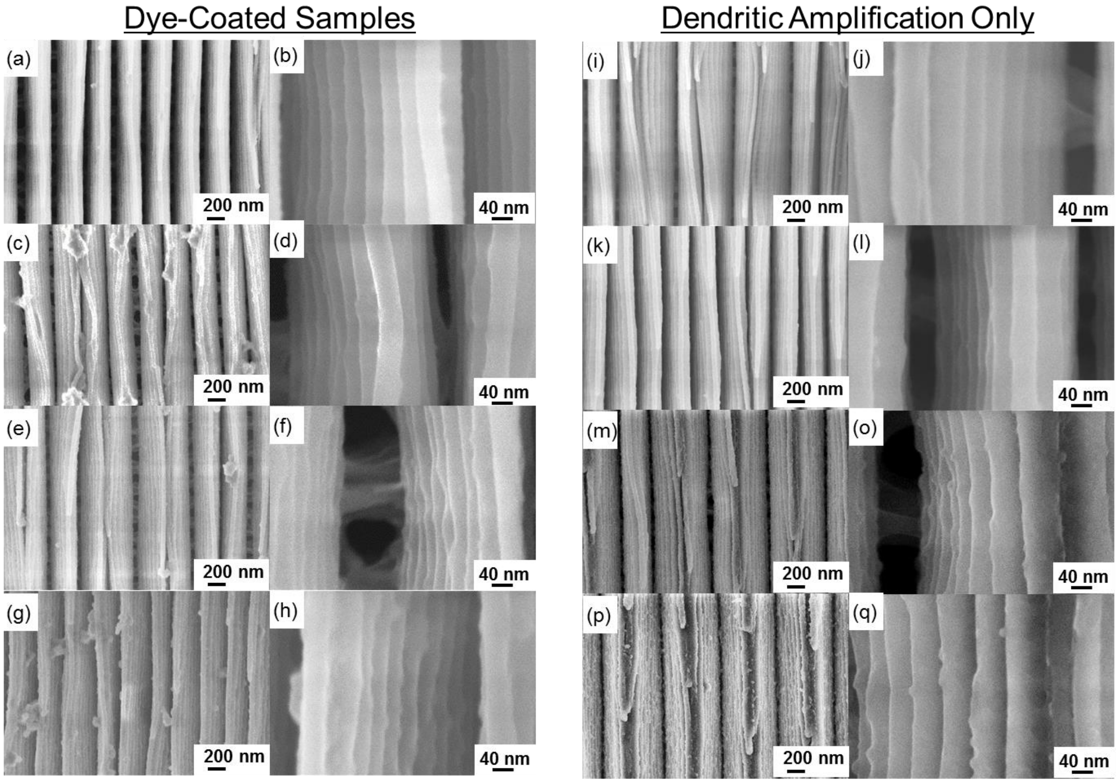

Figure 47. Intermediate and high magnification secondary electron images for coated scales with organic fluorescent dye multilayers for (a, b) 2 layers, (c, d) 5 layers, (e, f) 7 layers, and (g, h) 9 layers. Secondary electron images for dendritic amplification coated samples (*i.e.*, no fluorophore): (i, j) 6 layers, (k, l) 12 layers, (m, o) 18 layers, and (p, q) 24 layers. Intermediate magnification images demonstrate the array of single ridges are preserved, while the high magnification images show the retention of lamella on a single ridge.

2.6 Conclusions

This work has explored the application of layer-by-layer coatings to introduce fluorescence to structurally colored butterfly scales for the first time. Demonstration of the first bimodal (natural reflective template with emission from an artificial fluorophore), layer-by-layer alteration of color was achieved through multilayered fluorophore deposition onto blue, *Morpho rhetenor* scales. Alteration of fluorescent intensity, based on the number of dye-containing layers has been introduced, while maintaining the original scale material. The reflectance spectra for iteratively coated scales were red-shifted, from the relatively blue coloration of the uncoated scale to the relatively green coloration of scales coated with 10 dye-containing layers. Analysis of reflection spectra time series and varying illumination (white light versus long wavelength illumination) has confirmed that the reflectance alteration was due to the physical contributions of the deposited film (*i.e.*, thickness and refractive index) rather than fluorescence emission. Structural coloration was preserved and controllably red-shifted by the iterative deposition of organic fluorescent dye multilayers. Butterfly scales coated with only dendritic amplification layers (*i.e.*, no fluorophore) also show a red-shifted reflectance, based on the number of applied multilayers. These results demonstrate the first layer-by-layer alteration of butterfly scale reflectance with an organic film.

The relatively rapid photobleaching exhibited by dye-functionalized scales (approximately 75 % decrease in emission intensity after a 130 s exposure time) combined with the spectral overlap between the emitted light from the fluorophore and the reflected light from the scale, were likely causes for the lack of appreciable fluorescent emission-affected color under white light illumination. Increasing the number of dye containing layers on functionalized scales may result in a greater initial emission intensity (with respect to time). However, the effects of photobleaching as well as an increased spectral overlap of the scale reflectance (due to the red shift in reflection upon the application of successive dye-containing layers) make the significant contribution of fluorescence to the white light illumination unlikely with the application of further BCECF multilayers.

The fluorescent layer-by-layer coating process developed through this work may find application in the coating of synthetic optical templates. Addressing the relatively high materials cost for this process, and exploring the use of other fluorescent compounds, may enable the realization of anti-counterfeiting applications [94]. A possible route for cost reduction may be the integration of organic fluorescent dyes with single functional groups into multilayers. For instance, fluorescein isothiocyanate (FITC) is an amine-reactive dye that would be a more economical substitute for BCECF should such a multilayer process be developed. The use of more photostable emitters, such as quantum dots [95] or dyes with greater photostability [96], as well as switchable photochromic fluorescent dyes [94] would be interesting topics for further research.

2.7 References

[1] L. P. Biro and J. P. Vigneron, "Photonic nanoarchitectures in butterflies and beetles: valuable sources for bioinspiration," *Laser & Photonics Reviews,* vol. 5, pp. 27-51, Jan 2011.

[2] P. Vukusic and R. Sambles, "Photonic structures in biology," *Nature,* vol. 424, pp. 852-855, 2003.

[3] S. Kinoshita, S. Yoshioka, and J. Miyazaki, "Physics of structural colors," *Reports on Progress in Physics,* vol. 71, Jul 2008.

[4] M. Srinivasarao, "Nano-optics in the biological world: Beetles, butterflies, birds, and moths," *Chemical Reviews,* vol. 99, pp. 1935-1961, Jul 1999.

[5] A. A. Michelson, "On metallic colouring in birds and insects," *Philosophical Magazine,* vol. 21, pp. 554-567, Apr 1911.

[6] C. W. Mason, "Structural colors in insects. I," *Journal of Physical Chemistry,* vol. 30, pp. 383-395, Mar 1926.

[7] C. W. Mason, "Structural colors in insects III," *Journal of Physical Chemistry,* vol. 31, pp. 1856-1872, Jul-Dec 1927.

[8] C. W. Mason, "Structural colors in insects II," *Journal of Physical Chemistry,* vol. 31, pp. 321-354, Mar 1927.

[9] Ghiradel.H, T. Eisner, R. E. Silberglied, Aneshans.D, and H. E. Hinton, "Ultraviolet Reflection of a Male Butterfly - Interference Color caused by Thin-Layer Elaboration of Wing Scales," *Science,* vol. 178, pp. 1214-+, 1972.

[10] H. Ghiradella, "Development of ultraviolet-reflecting butterfly scales - how to make an interference filter," *Journal of Morphology,* vol. 142, pp. 395-409, 1974.

[11] H. Ghiradella and W. Radigan, "Development of butterfly scales. 2. Struts, lattices, and surface-tension," *Journal of Morphology,* vol. 150, pp. 279-297, 1976.

[12] H. Ghiradella, "Structure of Iridescent Lepidopteran Scales - Variations on Several Themes," *Annals of the Entomological Society of America,* vol. 77, pp. 637-645, 1984.

[13] H. Ghiradella, "Structure and Development of Iridescent Lepidopteran Scales - The Papilionidae as a Showcase Family," *Annals of the Entomological Society of America,* vol. 78, pp. 252-264, 1985.

[14] H. Ghiradella, "Structure and development of iridescent butterfly scales - lattices and laminae," *Journal of Morphology,* vol. 202, pp. 69-88, Oct 1989.

[15] H. Ghiradella, "Light and Color on the Wing - Structural Colors in Butterflies and Moths," *Applied Optics,* vol. 30, pp. 3492-3500, Aug 1991.

[16] H. Ghiradella, "Structure of Butterfly Scales - Patterning in an Insect Cuticle," *Microscopy Research and Technique,* vol. 27, pp. 429-438, Apr 1994.

[17] H. Ghiradella, "Structure of butterfly scales - patterning an insect cuticle," *Microscopy Research and Technique*, vol. 27, pp. 429-438, Apr 1994.

[18] P. Vukusic, "Natural photonics," *Physics World*, vol. 17, pp. 35-39, Feb 2004.

[19] C. M. Eliason and M. D. Shawkey, "Rapid, reversible response of iridescent feather color to ambient humidity," *Optics Express*, vol. 18, pp. 21284-21292, Sep 2010.

[20] R. A. Potyrailo, H. Ghiradella, A. Vertiatchikh, K. Dovidenko, J. R. Cournoyer, and E. Olson, "Morpho butterfly wing scales demonstrate highly selective vapour response," *Nature Photonics*, vol. 1, pp. 123-128, Feb 2007.

[21] L. P. Biro, K. Kertesz, Z. Vertesy, and Z. Balint, "Photonic nanoarchitectures occurring in butterfly scales as selective gas/vapor sensors," in *Nature of Light: Light in Nature Ii*. vol. 7057, K. Creath, Ed., ed Bellingham: Spie-Int Soc Optical Engineering, 2008.

[22] N. L. Garrett, P. Vukusic, F. Ogrin, E. Sirotkin, C. P. Winlove, and J. Moger, "Spectroscopy on the wing: Naturally inspired SERS substrates for biochemical analysis," *Journal of Biophotonics*, vol. 2, pp. 157-166, Mar 2009.

[23] P. R. Stoddart, P. J. Cadusch, T. M. Boyce, R. M. Erasmus, and J. D. Comins, "Optical properties of chitin: surface-enhanced Raman scattering substrates based on antireflection structures on cicada wings," *Nanotechnology*, vol. 17, pp. 680-686, Feb 2006.

[24] B. T. Hallam, A. G. Hiorns, and P. Vukusic, "Developing optical efficiency through optimized coating structure: biomimetic inspiration from white beetles," *Applied Optics*, vol. 48, pp. 3243-3249, Jun 2009.

[25] A. D. Pris, Y. Utturkar, C. Surman, W. G. Morris, A. Vert, S. Zalyubovskiy, *et al.*, "Towards high-speed imaging of infrared photons with bio-inspired nanoarchitectures," *Nat Photon*, vol. 6, pp. 195-200, 2012.

[26] D. P. Gaillot, O. Deparis, V. Welch, B. K. Wagner, J. P. Vigneron, and C. J. Summers, "Composite organic-inorganic butterfly scales: Production of photonic structures with atomic layer deposition," *Physical Review E*, vol. 78, Sep 2008.

[27] J. Huang, X. Wang, and Z. L. Wang, "Controlled Replication of Butterfly Wings for Achieving Tunable Photonic Properties," *Nano Letters*, vol. 6, pp. 2325-2331, 2006.

[28] J. P. Vernon, "Morphology-Preserving Chemical Conversion of Bioorganic and Inorganic Templates," Doctor of Philosophy, Materials Science and Engineering, Georgia Institute of Technology, Atlanta, GA, 2012.

[29] F. Liu, W. Z. Shi, X. H. Hu, and B. Q. Dong, "Hybrid structures and optical effects in Morpho scales with thin and thick coatings using an atomic layer deposition method," *Optics Communications*, vol. 291, pp. 416-423, Mar 2013.

[30] L. Poladian, S. Wickham, K. Lee, and M. C. J. Large, "Iridescence from photonic crystals and its suppression in butterfly scales," *Journal of the Royal Society Interface*, vol. 6, pp. S233-S242, Apr 2009.

[31] B. D. Wilts, T. M. Trzeciak, P. Vukusic, and D. G. Stavenga, "Papiliochrome II pigment reduces the angle dependency of structural wing colouration in nireus group papilionids," *Journal of Experimental Biology*, vol. 215, pp. 796-805, Mar 2012.

[32] J. P. Vigneron, K. Kertesz, Z. Vertesy, M. Rassart, V. Lousse, Z. Balint, *et al.*, "Correlated diffraction and fluorescence in the backscattering iridescence of the male butterfly Troides magellanus (Papilionidae)," *Physical Review E,* vol. 78, Aug 2008.

[33] E. Van Hooijdonk, C. Barthou, J. P. Vigneron, and S. Berthier, "Detailed experimental analysis of the structural fluorescence in the butterfly Morpho sulkowskyi (Nymphalidae)," *Journal of Nanophotonics,* vol. 5, Nov 2011.

[34] K. Michielsen and D. G. Stavenga, "Gyroid cuticular structures in butterfly wing scales: biological photonic crystals," *Journal of the Royal Society Interface,* vol. 5, pp. 85-94, Jan 2008.

[35] J. Tang, S. M. Zhu, Z. X. Chen, C. L. Feng, Y. J. Shen, F. Yao, *et al.*, "Replication of polypyrrole with photonic structures from butterfly wings as biosensor," *Materials Chemistry and Physics,* vol. 131, pp. 706-713, Jan 2012.

[36] S.-H. Kang, T.-Y. Tai, and T.-H. Fang, "Replication of butterfly wing microstructures using molding lithography," *Current Applied Physics,* vol. 10, pp. 625-630, 2010.

[37] Q. Q. Yang, S. M. Zhu, W. H. Peng, C. Yin, W. L. Wang, J. J. Gu, *et al.*, "Bioinspired Fabrication of Hierarchically Structured, pH-Tunable Photonic Crystals with Unique Transition," *Acs Nano,* vol. 7, pp. 4911-4918, Jun 2013.

[38] J. Han, H. L. Su, D. Zhang, J. J. Chen, and Z. X. Chen, "Butterfly wings as natural photonic crystal scaffolds for controllable assembly of CdS nanoparticles," *Journal of Materials Chemistry,* vol. 19, pp. 8741-8746, 2009.

[39] R. J. Martin-Palma, C. G. Pantano, and A. Lakhtakia, "Biomimetization of butterfly wings by the conformal-evaporated-film-by-rotation technique for photonics," *Applied Physics Letters,* vol. 93, Aug 2008.

[40] M. R. Weatherspoon, Y. Cai, M. Crne, M. Srinivasarao, and K. H. Sandhage, "3D rutile titania-based structures with Morpho butterfly wing scale morphologies," *Angewandte Chemie-International Edition,* vol. 47, pp. 7921-7923, 2008.

[41] J. P. Vernon, A. Lethbridge, C. G. Cameron, Y. Cai, M. Kolle, J. Aizenberg, *et al.*, "Layer-by-Layer Conformal Coating and Replication of Butterfly Photonic Nanostructures with Higher Index Inorganic Materials," *In preparation*.

[42] C. Mille, E. C. Tyrode, and R. W. Corkery, "Inorganic chiral 3-D photonic crystals with bicontinuous gyroid structure replicated from butterfly wing scales," *Chemical Communications,* vol. 47, pp. 9873-9875, 2011.

[43] Y. Chen, J. J. Gu, D. Zhang, S. M. Zhu, H. L. Su, X. B. Hu, *et al.*, "Tunable three-dimensional ZrO(2) photonic crystals replicated from single butterfly wing scales," *Journal of Materials Chemistry,* vol. 21, pp. 15237-15243, 2011.

[44] Y. Chen, X. N. Zang, J. J. Gu, S. M. Zhu, H. L. Su, D. Zhang, *et al.*, "ZnO single butterfly wing scales: synthesis and spatial optical anisotropy," *Journal of Materials Chemistry,* vol. 21, pp. 6140-6143, 2011.

[45] J. W. Galusha, M. R. Jorgensen, and M. H. Bartl, "Diamond-Structured Titania Photonic-Bandgap Crystals from Biological Templates," *Advanced Materials,* vol. 22, pp. 107-+, Jan 2010.

[46] J. W. Galusha, L. R. Richey, M. R. Jorgensen, J. S. Gardner, and M. H. Bartl, "Study of natural photonic crystals in beetle scales and their conversion into

inorganic structures via a sol-gel bio-templating route," *Journal of Materials Chemistry,* vol. 20, pp. 1277-1284, 2010.
[47] M. R. Jorgensen and M. H. Bartl, "Biotemplating routes to three-dimensional photonic crystals," *Journal of Materials Chemistry,* vol. 21, pp. 10583-10591, 2011.
[48] M. R. Jorgensen, B. P. Yonkee, and M. H. Bartl, "Solid and hollow inorganic replicas of biological photonic crystals," *Scripta Materialia,* vol. 65, pp. 954-957, Dec 2011.
[49] J. P. Vernon, Y. N. Fang, Y. Cai, and K. H. Sandhage, "Morphology-Preserving Conversion of a 3D Bioorganic Template into a Nanocrystalline Multicomponent Oxide Compound," *Angewandte Chemie-International Edition,* vol. 49, pp. 7765-7768, 2010.
[50] J. P. Vernon, N. Hobbs, Y. Cai, A. Lethbridge, P. Vukusic, D. D. Deheyn, *et al.*, "3D photoluminescent lanthanide-doped barium titanate structures synthesized by coating and shape-preserving reaction of complex-shaped bioorganic templates," *Journal of Materials Chemistry,* vol. 22, pp. 10435-10437, 2012.
[51] S. M. Zhu, X. Y. Liu, Z. X. Chen, C. J. Liu, C. L. Feng, J. J. Gu, *et al.*, "Synthesis of Cu-doped WO3 materials with photonic structures for high performance sensors," *Journal of Materials Chemistry,* vol. 20, pp. 9126-9132, 2010.
[52] J. W. Wang and Y. M. Kuo, "Hierarchically porous cobalt oxyhydroxide derived from Morpho-butterfly wings: Preparation, characterization, and carbon monoxide detection at low temperatures," *Physica Status Solidi a-Applications and Materials Science,* vol. 210, pp. 494-502, Mar 2013.
[53] F. Liu, Y. P. Liu, L. Huang, X. H. Hu, B. Q. Dong, W. Z. Shi, *et al.*, "Replication of homologous optical and hydrophobic features by templating wings of butterflies Morpho menelaus," *Optics Communications,* vol. 284, pp. 2376-2381, May 2011.
[54] Y. N. Fang, J. D. Berrigan, Y. Cai, S. R. Marder, and K. H. Sandhage, "Syntheses of nanostructured Cu- and Ni-based micro-assemblies with selectable 3-D hierarchical biogenic morphologies," *Journal of Materials Chemistry,* vol. 22, pp. 1305-1312, 2012.
[55] Y. N. Fang, V. W. Chen, Y. Cai, J. D. Berrigan, S. R. Marder, J. W. Perry, *et al.*, "Biologically Enabled Syntheses of Freestanding Metallic Structures Possessing Subwavelength Pore Arrays for Extraordinary (Surface Plasmon-Mediated) Infrared Transmission," *Advanced Functional Materials,* vol. 22, pp. 2550-2559, Jun 2012.
[56] I. Ichinose, H. Senzu, and T. Kunitake, "Stepwise adsorption of metal alkoxides on hydrolyzed surfaces: A surface sol-gel process," *Chemistry Letters,* pp. 831-832, 1996.
[57] J. Silver, R. Withnall, T. G. Ireland, and G. R. Fern, "Novel nano-structured phosphor materials cast from natural Morpho butterfly scales," *Journal of Modern Optics,* vol. 52, pp. 999-1007, May 2005.
[58] M. Kucki, S. Landwehr, H. Ruhling, M. Maniak, and T. Fuhrmann-Lieker, "Light-emitting biological photonic crystals - The bioengineering of metamaterials," in *Photonic Crystal Materials and Devices III.* vol. 6182, R. M.

DeLaRue, P. Viktorovitch, C. Lopez, and M. Midrio, Eds., ed, 2006, pp. S1821-S1821.

[59] M. Kucki and T. Fuhrmann-Lieker, "Staining diatoms with rhodamine dyes: control of emission colour in photonic biocomposites," *Journal of the Royal Society Interface,* vol. 9, pp. 727-733, Apr 2012.

[60] M. R. Weatherspoon, M. S. Haluska, Y. Cai, J. S. King, C. J. Summers, R. L. Snyder, *et al.*, "Phosphor microparticles of controlled three-dimensional shape from phytoplankton," *Journal of the Electrochemical Society,* vol. 153, pp. H34-H37, 2006.

[61] D. H. Lee, T. Gutu, C. Jeffryes, G. L. Rorrer, J. Jiao, and C. H. Chang, "Nanofabrication of green luminescent Zn2SiO4 : Mn using biogenic silica," *Electrochemical and Solid State Letters,* vol. 10, pp. K13-K16, 2007.

[62] D. K. Gale, T. Gutu, J. Jiao, C. H. Chang, and G. L. Rorrer, "Detection of Immunocomplex Formation by Enhanced Photoluminescence of Antibody-Functionalized Diatom Biosilica," in *Bio-Inspired/Biomimetic Sensor Technologies and Applications*. vol. 7321, N. F. Fell and V. S. Swaminathan, Eds., ed, 2009.

[63] C. Jeffryes, R. Solanki, Y. Rangineni, W. Wang, C.-h. Chang, and G. L. Rorrer, "Electroluminescence and Photoluminescence from Nanostructured Diatom Frustules Containing Metabolically Inserted Germanium," *Advanced Materials,* vol. 20, pp. 2633-2637, 2008.

[64] Y. Cai, M. B. Dickerson, M. S. Haluska, Z. Kang, C. J. Summers, and K. H. Sandhage, "Manganese-Doped Zinc Orthosilicate-Bearing Phosphor Microparticles with Controlled Three-Dimensional Shapes Derived from Diatom Frustules," *Journal of the American Ceramic Society,* vol. 90, pp. 1304-1308, 2007.

[65] N. I. Kovtyukhova, E. V. Buzaneva, C. C. Waraksa, and T. E. Mallouk, "Ultrathin nanoparticle ZnS and ZnS : Mn films: surface sol-gel synthesis, morphology, photophysical properties," *Materials Science and Engineering B-Solid State Materials for Advanced Technology,* vol. 69, pp. 411-417, Jan 2000.

[66] Z. Q. Liang, K. L. Dzienis, J. Xu, and Q. Wang, "Covalent layer-by-layer assembly of conjugated polymers and CdSe nanoparticles: Multilayer structure and photovoltaic properties," *Advanced Functional Materials,* vol. 16, pp. 542-548, Mar 2006.

[67] O. V. Vassiltsova, S. K. Panda, Z. Y. Zhao, M. A. Carpenter, and M. A. Petrukhina, "Ordered fabrication of luminescent multilayered thin films of CdSe quantum dots," *Dalton Transactions,* pp. 9426-9432, 2009.

[68] S. Ishii, R. Ueji, S. Nakanishi, Y. Yoshida, H. Nagata, T. Itoh, *et al.*, "Fabrication of a quantum dot-polymer matrix by layer-by-layer conjugation," *Journal of Photochemistry and Photobiology a-Chemistry,* vol. 183, pp. 285-291, Oct 2006.

[69] Y. Tian, Q. He, C. Tao, and J. B. Li, "Fabrication of fluorescent nanotubes basel on layer-by-layer assembly via covalent bond," *Langmuir,* vol. 22, pp. 360-362, Jan 2006.

[70] I. Welterlich and B. Tieke, "Conjugated Polymer with Benzimidazolylpyridine Ligands in the Side Chain: Metal Ion Coordination and Coordinative Self-

Assembly into Fluorescent Ultrathin Films," *Macromolecules,* vol. 44, pp. 4194-4203, Jun 2011.

[71] K. Kim, S. Webster, N. Levi, D. L. Carroll, M. R. Pinto, and K. S. Schanze, "Luminescent core-shell photonic crystals from poly(phenylene ethynylene) coated silica spheres," *Langmuir,* vol. 21, pp. 5207-5211, May 2005.

[72] J. Sun, I. Ichinose, R. Takaki, A. Nakao, and T. Kunitake, "Enhanced emission in composite multilayers of amorphous TiO2-gel and Eu3+ ions," *Chemistry Letters,* pp. 742-743, Jul 2002.

[73] T. Yonezawa, H. Matsune, and T. Kunitake, "Layered Nanocomposite of Close-Packed Gold Nanoparticles and TiO2 Gel Layers," *Chemistry of Materials,* vol. 11, pp. 33-35, 1998.

[74] J. Y. Tseng, M. H. Lin, and L. K. Chau, "Preparation of colloidal gold multilayers with 3-(mercaptopropyl)-trimethoxysilane as a linker molecule," *Colloids and Surfaces a-Physicochemical and Engineering Aspects,* vol. 182, pp. 239-245, Jun 2001.

[75] S. Paul, J. G. Huang, and I. Ichinose, "Enantioselective anion exchange on a positively charged poly(L-lysine) layer assembled on thin TiO2-gel films," *New Journal of Chemistry,* vol. 29, pp. 1058-1063, 2005.

[76] H. Watanabe and T. Kunitake, "Spatial disposition of dye molecules within metal oxide nanotubes," *Chemistry of Materials,* vol. 20, pp. 4998-5004, Aug 2008.

[77] G. J. Wang, Y. N. Fang, P. Kim, A. Hayek, M. R. Weatherspoon, J. W. Perry, *et al.*, "Layer-By-Layer Dendritic Growth of Hyperbranched Thin Films for Surface Sol-Gel Syntheses of Conformal, Functional, Nanocrystalline Oxide Coatings on Complex 3D (Bio)silica Templates," *Advanced Functional Materials,* vol. 19, pp. 2768-2776, Sep 2009.

[78] M. R. Weatherspoon, M. B. Dickerson, G. Wang, Y. Cai, S. Shian, S. C. Jones, *et al.*, "Thin, conformal, and continuous SnO2 coatings on three-dimensional biosilica templates through hydroxy-group amplification and layer-by-layer alkoxide deposition," *Angewandte Chemie-International Edition,* vol. 46, pp. 5724-5727, 2007.

[79] A. Mejdoubi, C. Andraud, S. Berthier, J. Lafait, J. Boulenguez, and E. Richalot, "Finite element modeling of the radiative properties of Morpho butterfly wing scales," *Physical Review E,* vol. 87, Feb 2013.

[80] L. Plattner, "Optical properties of the scales of Morpho rhetenor butterflies: theoretical and experimental investigation of the back-scattering of light in the visible spectrum," *Journal of the Royal Society Interface,* vol. 1, pp. 49-59, Nov 2004.

[81] B. Gralak, G. Tayeb, and S. Enoch, "Morpho butterflies wings color modeled with lamellar grating theory," *Optics Express,* vol. 9, pp. 567-578, Nov 2001.

[82] M. A. Steindorfer, V. Schmidt, M. Belegratis, B. Stadlober, and J. R. Krenn, "Detailed simulation of structural color generation inspired by the Morpho butterfly," *Optics Express,* vol. 20, pp. 21485-21494, Sep 2012.

[83] R. H. Siddique, S. Diewald, J. Leuthold, and H. Holscher, "Theoretical and experimental analysis of the structural pattern responsible for the iridescence of Morpho butterflies," *Optics Express,* vol. 21, pp. 14351-14361, Jun 2013.

[84] R. T. Lee and G. S. Smith, "Detailed electromagnetic simulation for the structural color of butterfly wings," *Applied Optics,* vol. 48, pp. 4177-4190, Jul 2009.

[85] M. Kambe, D. Zhu, and S. Kinoshita, "Origin of Retroreflection from a Wing of the Morpho Butterfly," *Journal of the Physical Society of Japan,* vol. 80, May 2011.

[86] J. Boulenguez, S. Berthier, and F. Leroy, "Multiple scaled disorder in the photonic structure of Morpho rhetenor butterfly," *Applied Physics a-Materials Science & Processing,* vol. 106, pp. 1005-1011, Mar 2012.

[87] S. Berthier, E. Charron, and J. Boulenguez, "Morphological structure and optical properties of the wings of Morphidae," *Insect Science,* vol. 13, pp. 145-158, 2006.

[88] S. Banerjee and Z. Dong, "Optical characterization of iridescent wings of Morpho butterflies using a high accuracy nonstandard finite-difference time-domain algorithm," *Optical Review,* vol. 14, pp. 359-361, Nov-Dec 2007.

[89] P. Vukusic, J. R. Sambles, C. R. Lawrence, and R. J. Wootton, "Quantified interference and diffraction in single Morpho butterfly scales," *Proceedings of the Royal Society of London Series B-Biological Sciences,* vol. 266, pp. 1403-1411, Jul 1999.

[90] S. Kinoshita, S. Yoshioka, and K. Kawagoe, "Mechanisms of structural colour in the Morpho butterfly: cooperation of regularity and irregularity in an iridescent scale," *Proceedings of the Royal Society of London Series B-Biological Sciences,* vol. 269, pp. 1417-1421, Jul 2002.

[91] P. Vukusic and D. G. Stavenga, "Physical methods for investigating structural colours in biological systems," *Journal of the Royal Society Interface,* vol. 6, pp. S133-S148, Apr 2009.

[92] Y. H. Li, D. Wang, and J. M. Buriak, "Molecular Layer Deposition of Thiol-Ene Multilayers on Semiconductor Surfaces," *Langmuir,* vol. 26, pp. 1232-1238, Jan 2010.

[93] R. A. Potyrailo, T. A. Starkey, P. Vukusic, H. Ghiradella, M. Vasudev, T. Bunning, *et al.*, "Discovery of the surface polarity gradient on iridescent Morpho butterfly scales reveals a mechanism of their selective vapor response," *Proceedings of the National Academy of Sciences,* vol. 110, pp. 15567-15572, September 24, 2013 2013.

[94] B. Yoon, J. Lee, I. S. Park, S. Jeon, J. Lee, and J. M. Kim, "Recent functional material based approaches to prevent and detect counterfeiting," *Journal of Materials Chemistry C,* vol. 1, pp. 2388-2403, 2013.

[95] W. C. W. Chan and S. M. Nie, "Quantum dot bioconjugates for ultrasensitive nonisotopic detection," *Science,* vol. 281, pp. 2016-2018, Sep 1998.

[96] Y. Kim, S. H. Kim, M. Tanyeri, J. A. Katzenellenbogen, and C. M. Schroeder, "Dendrimer Probes for Enhanced Photostability and Localization in Fluorescence Imaging," *Biophysical Journal,* vol. 104, pp. 1566-1575, Apr 2013.

CHAPTER 3: Fluorescent Quantum Dot Multilayers on the Scales of *Morpho rhetenor*

3.1 Summary

Blue scales of *Morpho* butterflies have attracted considerable scientific interest as a photonic template owing to their intense reflection and relatively angle independent coloration. The intense, stable emission of light from quantum dot multilayers were combined with the high reflectivity *Morpho* scale, to provide the first demonstration of color mixing between reflected and emitted light on a single, modified butterfly scale. Additionally, this work represents the first demonstration of quantum dot multilayers applied to a prefabricated, photonic template. The overall emission intensity increased, and the reflected color red shifted, upon the iterative deposition of quantum dot-containing layers. Quantum dot-coated scales did display photoluminescent enhancement (*i.e.,* the increase in emission intensity with exposure time), but this time-dependent emission plateaued after 300 s. This enabled the characterization of time-independent emission intensity as a function of the number of applied quantum dot-containing layers. Cross-sectional TEM images confirmed that the coating was conformal after the application of 10 quantum dot-containing layers. The thickness of this quantum dot-bearing coating was 35 ± 10 nm.

3.2 Introduction

Nanostructures found within insect scales are a valuable source of inspiration for new solutions to technical challenges in optics and for improving certain existing optical technologies.[1, 2] In fact, scientists have studied the coloration in insect scales for over a century.[3-7] Mason suggested that the observed structural coloration for certain species was similar to thin film interference.[3, 5-7] Later, electron microscopy studies revealed intricate, 3-dimensional, hierarchical nanostructures on the scales of some insects.[3, 8-16]

Insect coloration can result from the complex interaction of light with the hierarchical features found within such scales.[2, 17, 18] Insect scales, and associated biomimetic analogs, have found some direct applications.[19-21] However, the addition of tailored, synthetic materials to such structures has expanded the range of potential applications and improved understanding of how such scale nanostructures interact with light.[22-28] Progress towards bioinspired design from insect scales could be advanced by a greater understanding as to how new optical functionalities can be introduced to biological nanostructures.

Fluorescence has been identified in the natural scales of numerous butterflies.[29-31] These results inspired the present exploration as to how synthetic fluorophores can be introduced onto hierarchically structured butterfly scales. The addition of synthetic fluorophores could expand the ability to tailor optical signatures by emissive coloration and temporal variation beyond that found in nature. The blue scales of the *Morpho rhetenor* butterfly were of particular interest as a photonic template owing to their intense reflection and relatively angle-independent coloration.[32-40]

Layer-by-layer material deposition is of specific interest for the incorporation of artificial fluorophores. Numerous studies have shown that such processing offers control over scale reflectance as a function of the number of applied layers.[25-28] However, efforts have not been made towards incorporating fluorescent emission from quantum dots in a layer-by-layer process on the scales of butterflies or biomimetic analogs. Prior efforts of layer-by-layer quantum dot coatings have been used to coat colloidal spheres.[41-44] The resulting quantum dot-functionalized spheres were used to self-assemble inverse opals so that quantum dot emission within a synthetic optical structure could be studied.[41-44] As of this point, no efforts have been made towards the examination of layer-by-layer quantum dot deposition on the reflected and emitted coloration of a prefabricated optical template. Increased photostability, relative to organic fluorescent dyes, and composition-tunable emission make quantum dots attractive as synthetic fluorophores [45] for the demonstration of color mixing with the high reflectivity *M. rhetenor* blue scales [32-40].

3.3 Literature Review

Numerous classes of materials have been applied to butterfly and beetle scales: polymers [46-48], chalcogenides [49, 50], ceramics [25, 28, 51-64], and metal/metal alloys [65, 66]. Layer-by-layer coating methods, such as Atomic Layer Deposition (ALD) and surface sol-gel, are effective means of altering the observed color of butterfly scales.[25-28] These existing methodologies alter scale reflectance though the iterative application of oxide coatings, with sub-nanometer precision per cycle.[25-27] Yet, the integration of prefabricated quantum dots into layer-by-layer deposition schemes for altering bioorganic nanostructure color has not been examined. Some methods have been applied towards integrating emissive components into butterflies [61, 67] and diatoms [68-74]. Thermal treatments in some of these processing steps can destroy the starting template material [61, 67, 70, 71, 74]. Alternatively, fluorophores can be incorporated during cell growth (*i.e.*, diatom cell growth) [68, 69, 73]. Additionally, covalent functionalization of a single fluorophore layer has been explored for diatoms [68, 72], but these efforts did not include a multilayer approach.

The multilayer approach is an effective means of increasing emission, or absorption, intensity with successive layers. Species incorporated into multilayer structures have included organic fluorescent dyes [75-77], rare earth ions [78], gold nanoparticles [79, 80], and chalcogenide nanoparticle films [81-87]. Both electrostatic [82-84] and covalent [85-87] quantum dot functionalization have been used for multilayer deposition. Such layer-by-layer coatings, using quantum dots, were utilized in the fabrication of luminescent photonic crystals.[41-44] However, these methods relied on the layer-by-layer deposition of quantum dots onto a colloidal suspension of microspheres, which were subsequently self-assembled into 3-dimensional photonic crystal.[41-44] No efforts have been made towards the layer-by-layer deposition of quantum dots onto a prefabricated 3-dimensional photonic structure.

Prior success (Chapter 2) with integrating organic fluorescent dyes into a multilayer coating provided motivation for the investigation of quantum dot integration into the dendritic amplification process (**Figure 48**). This process began with an initial surface functionalization of an aminosilane. Amine groups protruding from the surface were then reacted with a hyperbranched polyacrylate molecule, washed, then exposed to a solution of polyamine. Repeated exposures to polyacrylate and polyamine molecules, respectively, can yield approximately 3 nm of organic material per acrylate/amine layer.[88]

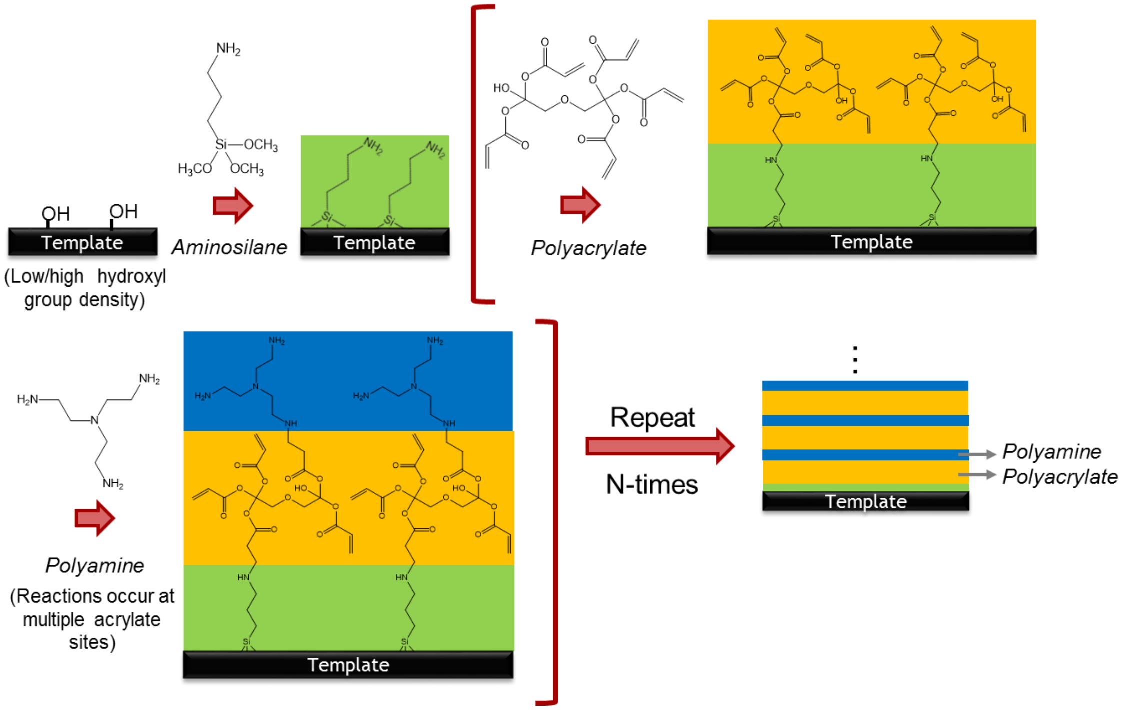

Figure 48. Schematic of the layer-by-layer dendritic amplification process. First, a hydroxyl-bearing surface is functionalized with an aminosilane. Subsequent layers are then iteratively deposited, via alternating exposure to polyacrylate and polyamine bearing solutions.

Prefabricated quantum dots are of specific interest for this work for increased photostability, relative to organic fluorescent dyes, and due to the wide variety of tailorable surface chemistries and emission wavelengths.[45] Control of particle size and composition are two means of changing the quantum dot fluorescent emission wavelength.[45] Amine-terminated quantum dots were selected, in order to take advantage of the Michael addition reaction [79, 80] utilized in the dendritic amplification process.

M. rhetenor blue scales were used as the coating template due to the intense reflection and relatively angle-independent coloration.[32-40] The photonic properties of these scales are well studied.[32-40, 89, 90] In addition, no reports exist describing fluorescent emission from these butterfly scales, making such scales attractive for exploring induced artificial fluorescence and structural color alteration. The chitin multilayers found within a single ridge structure (*i.e.,* lamella, highlighted in **Figure 49 (d, inset)**) produce the vibrant blue/green scale coloration through interference and diffraction (**Figure 49 (a, b)**).[36, 39, 40, 89] An absorber, thought to the melanin, is primarily concentrated in the scale base with the function of reducing the long wavelength reflection from the scale.[39, 40, 89, 90] The brown coloration of the scale oriented ridge side down ((**Figure 49 (c)**)) is a result of such absorption.[39, 40, 89, 90] Numerous other scale features (*i.e.,* offset lamella, irregular ridge height, tapered ridge tip, and ridge tilt) provide spectral contributions and/or broaden the angular reflectance of the scale.[32-40]

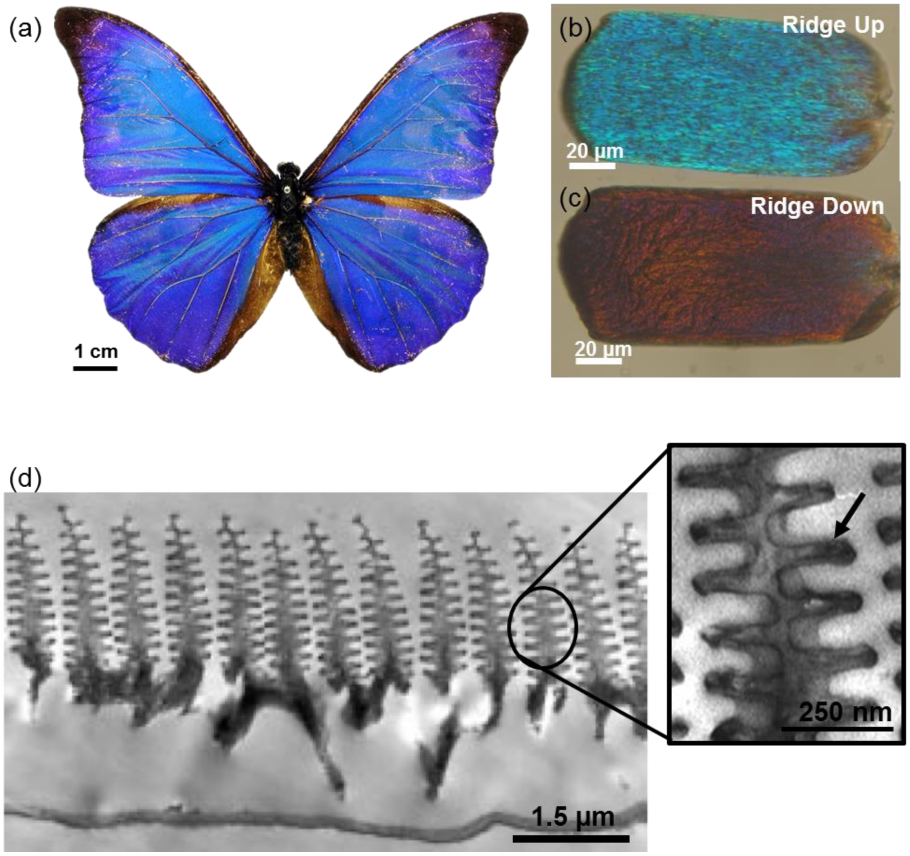

Figure 49. Optical and TEM images of the butterfly, *Morpho rhetenor*. (a) Optical image of the *M. rhetenor* butterfly © Smithsonian Institution National Museum of Natural History. Optical images of the iridescent blue scale responsible for the overall scale coloration, oriented (b) ridge-up and (c) ridge down. Coloration is dominantly structural in origin for scales oriented ridge-up. Ridge down orientation color is primarily due to an absorbing pigment at the scale base. (d) TEM image [39] of the scale cross-section showing the intricate, multilayer ridge structure, responsible for the overall blue coloration. (Inset) Higher magnification of the ridge structure with black arrow indicating the position of an individual lamella. (TEM images courtesy P. Vukusic)

The goal of this study was to analyze how tailored emissive and reflected coloration can be achieved on a prefabricated optical template. Specifically, the color mixing between the emitted light from prefabricated quantum dots, and reflected coloration, from the coated *M. rhetenor* template, was explored as a function of illumination sources. Additionally, the extent of induced emission intensity and reflectance alteration were both studied as a function of the number of applied coatings.

3.4 Experimental Procedures

3.4.1 Characterization of as-received quantum dots

Amine-functionalized quantum dots (Crystalplex, PA, USA) were received as a colloidal suspension (25 mg/mL) in water (1 mL total volume).

All Transmission Electron Microscopy (TEM) analyses were performed using a FEI Tecnai F30 microscope, 300 kV (FEI, OR, USA) by Dr. Ye Cai, Sandhage Group, Georgia Institute of Technology. The elemental composition of the quantum dots was confirmed with TEM-based EDS analyses (**Figure 53 (a)**). The nanoparticle TEM sample was prepared by immersing and withdrawing a copper TEM grid (300 mesh, Model: HC300-Cu, Electron Microscopy Sciences, PA, USA) in a 0.010 mg/mL solution of quantum dots in 20 vol% tetrahydrofuran (THF, anhydrous, ≥ 99.9%, Sigma Aldrich, MO, USA) in water (18.2 MΩ·cm, Milli-Q ultrapure, EMD Millipore, MA, USA). The specimen was dried under flowing, room temperature air for 20 minutes.

As-received quantum dots were diluted for in-solution optical analysis (courtesy of Dr. Vincent Chen, Perry Group, Georgia Institute of Technology) to a final concentration of 0.010 mg/mL in 20 vol% THF and 80 vol % 18.2 MΩ·cm water. Absorption measurements, using a Shimadzu UV-vis-NIR spectrometer (Model UV-3101PC, Shimadzu, Kyoto, Japan) instrument, were acquired from a quantum dot solution dispersed in a 1 mm path length quartz cuvette. Fluorescence emission from the same solution was characterized using a Horiba Fluorlog 3 instrument (Jobin Yvon, NJ, USA) using 336 nm excitation with 4 nm-slit widths in a 1 cm path length quartz cuvette.

3.4.2 Methodology for quantum dot multilayer coatings on *M. rhetenor*

Morpho rhetenor butterflies and all dendritic amplification precursors were purchased and used as described in Chapter 2. All precursor deposition reactions were applied at room temperature using petri dishes as incubation chambers and a custom glass funnel/stopcock for all washing steps (described in Chapter 2). Quantum dot solutions were diluted to 0.100 mg/mL in a solution of 20 vol% THF in 18.2 MΩ·cm water. A THF/water solution was necessary to enable the wetting of the butterfly scale.

Figure 50 details a schematic of the layer-by-layer coating process. The dendritic amplification process started with a single layer of aminosilane (N^1-(3-Trimethoxylsilylpropyl)diethylenetriamine, Technical grade, Sigma Aldrich, MO, USA). The aminosilane solution was diluted to 20 vol% in ethanol (200 proof, anhydrous. Koptec, PA, USA). Subsequent layers were applied by iterative, alternating exposure to solutions with a polyacrylate (Dipentaerythritol penta-/hexa-acrylate, Sigma Aldrich, MO, USA) and a polyamine (Tris(2-aminoethyl)amine, 96%, Sigma Aldrich, MO, USA), respectively. Both polyacrylate and polyamine solutions were prepared at 10 wt%, each, in ethanol. The butterfly scale surface was terminated with the polyacrylate prior to amine-functionalized quantum dot deposition. The wing sections were then thoroughly washed with approximately 30 mL of ethanol in a custom stopcock and then dried under flowing nitrogen (ultra high purity, Airgas, PA, USA) for 3 minutes. This drying step prior to quantum dot deposition is necessary to prevent the colloidal suspension from destabilizing due to ethanol contamination. Wing sections were removed from the petri dish after drying and placed in a 15 mL centrifuge tube (VWR International, PA, USA) with the quantum dot solution (1 mL quantum dot solution for every 1 x 1 cm of butterfly wing). The wing sections and quantum dots were incubated with gentle rocking on a rocker table (Model 260350, Boekel Scientific, PA, USA). A custom glass funnel/stopcock (**Figure 35**) was used for rinsing of the quantum dot-functionalized butterfly scales. Approximately 50 mL of 20 vol% THF in water was used for removal of excess, unbound quantum dots, followed by 30 mL rinse with ethanol. Subsequent dendritic amplification layers were applied, as previously described, starting with a polyamine layer to react to remaining surface acrylate groups. Incubation times for all steps were as follows: 10 minutes for the aminosilane, 1 hour for the polyacrylate, 10 minutes for the polyamine, and 3 minute for quantum dot exposures, respectively.

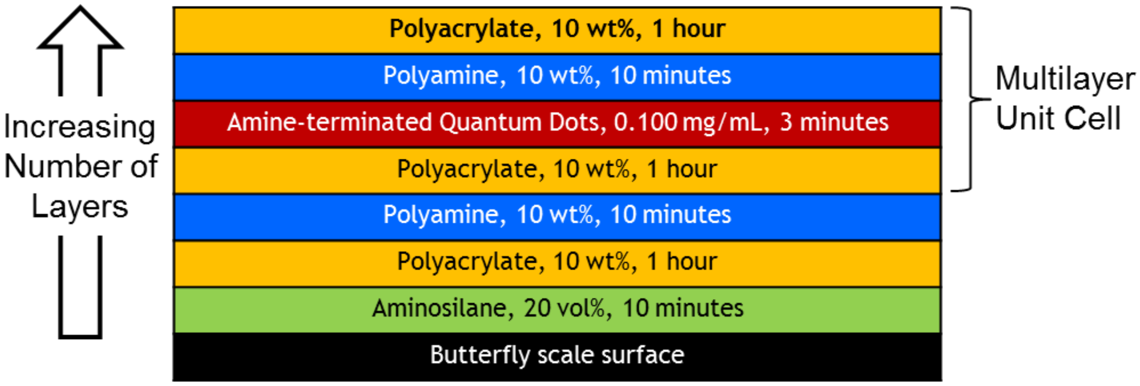

Figure 50. Coating schematic for covalent quantum dot multilayers on the scales of the *Morpho rhetenor* butterfly. Scale reflectance and induced fluorescence were studied as a function of iterative quantum dot multilayer unit cells.

The number of quantum dot layer-by-layer unit cells (**Figure 50**) was iteratively increased to study the effects of such increase coating on scale reflectance and induced fluorescent emission. Samples removed for optical and structural characterization were stored, dispersed as single scales on a glass slide, held within a petri dish with a strip of carbon tape (VWR International, PA, USA), wrapped in aluminum foil, and stored under ambient laboratory conditions. Samples intended for further coating were terminated with polyacrylate and dried under flowing nitrogen for 3 minutes. These samples were placed in a polystyrene petri dish (VWR International, PA, USA), wrapped in aluminum foil, placed in a Ziploc® bag, and stored in -20 ^{o}C freezer.

3.4.3 Optical characterization of quantum dot-functionalized *M. rhetenor* scales

Coated scales were removed from the wing membrane by gently brushing the coated wing section with a soft, nylon bristle paintbrush (McMaster Carr, GA, USA) onto an as-received glass microscope slide (Catalog number: 16004-418, VWR International, PA, USA). The brush was thoroughly cleaned before and after every contact with a given wing section by blowing the bristles with nitrogen. Tapping the brush on the surface of a clean glass slide, followed by visual observation, validated that scales were no longer entrained within the brush. The glass slide was stored in a 100 x 15 mm petri dish (VWR International, PA, USA) with a square of carbon tape (Ted Pella, CA, USA) to keep the slide position fixed. All petri dish-containing samples were wrapped in aluminum foil and stored until optical characterization was performed. Storage in aluminum foil helped mitigate any photoluminescent enhancement effects [91] of the quantum dot emission, prior to optical characterization.

Optical measurements were performed using an Olympus BX60 (Olympus America, Inc., PA, USA) upright microscope. Spectral measurements were acquired with a SEE 1000 microscope spectrometer (SEE Science, MA, USA) attached to the microscope camera port with software from Craic Technologies (Version 4.3.1, Craic Technologies, CA, USA).

Single scale reflectance measurements were acquired using an Olympus MPlan N 20 x objective (0.40 numerical aperture) relative to a diffuse reflectance standard (WS-1-SL, Ocean Optics, FL, USA), illuminated by a halogen lamp (Olympus

America, Inc., PA, USA). The illumination spectrum for this lamp is shown in **Figure 51**. The measurement spot size was approximately 14 µm x 14 µm. Y-axis intensity values are reported in arbitrary units (A.U.), rather than percent reflectance relative to the standard, to account for differences in light scattering between the reference standard and the butterfly scale.[92] Single scale fluorescence spectra were acquired with an Olympus MPlan FL N 50 x objective (0.80 numerical aperture) using a 6 µm x 6 µm spot size. The resulting emission spectrum was the measured signal minus the dark current (*i.e.*, references were not used for emission measurements). All fluorescence imaging and spectra were acquired using mercury lamp illumination (HBO 100 W lamp, Universal Arc Lamp Power Supply # 99030, SEE Science, MA, USA) in combination with a fluorescent filter cube (Chroma Technologies, VT, USA). Excitation light was filtered to transmit 325 – 375 nm (full width at half maximum) and the emission filter enabled light transmission above 425 nm (half-maximum wavelength). The dichroic mirror half-maximum wavelength was 415 nm. All imaging was performed with a 20 x objective using a Nikon D300 (Nikon USA, NY, USA) camera (Manual, ISO 200, automatic white balance). The camera was attached to the camera port of the microscope with a microscope adapter (MM-SLR, Martin Microscope, SC, USA). The error of 6 nm (as one standard deviation) was used to account for reflected peak wavelength uncertainty for coated *M. rhetenor* scales from separate wing sections on the same butterfly (Chapter 2, **Figure 36**).

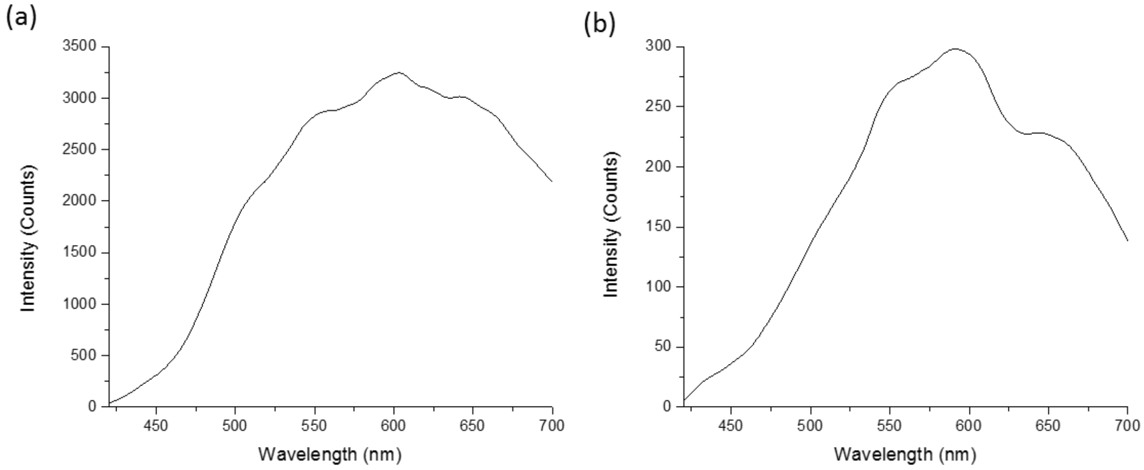

Figure 51. Lamp spectra for halogen lamps used in reflection analyses. (a) Lamp spectrum for microscope halogen lamp used for reflectance measurements as a function of the number of applied layers. (b) Lamp spectrum for external stereomicroscope light source used in color mixing experiments.

All statistical information is presented as an average with error bar ranges as ± one standard deviation. 18 separate reflection measurements (6 separate scales, with 3 measurements within each scale) were performed to determine the peak wavelength of coated scales. Single scale emission measurements were measured from 6 separate measurements on 6 separate scales, unless otherwise noted. Multiple measurements on a single scale were avoided to mitigate intensity variation due to photoluminescent enhancement. A 6 nm error bar was used in the event that one standard deviation was smaller than 6 nm to better represent the uncertainty in comparing peak reflection of scales from multiple, separate, coated wing sections. A single replicate coating experiment was performed, which validated the trends observed with emission intensity increase and red shifted reflectance with the number of applied layers (**Appendix D, Figure 75 (c, d)**).

Spectral and imaging analysis of combined emitted light from the quantum dots and the reflected coloration for the structurally colored scales of the coated *M. rhetenor* butterfly were obtained by using the experimental set-up in **Figure 52**. An objective with a long working distance and high numerical aperture were necessary for the delivery of external white light and the collection of light reflected from the scales. An Olympus LMPLFLN 50 x objective, with a numerical aperture of 0.50 and a 10.6 mm working distance was used for this measurement. UV excitation was provided through the mercury lamp (peak emission of 365 nm) of the microscope filtered through a fluorescence filter cube (excitation filter: 325 – 375 nm FWHM, dichroic mirror: 415 nm, and emission filter: 425 nm). White light illumination (**Figure 51**) was provided by a stereomicroscope light source (XD-301 series halogen cold light source, Alltion, Guangxi, China). Emission-only spectra were collected as fluorescence spectra (*i.e.*, signal minus dark current). Reflection spectra and the combined emission and reflection spectra were both collected with a reference spectrum obtained from a diffuse reflectance standard, unique to each illumination condition. The resulting spectra are averages of 6 separate measurements for each illumination condition with ± one standard deviation as the error range.

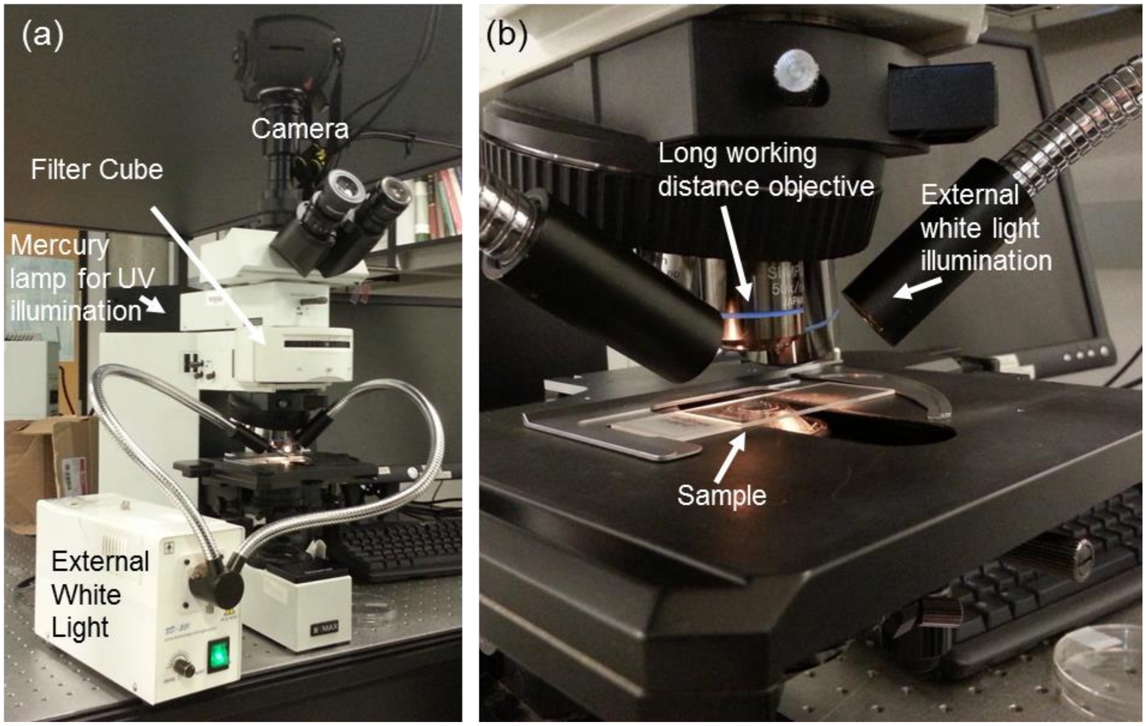

Figure 52. Experimental set-up for color mixing analyses of quantum dot-functionalized butterfly scales. (a) Overall system arrangement revealing the placement of the mercury lamp (at the back of the microscope) which was filtered with the fluorescence filter cube used for emission analysis on quantum dot-functionalized butterfly scales. White light was introduced, externally, through a stereomicroscope light source. (b) Detail of the sample placement and optical stage. A long working distance objective with high numerical aperture (50 x, 10.6 mm working distance, 0.50 numerical aperture) was necessary for imaging of a single butterfly scale under external white light illumination.

3.4.4 Structural characterization of quantum dot-functionalized *M. rhetenor* scales

Scanning electron microscopy (SEM) was performed using a Hitachi SU8010 microscope (Hitachi, Tokyo, Japan). Double-sided carbon tape was affixed to an aluminum SEM stub (Ted Pella, CA, USA) to serve as the sample holder. Single scales, dispersed on a glass slide were placed on the carbon tape by inverting the SEM aluminum stub and gently pressing down on the glass slide containing the dispersed single scales. Visual inspection after the removal of the aluminum stub confirmed that some scales were transferred to the carbon tape in both ridge-up and ridge-down orientations. This method provided a sufficient number of scales for SEM imaging and preserved the relatively limited amount of samples. Cross-sectional, HAADF TEM analysis was provided courtesy of Dr. Ye Cai (Sandhage Group, Georgia Institute of Technology). The butterfly wing section was prepared for TEM imaging by epoxy infiltration through a wing section sandwiched between two glass coverslips, followed by Ar-ion milling.

3.5 Results and Discussion

3.5.1 Quantum dot selection, as received characterization, and quantum dot multilayer process development

Reducing the dimensions of semiconductor materials to 10's of nm can result in quantum confinement effects, which can enable tunable energy gaps, and, thus, variable fluorescence emission.[45] Both size and composition can be used to modify the emissive properties of nanocrystalline particles.[45] The addition of a thin shell, of a wider band gap material than the core quantum dot material (*e.g.*, ZnS in the case of a CdSe core), has been shown to increase the fluorescence quantum yield and to help protect the quantum dot core from the surrounding environment.[45] Increases in fluorescence quantum yield occur through passivation of surface trap states (such as dangling bonds) by the shell material.[45] Overall, this reduces the number of non-radiative recombination pathways to the electron-hole pair generated within the core.[45] Such quantum dot designs (also known as Type I quantum dots [45]) are ideal for integration onto bioorganic nanostructures, due to the bright, stable, light emission of such quantum dots. Additionally, a variety of surface-functionalized quantum dots are commercially available (*e.g.,* carboxyl-, hydroxyl-, and amine-functionalities), which facilitate nanoparticle integration into a layer-by-layer dendritic amplification process.

The quantum dot elemental composition was qualitatively consistent with manufacturer's report of compositionally tuned, CdS_xSe_{1-x}/ZnS core/shell quantum dots

[45]. The peaks due to copper (**Figure 53 (a)**) were attributed to the sample holder. TEM imaging (**Figure 53 (a, b)**) confirmed that the particle size was near that reported by the manufacturer (5.5 – 6.5 nm). Scanning Transmission Electron Microscopy High Angle Annular Dark Field (STEM HAADF) images confirmed the core/shell structure of the as-received quantum dots. This method enables imaging of elemental distribution through contrast based on atomic number (*i.e.,* Z-contrast imaging). Quantum dot core materials, rich in Cd (Z = 48) appear brighter than the shell material containing Zn and S (Z = 30 and Z = 16, respectively). The color in the **Figure 53 (b)** corresponds to an intensity map, rather than an elemental map. Regions in the image with a white/yellow color correspond to a greater intensity (*i.e.,* higher atomic number). Blue regions correspond to a low intensity (*i.e.*, low atomic number).

The absorption measurements (**Figure 53 (c)**) revealed a broad absorption, increasing towards lower wavelengths, which was consistent with quantum dot suspensions.[45] Emission measurements (**Figure 53**) confirmed that the quantum dot fluorescence intensity maximum occurred near the peak wavelength reported by the manufacturer (measured: 625 ± 2 nm, reported: 630 ± 5 nm)

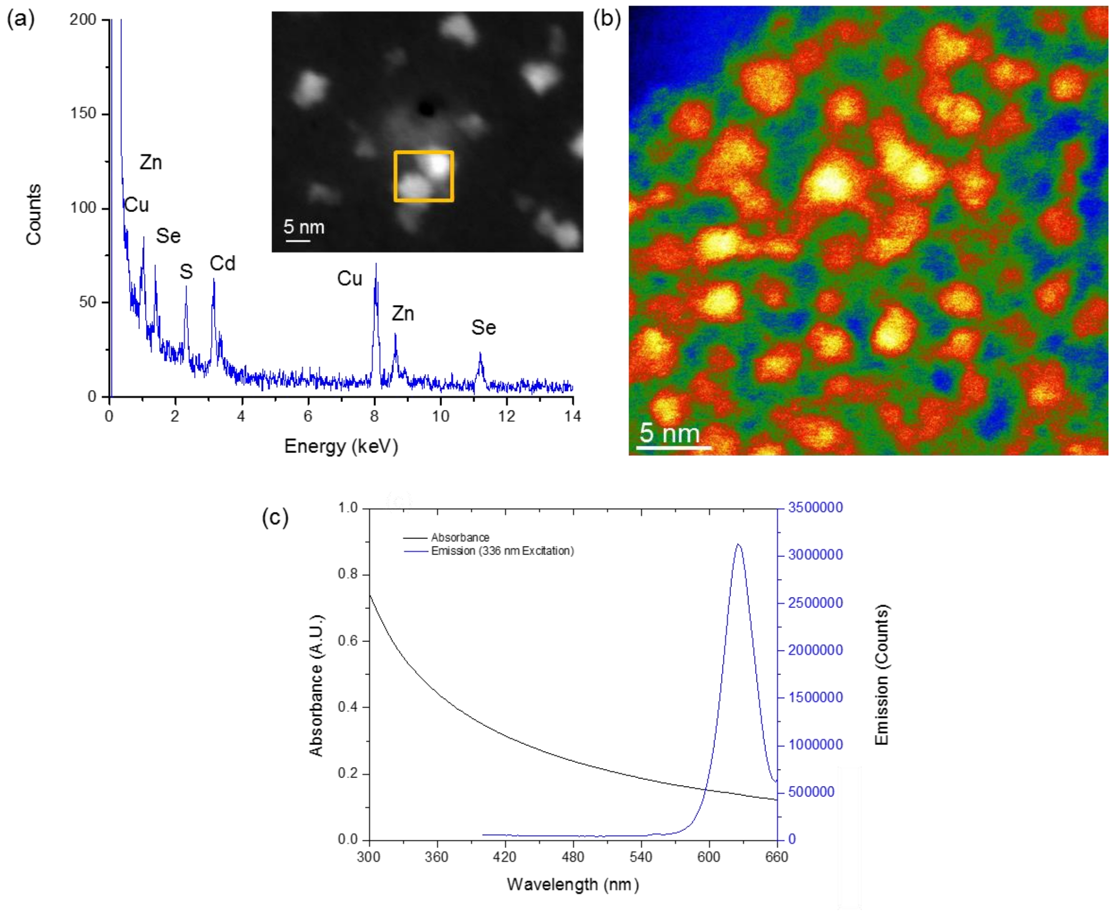

Figure 53. As-received quantum dot chemical, structural, and optical characterization. (a) Energy Dispersive X-ray Spectroscopy (EDS) of as-received quantum dots measured in a Transmission Electron Microscope (TEM). The copper peaks are due to the sample holder. Elemental composition is consistent with CdS$_x$Se$_{1-x}$/ZnS core/shell structure quantum dots.[45] (b) Z-contrast STEM image of quantum dots, confirming the presence of core/shell structured quantum dots. Quantum dots were approximately the same size as reported by the manufacturer (5.5 – 6.5 nm). All TEM analyses courtesy of Dr. Ye Cai, Sandhage Group, Georgia Institute of Technology. (c) Absorption and emission measurements of in-solution quantum dots 0.010 mg/mL in 20 vol% THF in water (average of 3 separate measurements). A broad absorption was observed and is characteristic of quantum dot suspensions. The measured peak emission (625 ± 2 nm) was near that reported by the manufacturer (630 ± 5 nm). In-solution quantum dot optical analyses courtesy of Dr. Vincent Chen, Perry Group, Georgia Institute of Technology.

Amine-functionalized quantum dots, with a fluorescence peak emission centered at 625 ± 2, nm were selected for multilayer integration (**Figure 54**). Amine groups were easily integrated into the dendritic amplification chemistry through a Michael addition reaction.[88] The *M. rhetenor* scale exhibits a region of low reflectivity from approximately 560 – 700 nm due to absorption inherent to the scale material (**Figure**

54).[39, 40, 89, 90] Red-emitting quantum dots were selected to add a fluorescence coloration, so that color mixing between the reflected/emitted colorations could be explored on this structurally colored template. Emission within this spectral region could significantly alter the reflection of the coated *M. rhetenor* scales.

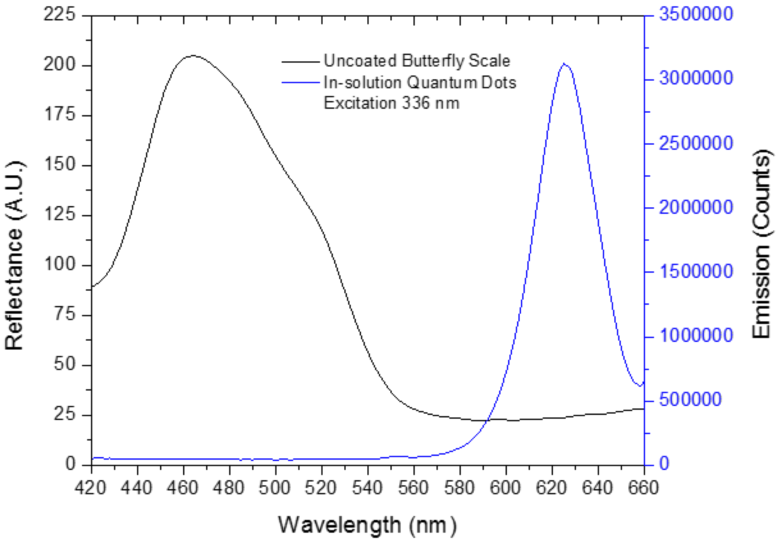

Figure 54. Reflection spectrum (left, black) from uncoated *M. rhetenor* scales with a peak reflectance at 464 ± 5 nm. Long wavelength reflectance is relatively low due to absorption from the scale material.[39, 40, 89, 90] Emission spectra (right, blue) for in-solution quantum dot suspension 0.010 mg/mL with a peak emission at 625 ± 2 nm. The addition of emissive color in the long wavelength region could significantly alter the color of the scale. (In solution analyses of quantum dot emission courtesy of Dr. Vincent Chen, Perry Group, Georgia Institute of Technology).

3.5.2 Quantum dot monolayer emission study

A quantum dot monolayer was deposited onto a *M. rhetenor* blue scale after an initial dendritic amplification deposition process, to validate the reported photostability [45] and successful covalent functionalization of amine-bearing quantum dots to the acrylate-terminated butterfly scale. Imaging and emission measurements for an uncoated scale are shown for comparison (**Figure 55 (a, c)**). A schematic illustrating the layer-by-layer surface functionalization process is shown as an inset to **Figure 55 (b)**. Both uncoated and functionalized scales were illuminated with UV light filtered from a mercury lamp (excitation: 325 – 375 nm band pass, emission: 425 nm long pass) and spectra were collected in 30 s increments to explore the quantum dot time-dependent emission. A weak emission, peaked at 507 ± 3 nm, was collected from the uncoated scales. All spectral acquisition (**Figure 55**) was performed on the same spot for each scale (*i.e.*, coated and uncoated). The emission image series were acquired on the same scale, but not on the exact scale from which emission spectra were obtained. The use of separate scales between the spectra collection and image collection was necessary to properly characterize the time-dependent emission phenomena over the desired time interval. This behavior (**Figure 55**) was consistent across all measured uncoated scales. The emission intensity rapidly decreased, reaching an approximately 60 % decrease in intensity after 10 minutes of light exposure.

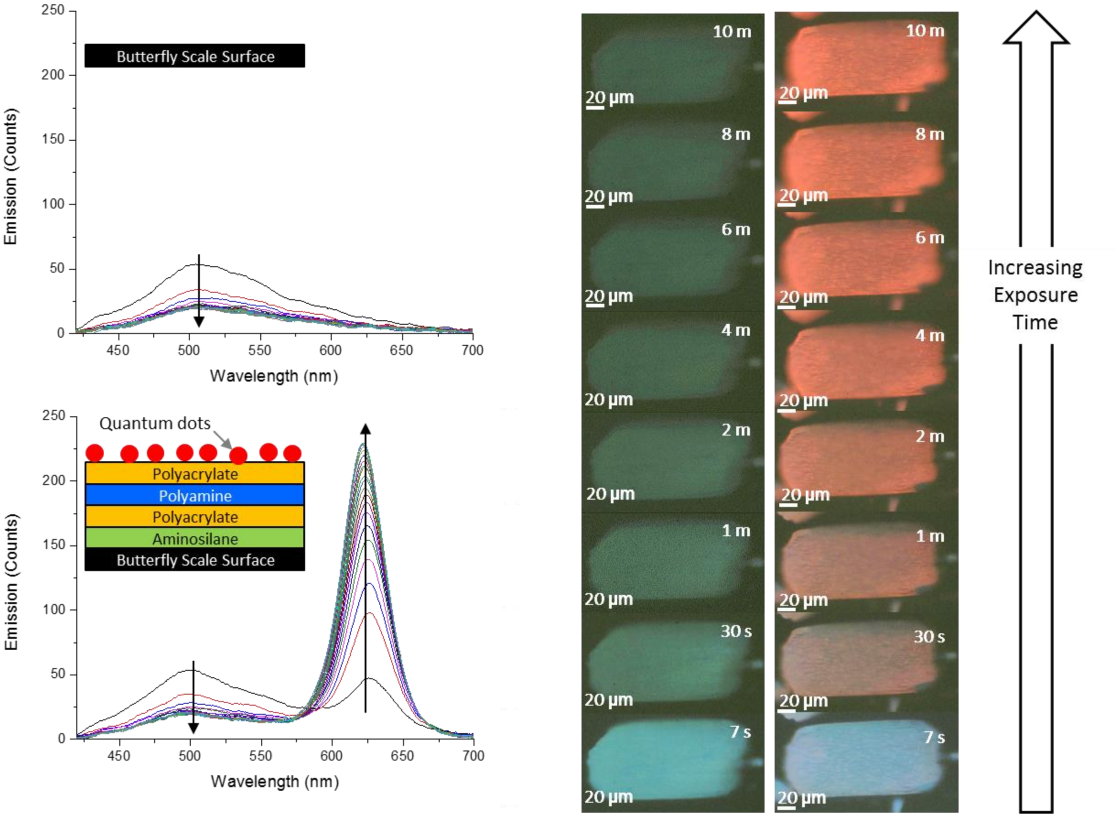

Figure 55. Emission spectra collected in 30 s increments for a total of 630 s for (a) an uncoated butterfly scale and (b) single quantum dot monolayer functionalized scale. Black arrows indicate the trend in the spectral changes with increasing illumination time. Emission intensity decreases relatively quickly for uncoated scales, reaching 60 % decrease in emission intensity over 10-minutes of exposure. Quantum dot-functionalized scales experience approximately 387 % increase in emission intensity after a 10-minute exposure period. Time-series optical images for both (c) uncoated and (d) coated butterfly scales.

Quantum dot-functionalized scales demonstrated an approximate 400 % increase in emission intensity (624 ± 3 nm) as the illumination time increased. The increase in emission intensity with increased exposure time (also known as photoluminescent enhancement) is a well reported phenomena within the quantum dot research community.[91] Several authors suggest that there is a dark fraction of quantum dots which are “activated” by photoinduced changes to defects within or on the quantum dot surface.[91] This dark fraction has been reported for both surface-functionalized [93] and in-solution [94] quantum dots. Defects within the quantum dot, or on the quantum dot surface, may act as sites for non-radiative recombination [91] so that the quantum dot is non-emitting (*i.e.*, dark).[91] Various mechanisms could be responsible for removing such defects: photo-annealing, photo-etching of surface dangling bonds, or ligand rearrangement.[91] Determination of the exact mechanism of photoluminescent enhancement is still an active area of research.[91]

Fluorescent multilayers using organic fluorescent dyes (**Chapter 2**) displayed photobleaching behavior (*i.e.,* a decrease in the emission intensity with increasing exposure time). Measurements were performed as quickly as possible (approximately 5 – 10 s) to best minimize intensity variations due to excitation light exposure. Conversely, the quantum dot emission increased over time, necessitating methodology development for characterizing the emission intensity increase with the number of quantum dot layers, without a significant time dependent contribution.

Five separate samples were measured in 30 second intervals for a total of 10 minutes, with each sample functionalized with a quantum dot monolayer (**Figure 55 (b)**). The emission intensity began to plateau after the first 180 s of excitation light exposure (**Figure 56 (a, b)**). The same behavior was observed for all 5 measured samples (**Figure 56 (a, b)**) with some scale-to-scale intensity variation. The error due to sample-to-sample variation is much greater than the error due to time-dependent emission after approximately 300 s of light exposure. Sample-to-sample variation could be normalized by tracking the percentage increase in emission intensity as a function of exposure time (**Figure 56 (c, d)**). These results show that the time-dependent signal was minimized after approximately 300 s of exposure to the excitation light. A cut-off value, of 2 % increase in emission intensity over 2 minutes (*i.e.,* 4 separate measurements), was defined from these measurements so that the non-time-dependent emission intensity increase due to the number of quantum dot-containing multilayers could be investigated.

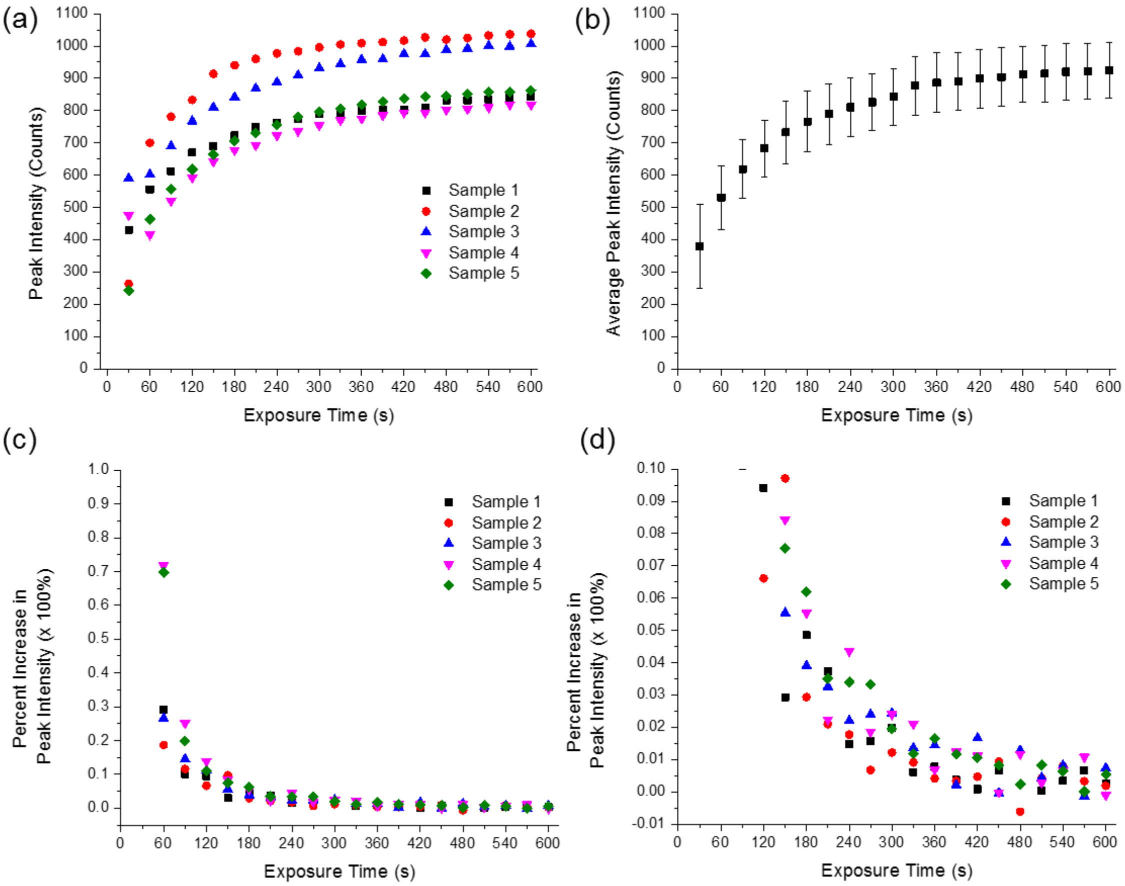

Figure 56. Characterization of the time-dependent emission intensity increase for a quantum dot functionalized butterfly scale. The peak intensity is plotted as a function of exposure time for (a) all five measured samples and the (b) average intensity change. Tracking the percent increase in emission intensity normalizes sample-to-sample variation (c, d). The time dependence for emission intensity was relatively minor after 300 s of light exposure. A change of 2 % or less over a period of 4 minutes was used as a cut-off value for evaluating time-independent quantum dot multilayer measurements.

3.5.3 Fluorescence characterization of quantum dot multilayers on *M. rhetenor* scales

The emission intensity increase as a function of the number of quantum dot multilayers was investigated for functionalized *M. rhetenor* scales. Amine-functionalized quantum dots were deposited onto acrylate-terminated surfaces. After washing, the scales were incubated in a solution of polyamine, to bond to any remaining, sterically accessible, surface acrylate groups. Subsequent layering of polyacrylate and then polyamine continued. A schematic illustrating the quantum dot multilayer functionalization process is shown as the inset in **Figure 57 (a)**. Spectral measurements and imaging confirmed that the emission intensity increased with the iterative deposition of quantum dot-containing layers, up to 10 multilayer unit cells. Images were acquired after 10 minutes of light exposure.

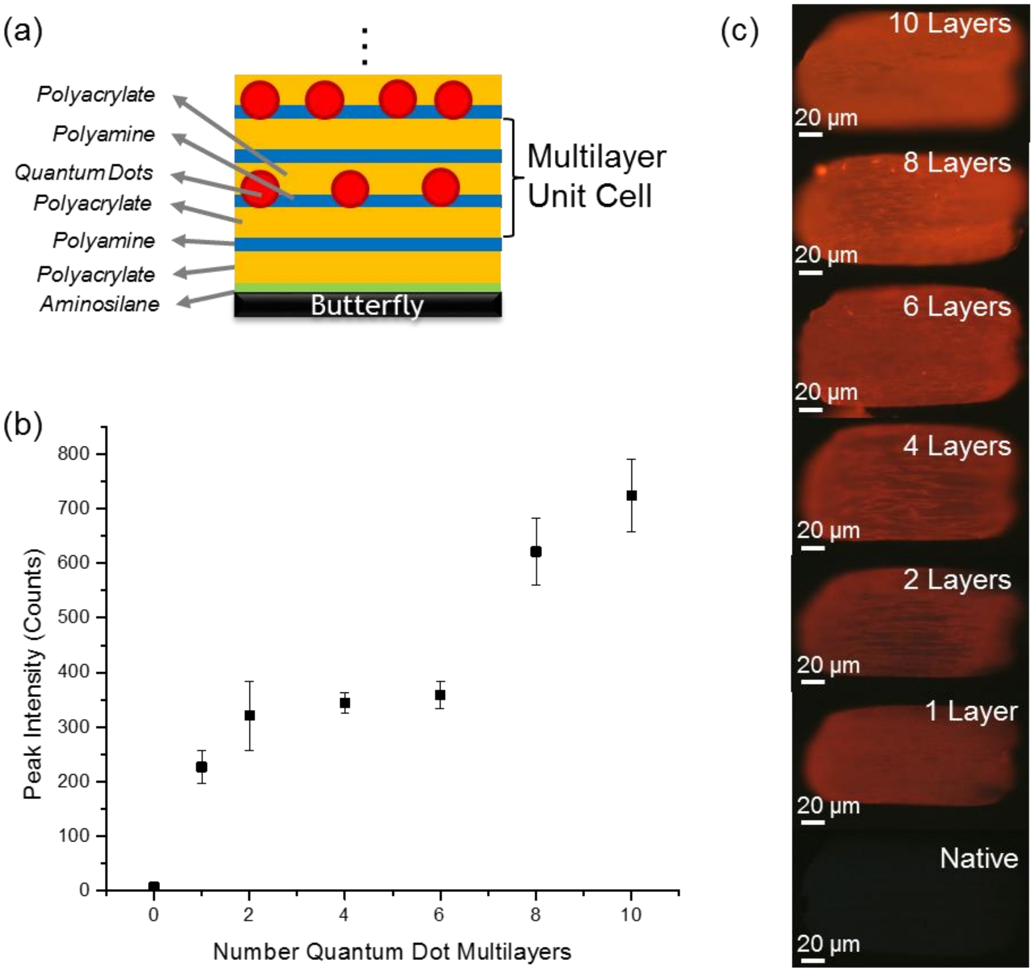

Figure 57. Fluorescence intensity increase with iterative deposition of quantum dot containing layers onto the scales of *M. rhetenor*. (a) Schematic illustrating quantum dot multilayer deposition. (b) Average emission intensity as a function of the number of quantum dot-containing layers. Time-dependent emission intensity was tracked as a function of time until a percent change of 2% or less was maintained after 2 minutes (4 measurements). (c) Images of functionalized scales after 10 minutes of light exposure. All spectra and peak intensity values were averaged from 6 separate measurements on separate scales with ± one standard deviation as the error.

3.5.4 Reflectance characterization of quantum dot multilayers on *M. rhetenor* scales

Individual reflectance spectra for coated samples are shown in **Figure 58**. The relatively blue scale coloration (**Figure 58, insets**) was maintained for cycles 1, 2, and 4, becoming progressively greener, and darker, for cycles 6 and 8. Finally, the reflected scale coloration was mostly gone by cycle 10. Spectra collected on cycles 2 and 4 display a considerable variation in peak wavelength within the range of 400 – 500 nm (**Figure 58**). The inter- and intra-sample variation was too great to define an average peak wavelength for these samples. Scale reflectance from cycles 6, 8, and 10-coated samples displayed a consistent spectral shape, each having two distinct peaks (**Figure 58)**. However, the relative intensity of each peak varied for cycles 6 and 8 (*i.e.*, the low wavelength peak may be higher for one measurement, but not another).

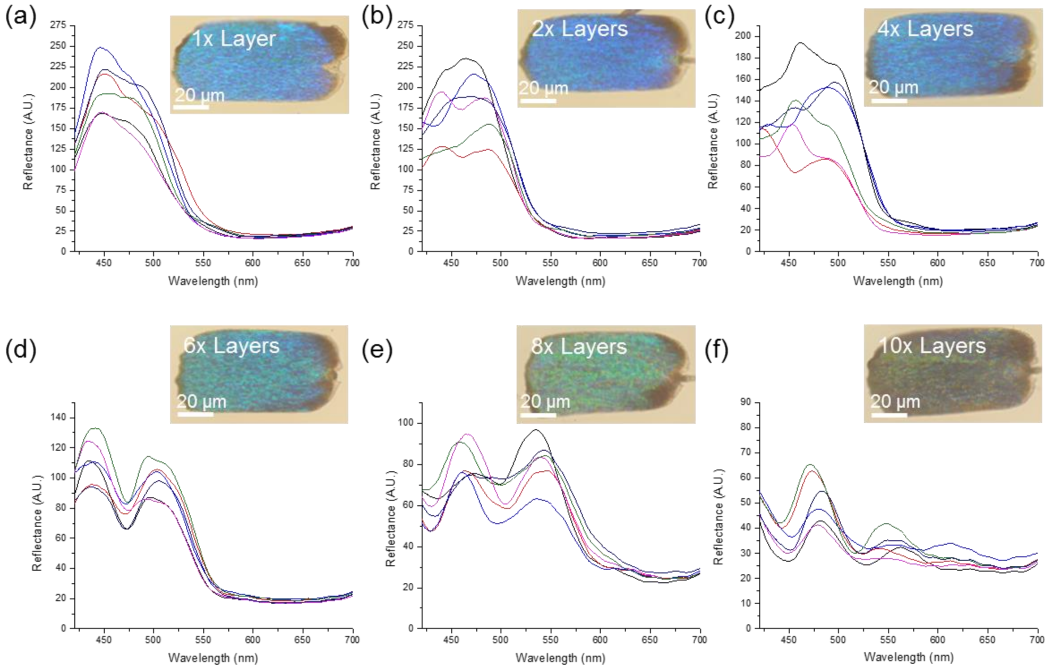

Figure 58. Individual reflection spectra and images for quantum dot-functionalized *M. rhetenor* scales: (a) 1 layer, (b) 2 layers, (c) 4 layers, (d) 6 layers, (e) 8 layers, and (f) 10 layers. A relatively blue coloration was preserved for layers 1 – 4. A gradual red shift was qualitatively observed for scales coated with 6 – 10 layers.

Figure 59 summaries the reflectance alteration of the quantum dot multilayer-coated *M. rhetenor* scales. All measurements are reported as averages, with ± one standard deviation as the error bar ranges, except for cycles 2 and 4. The peak wavelength values for these two samples represent the peaks found on the individual spectra displayed in **Figure 58** with error bars reported as the instrument error (*i.e.*, ± 3 nm). The various peak positions between 400 and 500 nm were consistent with the overall blue coloration observed from the optical images of the coated scales **Figure 58 (insets for b and c)**. An overall red-shift was observed as the number of layers increases for cycles 6 through 10, which was consistent with prior studies reflectance studies of layer-by-layer coatings for as-coated, butterfly scale structures.[27, 28]

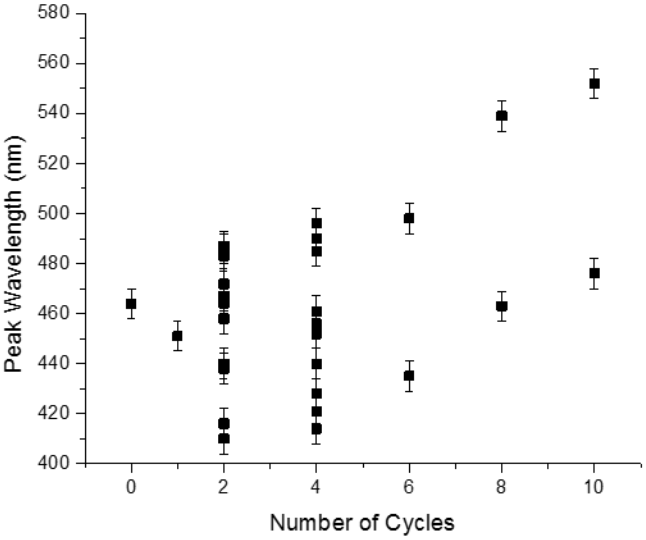

Figure 59. Summary of reflectance alteration of quantum dot coated samples as a function of number of coated layers. All samples are reported as averages (with ± 1 standard deviation error bar ranges), except for cycles 2 and 4. Peak positions from individual spectra are shown with the error in comparing scales from different areas of the butterfly wing (± 6 nm). A total of 18 spectra were averaged across 6 separate scales. Cycles 2 and 4 displayed considerable variation in peak position in the range of 400 – 500 nm. A gradual red shift was observed for both long and short wavelength peaks for cycles 6 – 10.

Quantum dot emission, peaked at 624 ± 3 nm, was not observed under white light illumination used for the reflectance measurements. It is unlikely that the quantum dot absorption spectrum (**Figure 53 (c)**) caused the creation of multiple peaks within the reflection spectra (cycles 2 – 10) as the spectral shape for the absorbance was broad and monotonically increased for shorter wavelengths. Reflectance alteration of the *M. rhetenor* scales using only dendritic amplification layers (*i.e.*, no quantum dots) was performed as a control experiment for the effect of layer-by-layer coatings on the template reflectance.

A net red shift in the reflection spectrum occurred with increasing number of dendritic amplification layers (**Figure 60**). A single peak was observed for cycles 3 – 15. A second peak began to appear at cycle 18 and gradually became more prominent for higher number of coating layers. The appearance of two prominent peaks for cycles 27 –

36 (**Figure 60**) was very similar to the results of cycles 6 – 10 for the quantum dot multilayer reflectance (**Figure 58**). This similarity in the appearance of two peak with the increase in number of applied layers (between dendritic amplification and quantum dot multilayers) may be due the red shift of a UV reflection for the uncoated *M. rhetenor* scale. Prior studies [39, 95] have demonstrated that *M. rhetenor* scales have a considerable amount of reflected light within the 300 – 400 nm wavelength range. Such reflected intensity could become more prominent, within the visible region, with the spectral red shift that occurs with the application of a sufficient number of applied multilayers.

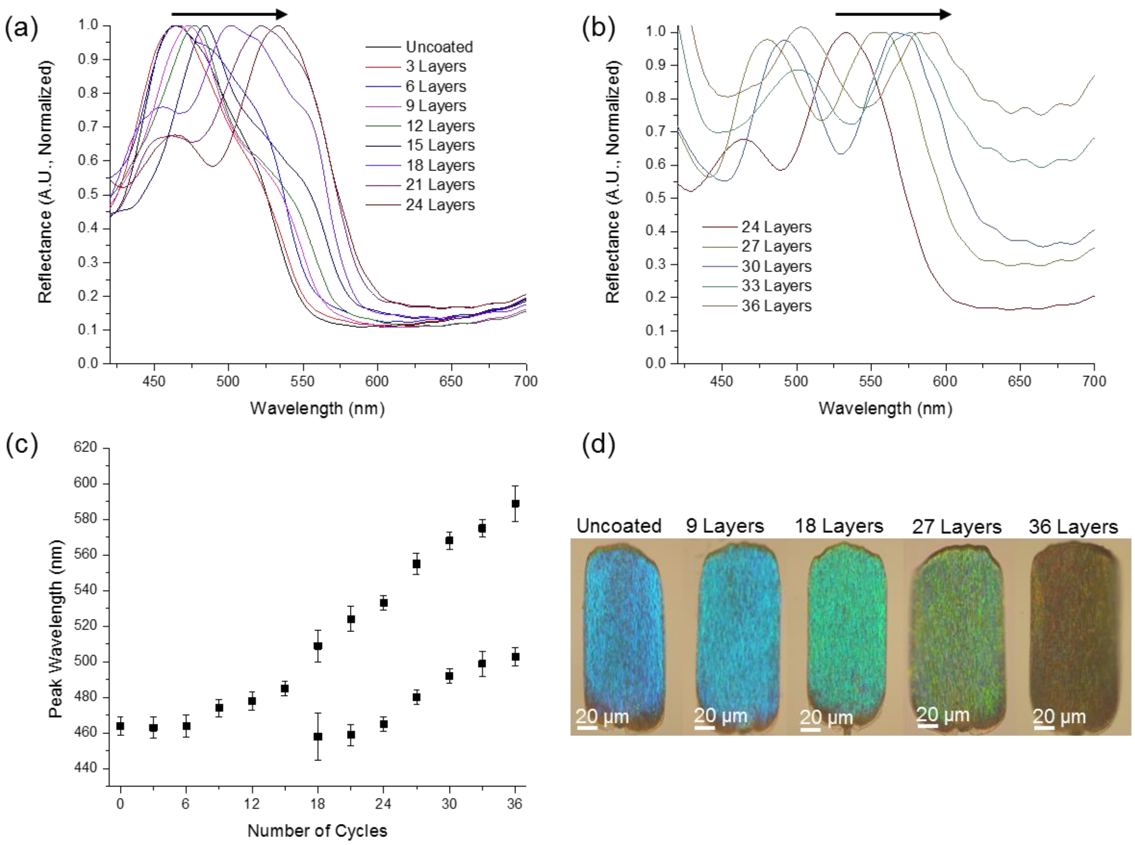

Figure 60. Reflectance alteration of *M. rhetenor* scales with dendritic amplification multilayers (*i.e.*, no quantum dots). (a) Averaged reflection spectra for uncoated scales and coated scales (cycles 3 – 27). (b) Individual spectra for cycles 27 – 36 displayed a gradually more prominent short wavelength peak, in addition to the long wavelength peak. (c) Summary of the peak wavelength shift as a function of number of applied layers, displaying an overall red shift. (d) Bright field optical images for uncoated, 9, 18, 27, and 36 layers. All spectra and peak wavelength values were averaged from at least 18 separate measurements with 3 measurements on each scale with ± one standard deviation as the error.

A net red shift in the reflection spectrum was observed for quantum dot-coated scales (**Figure 59**) as well as scales coated with only dendritic amplification layers (**Figure 60**). Refractive index and filling fraction contributions of both films are the likely sources of this red shift, assuming the structure did not shrink or expand due to the application of coating layers.[96, 97] The refractive index of uncoated scales was 1.56.[39] The exact refractive index of the CdS$_x$Se$_{1-x}$/ZnS core/shell quantum dots used in this study is unknown. However, bulk CdS, CdSe, and ZnS have a relatively high (compared to the uncoated scale) refractive index values of approximately 2.53, 2.760, and 2.388, respectively.[98] The host matrices (*i.e.*, dendritic amplification layers) have refractive indices of 1.46, 1.49, and 1.50 for the aminosilane, polyacrylate, and polyamine, respectively. All refractive index values were obtained from chemical documentation provided by Sigma Aldrich, MO, USA.

3.5.5 Combined reflected and emitted coloration from quantum dot-functionalized *M. rhetenor* scales

Control over scale color through changing the illumination source was of particular interest for this work. The high reflectivity of the structurally colored template [32-40], combined with the spectral separation of the coated scale reflectance peak and the quantum dot emission created a synergy between the template and the applied fluorophore for such a color mixing effect. Also, the photoluminescent enhancement demonstrated by the quantum dots functionalized to the *Morpho* scales provided an additional benefit for the stable, intense fluorescent emission. Qualitative coloration as well as quantitative spectra were obtained from a scale coated with 6 quantum dot layers under only UV excitation, white light only, and combined white light and UV excitation (**Figure 61**). A sample with 6 quantum dot-containing layers was selected for this analysis, as it was the best compromise between reflected coloration and emitted intensity. These results demonstrate the combined coloration through emissive and reflected light under simultaneous UV and white light. Spectral analysis demonstrated the preservation of both the emitted and reflected spectra under the combined illumination of intense UV and white light. The individual emission and reflection spectra were preserved under only UV excitation and white light-only illumination, respectively.

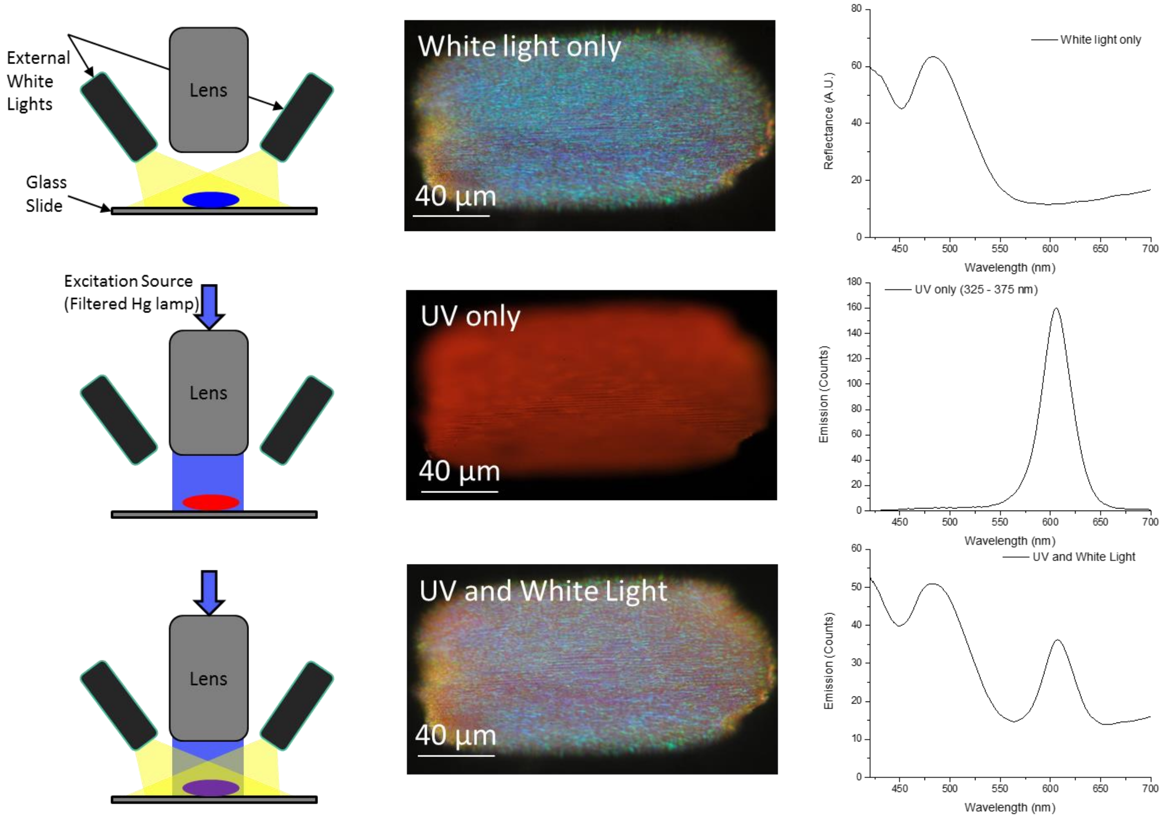

Figure 61. Color mixing between the emitted light from quantum dots and the reflected light from a scale coated with 6 quantum dot-containing layers. A relatively blue color was observed under white-light only illumination and a red emission was visible under UV-only illumination. The simultaneous UV and white light illumination resulted in the mixing of both emitted and reflected coloration.

3.5.6 Structural characterization of quantum dot multilayers on *M. rhetenor* scales

The surface polarity gradient discovered [95] throughout the thickness of the ridges in *Morpho* butterflies may affect the film continuity due to a spatially varying surface chemistry. However, Scanning Transmission Electron Microscopy High Angle Annular Dark Field (STEM HAADF) images confirmed the quantum dot film conformally coated the *Morpho rhetenor* nanostructure after the application of 10 layers. HAADF imaging (courtesy of Dr. Ye Cai, Sandhage Group, Georgia Institute of Technology) was used because it enabled high contrast between the quantum dot-containing film (*i.e.,* high atomic number) and the epoxy / butterfly scale chitin (*i.e.,* low atomic number). Low magnification images detail numerous ridges with a conformal coating of quantum dot multilayers (*i.e.,* the white outline) (**Figure 62 (a)**). Individual quantum dots were observed under high magnification (**Figure 62 (b)**). The quantum dot host-matrix (*i.e.,* dendritic amplification layers) could not be distinguished from the chitin or epoxy due to similar atomic constituents (*i.e.,* low atomic number elements, such as carbon, oxygen, and nitrogen). Measurements acquired from a series of STEM images approximate the overall film thickness as 35 ± 10 nm for this 10-layer coated sample (measurements acquired from 2 images, with a total of 65 individual measurements).

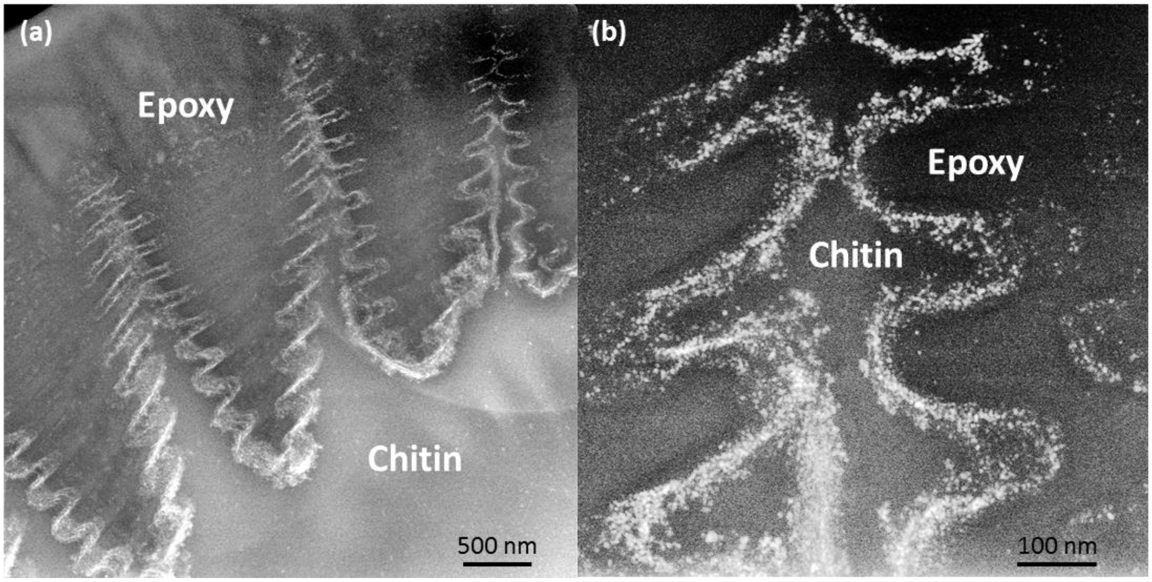

Figure 62. Scanning Transmission Electron Microscopy High Angle Annular Dark Field (STEM HAADF) imaging of a single butterfly scale coated with 10 quantum dot-containing layers. (a) Low magnification image showing the conformal coating across multiple, hierarchically structured ridges. (b) High magnification image of a single ridge section detailing the deposition of individual quantum dots.

Secondary electron images (**Figure 63**) for selected samples demonstrated that the overall butterfly scale structure was preserved throughout the coating process up to, and including, 8 quantum dot-containing layers. Intermediate magnification images reveal the preservation of individual ridges, and high magnification images show individual lamella on a single ridge. Comparison between the uncoated butterfly scale and cycle 1 show very little qualitative change. Visible roughness/particles for the film began to appear at cycle 4 and increased for higher number of cycles.

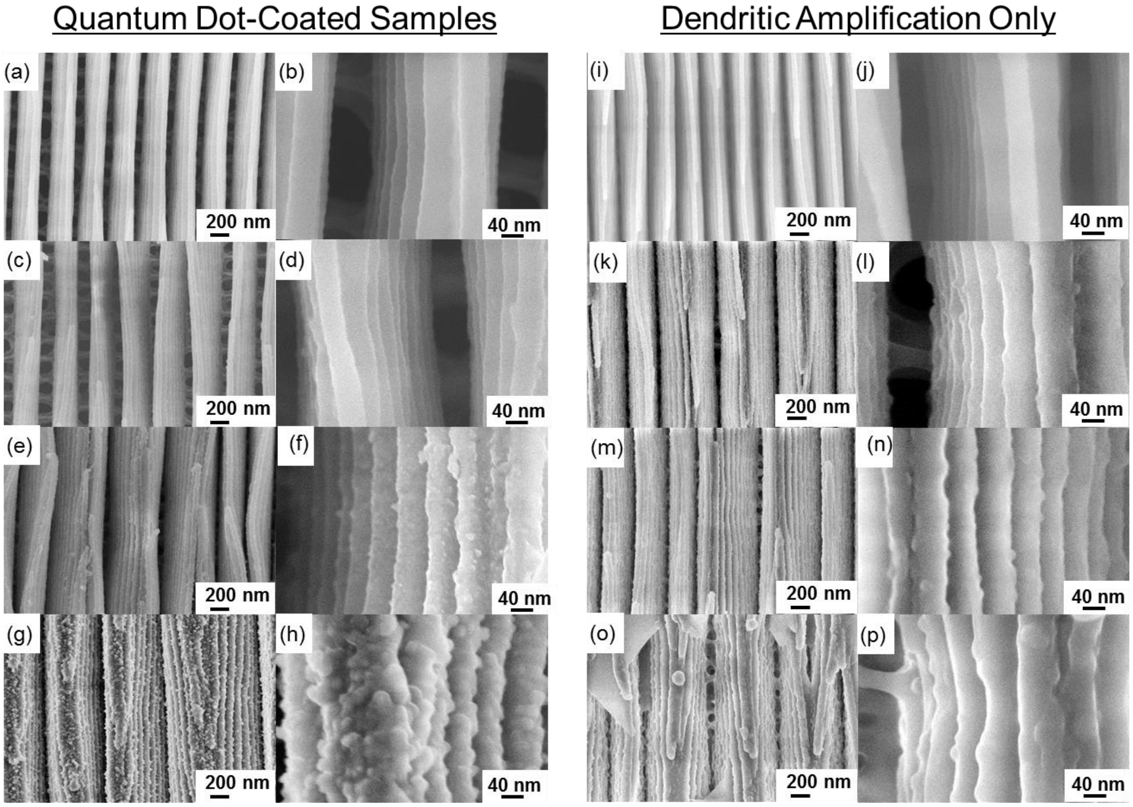

Figure 63. Secondary electron images for (a, b) native and quantum dot multilayer coated samples for (c, d) 1 layer, (e, f) 4 layers, and (g, h) 10 layers. Secondary electron images of control samples coated with only dendritic amplification layers (*i.e.*, no quantum dots): (i, j) 9 layers, (k, l) 18 layers, (m, n) 27 layers, and (o, p) 36 layers. The starting butterfly scale structure (i.e., individual ridges and lamella) is preserved through the coating processes. Scales coated with 10 quantum dot-containing layers and 36 dendritic amplification layers have lost some distinction between individual lamella.

Secondary electron images of scales coated with only dendritic amplification layers show that individual scale features, such as single ridges and single lamella, were preserved throughout the coating process, until approximately 36 layers (**Figure 63**). The distinction between individual lamella became unclear after the application of 36 dendritic amplification layers due to excessive film deposition. The relatively dark brown appearance of a representative scale validated this result as the structural color was mostly removed. Each quantum dot multilayer was approximately equivalent to 3 dendritic amplification layers (based on the number of polyacrylate and polyamine layers deposited within the quantum dot multilayer unit cell, **Figure 57 (a)**). Comparison of secondary electron images between quantum dot (**Figure 63 (e, f)**) and dendritic amplification specimens (**Figure 63 (k, l)**) suggested that the observed roughness observed in the quantum dot specimens was due to quantum dot aggregates rather than the dendritic amplification precursors.

3.6 Conclusions

Emissive coloration from prefabricated quantum dots has been added to the structural coloration found within the scales of the *Morpho rhetenor* butterfly. This represents the first study of tailored, layer-by-layer quantum dot deposition onto a prefabricated optical nanostructure. Synergy between the high reflectivity, structurally colored template, and the intense and stable emission from the functionalized quantum dots, enabled the first demonstration of reflected and emitted color mixing on a single butterfly scale. The coloration of a single scale was altered between emissive only (from quantum dots), reflection only (from the coated *M. rhetenor* template), and combined emission and reflection upon changing the illumination source. The emission intensity increased with successive quantum dot containing layers, up to 10 cycles. All samples exhibited an increase in emission intensity with continued exposure to the excitation light (325 – 375 nm) (*i.e.,* photoluminescent enhancement). However, the time-dependent emission intensity plateaued after approximately 300 s, which enabled the time-independent characterization of emission intensity as a function of the number of applied layers. The scale reflectance underwent a net red shift as the number of applied quantum dot-containing layers increased. Cross-sectional TEM imaging of a 10-layer specimen revealed the quantum dot-containing film conformally coated the butterfly nanostructure. The coating thickness was approximately 35 ± 10 nm.

Future efforts could expand the range of emissive components integrated into the multilayer films by including quantum dots with a variety of emitted wavelengths. Detailed study of how film deposition parameters (such as incubation time, concentration, number of host matrix layers between each quantum dot-containing layer, etc.) affect the film morphology and fluorescent emission would be valuable for the tailorable integration of multiple quantum dots. The multilayer film developed through this work could be applied to other templates, such as synthetic photonic crystals, possibly leading towards applications in anti-counterfeiting [99] and lasers [100].

3.7 References

[1] P. Vukusic, "Natural photonics," *Physics World*, vol. 17, pp. 35-39, Feb 2004.

[2] L. P. Biro and J. P. Vigneron, "Photonic nanoarchitectures in butterflies and beetles: valuable sources for bioinspiration," *Laser & Photonics Reviews,* vol. 5, pp. 27-51, Jan 2011.

[3] M. Srinivasarao, "Nano-optics in the biological world: Beetles, butterflies, birds, and moths," *Chemical Reviews,* vol. 99, pp. 1935-1961, Jul 1999.

[4] A. A. Michelson, "On metallic colouring in birds and insects," *Philosophical Magazine,* vol. 21, pp. 554-567, Apr 1911.

[5] C. W. Mason, "Structural colors in insects. I," *Journal of Physical Chemistry,* vol. 30, pp. 383-395, Mar 1926.

[6] C. W. Mason, "Structural colors in insects III," *Journal of Physical Chemistry,* vol. 31, pp. 1856-1872, Jul-Dec 1927.

[7] C. W. Mason, "Structural colors in insects II," *Journal of Physical Chemistry,* vol. 31, pp. 321-354, Mar 1927.

[8] Ghiradel.H, T. Eisner, R. E. Silberglied, Aneshans.D, and H. E. Hinton, "Ultraviolet Reflection of a Male Butterfly - Interference Color caused by Thin-Layer Elaboration of Wing Scales," *Science,* vol. 178, pp. 1214-+, 1972.

[9] H. Ghiradella, "Development of ultraviolet-reflecting butterfly scales - how to make an interference filter," *Journal of Morphology,* vol. 142, pp. 395-409, 1974.

[10] H. Ghiradella and W. Radigan, "Development of butterfly scales. 2. Struts, lattices, and surface-tension," *Journal of Morphology,* vol. 150, pp. 279-297, 1976.

[11] H. Ghiradella, "Structure of Iridescent Lepidopteran Scales - Variations on Several Themes," *Annals of the Entomological Society of America,* vol. 77, pp. 637-645, 1984.

[12] H. Ghiradella, "Structure and Development of Iridescent Lepidopteran Scales - The Papilionidae as a Showcase Family," *Annals of the Entomological Society of America,* vol. 78, pp. 252-264, 1985.

[13] H. Ghiradella, "Structure and development of iridescent butterfly scales - lattices and laminae," *Journal of Morphology,* vol. 202, pp. 69-88, Oct 1989.

[14] H. Ghiradella, "Light and Color on the Wing - Structural Colors in Butterflies and Moths," *Applied Optics,* vol. 30, pp. 3492-3500, Aug 1991.

[15] H. Ghiradella, "Structure of Butterfly Scales - Patterning in an Insect Cuticle," *Microscopy Research and Technique,* vol. 27, pp. 429-438, Apr 1994.

[16] H. Ghiradella, "Structure of butterfly scales - patterning an insect cuticle," *Microscopy Research and Technique,* vol. 27, pp. 429-438, Apr 1994.

[17] P. Vukusic and R. Sambles, "Photonic structures in biology," *Nature,* vol. 424, pp. 852-855, 2003.

[18] S. Kinoshita, S. Yoshioka, and J. Miyazaki, "Physics of structural colors," *Reports on Progress in Physics,* vol. 71, Jul 2008.

[19] R. A. Potyrailo, H. Ghiradella, A. Vertiatchikh, K. Dovidenko, J. R. Cournoyer, and E. Olson, "Morpho butterfly wing scales demonstrate highly selective vapour response," *Nature Photonics,* vol. 1, pp. 123-128, Feb 2007.

[20] L. P. Biro, K. Kertesz, Z. Vertesy, and Z. Balint, "Photonic nanoarchitectures occurring in butterfly scales as selective gas/vapor sensors," in *Nature of Light: Light in Nature Ii.* vol. 7057, K. Creath, Ed., ed Bellingham: Spie-Int Soc Optical Engineering, 2008.

[21] C. M. Eliason and M. D. Shawkey, "Rapid, reversible response of iridescent feather color to ambient humidity," *Optics Express,* vol. 18, pp. 21284-21292, Sep 2010.

[22] P. R. Stoddart, P. J. Cadusch, T. M. Boyce, R. M. Erasmus, and J. D. Comins, "Optical properties of chitin: surface-enhanced Raman scattering substrates based on antireflection structures on cicada wings," *Nanotechnology,* vol. 17, pp. 680-686, Feb 2006.

[23] N. L. Garrett, P. Vukusic, F. Ogrin, E. Sirotkin, C. P. Winlove, and J. Moger, "Spectroscopy on the wing: Naturally inspired SERS substrates for biochemical analysis," *Journal of Biophotonics,* vol. 2, pp. 157-166, Mar 2009.

[24] A. D. Pris, Y. Utturkar, C. Surman, W. G. Morris, A. Vert, S. Zalyubovskiy, *et al.*, "Towards high-speed imaging of infrared photons with bio-inspired nanoarchitectures," *Nat Photon,* vol. 6, pp. 195-200, 2012.

[25] D. P. Gaillot, O. Deparis, V. Welch, B. K. Wagner, J. P. Vigneron, and C. J. Summers, "Composite organic-inorganic butterfly scales: Production of photonic structures with atomic layer deposition," *Physical Review E,* vol. 78, Sep 2008.

[26] J. Huang, X. Wang, and Z. L. Wang, "Controlled Replication of Butterfly Wings for Achieving Tunable Photonic Properties," *Nano Letters,* vol. 6, pp. 2325-2331, 2006.

[27] J. P. Vernon, "Morphology-Preserving Chemical Conversion of Bioorganic and Inorganic Templates," Doctor of Philosophy, Materials Science and Engineering, Georgia Institute of Technology, Atlanta, GA, 2012.

[28] F. Liu, W. Z. Shi, X. H. Hu, and B. Q. Dong, "Hybrid structures and optical effects in Morpho scales with thin and thick coatings using an atomic layer deposition method," *Optics Communications,* vol. 291, pp. 416-423, Mar 2013.

[29] B. D. Wilts, T. M. Trzeciak, P. Vukusic, and D. G. Stavenga, "Papiliochrome II pigment reduces the angle dependency of structural wing colouration in nireus group papilionids," *Journal of Experimental Biology,* vol. 215, pp. 796-805, Mar 2012.

[30] J. P. Vigneron, K. Kertesz, Z. Vertesy, M. Rassart, V. Lousse, Z. Balint, *et al.*, "Correlated diffraction and fluorescence in the backscattering iridescence of the male butterfly Troides magellanus (Papilionidae)," *Physical Review E,* vol. 78, Aug 2008.

[31] E. Van Hooijdonk, C. Barthou, J. P. Vigneron, and S. Berthier, "Detailed experimental analysis of the structural fluorescence in the butterfly Morpho sulkowskyi (Nymphalidae)," *Journal of Nanophotonics,* vol. 5, Nov 2011.

[32] R. T. Lee and G. S. Smith, "Detailed electromagnetic simulation for the structural color of butterfly wings," *Applied Optics,* vol. 48, pp. 4177-4190, Jul 2009.

[33] M. Kambe, D. Zhu, and S. Kinoshita, "Origin of Retroreflection from a Wing of the Morpho Butterfly," *Journal of the Physical Society of Japan,* vol. 80, May 2011.

[34] M. A. Steindorfer, V. Schmidt, M. Belegratis, B. Stadlober, and J. R. Krenn, "Detailed simulation of structural color generation inspired by the Morpho butterfly," *Optics Express,* vol. 20, pp. 21485-21494, Sep 2012.

[35] L. Plattner, "Optical properties of the scales of Morpho rhetenor butterflies: theoretical and experimental investigation of the back-scattering of light in the visible spectrum," *Journal of the Royal Society Interface,* vol. 1, pp. 49-59, Nov 2004.

[36] S. Berthier, E. Charron, and J. Boulenguez, "Morphological structure and optical properties of the wings of Morphidae," *Insect Science,* vol. 13, pp. 145-158, 2006.

[37] R. H. Siddique, S. Diewald, J. Leuthold, and H. Holscher, "Theoretical and experimental analysis of the structural pattern responsible for the iridescence of Morpho butterflies," *Optics Express,* vol. 21, pp. 14351-14361, Jun 2013.

[38] J. Boulenguez, S. Berthier, and F. Leroy, "Multiple scaled disorder in the photonic structure of Morpho rhetenor butterfly," *Applied Physics a-Materials Science & Processing,* vol. 106, pp. 1005-1011, Mar 2012.

[39] P. Vukusic, J. R. Sambles, C. R. Lawrence, and R. J. Wootton, "Quantified interference and diffraction in single Morpho butterfly scales," *Proceedings of the Royal Society of London Series B-Biological Sciences,* vol. 266, pp. 1403-1411, Jul 1999.

[40] S. Kinoshita, S. Yoshioka, and K. Kawagoe, "Mechanisms of structural colour in the Morpho butterfly: cooperation of regularity and irregularity in an iridescent

scale," *Proceedings of the Royal Society of London Series B-Biological Sciences,* vol. 269, pp. 1417-1421, Jul 2002.

[41] A. L. Rogach, N. A. Kotov, D. S. Koktysh, A. S. Susha, and F. Caruso, "II-VI semiconductor nanocrystals in thin films and colloidal crystals," *Colloids and Surfaces a-Physicochemical and Engineering Aspects,* vol. 202, pp. 135-144, Apr 9 2002.

[42] A. Sukhanova, A. V. Baranov, D. Klinov, V. Oleinikov, K. Berwick, J. H. M. Cohen, *et al.*, "Self-assembly of charged microclusters of CdSe/ZnS core/shell nanodots and nanorods into hierarchically ordered colloidal arrays," *Nanotechnology,* vol. 17, pp. 4223-4228, Aug 28 2006.

[43] D. Y. Wang, A. L. Rogach, and F. Caruso, "Composite photonic crystals from semiconductor nanocrystal/polyelectrolyte-coated colloidal spheres," *Chemistry of Materials,* vol. 15, pp. 2724-2729, Jul 15 2003.

[44] F. Fleischhaker and R. Zentel, "Photonic crystals from core-shell colloids with incorporated highly fluorescent quantum dots," *Chemistry of Materials,* vol. 17, pp. 1346-1351, Mar 22 2005.

[45] P. Reiss, M. Protiere, and L. Li, "Core/Shell Semiconductor Nanocrystals," *Small,* vol. 5, pp. 154-168, Jan 2009.

[46] J. Tang, S. M. Zhu, Z. X. Chen, C. L. Feng, Y. J. Shen, F. Yao, *et al.*, "Replication of polypyrrole with photonic structures from butterfly wings as biosensor," *Materials Chemistry and Physics,* vol. 131, pp. 706-713, Jan 2012.

[47] S.-H. Kang, T.-Y. Tai, and T.-H. Fang, "Replication of butterfly wing microstructures using molding lithography," *Current Applied Physics,* vol. 10, pp. 625-630, 2010.

[48] Q. Q. Yang, S. M. Zhu, W. H. Peng, C. Yin, W. L. Wang, J. J. Gu, *et al.*, "Bioinspired Fabrication of Hierarchically Structured, pH-Tunable Photonic Crystals with Unique Transition," *Acs Nano,* vol. 7, pp. 4911-4918, Jun 2013.

[49] J. Han, H. L. Su, D. Zhang, J. J. Chen, and Z. X. Chen, "Butterfly wings as natural photonic crystal scaffolds for controllable assembly of CdS nanoparticles," *Journal of Materials Chemistry,* vol. 19, pp. 8741-8746, 2009.

[50] R. J. Martin-Palma, C. G. Pantano, and A. Lakhtakia, "Biomimetization of butterfly wings by the conformal-evaporated-film-by-rotation technique for photonics," *Applied Physics Letters,* vol. 93, Aug 2008.

[51] M. R. Weatherspoon, Y. Cai, M. Crne, M. Srinivasarao, and K. H. Sandhage, "3D rutile titania-based structures with Morpho butterfly wing scale morphologies," *Angewandte Chemie-International Edition,* vol. 47, pp. 7921-7923, 2008.

[52] J. P. Vernon, A. Lethbridge, C. G. Cameron, Y. Cai, M. Kolle, J. Aizenberg, *et al.*, "Layer-by-Layer Conformal Coating and Replication of Butterfly Photonic Nanostructures with Higher Index Inorganic Materials," *In preparation*.

[53] C. Mille, E. C. Tyrode, and R. W. Corkery, "Inorganic chiral 3-D photonic crystals with bicontinuous gyroid structure replicated from butterfly wing scales," *Chemical Communications,* vol. 47, pp. 9873-9875, 2011.

[54] Y. Chen, J. J. Gu, D. Zhang, S. M. Zhu, H. L. Su, X. B. Hu, *et al.*, "Tunable three-dimensional ZrO(2) photonic crystals replicated from single butterfly wing scales," *Journal of Materials Chemistry,* vol. 21, pp. 15237-15243, 2011.

[55] Y. Chen, X. N. Zang, J. J. Gu, S. M. Zhu, H. L. Su, D. Zhang, *et al.*, "ZnO single butterfly wing scales: synthesis and spatial optical anisotropy," *Journal of Materials Chemistry,* vol. 21, pp. 6140-6143, 2011.

[56] J. W. Galusha, M. R. Jorgensen, and M. H. Bartl, "Diamond-Structured Titania Photonic-Bandgap Crystals from Biological Templates," *Advanced Materials,* vol. 22, pp. 107-+, Jan 2010.

[57] J. W. Galusha, L. R. Richey, M. R. Jorgensen, J. S. Gardner, and M. H. Bartl, "Study of natural photonic crystals in beetle scales and their conversion into inorganic structures via a sol-gel bio-templating route," *Journal of Materials Chemistry,* vol. 20, pp. 1277-1284, 2010.

[58] M. R. Jorgensen and M. H. Bartl, "Biotemplating routes to three-dimensional photonic crystals," *Journal of Materials Chemistry,* vol. 21, pp. 10583-10591, 2011.

[59] M. R. Jorgensen, B. P. Yonkee, and M. H. Bartl, "Solid and hollow inorganic replicas of biological photonic crystals," *Scripta Materialia,* vol. 65, pp. 954-957, Dec 2011.

[60] J. P. Vernon, Y. N. Fang, Y. Cai, and K. H. Sandhage, "Morphology-Preserving Conversion of a 3D Bioorganic Template into a Nanocrystalline Multicomponent Oxide Compound," *Angewandte Chemie-International Edition,* vol. 49, pp. 7765-7768, 2010.

[61] J. P. Vernon, N. Hobbs, Y. Cai, A. Lethbridge, P. Vukusic, D. D. Deheyn, *et al.*, "3D photoluminescent lanthanide-doped barium titanate structures synthesized by coating and shape-preserving reaction of complex-shaped bioorganic templates," *Journal of Materials Chemistry,* vol. 22, pp. 10435-10437, 2012.

[62] S. M. Zhu, X. Y. Liu, Z. X. Chen, C. J. Liu, C. L. Feng, J. J. Gu, *et al.*, "Synthesis of Cu-doped WO3 materials with photonic structures for high performance sensors," *Journal of Materials Chemistry,* vol. 20, pp. 9126-9132, 2010.

[63] J. W. Wang and Y. M. Kuo, "Hierarchically porous cobalt oxyhydroxide derived from Morpho-butterfly wings: Preparation, characterization, and carbon monoxide detection at low temperatures," *Physica Status Solidi a-Applications and Materials Science,* vol. 210, pp. 494-502, Mar 2013.

[64] F. Liu, Y. P. Liu, L. Huang, X. H. Hu, B. Q. Dong, W. Z. Shi, *et al.*, "Replication of homologous optical and hydrophobic features by templating wings of butterflies Morpho menelaus," *Optics Communications,* vol. 284, pp. 2376-2381, May 2011.

[65] Y. N. Fang, J. D. Berrigan, Y. Cai, S. R. Marder, and K. H. Sandhage, "Syntheses of nanostructured Cu- and Ni-based micro-assemblies with selectable 3-D hierarchical biogenic morphologies," *Journal of Materials Chemistry,* vol. 22, pp. 1305-1312, 2012.

[66] Y. N. Fang, V. W. Chen, Y. Cai, J. D. Berrigan, S. R. Marder, J. W. Perry, *et al.*, "Biologically Enabled Syntheses of Freestanding Metallic Structures Possessing Subwavelength Pore Arrays for Extraordinary (Surface Plasmon-Mediated) Infrared Transmission," *Advanced Functional Materials,* vol. 22, pp. 2550-2559, Jun 2012.

[67] J. Silver, R. Withnall, T. G. Ireland, and G. R. Fern, "Novel nano-structured phosphor materials cast from natural Morpho butterfly scales," *Journal of Modern Optics,* vol. 52, pp. 999-1007, May 2005.

[68] M. Kucki, S. Landwehr, H. Ruhling, M. Maniak, and T. Fuhrmann-Lieker, "Light-emitting biological photonic crystals - The bioengineering of metamaterials," in *Photonic Crystal Materials and Devices III*. vol. 6182, R. M. DeLaRue, P. Viktorovitch, C. Lopez, and M. Midrio, Eds., ed, 2006, pp. S1821-S1821.

[69] M. Kucki and T. Fuhrmann-Lieker, "Staining diatoms with rhodamine dyes: control of emission colour in photonic biocomposites," *Journal of the Royal Society Interface,* vol. 9, pp. 727-733, Apr 2012.

[70] M. R. Weatherspoon, M. S. Haluska, Y. Cai, J. S. King, C. J. Summers, R. L. Snyder*, et al.*, "Phosphor microparticles of controlled three-dimensional shape from phytoplankton," *Journal of the Electrochemical Society,* vol. 153, pp. H34-H37, 2006.

[71] D. H. Lee, T. Gutu, C. Jeffryes, G. L. Rorrer, J. Jiao, and C. H. Chang, "Nanofabrication of green luminescent Zn2SiO4 : Mn using biogenic silica," *Electrochemical and Solid State Letters,* vol. 10, pp. K13-K16, 2007.

[72] D. K. Gale, T. Gutu, J. Jiao, C. H. Chang, and G. L. Rorrer, "Detection of Immunocomplex Formation by Enhanced Photoluminescence of Antibody-Functionalized Diatom Biosilica," in *Bio-Inspired/Biomimetic Sensor Technologies and Applications*. vol. 7321, N. F. Fell and V. S. Swaminathan, Eds., ed, 2009.

[73] C. Jeffryes, R. Solanki, Y. Rangineni, W. Wang, C.-h. Chang, and G. L. Rorrer, "Electroluminescence and Photoluminescence from Nanostructured Diatom Frustules Containing Metabolically Inserted Germanium," *Advanced Materials,* vol. 20, pp. 2633-2637, 2008.

[74] Y. Cai, M. B. Dickerson, M. S. Haluska, Z. Kang, C. J. Summers, and K. H. Sandhage, "Manganese-Doped Zinc Orthosilicate-Bearing Phosphor Microparticles with Controlled Three-Dimensional Shapes Derived from Diatom Frustules," *Journal of the American Ceramic Society,* vol. 90, pp. 1304-1308, 2007.

[75] Y. Tian, Q. He, C. Tao, and J. B. Li, "Fabrication of fluorescent nanotubes basel on layer-by-layer assembly via covalent bond," *Langmuir,* vol. 22, pp. 360-362, Jan 2006.

[76] I. Welterlich and B. Tieke, "Conjugated Polymer with Benzimidazolylpyridine Ligands in the Side Chain: Metal Ion Coordination and Coordinative Self-Assembly into Fluorescent Ultrathin Films," *Macromolecules,* vol. 44, pp. 4194-4203, Jun 2011.

[77] K. Kim, S. Webster, N. Levi, D. L. Carroll, M. R. Pinto, and K. S. Schanze, "Luminescent core-shell photonic crystals from poly(phenylene ethynylene) coated silica spheres," *Langmuir,* vol. 21, pp. 5207-5211, May 2005.

[78] J. Sun, I. Ichinose, R. Takaki, A. Nakao, and T. Kunitake, "Enhanced emission in composite multilayers of amorphous TiO2-gel and Eu3+ ions," *Chemistry Letters,* pp. 742-743, Jul 2002.

[79] T. Yonezawa, H. Matsune, and T. Kunitake, "Layered Nanocomposite of Close-Packed Gold Nanoparticles and TiO2 Gel Layers," *Chemistry of Materials,* vol. 11, pp. 33-35, 1998.

[80] J. Y. Tseng, M. H. Lin, and L. K. Chau, "Preparation of colloidal gold multilayers with 3-(mercaptopropyl)-trimethoxysilane as a linker molecule," *Colloids and Surfaces a-Physicochemical and Engineering Aspects,* vol. 182, pp. 239-245, Jun 2001.

[81] H. Zhang, B. Yang, R. B. Wang, G. Zhang, X. L. Hou, and L. X. Wu, "Fabrication of a covalently attached self-assembly multilayer film based on CdTe nanoparticles," *Journal of Colloid and Interface Science,* vol. 247, pp. 361-365, Mar 2002.

[82] A. Shavel, N. Gaponik, and A. Eychmuller, "The assembling of semiconductor nanocrystals," *European Journal of Inorganic Chemistry,* pp. 3613-3623, Sep 2005.

[83] C. A. Constantine, K. M. Gattas-Asfura, S. V. Mello, G. Crespo, V. Rastogi, T. C. Cheng*, et al.*, "Layer-by-layer biosensor assembly incorporating functionalized quantum dots," *Langmuir,* vol. 19, pp. 9863-9867, Nov 2003.

[84] C. X. Jiang, N. Yang, X. Wang, D. B. Chen, and A. Y. Zhong, "Layer-by-layer Assembly of Acrylate Copolymers and CdTe Nanoparticles," *Iranian Polymer Journal,* vol. 18, pp. 811-820, Oct 2009.

[85] Z. Q. Liang, K. L. Dzienis, J. Xu, and Q. Wang, "Covalent layer-by-layer assembly of conjugated polymers and CdSe nanoparticles: Multilayer structure and photovoltaic properties," *Advanced Functional Materials,* vol. 16, pp. 542-548, Mar 2006.

[86] O. V. Vassiltsova, S. K. Panda, Z. Y. Zhao, M. A. Carpenter, and M. A. Petrukhina, "Ordered fabrication of luminescent multilayered thin films of CdSe quantum dots," *Dalton Transactions,* pp. 9426-9432, 2009.

[87] S. Ishii, R. Ueji, S. Nakanishi, Y. Yoshida, H. Nagata, T. Itoh*, et al.*, "Fabrication of a quantum dot-polymer matrix by layer-by-layer conjugation," *Journal of Photochemistry and Photobiology a-Chemistry,* vol. 183, pp. 285-291, Oct 2006.

[88] G. J. Wang, Y. N. Fang, P. Kim, A. Hayek, M. R. Weatherspoon, J. W. Perry*, et al.*, "Layer-By-Layer Dendritic Growth of Hyperbranched Thin Films for Surface Sol-Gel Syntheses of Conformal, Functional, Nanocrystalline Oxide Coatings on Complex 3D (Bio)silica Templates," *Advanced Functional Materials,* vol. 19, pp. 2768-2776, Sep 2009.

[89] A. Mejdoubi, C. Andraud, S. Berthier, J. Lafait, J. Boulenguez, and E. Richalot, "Finite element modeling of the radiative properties of Morpho butterfly wing scales," *Physical Review E,* vol. 87, Feb 2013.

[90] B. Gralak, G. Tayeb, and S. Enoch, "Morpho butterflies wings color modeled with lamellar grating theory," *Optics Express,* vol. 9, pp. 567-578, Nov 2001.

[91] S. F. Lee and M. A. Osborne, "Brightening, Blinking, Bluing and Bleaching in the Life of a Quantum Dot: Friend or Foe?," *Chemphyschem,* vol. 10, pp. 2174-2191, Sep 2009.

[92] P. Vukusic and D. G. Stavenga, "Physical methods for investigating structural colours in biological systems," *Journal of the Royal Society Interface,* vol. 6, pp. S133-S148, Apr 2009.

[93] Y. Ebenstein, T. Mokari, and U. Banin, "Fluorescence quantum yield of CdSe/ZnS nanocrystals investigated by correlated atomic-force and single-particle fluorescence microscopy," *Applied Physics Letters*, vol. 80, pp. 4033-4035, May 2002.
[94] J. Yao, D. R. Larson, H. D. Vishwasrao, W. R. Zipfel, and W. W. Webb, "Blinking and nonradiant dark fraction of water-soluble quantum dots in aqueous solution," *Proceedings of the National Academy of Sciences of the United States of America*, vol. 102, pp. 14284-14289, Oct 2005.
[95] R. A. Potyrailo, T. A. Starkey, P. Vukusic, H. Ghiradella, M. Vasudev, T. Bunning, *et al.*, "Discovery of the surface polarity gradient on iridescent Morpho butterfly scales reveals a mechanism of their selective vapor response," *Proceedings of the National Academy of Sciences*, vol. 110, pp. 15567-15572, September 24, 2013 2013.
[96] J. D. Joannopoulos, *Photonic crystals : molding the flow of light*, 2nd ed. Princeton: Princeton University Press, 2008.
[97] K. Michielsen and D. G. Stavenga, "Gyroid cuticular structures in butterfly wing scales: biological photonic crystals," *Journal of the Royal Society Interface*, vol. 5, pp. 85-94, Jan 2008.
[98] E. D. Palik, *Handbook of Optical Constants of Solids*: Elsevier, 1998.
[99] B. Yoon, J. Lee, I. S. Park, S. Jeon, J. Lee, and J. M. Kim, "Recent functional material based approaches to prevent and detect counterfeiting," *Journal of Materials Chemistry C*, vol. 1, pp. 2388-2403, 2013.
[100] K. J. Vahala, "Optical microcavities," *Nature*, vol. 424, pp. 839-846, Aug 2003.

CHAPTER 4: Conclusions

The challenge of understanding how 3-dimensional bioorganic nanostructures achieve coloration, as well as the development of layer-by-layer synthetic coating approaches for modifying such coloration, were addressed in this work. A first-of-its-kind approach was developed for isolating individual scale components, and scale component combinations. Such an approach was applied to unambiguously determine the optical contribution of each nanostructured component within the green scales of the *Parides sesostris* butterfly. A widely applicable method of scale component isolation was developed for Focused Ion Beam (FIB) systems. This method was an improvement over previous top-down milling approaches [1-3], which could result in uneven ion milling due to a spatially varying material density within the milled material. The approach developed in this work relied on the complete removal of scale material by milling scale component nanostructures from the side. This way, scale components with large, spatial variations in material density could be uniformly removed.

Precise isolation of scale components, followed by optical characterization, enabled the correlation of optical appearance to particular scale components, or scale component combinations. While the existing hypothesis of scale coloration (a localized pigment filter that absorbs UV and blue wavelengths [4, 5]) was validated, it was found to be not the only, nor dominant, scale coloration mechanism. The presence of a different coloration mechanism was demonstrated by the blue scale coloration (as observed through the ridges). Such a change in coloration was obtained when, at least 1.3 µm of the scale base was removed (*i.e.*, removal of the thin, solid membrane and a portion of the gyroid polycrystal, leaving a separate portion of the gyroid polycrystal intact with the ridge structure). Careful analyses excluded thin film interference from the thin, solid membrane and localized fluorescent emission as other, dominant coloration mechanisms.

Measurements of the pore spacings across the thickness of single, hexagonal gyroid polycrystal domains resulted in the discovery of a graded pore spacing throughout the thickness of the measured domains. The pore spacing was greater at the base of the scale (near the thin, solid membrane) and smaller near the ridge structure. This discovery provided the first report of a graded period (*i.e.*, chirped) 3-dimensional photonic crystal-like structure found in nature. An individual *P. sesostris* green scale was specifically milled to remove a gradient amount of the polycrystal across the scale length. Qualitative imaging of the gradient, trench-milled scale revealed a blue shift in the reflected color along the direction of a greater amount of removed polycrystal material. Subsequent reflection measurements across the milled gradient quantitatively confirmed this observation. Overall, the isolation and interrogation approach applied to the *P. sesostris* scale enabled the direct testing of hypotheses of scale coloration, the discovery of new structural features, and a new (a greater) understanding of the overall green scale coloration mechanism.

The characterization of fluorescent emission from the green scales of the *P. sesostris* butterfly inspired the investigation for how artificial fluorophores could be incorporated onto 3-dimensional optical nanostructures to affect the emission intensity and reflected coloration of the initial template. The high visibility and relatively constant coloration as a function of viewing angle [6, 7] inspired the selection of the structurally colored, blue scales of the *Morpho rhetenor* butterfly as the coating template for this investigation. The color mixing between the reflected light from the functionalized, structurally colored template and the emitted light, from the applied fluorophore, was of primary interest for this work.

A layer-by-layer, dendritic amplification process [8, 9] was selected to provide a fluorophore host matrix for the multilayered integration of an organic, fluorescent, dye (2’,7’-Bis(2-carboxyethyl)-5(6)-carboxyfluorescein, BCECF). The intensity of the induced fluorescent emission increased, and the coated scale reflection underwent a net red shift, with increasing numbers of applied layers, up to 10 dye-containing layers. This work provided the first layer-by-layer alteration of both emitted and reflected color (*i.e.,* bimodal coloration) of butterfly scales. The induced fluorescence from the deposited dye-containing-layers photobleached with increased exposure to light. (The emission intensity dropped approximately 75 % after 130 s of excitation light exposure). Photobleaching, in addition to the spectral overlap between the dye emission and the coated template reflection, excluded application of this template/fluorophore combination for the demonstration of reflected and emitted color mixing.

A second approach for achieving color mixing between emitted and reflected light utilized a layer-by-layer deposition of quantum dots onto the *Morpho rhetenor* template. Quantum dot emission was selected to emit in the low reflectivity wavelength range of the uncoated *Morpho* template (approximately 600 – 700 nm) to ensure a greater spectral separation between the emission and reflection spectra. Amine-terminated quantum dots were integrated into a layer-by-layer dendritic amplification process [8, 9] and applied to the blue, *Morpho rhetenor* scales. The emitted intensity (due to the quantum dots) increased and the coated scale reflection underwent a net red shift with an increasing number of applied layers, up to 10 quantum dot-containing layers. All quantum dot-functionalized scales exhibited photoluminescent enhancement (*i.e.*, the increase of emission intensity with exposure time, approximately 400 % over a 10 minute exposure time). Color mixing, between the emitted light from the functionalized quantum dots and the coated scale reflection, was successfully demonstrated as a result of photoluminescent enhancement and the spectral separation of template reflection and induced emission. This work provided the first layer-by-layer deposition of quantum dots to a prefabricated optical nanostructure. Additionally, this was the first report of color mixing between emitted and reflected light on a single butterfly scale.

Overall, this research has contributed to the understanding of bioorganic nanostructure coloration, as well as to the development of synthetic approaches for modifying such coloration through induced fluorescence emission and reflectance alteration. Future investigations could apply a similar isolation and interrogation approach for other structurally colored bioorganic nanostructures. Use of virtual models of the *P. sesostris* green scale, which may be enabled through nanoscale tomography [2, 10] methods, may enable a greater understanding of the coloration mechanism presented through this work. Additional control of template (either synthetic or natural in origin) emission and reflection may be obtained through the investigation of the layer-by-layer deposition of other organic dyes, quantum dots with different emission peaks, and multiple fluorophores integrated within a single multilayer film.

4.1 References

[1] J. W. Galusha, M. R. Jorgensen, and M. H. Bartl, "Diamond-Structured Titania Photonic-Bandgap Crystals from Biological Templates," *Advanced Materials,* vol. 22, pp. 107-+, Jan 2010.

[2] J. W. Galusha, L. R. Richey, M. H. Bartl, and Ieee, "High Resolution Three-Dimensional Reconstruction of Photonic Crystal Structure found in Beetle Scales," in *2008 Digest of the Leos Summer Topical Meetings*, ed, 2008, pp. 83-84.

[3] J. W. Galusha, L. R. Richey, J. S. Gardner, J. N. Cha, and M. H. Bartl, "Discovery of a diamond-based photonic crystal structure in beetle scales," *Physical Review E*, vol. 77, May 2008.

[4] B. D. Wilts, K. Michielsen, H. De Raedt, and D. G. Stavenga, "Iridescence and spectral filtering of the gyroid-type photonic crystals in Parides sesostris wing scales," *Interface Focus*, December 21, 2011 2011.

[5] L. Poladian, S. Wickham, K. Lee, and M. C. J. Large, "Iridescence from photonic crystals and its suppression in butterfly scales," *Journal of the Royal Society Interface*, vol. 6, pp. S233-S242, Apr 2009.

[6] P. Vukusic, J. R. Sambles, C. R. Lawrence, and R. J. Wootton, "Quantified interference and diffraction in single Morpho butterfly scales," *Proceedings of the Royal Society of London Series B-Biological Sciences*, vol. 266, pp. 1403-1411, Jul 1999.

[7] S. Kinoshita, S. Yoshioka, and J. Miyazaki, "Physics of structural colors," *Reports on Progress in Physics*, vol. 71, Jul 2008.

[8] M. R. Weatherspoon, M. B. Dickerson, G. Wang, Y. Cai, S. Shian, S. C. Jones, *et al.*, "Thin, conformal, and continuous SnO2 coatings on three-dimensional biosilica templates through hydroxy-group amplification and layer-by-layer alkoxide deposition," *Angewandte Chemie-International Edition*, vol. 46, pp. 5724-5727, 2007.

[9] G. J. Wang, Y. N. Fang, P. Kim, A. Hayek, M. R. Weatherspoon, J. W. Perry, *et al.*, "Layer-By-Layer Dendritic Growth of Hyperbranched Thin Films for Surface Sol-Gel Syntheses of Conformal, Functional, Nanocrystalline Oxide Coatings on Complex 3D (Bio)silica Templates," *Advanced Functional Materials*, vol. 19, pp. 2768-2776, Sep 2009.

[10] J. H. Chen, Y. C. Lee, M. T. Tang, and Y. F. Song, "X-ray tomography and chemical imaging within butterfly wing scales," in *Synchrotron Radiation Instrumentation, Pts 1 and 2*. vol. 879, J. Y. Choi and S. Rah, Eds., ed, 2007, pp. 1940-1943.

APPENDIX A: Supplemental Information for Chapter 1: Optical Characterization of Isolated Scale Component Nanostructures of the Butterfly, *Parides sesostris*

Needle mounting butterfly scales can cause some damage to the optical nanostructures present within the scale. **Figure 64 (a, b)** illustrates examples of excess epoxy flowing into the scale structure, resulting in a loss in color. The needle can sometimes penetrate into the scale (**Figure 64 (c)**). Despite these effects, milling away from excess epoxy or damage due to the needle can enable structure optical property correlation (**Figure 64 (c)**).

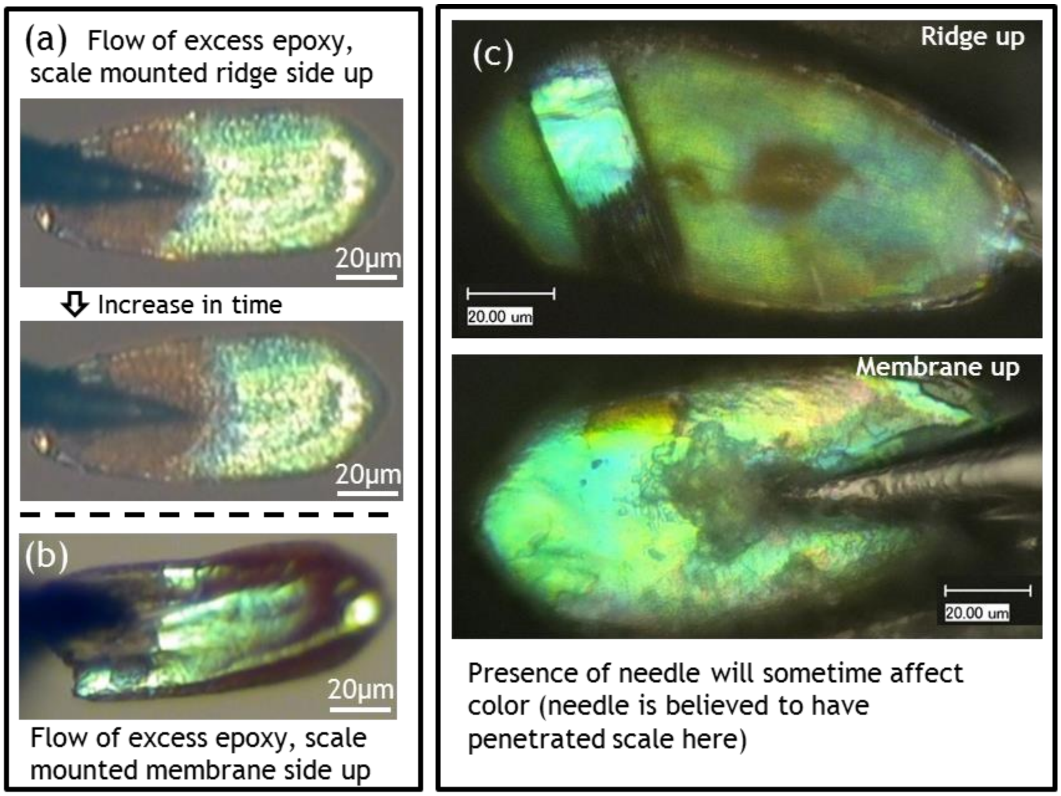

Figure 64. Presence of excess material around scale can alter scale color. (a) Epoxy wetting the through the scale (ridge-up) as a function of time. (b) Epoxy overflow and possible infiltration can also occur with the membrane-up. (c) The needle can sometimes puncture through scale, minimizing available area for measurements.

Multiple scale component structures were isolated to correlate optical appearance with scale component structures. This correlation is summarized in **Chapter 1, Figure 16**. Evidence for each milled scale component combination are shown in the following figures: **Figure 65** through **Figure 67**.

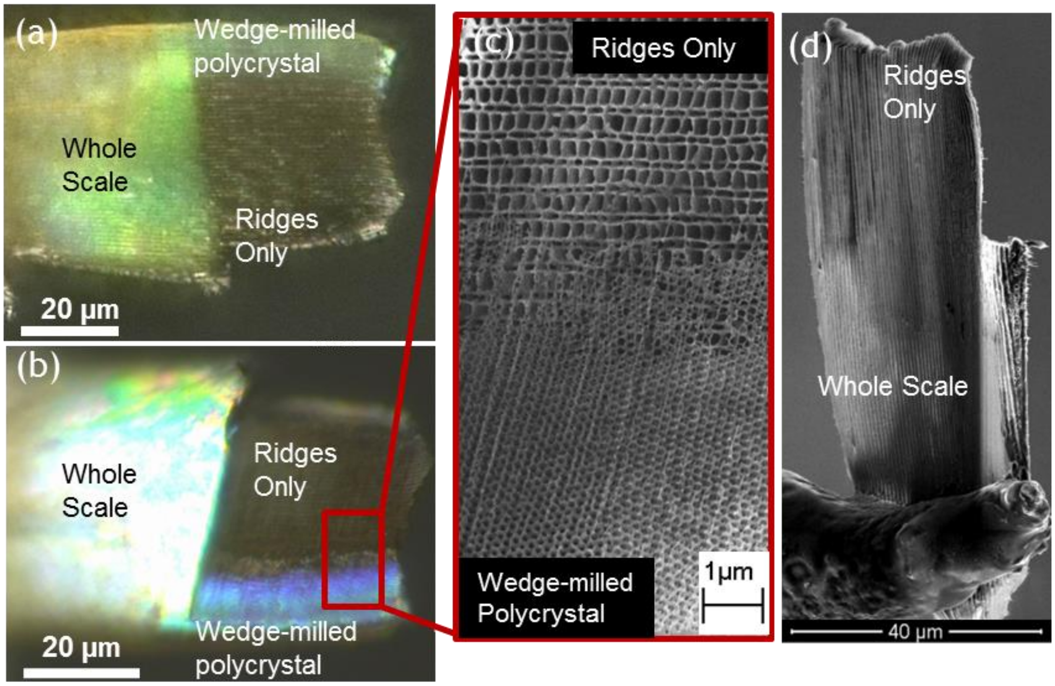

Figure 65. Structure-optical appearance correlation – ridge structure. (a) Bright field image of a scale oriented ridge side up and (b) membrane side up. (c) Secondary electron image of exposed ridge-only and wedge-milled polycrystal. (d) Secondary electron image showing preservation of ridge structure the scale is oriented ridge side up.

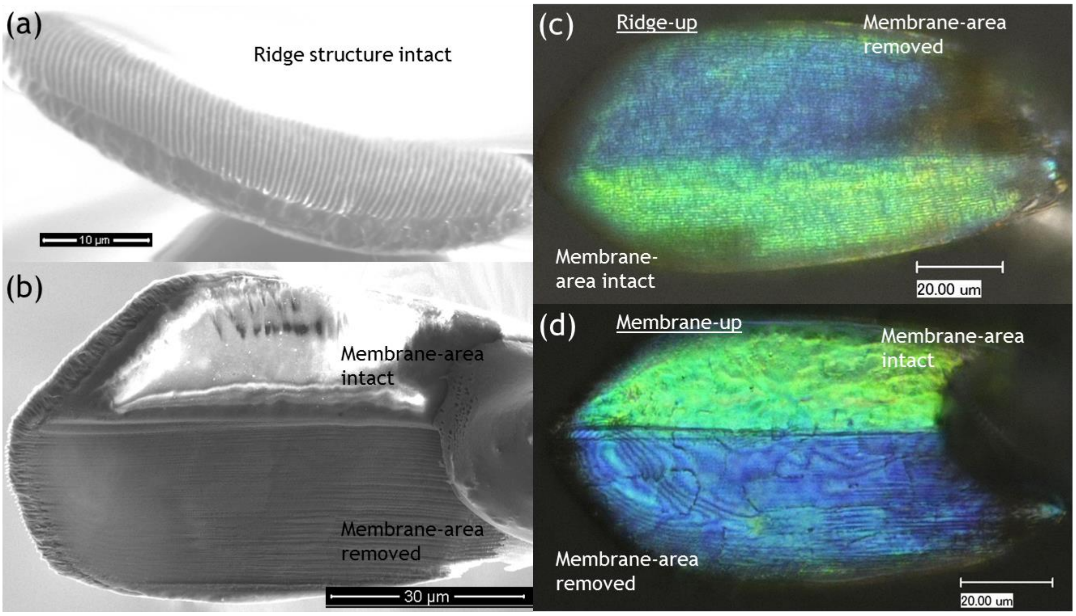

Figure 66. Structure-optical appearance correlation – ridge structure and polycrystal (*i.e.*, membrane removed). (a) Secondary electron image showing preservation of ridge structure and (b) removal of membrane-area to expose polycrystal on one-half of the scale, while leaving the membrane-area intact on the other half. (c) Bright field optical image of scale oriented ridge side up and (d) membrane side up.

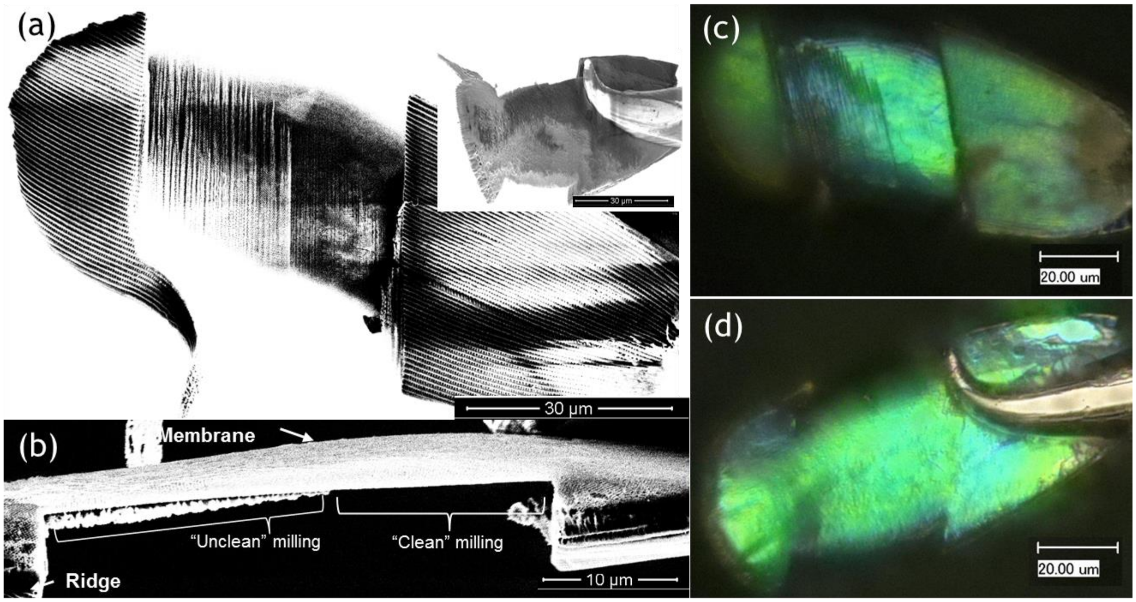

Figure 67. Structure-optical appearance correlation – polycrystal and membrane-area. (a) SEM image of specimen, post milling, showing exposed polycrystal and membrane-area in between whole scale regions. (Inset) intact membrane-area. (b) SEM image of scale side view showing clean versus unclean milled regions. Observations for color assignment were made on the clean-milled region to negate the artificial roughness (*i.e.*, curtaining, caused by high-energy ion milling). Removal of roughness in this region would have caused the sample to warp due to the ion beam interaction and loss of structural integrity. (c) Bright field optical image oriented ridge side up and (d) membrane side up.

Initial experiments for determination of the role of fluorescence in the overall scale coloration utilized UV treatments in an attempt to degrade the fluorophore within the scale (**Figure 68**). Two-months of continuous exposure to UV light (peak wavelength of 254 nm) were required before any color change in the scales occurred (courtesy of Russell Shimada and Dr. Dimitri Deheyn, Scripps Institute of Oceanography). The scale coloration went from green to blue due to the UV light treatment. However, structural analysis of the polycrystal revealed a significant shrinkage of the scale. Pore spacing measurements across the whole polycrystal thickness (hexagonal face) went from 235 ± 19 nm to 197 ± 16 nm after the UV treatment. Back-of-the envelope calculations with the Bragg equation suggested that a structural color blue shift occurred in addition to the possible degradation of the scale fluorophore. The diffracted wavelength (for a grating material of refractive index 1.56 and angle of 50 ^{o}) shifted from 562 nm to 471 nm, from the native to the UV-treated scales. This result inspired the use of long pass filter measurements [1] to remove the short wavelength light from the scale illumination so that the contribution of fluorescence as the sole source of color could be determined.

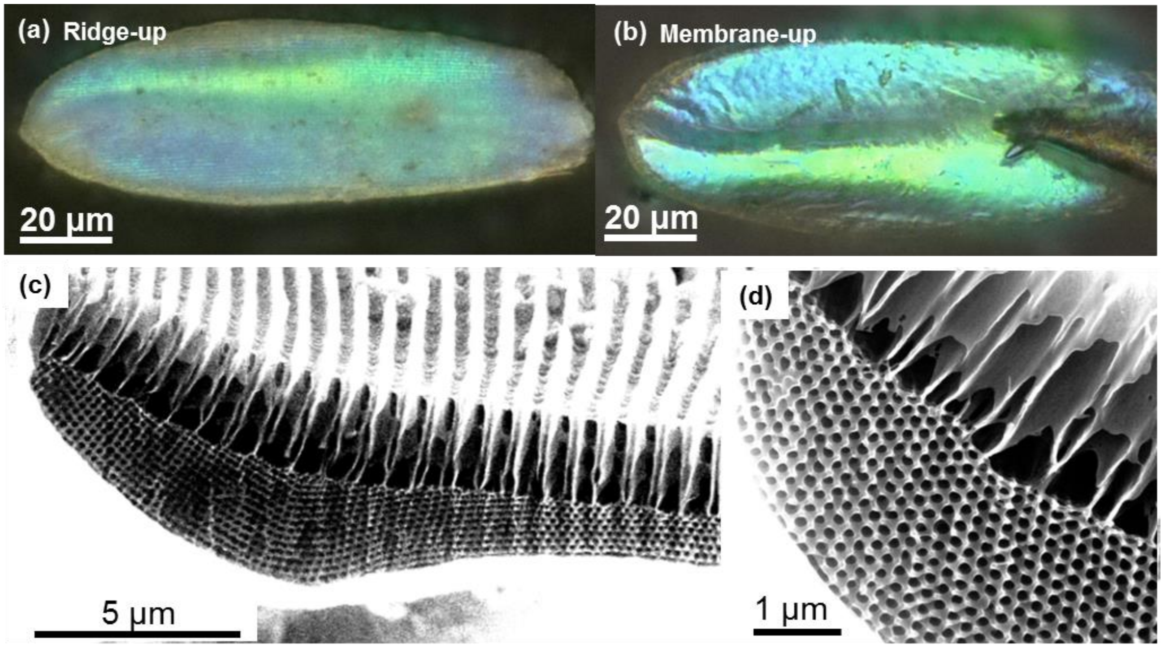

Figure 68. (a) Bright field optical microscopy image showing a UV-treated scale ridge-up and (b) membrane up. UV-treated scales were exposed to mercury light (λ_{peak}=254 nm) for two months (courtesy Dr. Dimitri Dehyen group, Scripps Institute of Oceanography). (c) Secondary electron images from a FIB-milled cross-section of the same photobleached scale showing structural preservation of the polycrystal and the ridges.

FIB milling of the *P. sesostris* ridge structure revealed that the constituent structures: fins and nanotube array, share the same period of 742 ± 15 nm. **Figure 69** provides additional evidence of the shared periodicity.

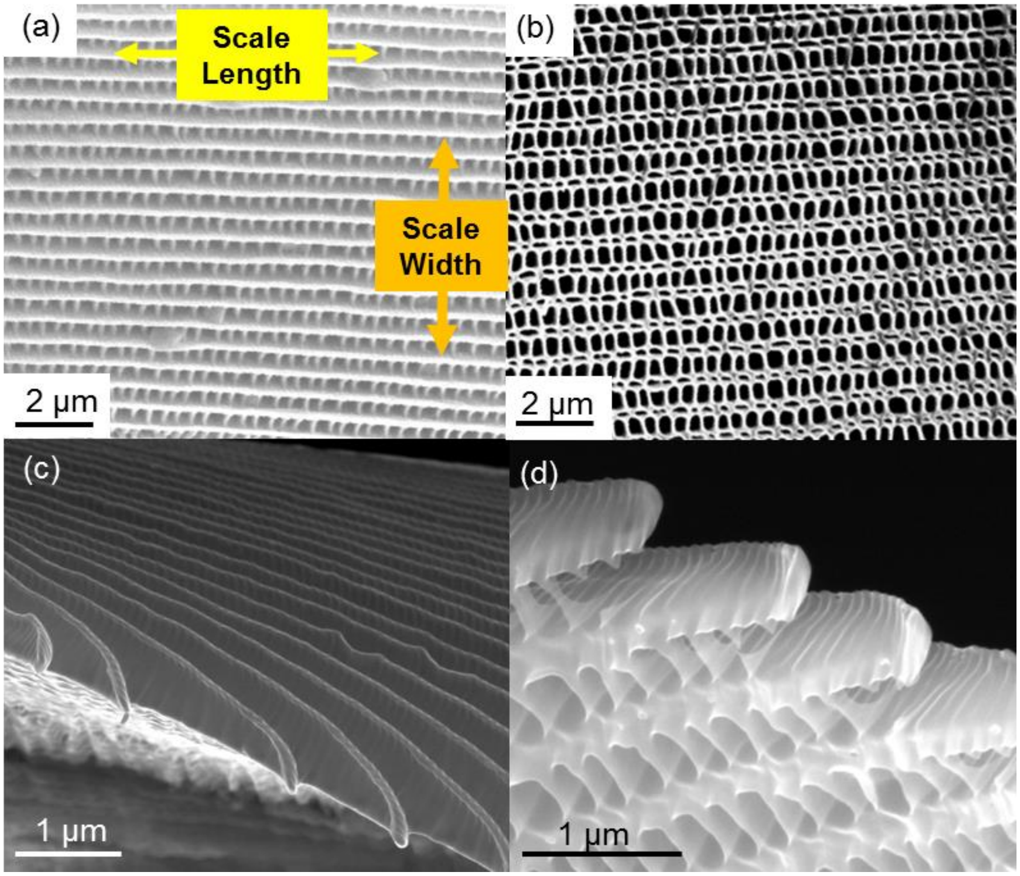

Figure 69. Secondary electron images of the fin and nanotube array, located in the *P. sesostris* ridge structure. (a) Intermediate magnification showing the upper surface of the ridge structure. (b) Intermediate magnification of the underside of an isolated ridge structure (*i.e.*, the ridge structure was viewed from where the polycrystal was, prior to milling). (c) High magnification of the upper portion of the isolated fin structure. (d) Underside of the same region of isolated fins, demonstrating that the fin structure shared the same periodicity as the nanotube array. The structural spacing was periodic in the direction of the scale width (*i.e.*, fins run parallel with the scale length).

A.1 References

[1] B. D. Wilts, T. M. Trzeciak, P. Vukusic, and D. G. Stavenga, "Papiliochrome II pigment reduces the angle dependency of structural wing colouration in nireus group papilionids," *Journal of Experimental Biology,* vol. 215, pp. 796-805, Mar 2012.

APPENDIX B: *In situ* Investigation of the Dendritic Amplification Process using Quartz Crystal Microbalance (QCM)

B.1 Summary

Incubation time dependence for the precursors involved in the layer-by-layer, dendritic amplification process were studied, *in situ*, using Quartz Crystal Microbalance with Dissipation (QCM-D). These efforts enabled a reduction in the time required for application of dendritic amplification layers to bioorganic nanostructures in **Chapter 2** and **3**. Overall, the aminosilane deposition was reduced from an overnight step to 10 minutes and the polyamine deposition was reduced from 1 hour to 10 minutes. The reduction in incubation time maintained the same film growth (*i.e.*, frequency shift per cycle) as the precursors (*i.e.*, aminosilane, polyacrylate, and polyamine) with 1 hour deposition times. These results suggested that the aminosilane and polyamine depositions reach surface saturation in the allotted deposition time (10 minutes). Film growth was sensitive to the incubation time of the polyacrylate solution, where the overall film growth was considerably reduced when the polyacrylate incubation time was reduced from 1 hour to 30 minutes.

B.2 Introduction

Chapter 2 and **3** utilized the dendritic amplification process to integrate an organic fluorescent dye and quantum dots into multilayers, respectively. Prior to these investigations, the incubation time dependence for the layer-by-layer dendritic amplification method were studied using *in situ* Quartz Crystal Microbalance (QCM) analysis. Prior studies utilized this deposition to amplify functional groups such that continuous conformal films could be deposited.[1-5] Such amplification steps typically involved five dendritic amplification deposition cycles.

The layer-by-layer, dendritic amplification process (**Figure 70**) began by reacting to an aminosilane molecule with hydroxyl groups onto a hydroxyl-poor surface. The resulting amine groups, protruding from the surface, were iteratively exposed to solutions of a hyperbranched acrylate and then a polyamine, respectively. Incubation times, prior to this study were overnight, 1 hour, and 1 hour for the aminosilane, polyacrylate, and polyamine, respectively.

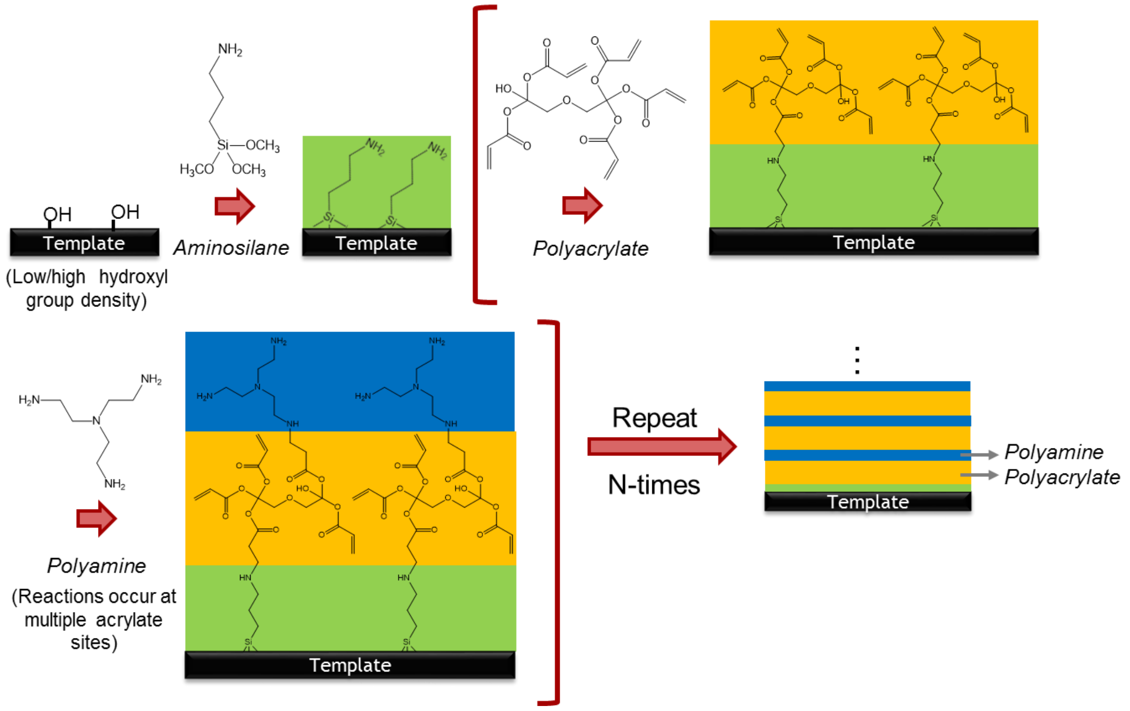

Figure 70. Schematic of the layer-by-layer dendritic amplification process. First, a hydroxyl-bearing surface is functionalized with an aminosilane. Subsequent layers are then iteratively deposited, via alternating exposure to polyacrylate and polyamine bearing solutions.

B.3 Experimental Procedures

B.3.1 Creation of dendritic amplification solutions

Initial layers of the dendritic amplification process were deposited, starting with a single functionalization of aminosilane (N^1-(3-Trimethoxylsilylpropyl)diethylenetriamine, Technical grade, Sigma Aldrich, MO, USA). The aminosilane solution was diluted to 20 vol% in ethanol (200 proof, anhydrous. Koptec, PA, USA). Subsequent layers were iteratively coated through repeated exposures of polyacrylate (Dipentaerythritol penta-/hexa-acrylate, Sigma Aldrich, MO, USA) and polyamine (Tris(2-aminoethyl)amine, 96%, Sigma Aldrich, MO, USA), respectively. Both polyacrylate and polyamine solutions were diluted to 10 wt%, each, in ethanol. All precursor solutions were made fresh for each QCM experiment. Additionally, the ethanol wash was acquired from the same source as the ethanol used to create the precursor deposition solutions.

B.3.2 Quartz Crystal Microbalance with Dissipation (QCM-D) operation principle

Quartz Crystal Microbalance with Dissipation (QCM-D) was an *in situ* characterization method, which enabled an understanding of the extent of surface functionalization and film growth for layer-by-layer coating processes. This capability was attractive because it enabled an optimization of precursor deposition times for the dendritic amplification process. The QCM method was extremely sensitive to surface changes in the z-direction, capable of measuring monolayer formation.[6] (Film uniformity in the xy-plane is assumed.)[6] SiO_2 was selected as a model system to study the dendritic amplification coating process due to the availability of commercial-off-the-shelf, hydroxylated, QCM sensor surfaces.

A QCM-D, E4 system from Biolin Scientific (Västra Frölunda, Sweden) was used to study the layer-by-layer deposition of dendritic amplification layers. Fluid was pumped from a solution reservoir into a flow module (PTFE flow module 401, Biolin Scientific, Västra Frölunda, Sweden) containing the sensor. Next, the fluid was removed from the sensor region, by a down-stream peristaltic pump (Model: ISM935C, Ismatec, IDEX Corporation, IL, USA), and into a waste beaker. QCM-D technology measured the frequency shift and dissipation of a piezoelectric quartz crystal resonator after it was electrically excited. The electrical stimulus caused a mechanical shearing oscillation in the plane of the resonator thickness. The measured, resonance frequency increased or decreased with the removal, or addition of mass, respectively.

The dissipation factor (D) represents the sum of all energy losses per crystal oscillation, providing an indication of film rigidity.[6] For example, an elongated molecule tethered to a surface, such that it is extended into the fluid, has a larger dissipation than the same molecule lying flat across the surface.[6, 7] A molecule lying flat on the sensor surface more easily couples to the motion of the sensor, resulting in a smaller energy loss per oscillation cycle (*i.e.*, a smaller dissipation).[6, 7] The tethered, elongated molecule has a poor coupling to the sensor motion, resulting in a greater energy loss per cycle and a larger dissipation.[6, 7]

Shifts in the fundamental resonator frequency (*i.e.*, 1) and its harmonics (*i.e.*, 3, 5, 7, 9, 11, and 13) were monitored simultaneously. These correspond to the 5, 15, 25, 35, 45, 55, 65, and 75 MHz frequencies, respectively. Dissipation from each harmonic was acquired, simultaneously, with the resonance frequency shifts. There was a trade-off in mass sensitivity and radial distribution of the harmonic amplitude. Lower harmonics had a greater sensing area, but suffered from noise and were often unstable. Higher harmonics were less sensitive towards the sensor edge, but were limited by a smaller film penetration depth. The 5th harmonic, corresponding to the 25 MHz frequency, was selected as the best compromise between these two sensitivities. **Figure 71** illustrates the radial amplitude distribution, with normalized intensity, for a number of harmonics. All discussions of film growth (*i.e.*, frequency shift versus number of cycles) only considered the 5th harmonic.

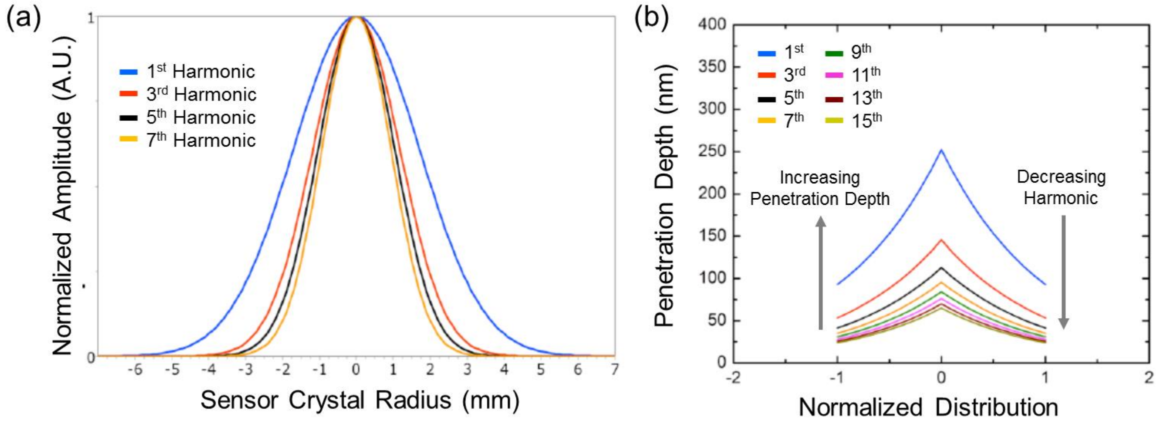

Figure 71. Normalized radial amplitude distribution for the fundamental frequency (5 MHz) and 3rd (15 MHz), 5th (25 MHz), and 7th (35 MHz) harmonics. The 5th harmonic was selected as the best compromise between penetration depth and noise due to larger areal distributions effects and was used for subsequent calculations and monitoring of film growth. Data courtesy of Biolin Scientific (Västra Frölunda, Sweden).

Harmonic splitting, where each harmonic has a different value, indicates viscoelastic (*i.e.*, highly dissipative) film behavior. Sensor motion varied with each resonance frequency. Rigid film motion coupled to the motion of the sensor such that they were both in-phase across many of the harmonics, resulting in similar values of frequency and dissipation shift. The fluid surrounding the film caused film movement to be out-of-phase with the sensor, which damped film motion, and resulted in viscoelastic behavior. The extent of out-of-phase movement of the film, for each harmonic, caused the harmonics to have different frequency shift and dissipation values, for a given fluidic environment. Such phenomena were important for understanding the differences in frequency shift behavior between the polyacrylate- and the polyamine-terminated surfaces.

Finally, QCM-D was a wet measurement technique. In other words, that the data contained the mass change of the resonator due to the deposited film and mass of solvent interacting with the film.[6, 7] Viscoelastic films will generally have a greater solvent mass than rigid films and, thus, having a greater dissipation (*i.e.*, more opportunities exist to loose mechanical energy in the case of a solvated film).[6, 7]

B.3.3 Cleaning protocol for SiO_2 QCM sensors and PTFE flow modules

A wide variety of flow modules were available from Q-Sense (*i.e.*, electrochemistry, titanium, etc.). The polytetrafluoroethylene (PTFE) module was selected for this work to prevent precursor deposition inside the flow module, which could not be controlled in the case of the titanium flow module due to the surface hydroxyl groups present on the oxide surface.

SiO_2-coated (~ 50 nm) QCM sensors were purchased from Q-sense (Model QSX 303, Västra Frölunda, Sweden) Sensors were cleaned by a 10 minute UV/Ozone treatment (UV/Ozone ProCleaner^{TM}, Bioforce Nanosciences, CA, USA). Followed by a 30 minute soak in 2 wt% sodium dodecyl sulfate (Biotechnology grade, Amresco, OH, USA) solution in 18.2 MΩ·cm water (Milli-Q ultrapure, EMD Millipore, MA, USA)). Sensors were rinsed copiously with water (approximately 100 mL each) and dried in compressed nitrogen (Ultra High Purity, AirGas, PA, USA) for 5 minutes. Finally, sensors were treated with another 10 minute UV/Ozone treatment. Then, sensors were immediately placed in a clean, PTFE flow module for QCM coating studies.

The applicability of an organic etchant (80 ^{o}C solution of 1:1:5 $NH_4OH:H_2O_2:H_2O$ for 10 minutes) was explored as another cleaning method, but ended in irreparable damage to the QCM sensor (*i.e.,* half of the sensor was etched away). Further use of either NH_4OH or H_2O_2 in deposition or cleaning processes was avoided in order to conserve sensors.

Thorough flow module cleaning was performed in between non-related experiments (*i.e.,* after other users who run disparate experiments compared to dendritic amplification multilayer deposition). The cleaning began by disassembling the nonelectrical portions of the module, followed by immersion in 2 wt% sodium dodecyl sulfate solution followed by sonication (Branson 2510, Bransonic, CT, USA) at 40 ^{o}C for 30 minutes. Module components were then rinsed with 18.2 MΩ·cm water and sonicated at 40 ^{o}C for 30 minutes with fresh 18.2 MΩ·cm water. Components were subsequently removed and dried with a Kimwipe (Kimberly-Clark Corporation, TX, USA) and dry nitrogen for 5 minute, or until dry. The module components (including the tubes) were reassembled and immediately used for deposition studies.

Minimum cleaning of the PTFE QCM flow modules involved flushing the system with 30 mL of 2 wt% sodium dodecyl sulfate solution followed by 50 mL of 18.2 MΩ·cm water. This protocol was followed in between experiments involving only dendritic amplification layers (*i.e.,* no other users operated the equipment between experiments). Following the system flush, the modules were opened to remove the sensor and the pump tubing. All components of the module were then dried under compressed nitrogen and stored for use on the following day.

B.3.4 QCM-D measurement methodology

Real-time data acquisition (in air, then in ethanol) was used to confirm adequate sensor performance for a stable baseline (*i.e.*, an unchanging frequency shift over the course of a minute (0 Hz/min)). Deviations from parallel frequency shift and dissipation, between the harmonics and over time, indicated that the sensor was not ready to be used for data acquisition. Possible effects for this include (1) mounting errors, which caused time-dependent, mechanical stresses on the resonator, (2) incomplete temperature stabilization, (3) damages to the sensor (*e.g.*, chips, scratches, etc.), and (4) incomplete sensor cleaning, resulting in material wash-off.[8] It was best to; first, verify a stable baseline in air so that the sensor can be easily remounted without having to dry the flow module and tubing after resetting the sensor. Next, a baseline was acquired in ethanol (or any other solvent used for precursors) and the experiment was started. Anomalous deviations (either positive or negative) in frequency shift and dissipation can occur during measurement due to macroscopic structural defects in the sensor; air bubble formation; and impediments in the fluid channel, which cause pressure waves from the down-stream, peristaltic pump.[8] Thorough cleaning of the tubing flow module and sensors, in addition to care in sensor handling, was critical to the success of the measurement. Total time required to reach a stable baseline in the solvent of interest ranged between 30 minutes and 2 hours.

QCM sensor resonance frequencies varied with temperature. Thus, control over the temperature during the measurement was critical for reliable data. For instance, simultaneous frequency changes due to chemisorption and temperature convolute the interpretation of the film growth because these two effects cannot be subtracted without extensive control samples. An example of such frequency and dissipation variations are shown in **Figure 72**.

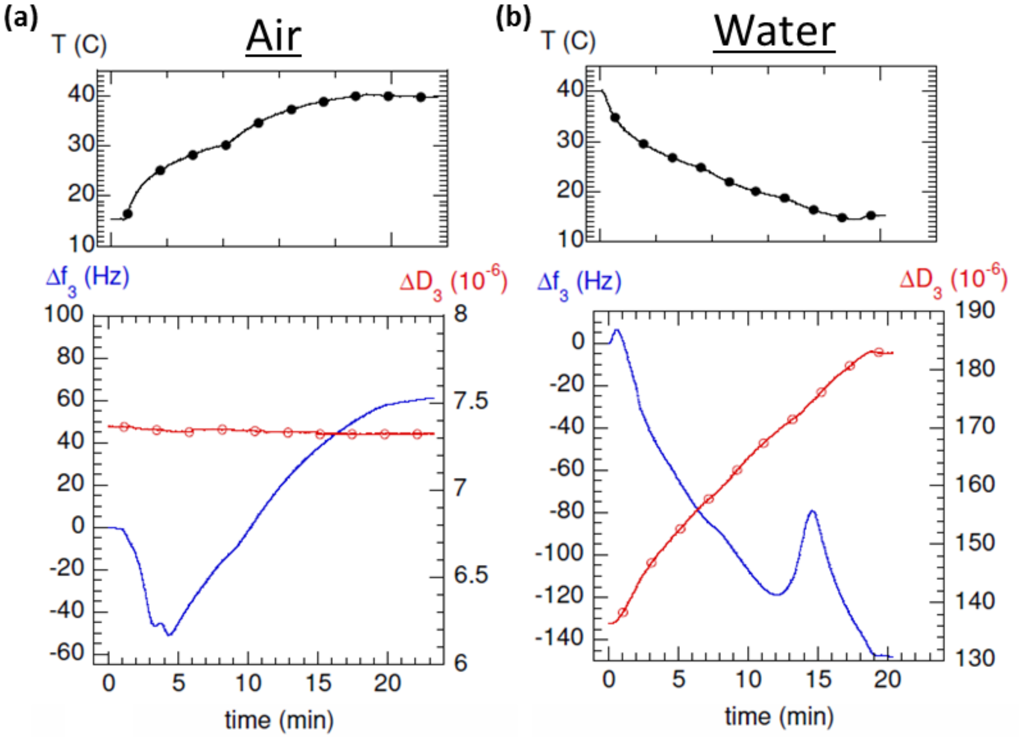

Figure 72. Unsteady-state QCM sensor temperature dependence. Variation of frequency and dissipation shift for 3rd harmonic of a rigid film in (a) air and (b) water. Control of temperature was critical for artifact-free measurements. Data courtesy of Biolin Scientific (Västra Frölunda, Sweden).

All measurements were performed at 18 °C, slightly below the average room temperature of the laboratory (20 °C). It is advisable to perform the experiment at a slightly lower temperature than the solutions in order to avoid the release of solubilized gases when the liquid contacts the sensor surface.[8] All solutions were degassed for 15 minutes prior to performing QCM-D measurements using the degas feature of a sonicator (Branson 2510, Bransonic, CT, USA).

Film growth was monitored through analysis of frequency shift and dissipation during the wash step after each chemisorption. All dendritic amplification solutions were ethanol based. Bulk fluid properties (*i.e.*, viscosity and density) of the precursor solutions changed, relative to the pure ethanol wash solution, due to high precursor concentrations (as evidenced by the harmonic splitting, **Figure 73**). This prevented film growth monitoring for the frequency changes observed during the chemisorption step (*i.e.*, during the precursor deposition). Qualitative deposition kinetics were be obtained by studying the curvature of the frequency shift data for the chemisorption region. For example, the slope of frequency shift as a function of time indicates the relative rate of the deposition. However, the data still contained the bulk property effect, resulting in very large frequency and dissipation changes as well as harmonic splitting. Future efforts could explore the possibility of using modeling to deconvolute the effects of the bulk fluid property change and chemisorption for the precursor solutions.

Data points for the frequency change versus number of applied cycles were obtained by averaging all frequency shift and dissipation data points for the 5th harmonic, during the wash step following amine chemisorption. The frequency and dissipation responses were allowed to stabilize (*i.e.*, 0 Hz/min) for at least two minutes. This stabilization period typically provided 200 data points to contribute to the average and the error bar range of ± one standard deviation.

B.4 Results and Discussion

In situ studies on the dendritic amplification process were performed with QCM-D, for the first time, to understand film growth, in terms of frequency shift as a function of number of cycles, and the relative rates of chemisorption for each process step. Prior procedures used 37 ^{o}C, overnight aminosilane incubation, followed by hour-long incubations in polyacrylate and polyamine, respectively.[2] This study was conducted at a constant temperature of 18 ^{o}C to avoid the temperature dependent frequency response of the quartz crystal resonator. Such frequency changes could interfere with measuring the coating growth as a function of number of cycles. Secondly, an operational temperature slightly below the stock solution/laboratory temperature (20 ^{o}C) helped avoid the formation of bubbles where the fluid contacts the sensor. This effect also prevented data acquisition on the coating growth.

Representative, initial precursor incubations for the dendritic amplification process are shown in **Figure 73**. The frequency shift as a function of time for the aminosilane step had no apparent change after the first 4 minutes and the incubation was terminated after an hour. This suggested that the surface functionalization, under the studied conditions, was completed within the first few minutes of the precursor incubation. Thus, longer incubation times should not significantly affect the amount of material deposited. (Note: Previous studies [2] used an overnight incubation for the aminosilane without an *in situ* understanding the aminosilane reaction kinetics through QCM to guide coating process development.)

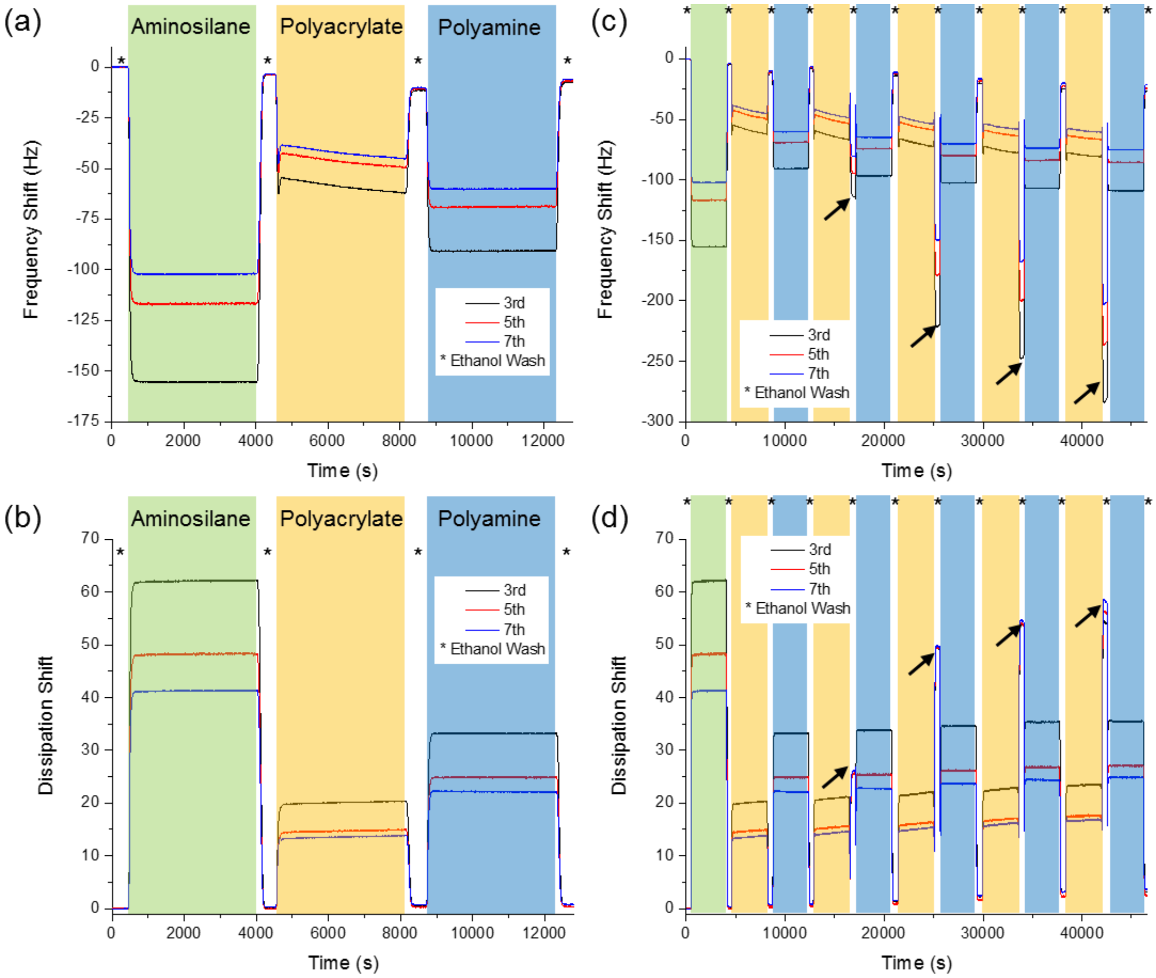

Figure 73. Representative *in situ* measurement of film growth for dendritic amplification process. (a) Frequency and (b) dissipation shift as a function of time for the first 3 deposition steps. Total (c) frequency and (d) dissipation shift as a function of time up to 5 layers. A greater viscoelastic behavior occurred in the step after polyacrylate deposition. Black arrows in (c) and (d) highlight the frequency and dissipation shift, respectively, for the polyacrylate wash steps displaying viscoelastic behavior.

The deposition continued with 1-hour polyacrylate and 1-hour polyamine functionalization, respectively. The polyacrylate never reached a constant frequency shift value, with respect to time, during the hour-long incubation (**Figure 73 (a)**). Harmonic splitting occurred as a result of the changes in bulk fluid properties (*i.e.*, viscosity and density) for each precursor solution during the chemisorption step. High precursor concentrations caused the bulk fluid properties of the solution to change, relative to the pure solvent properties (ethanol in this case). The bulk fluid property change prevented direct comparisons between precursor solutions. Overall film growth was monitored through tracking the frequency shifts during each ethanol wash step.

An increase in frequency shift was observed after comparison of the polyacrylate (-10.8 ± 0.1 Hz) and polyamine wash step (-6.7 ± 0.1 Hz) (**Figure 73 (a)**). Separate studies of film thickness monitored with ellipsometry confirmed the additive deposition as the number of applied layers increase, up to 6 cycles.[5] It may be possible that the frequency shift increase (and dissipation decrease) from the polyacrylate solution to the polyamine solution was a result of cross-linking and/or the removal of entrained solvent [7] in the acrylate-terminated film. This was supported by the progressively greater viscoelastic behavior for the polyacrylate wash steps as the number of layers increased.

Harmonic splitting occurred for the wash step after the polyacrylate solution (see black arrows in **Figure 73 (c, d)**), but not for the post-polyamine wash. This effect was likely due to more viscoelastic film behavior. An increased interaction of the solvent with the polyacrylate-bearing surface resulted a greater number of damping mechanisms available to dissipate mechanical energy. Mechanical motion of the sensor varied, depending on the harmonic, which caused a disparity for the frequency and dissipation shift values across the measured harmonics. The harmonic splitting, in this case, was not due to bulk fluid property change because the data acquisition was acquired in pure ethanol (*i.e.*, the same solvent in which the baseline was collected). Increases in dissipation as a result of subsequent acrylate layer depositions also demonstrated more viscoelastic behavior (black arrows, **Figure 73 (d)**). Film growth was tracked using only the amine terminated steps from this point forward.

The overall film growth, in terms of the frequency shift as a function of number of cycles, for the amine-terminated steps is shown in **Figure 74**. The film underwent linear growth, up to 5 cycles, in agreement with prior reports [5], which used ellipsometry to track film growth. Film growth, expressed in frequency shift, showed close agreement across multiple sensors, resulting in a growth rate of approximately 5.6 ± 1.1 (-Hz)/cycle. The error bar range was obtained by multiplying the instrument error of 0.5 Hz/hour by the total time for each cycle, including wash steps (60 minutes for polyacrylate and polyamine, and a total wash time of 15 min for both cycles, which left 135 min/cycle for this coating process).

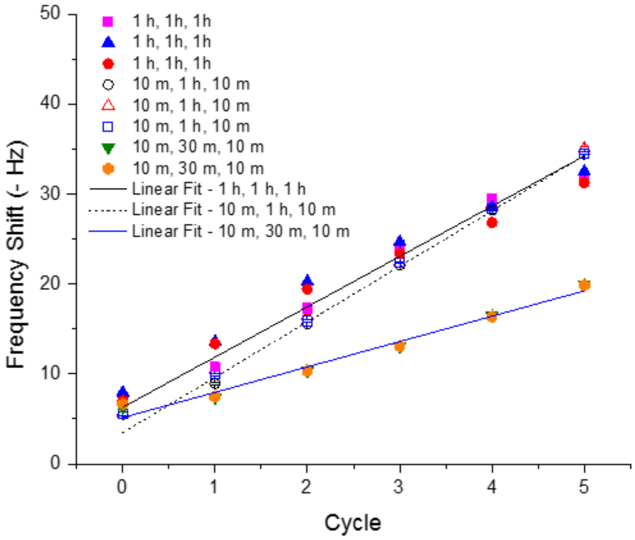

Figure 74. Summary of film growth studies with varied precursor incubation times. Only the frequency shift of amine-terminated surfaces are shown. Incubation times in the plot legend were reported as the following: aminosilane, polyacrylate, and polyamine. The aminosilane incubation was only performed once, as cycle 0. Polyacrylate and polyamine were iteratively applied for continued film growth. The overall film growth resulted in little change when the aminosilane and polyamine reaction steps were reduced from 1 hour to 10 minutes. A considerable reduction in growth occurred when the polyacrylate incubation was reduced to 30 minutes from 1 hour.

The relatively flat frequency shift during the chemisorption step suggested that incubation times for the aminosilane and the polyamine could be shortened, while maintaining the same film growth. That is, the aminosilane and polyamine precursors saturated the surface before the end of the hour-long incubation. Therefore, both amine functionalization steps were reduced to 10 minutes, each, and the overall film growth was monitored for the amine-terminated steps (**Figure 74**). Quantitative analysis of the film growth confirmed that the growth was linear and equivalent to the 1-hour incubation conditions (6.2 ± 0.7 (- Hz)/cycle). Time per cycle for this coating process was approximately 85 min/cycle. This result supported the hypothesis that the extent of surface functionalization was completed in less than an hour.

Next, the sensitivity of the overall film growth to the polyacrylate incubation time was studied by limiting it to 30 minutes (**Figure 74**). The resulting film growth rate, 2.8 ± 0.5 (- Hz)/cycle (approximate time per cycle was 55 min), was much smaller than the growth observed for 1 hour polyacrylate deposition. These results confirmed that the overall film growth was sensitive to the incubation time of the polyacrylate precursor. This result was in agreement with prior studies [5], which claimed that sterically-accessible amine groups were present after the 1 hour long acrylate incubation as a result of the incomplete surface coverage of the polyacrylate precursor, under the tested incubation conditions.

B.5 Conclusions

QCM has been used to monitor the film growth of a layer-by-layer dendritic amplification process for the first time. The precursor incubation times were reduced from one overnight step to 10 minutes, in the case of the aminosilane and 1 hour to 10 minutes, for the polyamine. The overall film growth (expressed as frequency shift per cycle) was sensitive to the incubation time for the polyacrylate step, resulting in a considerable decrease in film growth when the incubation time is reduced to 30 minutes from 1 hour. Further study could apply viscoelastic modeling to better understand the film deposition for this process. Additional work could examine the rate-limiting step for the coating process.

B.6 References

[1] J. P. Vernon, "Morphology-Preserving Chemical Conversion of Bioorganic and Inorganic Templates," Doctor of Philosophy, Materials Science and Engineering, Georgia Institute of Technology, Atlanta, GA, 2012.

[2] Y. N. Fang, J. D. Berrigan, Y. Cai, S. R. Marder, and K. H. Sandhage, "Syntheses of nanostructured Cu- and Ni-based micro-assemblies with selectable 3-D hierarchical biogenic morphologies," *Journal of Materials Chemistry,* vol. 22, pp. 1305-1312, 2012.

[3] Y. N. Fang, V. W. Chen, Y. Cai, J. D. Berrigan, S. R. Marder, J. W. Perry, *et al.*, "Biologically Enabled Syntheses of Freestanding Metallic Structures Possessing Subwavelength Pore Arrays for Extraordinary (Surface Plasmon-Mediated) Infrared Transmission," *Advanced Functional Materials,* vol. 22, pp. 2550-2559, Jun 2012.

[4] M. R. Weatherspoon, M. B. Dickerson, G. Wang, Y. Cai, S. Shian, S. C. Jones, *et al.*, "Thin, conformal, and continuous SnO2 coatings on three-dimensional biosilica templates through hydroxy-group amplification and layer-by-layer alkoxide deposition," *Angewandte Chemie-International Edition,* vol. 46, pp. 5724-5727, 2007.

[5] G. J. Wang, Y. N. Fang, P. Kim, A. Hayek, M. R. Weatherspoon, J. W. Perry, *et al.*, "Layer-By-Layer Dendritic Growth of Hyperbranched Thin Films for Surface Sol-Gel Syntheses of Conformal, Functional, Nanocrystalline Oxide Coatings on Complex 3D (Bio)silica Templates," *Advanced Functional Materials,* vol. 19, pp. 2768-2776, Sep 2009.

[6] F. Hook, "Development of a novel QCM technique for protein adsorption studies," Ph.D. , Department of Biochemistry and Biophysics
Department of Applied Physics, Chalmers University of Technology, Goteborg, Sweden, 1997.

[7] F. Hook, B. Kasemo, T. Nylander, C. Fant, K. Sott, and H. Elwing, "Variations in coupled water, viscoelastic properties, and film thickness of a Mefp-1 protein film during adsorption and cross-linking: A quartz crystal microbalance with dissipation monitoring, ellipsometry, and surface plasmon resonance study," *Analytical Chemistry,* vol. 73, pp. 5796-5804, Dec 2001.

[8] M. Edvardsson, Ed., *Q-Sense E4 Operator Manual*. Sweden: Q-Sense, 2010, p.^pp. Pages.

APPENDIX C: Recommendations for the Application of Layer-by-Layer Emissive Coatings to *Morpho rhetenor* Butterfly Wings

Wing sections for the *M. rhetenor* were relatively delicate. This posed a challenge for coating numerous cycles onto the same wing section. Handling wing sections with tweezers can destroy the scale features responsible for structural coloration and rip the wing section into many, smaller pieces. Copper and stainless still clips (McMaster Carr, GA, USA) were used in an attempt to hold the wing sections in place over a glass slide, reducing wing section handling. However, the *M. rhetenor* wing sections still ripped due to movement of the wing section during wash steps. Additional contamination issues occurred with both copper and stainless steel clips upon prolonged incubation in ethanol and amine-containing/ethanol solutions. The solution and wing section would turn blue (for copper clips) and dark yellow/brown (for stainless steel clips). Further use of metal clips was abandoned for this reason.

Use of the petri dish system, described in Chapter 2 is recommended. However, the use of permanent marker to mark such containers for each processing step (aminosilane, polyacrylate, polyamine, etc.) is not recommended. Ethanol will easily solvate the marker residue, greatly increasing the potential for contamination. Post-it® notes (3M, MN, USA) were used to designate containers which were not in use, which prevented container mix-up and contamination, as the post-it notes were never exposed to solvents.

APPENDIX D: Replicate Emission and Reflection Alteration Experiments for Organic Fluorescent Dye and Quantum Dot Multilayers

Separate sets of *Morpho rhetenor* wing sections were coated with, both, organic fluorescent dye and quantum dot multilayers. Emission and reflection analyses for each coating process confirmed the same trends reported in **Chapter 2** and **3**. Emission intensity increased and peak reflected wavelength red shifted as the number of organic fluorescent dye-containing multilayers increased (**Figure 75 (a, b)**), up to 7 cycles. Emission intensity increased and peak reflected wavelength red shifted as the number of quantum dot-containing multilayers increased (**Figure 75 (a, b)**), up to 8 cycles.

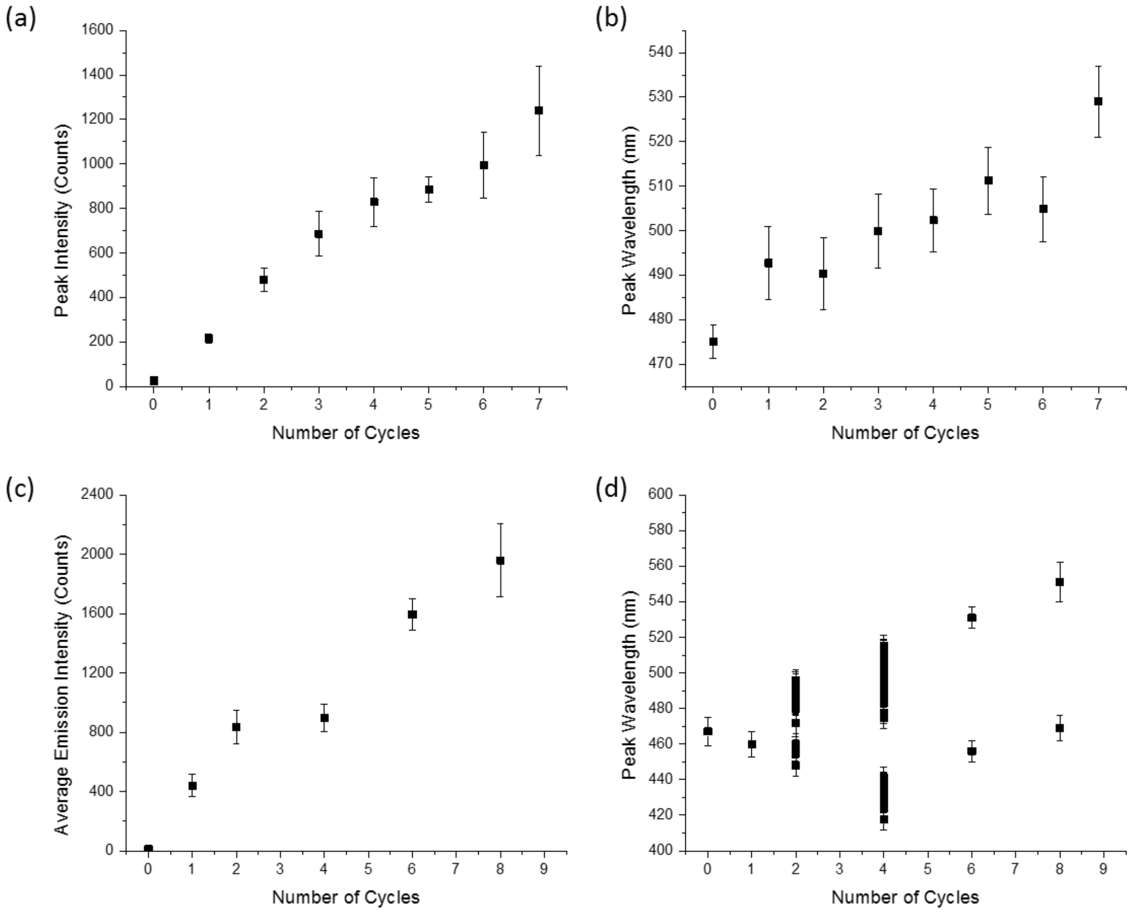

Figure 75. Replicate organic fluorescent dye and quantum dot multilayers applied to the scales of *Morpho rhetenor*. (a) Emission intensity and (b) peak wavelength as a function of applied organic dye-containing layers. (c) Emission intensity and (d) peak wavelength as a function of applied quantum dot-containing layers.

VITA

Craig Granberry Cameron

Craig Granberry Cameron was born to Hugh and Nancy Cameron in 1988. He graduated from Sterling High School (Sterling, Illinois) in 2005. He then continued a Cameron family tradition by becoming a 3rd generation Purdue engineer. In May 2009, he graduated with a Bachelors of Science degree in Chemical Engineering with 2-years under the guidance of Dr. Hugh Hillhouse in research for nanostructured photovoltaics. He continued his engineering education under the guidance of Dr. Kenneth H. Sandhage in the School of Materials Science and Engineering at the Georgia Institute of Technology in Atlanta, GA in the fall of 2009. Craig was awarded the Department of Defense SMART Scholarship for Service in April 2010. He will fulfill his service commitment to the U.S. Navy at the Naval Surface Warfare Center (NSWC) in Crane, Indiana upon completion of graduation requirements in May 2014. When not working on research, Craig enjoys photography, hiking, and playing with his two monster-sized dogs: Worf and Neelix.